

LONG SPANS WITH TRANSPORTABLE PRECAST PRESTRESSED GIRDERS

By

NATASSIA R. BRENKUS

A THESIS PRESENTED TO THE GRADUATE SCHOOL
OF THE UNIVERSITY OF FLORIDA IN PARTIAL FULFILLMENT
OF THE REQUIREMENTS FOR THE DEGREE OF
MASTER OF ENGINEERING

UNIVERSITY OF FLORIDA

2013

© 2013 Natassia R. Brenkus

To my family

ACKNOWLEDGMENTS

For their significant help and constant patience, I would like to thank the entire team of the FDOT Structures Research Center. I would also like to thank Dr. Trey Hamilton, for helping me get here.

TABLE OF CONTENTS

| | <u>page</u> |
|--|-------------|
| ACKNOWLEDGMENTS..... | 4 |
| LIST OF TABLES..... | 8 |
| LIST OF FIGURES..... | 10 |
| ABSTRACT | 18 |
| CHAPTER | |
| 1 INTRODUCTION | 20 |
| 2 LITERATURE REVIEW | 22 |
| 2.1 History of Spliced Concrete Girders | 22 |
| 2.2 Current Design Practice: Continuity vs. Simple Span Design | 24 |
| 2.3 Advantages of Long-span Precast Concrete Girders | 26 |
| 2.4 Disadvantages of Long-span Precast Concrete Girders | 29 |
| 2.5 Current Construction Techniques: Splice Types | 30 |
| 2.6 Current Construction Techniques: Assembly | 36 |
| 2.7 Current Construction Techniques: Design | 39 |
| 2.8 Prestressing Strand Couplers | 42 |
| 3 PROTOTYPE DESIGN–FIB96 | 47 |
| 3.1 Splice Conceptual Design | 47 |
| 3.2 Prototype Bridge and Beam | 49 |
| 3.3 Bridge Design Details..... | 50 |
| 3.4 Loads | 52 |
| 3.5 Prestressing Strand Pattern Design | 56 |
| 3.6 Moment-Curvature | 60 |
| 3.7 Splice Considerations | 63 |
| 4 STRAND COUPLER SELECTION AND TESTING | 64 |
| 4.1 Ultimate Strength Tests of 0.6-in. Diameter Coupler | 65 |
| 4.2 Calibration of 0.5-in. Diameter Coupler | 69 |
| 5 TEST SPECIMEN DESIGN | 72 |
| 5.1 Detailing Considerations | 74 |
| 5.2 Flexure Service and Cracking Test Design | 80 |
| 5.3 Moment Strength Test Design..... | 83 |
| 5.4 Shear Test Design | 87 |

| | | |
|------|---|-----|
| 5.5 | Fatigue Test Design | 89 |
| 6 | SPECIMEN CONSTRUCTION AND SPLICE ASSEMBLY | 93 |
| 6.1 | Segment Production..... | 93 |
| 6.2 | Segment Assembly Frames | 98 |
| 6.3 | Segment Alignment Procedure | 99 |
| 6.4 | Strand Stressing..... | 105 |
| 6.5 | Formwork and Concrete Placement..... | 106 |
| 6.6 | Splice Modifications | 110 |
| 7 | TEST PROCEDURE AND INSTRUMENTATION | 113 |
| 7.1 | Construction and Splice Assembly | 113 |
| 7.2 | Flexure | 119 |
| 7.3 | Shear | 122 |
| 7.4 | Fatigue | 126 |
| 8 | PRESTRESS LOSSES..... | 130 |
| 9 | SPLICE ASSEMBLY RESULTS AND DISCUSSION | 142 |
| 10 | FLEXURAL RESULTS AND DISCUSSION | 154 |
| 10.1 | Flexure–XC..... | 154 |
| 10.2 | Flexure–X1 | 158 |
| 10.3 | Service and Cracking Behavior..... | 161 |
| 10.4 | Comparison of Flexure Strength..... | 171 |
| 11 | SHEAR RESULTS AND DISCUSSION | 176 |
| 11.1 | Shear–SC | 176 |
| 11.2 | Shear–SB | 178 |
| 11.3 | Shear–SU | 182 |
| 11.4 | Shear–SU2 | 185 |
| 11.5 | Comparison of Service and Cracking Behavior | 189 |
| 11.6 | Comparison of Shear Strength | 200 |
| 12 | FATIGUE RESULTS AND DISCUSSION..... | 206 |
| 12.1 | Specimen FC..... | 206 |
| 12.2 | Specimen F1..... | 216 |
| 12.3 | Specimen F2..... | 227 |
| 12.4 | Discussion and Comparison of Behavior | 238 |
| 13 | DISCUSSION AND OBSERVATIONS..... | 256 |
| 13.1 | Closure Pour Observations..... | 257 |

| | | |
|------|------------------------------|-----|
| 13.2 | Coupler Observations | 260 |
| 14 | SUMMARY AND CONCLUSIONS..... | 261 |
| | LIST OF REFERENCES | 264 |
| | BIOGRAPHICAL SKETCH..... | 269 |

LIST OF TABLES

| <u>Table</u> | <u>page</u> |
|---|-------------|
| 3-1 Typical FIB96 section properties | 52 |
| 3-2 Non-composite dead loads | 53 |
| 3-3 Composite dead loads | 53 |
| 3-4 Design limit states | 55 |
| 3-5 Summary of Service I limit states (precast segments at release)..... | 58 |
| 3-6 Summary of Service I limit states (deck placement)..... | 58 |
| 3-7 Summary of Service I limit state check at the extreme top fiber..... | 59 |
| 3-8 Summary of Service III limit state check at the extreme bottom fiber..... | 59 |
| 3-9 Fatigue limit state check at the extreme bottom fiber at splice..... | 59 |
| 3-10 Strength I flexure and shear checks for spliced length..... | 60 |
| 3-11 Strength II flexure and shear checks for spliced length..... | 60 |
| 4-1 0.5-in. dia. coupler calibration load procedure | 70 |
| 5-1 Stress state of FIB96: Serviceability..... | 81 |
| 5-2 Stress state of test specimen: Serviceability | 81 |
| 5-3 Stress state of FIB96: Fatigue..... | 90 |
| 5-4 Stress state of test specimen: Fatigue | 91 |
| 5-5 Loading procedure: Fatigue | 91 |
| 6-1 Construction and testing schedule | 96 |
| 6-2 Specimen identification | 97 |
| 7-1 Spliced specimens | 119 |
| 7-2 Fatigue specimen load procedure..... | 129 |
| 8-1 Jacking prestress | 133 |
| 8-2 Measured initial prestress | 134 |

| | |
|---|-----|
| 8-3 Measured effective prestress | 134 |
| 8-4 Measured prestress losses | 135 |
| 8-5 PCI prestress losses | 136 |
| 8-6 Effective prestress force by decompression..... | 140 |
| 9-1 Spliced specimens: strand loads per load cell | 148 |
| 11-1 First crack of shear specimens..... | 190 |
| 11-2 Shear specimens' ultimate behavior at vertical interface | 203 |
| 12-1 F1: Stress ranges measured during fatigue cycling | 240 |
| 12-2 F2: Stress ranges measured during fatigue cycling | 241 |
| 12-3 Ductility ratios..... | 251 |
| 13-1 Flexural cracking behavior | 256 |
| 13-2 Web shear cracking | 257 |

LIST OF FIGURES

| <u>Figure</u> | <u>page</u> |
|--|-------------|
| 2-1 Precast segmented spans used with simple supports..... | 26 |
| 2-2 Curved roadway constructed with spliced girders | 27 |
| 2-3 Nonprestressed reinforcement CIP splice | 30 |
| 2-4 Post-tensioned CIP splice | 32 |
| 2-5 Post-tensioned duct for CIP splice | 33 |
| 2-6 Gandy bridge splice connection detail..... | 34 |
| 2-7 Stitched splice..... | 35 |
| 2-8 Match-cast splice | 36 |
| 2-9 Launching assembled girder using trolley | 37 |
| 2-10 Prestressing against internal restraint | 39 |
| 2-11 Shear keys required by AASHTO-LRFD | 40 |
| 2-12 204th Street Bridge | 42 |
| 2-13 Prestressing strand coupler types | 43 |
| 2-14 Turnbuckle-style coupler | 44 |
| 2-15 Repair of severed strand using a coupler..... | 44 |
| 3-1 Prototype splice design | 48 |
| 3-2 Elevation view of FIB96 with two splices..... | 49 |
| 3-3 Prototype design | 50 |
| 3-4 Composite section..... | 52 |
| 3-5 Strand layouts | 57 |
| 3-6 Moment-curvature of FIB96: Continuous strand vs. coupled strand..... | 61 |
| 3-7 FIB96 strain at flexural capacity: Continuous vs. coupled strand | 62 |
| 4-1 Turnbuckle-style coupler components..... | 64 |

| | |
|--|-----|
| 4-2 SMO tensile tests of 0.6-in. dia. coupler..... | 66 |
| 4-3 Strand rupture of 0.6-in. dia. coupler..... | 66 |
| 4-4 UF tensile test set-up of 0.6-in. dia. coupler..... | 67 |
| 4-5 Comparison of 0.6-in. dia. coupler and strand behavior..... | 68 |
| 4-6 Stress-strain models and test data for coupled and continuous strand..... | 69 |
| 4-7 SMO tensile test set-up of 0.5-in. dia. coupler | 70 |
| 4-8 Coupler strain gage calibration..... | 71 |
| 5-1 AASHTO II cross-section | 73 |
| 5-2 Test specimens..... | 74 |
| 5-3 Detailing considerations | 75 |
| 5-4 Bracket attachment to beam | 76 |
| 5-5 Shear keys in test specimen | 78 |
| 5-6 Rebar coupler..... | 80 |
| 5-7 Protruding strand..... | 80 |
| 5-8 Flexure test set-up | 82 |
| 5-9 Simplified bottom flange of FIB96 cross-section | 85 |
| 5-10 Material properties of 270-ksi lo-lax strand | 86 |
| 5-11 FIB96 prototype vs. AASHTO II test specimen: strain state at flexural capacity .. | 86 |
| 5-12 Shear test set-up..... | 88 |
| 6-1 Bed layout | 94 |
| 6-2 Coped region of bonded segments | 95 |
| 6-3 Segments after concrete is cast with top roughened for deck placement | 96 |
| 6-4 Elevation of assembly frames | 98 |
| 6-5 Photo and schematic of splice assembly frame and beam segments..... | 100 |
| 6-6 Coupler installation on unbonded strand..... | 101 |

| | | |
|------|--|-----|
| 6-7 | Coupled strand prior to prestressing | 102 |
| 6-8 | Coupled stirrups | 102 |
| 6-9 | Extend plunger | 103 |
| 6-10 | Detensioning chair, chucks, and load cells on the unbonded segment | 103 |
| 6-11 | Tightening the turnbuckles to seat detensioning chair | 104 |
| 6-12 | Tightening the turnbuckles | 105 |
| 6-13 | Splice stressed with lock-nuts engaged | 106 |
| 6-14 | Closure pour formwork in place..... | 107 |
| 6-15 | Seams sealed | 107 |
| 6-16 | Pouring the closure | 108 |
| 6-17 | Top of finished closure pour..... | 108 |
| 6-18 | Formwork removed | 109 |
| 6-19 | Splice complete..... | 110 |
| 6-20 | Closure face | 111 |
| 6-21 | Additional stirrup | 111 |
| 6-22 | Epoxy in closure pour..... | 112 |
| 7-1 | Gaged stirrup locations | 114 |
| 7-2 | Placement of VWSG | 115 |
| 7-3 | VWSG installation near centroid of strand pattern | 115 |
| 7-4 | Splice assembly: Instrumentation in closure joint..... | 117 |
| 7-5 | Splice assembly: Coupler strain..... | 117 |
| 7-6 | Splice assembly: Vertical displacement gages..... | 118 |
| 7-7 | Splice assembly: Longitudinal displacement string-pots | 118 |
| 7-8 | Four-point flexural test set-up | 120 |
| 7-9 | Flexure: Vertical displacement gages | 121 |

| | |
|--|-----|
| 7-10 Flexure: Out-of-plane displacement gages | 121 |
| 7-11 Spliced beams: Load cells | 122 |
| 7-12 Spliced shear test set-ups..... | 123 |
| 7-13 Control shear test set-up..... | 124 |
| 7-14 Shear: Vertical displacement gages..... | 125 |
| 7-15 Fatigue test set-up | 127 |
| 7-16 Fatigue: Vertical displacement gages | 128 |
| 8-1 Prestress force | 131 |
| 8-2 Measured prestress losses vs. PCI..... | 137 |
| 8-3 Decompression strain gages..... | 138 |
| 8-4 Decompression | 139 |
| 9-1 Load history of X1 | 142 |
| 9-2 Stressing procedure | 143 |
| 9-3 Strand load..... | 144 |
| 9-4 Strand load based on calibrated coupler strain | 145 |
| 9-5 Tie-down deflections | 146 |
| 9-6 Support deflections | 147 |
| 9-7 STM: assumed dimensions..... | 149 |
| 9-8 Tie strain | 150 |
| 9-9 Strain in top flange | 152 |
| 9-10 Transfer length strain | 153 |
| 10-1 XC: Ultimate | 154 |
| 10-2 XC: First crack at midspan | 155 |
| 10-3 XC: Permanent set..... | 156 |
| 10-4 XC: Compressive concrete strain at midspan | 157 |

| | | |
|-------|---|-----|
| 10-5 | XC: Midspan strain profile | 157 |
| 10-6 | X1: Ultimate..... | 158 |
| 10-7 | X1: Vertical crack at interface | 159 |
| 10-8 | X1: Superficial cracks at overlap | 159 |
| 10-9 | X1: Flexural cracking..... | 160 |
| 10-10 | X1: Deck strain..... | 161 |
| 10-11 | XC and X1: Elastic behavior..... | 162 |
| 10-12 | XC: VWSG vs. bottom flange strain gage | 164 |
| 10-13 | XC vs. X1: first crack..... | 166 |
| 10-14 | Dry joint interface post-demolition..... | 167 |
| 10-15 | XC vs. X1: final cracking patterns | 168 |
| 10-16 | X1: String-pots across closure | 169 |
| 10-17 | X1: Opening at joint during test..... | 170 |
| 10-18 | Out-of-plane displacement..... | 171 |
| 10-19 | XC and X1: Flexural Strength | 172 |
| 10-20 | Damage to X1 following testing with spalled concrete in compression zone and wide, permanent crack | 173 |
| 10-21 | X1: Strand load | 174 |
| 11-1 | SC: Ultimate..... | 176 |
| 11-2 | SC: Crack pattern..... | 177 |
| 11-3 | SC: Strain at load point | 178 |
| 11-4 | SB: Ultimate | 179 |
| 11-5 | SB: First crack..... | 179 |
| 11-6 | SB: Strand slip | 180 |
| 11-7 | SB: Deck at failure | 181 |
| 11-8 | SB specimen: Strain at load point..... | 181 |

| | | |
|-------|--|-----|
| 11-9 | SU: Ultimate | 182 |
| 11-10 | SU: First crack..... | 183 |
| 11-11 | SU: Joint at failure..... | 184 |
| 11-12 | SU: Strain at load point | 184 |
| 11-13 | SU2: Ultimate | 185 |
| 11-14 | SU2: First crack..... | 186 |
| 11-15 | SU2: Flexural crack at 149 kip | 187 |
| 11-16 | SU2: Joint at failure..... | 188 |
| 11-17 | SU2: Strain at load point | 188 |
| 11-18 | Bond patterns of shear tests | 189 |
| 11-19 | Shear comparison: Elastic behavior..... | 190 |
| 11-20 | Shear specimens: First crack locations..... | 191 |
| 11-21 | SC vs. SB: Crack pattern | 193 |
| 11-22 | SU vs. SU2: Crack pattern | 194 |
| 11-23 | SU2: Bottom strain at vertical crack location..... | 195 |
| 11-24 | SU2: Strand load..... | 196 |
| 11-25 | Coupler strain gages | 197 |
| 11-26 | SU: Strand load..... | 198 |
| 11-27 | Post-test: End view of unbonded segment..... | 199 |
| 11-28 | Ultimate behavior | 201 |
| 11-29 | Shear location of interest | 203 |
| 12-1 | FC: Static conditioning | 207 |
| 12-2 | FC: First crack..... | 207 |
| 12-3 | FC: Decompression load cycles..... | 208 |
| 12-4 | FC: Decompression strain readings | 209 |

| | |
|--|-----|
| 12-5 FC: Fatigue | 210 |
| 12-6 FC: Ultimate | 212 |
| 12-7 FC crack progression | 213 |
| 12-8 FC: Ultimate | 215 |
| 12-9 FC strand | 216 |
| 12-10 F1: Static conditioning..... | 217 |
| 12-11 F1: Joint opening..... | 217 |
| 12-12 F1: Coupler strain..... | 218 |
| 12-13 F1: Decompression load cycles | 219 |
| 12-14 F1: Decompression strain readings..... | 220 |
| 12-15 F1: Fatigue | 221 |
| 12-16 F1: Ultimate..... | 223 |
| 12-17 F1: Crack pattern | 224 |
| 12-18 F1: Ultimate..... | 224 |
| 12-19 F1: Post-failure..... | 225 |
| 12-20 F1: Deck strain | 226 |
| 12-21 F1 | 227 |
| 12-22 F2: Precrack..... | 228 |
| 12-23 F2: First crack | 228 |
| 12-24 F2: Precrack coupler strain | 229 |
| 12-25 F2: First cracks with strain gages..... | 230 |
| 12-26 F2: Static load cycles | 231 |
| 12-27 F2: Decompression strain readings..... | 232 |
| 12-28 F2: Fatigue | 233 |
| 12-29 F2: Cracking after 2 million cycles..... | 234 |

| | | |
|-------|---|-----|
| 12-30 | F2: Ultimate..... | 235 |
| 12-31 | F2 crack progression..... | 235 |
| 12-32 | F2: Deck strain..... | 237 |
| 12-33 | F2..... | 237 |
| 12-34 | F1: Cracks at start of fatigue..... | 238 |
| 12-35 | F2: Cracks at start of fatigue..... | 242 |
| 12-36 | F2: Section degradation due to fatigue..... | 244 |
| 12-37 | Fatigue: Deflection at start and end of tests..... | 245 |
| 12-38 | Post-fatigue failure: FC, F1 and F2..... | 246 |
| 12-39 | AASHTO: FC, F1, and F2..... | 248 |
| 12-40 | Static vs. Post-fatigue failure: Control specimens..... | 249 |
| 12-41 | Static vs. Post-fatigue failure: Spliced specimens..... | 249 |
| 12-42 | F1: Post-failure..... | 252 |
| 12-43 | F1: Wedge seating..... | 252 |
| 12-44 | F2: Post-failure..... | 253 |
| 12-45 | F2: Fatigue wear..... | 253 |
| 12-46 | F1: Load cells..... | 254 |
| 12-47 | F2: Load cells..... | 255 |
| 13-1 | Bond at vertical interface..... | 258 |
| 13-2 | F2: Concrete intruding into unbonded length..... | 258 |
| 13-3 | SB: Void at reentrant corner..... | 259 |
| 13-4 | Shear keys..... | 260 |
| 13-5 | SU..... | 260 |

Abstract of Thesis Presented to the Graduate School
of the University of Florida in Partial Fulfillment of the
Requirements for the Degree of Master of Engineering

LONG SPANS WITH TRANSPORTABLE PRECAST PRESTRESSED GIRDERS

By

Natassia R. Brenkus

December 2013

Chair: Homer R. Hamilton, III
Major: Civil Engineering

A splice design for prestressed precast segments was developed and integrated into a simply-supported 208-ft span of 96-in.-deep I-girders. In the proposed splice design, transportable segments are pretensioned at a precast yard, and the strands are cut prior to transport and then spliced on site. Prestressing force is applied to the system by a hydraulic jack on each side of the girder web. External brackets transfer the force from the hydraulic jacks to the precast segments by thru-bolts that pass through the web of the beam. The internal restraint provided by the coupled prestressing strand resists the jacking force, and the prestressing strand is stressed.

Due to limitations in laboratory capabilities and research budget, behavioral aspects of the splice deemed most critical were tested using an AASHTO Type II cross-section; due to its smaller size, it was possible to construct duplicate test specimens to assess its constructability as well as its behavior under load.

Nine precast pretensioned beam specimens were constructed and tested to evaluate the splice assembly procedure behavior: three control specimens and six spliced specimens. Fifteen precast prestressed segments were constructed at a precast facility. The precast segments were then transported to the FDOT Structures Research

Lab where six spliced specimens were assembled, the splices stressed, and closures poured. Decks were poured on all specimens. Though labor-intensive, the prestressed splice concept was constructible.

Load testing of the completed specimens was conducted to evaluate flexural, shear, and fatigue behavior. Prestress losses were measured and cracking development was observed to assess service behavior. Additional component testing of the coupler used in the splice design was performed at the State Materials Office.

Flexural strength of spliced specimens exceeded the AASHTO-LRFD predicted values for bonded strand (15%) and unbonded strand (24%). Shear behavior was evaluated by testing a high moment-to-shear ratio (of 3.7). In the one specimen that did exhibit the characteristics of a shear failure, the exhibited shear strength exceeded that calculated per AASHTO-LRFD modified compression field theory. All other specimens tested in the shear set-up failed in flexure. Fatigue of spliced specimens did not impact the strength or deflection at ultimate; it did affect ductility and failure mode.

CHAPTER 1 INTRODUCTION

Due to truck weight limitations restricting their transport, simply-supported prestressed bridge girder spans have been limited to approximately 180 ft. Splice connections allow longer span bridges to be constructed using shorter, lighter segments that are assembled prior to or during final erection. Spliced girders, however, have typically been designed to span continuously over the supports. Providing continuity at the supports while ensuring redundancy of design and increased material efficiency requires consideration of the stresses generated by time-dependent movements over its life span. The designer must carefully check and accommodate stress changes due to thermal effects, creep, shrinkage, and secondary moments. On the other hand, simple-span designs may reduce the amount of up-front design time required. Furthermore, such systems may prove more accommodating for vertical and horizontal curves in the span.

The recent development and implementation of the new Florida I-beams (FIB) have introduced several new sections capable of achieving spans longer than currently transportable as single pieces. The new FIB96, for example, is capable of spanning a maximum of 208 ft with 8.5-ksi concrete; using 10-ksi concrete, the maximum span is estimated at 215 ft (FDOT Temporary Design Bulletins C09-01 and C09-05). Depending on the specified concrete strength, additional FIB sections are capable of achieving spans beyond 190 ft, the currently transportable length. As AASHTO and Florida bulb-tee sections will not be used in future FDOT projects, available sections for use as a prototype for the splice design were limited to the new Florida I-beams.

The objectives of this research were to identify potential splice techniques to lengthen the span of transportable precast prestressed concrete girders and to develop and test a splice design. A literature review was conducted to identify current construction practices, splice types, and design systems used to lengthen the span of transportable precast prestressed concrete girders. A review of research and past designs using splice connections was also performed (Chapter 2). A prototype design using the FIB96 section was then developed (Chapter 3) along with a number of possible splice configurations. A coupler component for the splice design was tested; results are presented in Chapter 4. From the FIB96 prototype, a scaled test specimen was designed and tested. The specimen and splice designs are reported in Chapter 5, with the specimen construction and splice assembly details included in Chapter 6. Test procedures and instrumentation are covered in Chapter 7. Prestress loss measurements and splice assembly results are included in Chapters 8 and 9, respectively. Load tests were then conducted on the assembled specimens to determine flexural service and ultimate behavior (Chapter 10), shear behavior (Chapter 11), and fatigue performance (Chapter 12). Additional discussion is provided in Chapter 13. The research is then summarized along with key findings in Chapter 14. Recommendations are provided in Chapter 15.

CHAPTER 2 LITERATURE REVIEW

A literature review was conducted to identify current construction practices, splice types, and design systems used to lengthen the span of transportable precast prestressed concrete girders. Section 2.1 covers the history of spliced concrete girders. Section 2.2 covers the current design practices of both continuous and simple spans. The advantages and disadvantages of long-span precast concrete girders are covered in Sections 2.3 and 2.4, respectively. Current construction techniques of splice types, assembly, and design are cover in Sections 2.5, 2.6, and 2.7, respectively. A review of prestressing couplers is covered in Section 2.8.

2.1 History of Spliced Concrete Girders

Despite being more cost-effective and easier to maintain than steel superstructures, concrete has long been passed up for use in spans longer than 150 ft due to weight and length limitations preventing their transportation to the jobsite (Abdel-Karim and Tadros 1992). State highway and railway restrictions (imposed by the weight limits of currently in-use bridges) prevent the transport of these massive girders (Abdel-Karim and Tadros 1992; Ralls et al. 2000; PCI 2004). In response, engineers have turned to the development of splice connections for precast concrete girders to reduce segments to more manageable sizes.

The use of a splice to lengthen the span of concrete girders first appeared in the 1950s, while spliced precast concrete segments have been in use since the 1960s as segmental box girders (Lacey et al.1971). In 1968, the Precast/Prestressed Concrete Institute (PCI) published a report encouraging the use of precast segments in spliced construction, presenting many advantages of precast construction, as well as some

design guidance for precast splices. The collective standardization of girder section geometry by AASHTO, PCI, and the Bureau of Public Roads in the 1960s further advanced the use of precast segments in highway bridge construction (Ralls et al. 2000). In 1982, a joint PCI-PTI committee published “Recommended Practice for Precast Post-Tensioned Segmental Construction” (Joint PCI-PTI Committee 1982). Over the years, the technique of splicing precast concrete girders has been used more frequently, with other innovations such as high-performance concrete, optimized section geometries and advances in pre- and post-tensioning techniques allowing the use of longer spans. Rabbat and Russell (1982) proposed optimized I-girder sections. Lounis et al. (1997) proposed optimized bulb-tee sections for conventional and segmental post-tensioned construction.

Nevertheless, despite a growing body of research and limited implementation by some state transportation departments, utilization of long-span splicing has not become widespread. Instead, knowledge gained and techniques used have remained mostly job-specific, and have not been made widely available to the engineering community for use on similar projects. In an effort to disseminate a collection of information on prior projects, as well as provide design recommendations and standardized specifications, the Transportation Research Board published NCHRP Report 517 in 2004. Ultimately, research has found that incremental changes in conventional design methods and materials result in relatively small increases in span, but splicing techniques can increase the span lengths of precast prestressed concrete girders greatly. The advantages of spliced concrete girders have encouraged increasing use and further research. (Castrodale and White 2004)

2.2 Current Design Practice: Continuity vs. Simple Span Design

Lounis et al. (1997) noted a change in the design trend from simple-span to continuous-span bridge girders. This change allowed longer spans and the elimination of costly and difficult to maintain deck joints (Lounis et al. 1997). According to the PCI Bridge Manual, simple-spans have some performance issues, citing beam end rotation at the piers. This rotation results in significant cracking of the deck, allowing water to leak through the deck and cause corrosion of the reinforcing steel and deterioration of the beam ends (PCI 2004). Elimination of the deck joint enhances deck durability and minimizes maintenance and life cycle costs (Lounis et al. 1997); continuity designs are more structurally efficient and perform better in the long term in certain types of construction (PCI 2004). The NCHRP Report 517 identified circumstances in which continuity designs were considered viable (Castrodale and White 2004):

1. Long span crossings, especially over waterways;
2. Sites with restricted overhead clearance;
3. Sites with limited substructure locations;
4. Designs where the reduction of pier quantity results in the most economical design.

By 2004, in a survey of several hundred spliced girder projects, Castrodale and White (2004) found that continuity designs account for a majority of spliced precast concrete (PCC) bridges in North America. In these continuous span designs, the splice location is chosen at the inflection point of the moment caused by dead load. Continuity is achieved through several methods: deck reinforcement, post-tensioning, or the use of coupling beams with either prestressing or nonprestressed high-strength rods (Ralls et

al. 2000). A common method of achieving continuity is through full-length post-tensioning (Abdel-Karim and Tadros 1992).

Advantages of continuous span designs include redundancy of design, elimination of deck joints, and material efficiency; however, continuity designs have their own drawbacks. Continuity designs are complex and require careful consideration of the long-term effects of camber and deflection caused by creep, shrinkage, thermal effects, and secondary moments. Furthermore, the on-site construction process for continuity designs is more labor-intensive than for simple spans.

In its review of projects in the United States, the NCHRP found spliced concrete girders to be most commonly used in multi-span continuous bridge designs.

Nevertheless, the committee suggests several applications where the use of spliced PCC girders in simple-span designs may be advantageous (Castrodale and White 2004):

1. Remote locations where midspan piers are impossible;
2. Situations where the available or preferred equipment is better suited to handle shorter spans;
3. Single-point urban interchanges, where an overpass bridge is used to span over another roadway without a midspan pier.

Jaber et al. (2006) reported on the design and construction of a Nebraska bridge using 207-ft simple span precast girders (Figure 2-1). The girders were constructed in three segments, thus making them transportable to the site by truck. The segment configuration was such that the wet-joints were located away from the midspan, allowing a reduction in the number of pretensioned strands in the outside segments. Segments were placed on the piers and two falsework towers located under the splices. Post-tensioning tendons with a parabolic profile were placed from end-to-end within the

span. The authors indicate that the final bridge cost was competitive with structural steel.

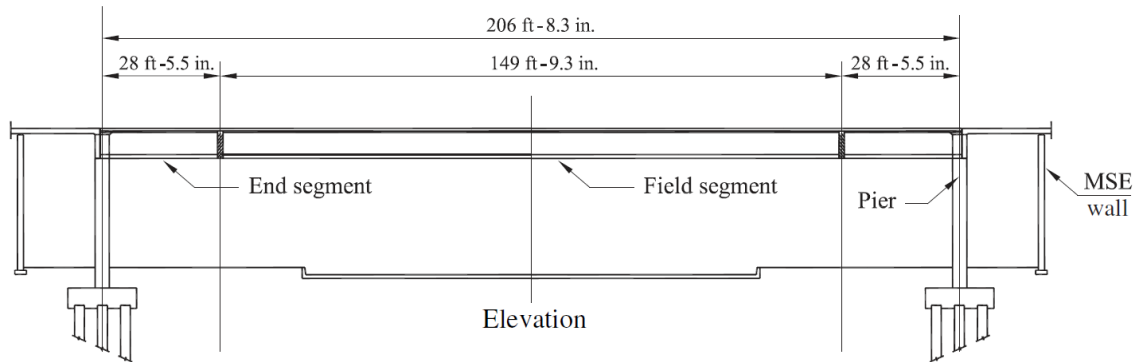


Figure 2-1. Precast segmented spans used with simple supports (Jaber et al. 2006).

2.3 Advantages of Long-span Precast Concrete Girders

One significant benefit of spliced long-span precast concrete girders is their ability to accommodate curved alignments (Figure 2-2). When a curve in the roadway is required, the splice location can be situated in order to provide a point of curvature between short segment lengths (PCI 2004). Similarly, spliced segments can be arranged such that the placement of the piers avoids obstacles on the ground, such as railroad tracks, utilities or other roadways (Castrodale and White 2004). Because the designer has more flexibility when specifying span lengths and locations of piers, spliced construction allows the placement of piers and spans as necessary for the geometry of the road (Weigel et al. 2003; PCI 2004).



Figure 2-2. Curved roadway constructed with spliced girders (Abdel-Karim and Tadros 1992b)

The utilization of PCC spliced girders for long spans offers multiple advantages over steel, including increased durability, rapid erection, condensed overall construction time, limited or no environmental impact, reduced cost, and simplified transportation of construction materials (Castrodale and White 2004; Abdel-Karim and Tadros 1992). Furthermore, steel sections require extensive maintenance and present potential environmental risk when being stripped and repainted; again, the use of spliced segmental construction permits concrete bridge girders appears to be an attractive alternative. In environmentally sensitive areas, such as Rock Cut Bridge in Washington, spliced PCC girders provide an ideal solution for eliminating risk to river wildlife (Nicholls and Prussack 1997).

When considering waterway bridges, the increased span length and subsequent elimination of some piers reduces susceptibility to scour, environmental impact, and the risk of barge collision and damage (Abdel-Karim and Tadros 1992). Furthermore, the use of fewer piers results in a reduction of both the quantity of shielding dolphins and

accumulated water-borne debris. In locations where minimal disturbance of the waterway is permitted (to reduce the impact on salmon runs, for example), mid-stream piers may not even be an option (Nicholls and Prussack 1997). In extreme marine environments, such as Florida, where scour is a primary concern, the reduction in the quantity of piers is a significant benefit of long-span construction (Ronald 2001).

Comparative costs of steel versus spliced precast concrete (PCC) designs have been investigated by several researchers. Abdel-Karim and Tadros (1992) presented two case studies of bridges in Kentucky, the use of a concrete superstructure instead of steel resulted in a savings of 25-35%. In a separate comparison of six bids—five steel designs and one spliced PCC design—for the construction of a bridge in South Carolina, the concrete design represented a possible savings in all but one bid. Although the most economical design presented was indeed steel, the overall trend of possible savings of up to 50% for the construction phase is noteworthy. Castrodale and White (2004) presented an estimated cost comparison for a number of bridges in North America.

The perceived potential savings of the spliced concrete designs have been large enough for contractors to request a spliced concrete design in favor of a steel superstructure design. (The longest spliced concrete span to date, the Moore Haven Bridge in Florida at 320 ft, was originally designed with a steel plate superstructure, but was redesigned as a spliced PCC span to reduce overall project cost.) (PCI 2004)

Beyond the construction phase, the use of spliced PCC girders provides further benefits. The use of a concrete superstructure in place of steel eliminates costly repainting, the costs (both economic and environmental) associated with the removal of

old paint, as well as the inconvenience of road closures. Abdel-Karim and Tadros noted that maintenance and repair costs were not taken into consideration during selection from the six bids for the South Carolina Bridge; if they had, the concrete design may have proven most cost-effective. Furthermore, with the current trend of rising steel prices, concrete construction is becoming ever more attractive.

In comparison with cast-in-place, precast concrete usually reduces overall construction costs. Because precast segments can be manufactured at the precast plant while the substructure is under construction at the jobsite, the construction work schedule can be significantly condensed. Precast segments also reduce the amount of time dedicated to the construction of formwork and other activities related to cast-in-place construction. The shortened construction schedule limits traffic delays and their associated labor costs.

Several state transportation departments, most notably Washington State Department of Transportation (WSDOT) and the Florida Department of Transportation (FDOT), have implemented the use of long span spliced PCC girders to accommodate longer spans. The WSDOT has been involved in a significant amount of research on spliced segmental construction. To this end, in 1998, WSDOT introduced several standard new deep I-beam sections optimized for use in spliced spans (Seguirant 1998).

2.4 Disadvantages of Long-span Precast Concrete Girders

Bridge construction making use of long-span precast concrete girders has some disadvantages. Most obviously, without the use of a splice connection, the extreme weight and length of single piece long-span girders restricts their transportation. When a splice connection eliminates this issue, there is increased jobsite labor, falsework, and

framing required to assemble the splice. If the splice connection is completed on the ground, there needs to be careful consideration of crane weight limitations.

Furthermore, long-span prestressed concrete girders require delicate handling to a degree not needed with long-span steel construction, as they exhibit a tendency to twist and deflect during handling and erection (Ronald 2001).

2.5 Current Construction Techniques: Splice Types

There are several types of concrete girder splices currently in use in highway bridge construction, the most common of which being the cast-in-place splice. Whereas the cast-in-place splice is not the most economical, it is the most popular due to its simple construction and flexibility with regards to field tolerances.

Both nonprestressed (conventional) reinforcement and prestressed cast-in-place splices are currently in use. During fabrication of either type of midspan cast-in-place splice, a temporary bent is constructed under the splice location. The two precast girder segments are lifted into place, meeting over the temporary bent. The closure pour is then formed, typically with a high-strength concrete. An example of a nonprestressed reinforcement splice is shown in Figure 2-3.

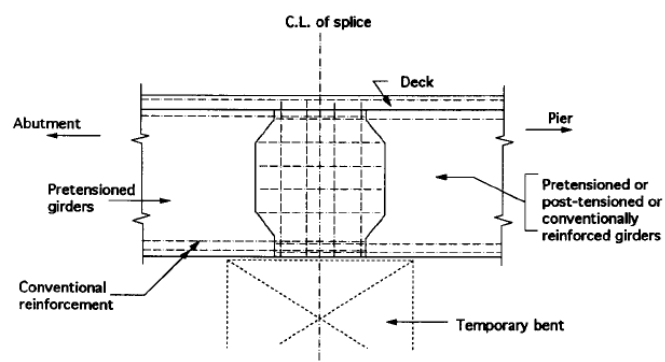


Figure 2-3. Nonprestressed reinforcement CIP splice (Abdel-Karim and Tadros 1992)

In simple-span construction, nonprestressed splices are located over the piers. The closure pour and deck concrete are poured simultaneously to create continuity over the supports for superimposed dead and live load cases. Under full service load, due to the lack of prestressing in the splice, the surface over the splice is expected to crack. To prevent or limit cracking, and the subsequent corrosion of the splice reinforcement, the designer must specify sufficient deck reinforcement. The splice must be long enough to provide a sufficient lap length of the reinforcing steel. In continuous systems, a nonprestressed splice is located at or near the inflection points of the moment diagram. Once the two girder segments are in place over the temporary bent, the projecting nonprestressed reinforcement is lapped together, and the closure pour is formed. (Abdel-Karim and Tadros 1992)

A typical post-tensioned cast-in-place splice is shown in Figure 2-4. After the post-tensioning ducts have been adequately aligned, the closure pour is formed at the splice location. After the splice concrete has cured, the post-tensioning strand is threaded through and stressed to the specified force. In comparison with nonprestressed splices, post-tensioned splices provide significant additional moment capacity.

Several issues must be considered when employing a post-tensioned cast-in-place splice. Frequently, standard I-girder sections must be modified to provide enough space for the PT duct, longitudinal reinforcement, shear stirrups, and code-mandated concrete cover; Florida bulb-tees with modified webs are commonly used in precast, prestressed spliced I-girder spans (Abdel-Karim and Tadros 1992; Ronald 2001). Accurate alignment of the PT duct is important to reduce the prestress losses caused by

friction. Rotation of the ends must be controlled by design to limit camber. Care must be taken not to damage the post-tensioning duct during erection; a damaged PT duct cannot be properly grouted. Without fully grouted tendons, the splice may incur additional prestress losses due to friction and may have reduced durability over its lifespan (FDOT 2004). Furthermore, care must be taken to completely seal the coupling zone and PT duct to prevent leakage of the post-tensioning grout and corrosion of the reinforcing steel (PCI 2004; FDOT 2004).

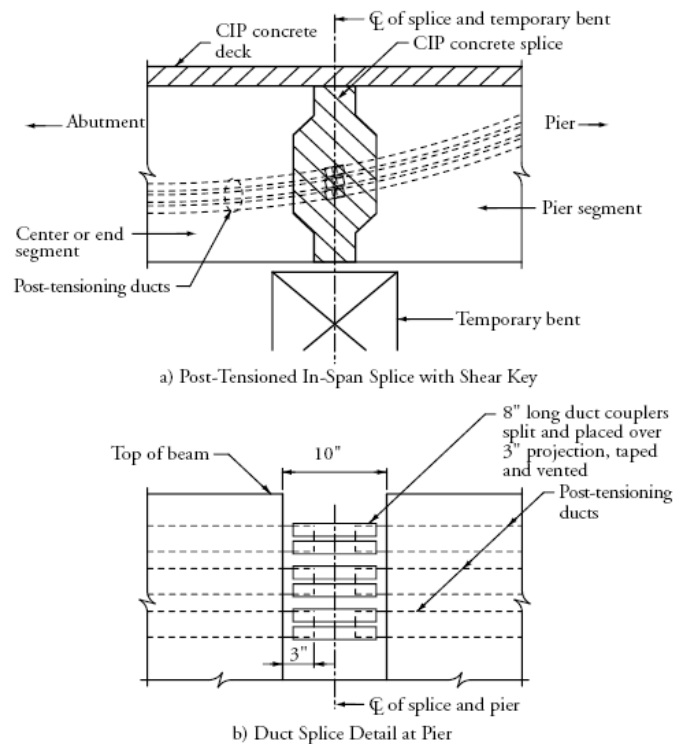


Figure 2-4. Post-tensioned CIP splice (PCI 2004)

Although cast-in-place splices are not the least expensive option (they require considerable jobsite labor), they are the most commonly used type of splice due to their simplicity and flexibility, accommodating fabrication and construction tolerances with ease; the permitted length of the gap between segments can be from 6 in. to 24 in.

(Abdel-Karim and Tadros 1992). The length of the closure pour was controlled by two considerations: the closure length must be sufficient to allow splicing of the conventional reinforcing steel and post-tensioning duct, but was limited to a length by the lack of prestressing steel and the small amount of longitudinal reinforcement (PCI 2004; Ronald 2001). Shear keys are commonly used in cast-in-place splices, such as those shown in Figure 2-3 and Figure 2-4, to provide mechanical interlock between two adjacent precast segments and the closure pour. Their presence also provides additional space in which to align the PT ducts and lap the reinforcing steel. (Ronald 2001)

The Westbound Gandy Bridge in Tampa, Florida is an example of a long span bridge with a cast-in-place post-tensioned splice. The center 234-ft channel span was formed by splicing four pairs of precast I-girder segments. Details of the PT duct and CIP splice connections are shown in Figure 2-5 and Figure 2-6, respectively.

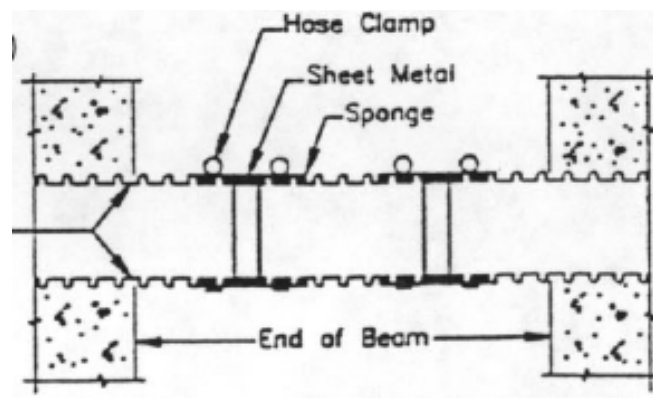


Figure 2-5. Post-tensioned duct for CIP splice (FDOT 1999)

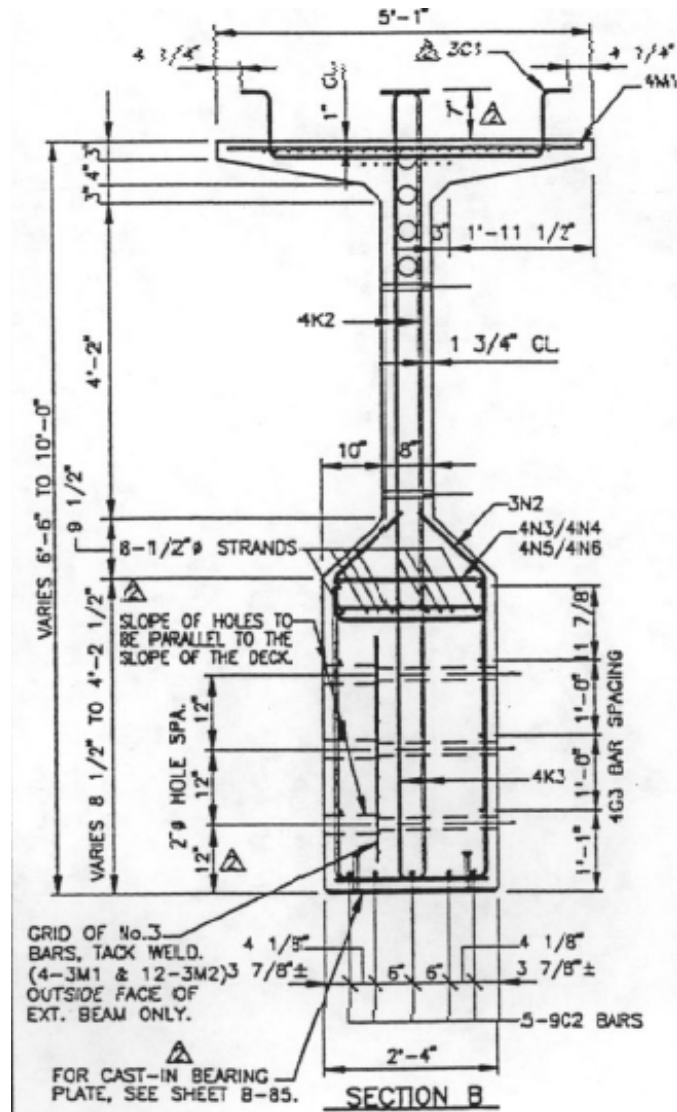


Figure 2-6. Gandy bridge splice connection detail (FDOT 1999)

Another type of cast-in-place splice currently in use is the stitched splice, in which short tendons or threaded bars are crisscrossed prior to post-tensioning. In this type of splice, the post-tensioned steel takes up only a short distance of the span, making this an attractive alternative for very long spans where full-length post-tensioning may be ineffective due to the large losses accumulated due to friction (PCI 2004). This method of splicing, however, has a few disadvantages. PT ducts must be quite large to accommodate the quantity of the prestressing steel and to provide

additional tolerance for alignment purposes. Furthermore, due to the short length of the prestressing steel, prestress losses during anchorage set may be large. Nevertheless, this method has been used in a few projects, such as the Shelby Creek Bridge in Kentucky (PCI 2004). An example of a stitched splice detail is shown in Figure 2-7.

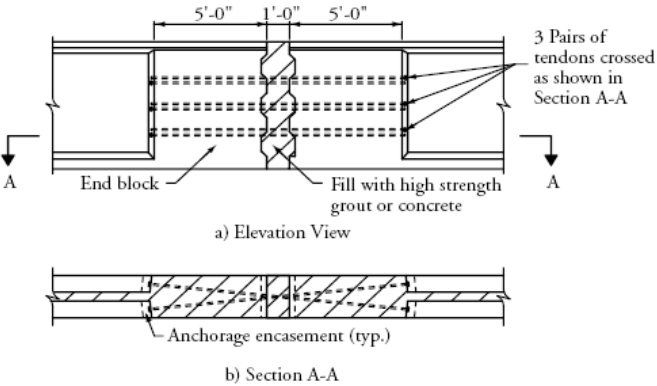


Figure 2-7. Stitched splice (PCI 2004)

Match-cast splices are an alternative to cast-in-place splices. This method eliminates the need for formwork and a closure pour at the construction site. Instead, the two girder segments are cast adjacent to each other in the precast yard, with a machined steel header precisely aligning the post-tensioning ducts and prestressing strands. After they have each cured, the segments are torch-cut through holes in the header, separated, and hauled to the construction site. On site, one of the segments is placed on its pier and a temporary bent. The second adjoining segment is then slid into place over the temporary pier, matching each segment's post-tensioning duct to form a continuous duct. Once reassembled, the small gap in the concrete is filled with epoxy and the girder surface is sealed. Tendons are then run through the splice and post-tensioned. Finally, the PT duct is grouted to protect the reinforcement against corrosion. An example match-cast splice detail is shown in Figure 2-8.

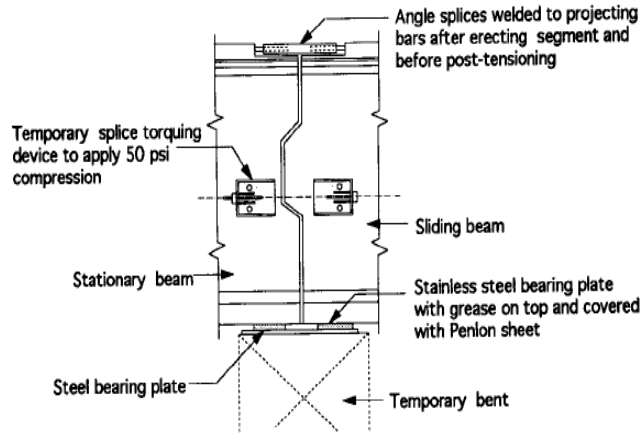


Figure 2-8. Match-cast splice (Abdel-Karim and Tadros 1992)

2.6 Current Construction Techniques: Assembly

Girders segments must be spliced either on the ground or in place (at the final elevation) with the aid of falsework. The preferred assembly location is on the ground if space and crane limits allow, as it eliminates costly temporary falsework. Additionally, construction of the splice on the ground allows easy access to materials and equipment that would otherwise have to be lifted to the mid-air splice location. When space allows, a secondary staging site is selected for assembly and post-tensioning of the girder. The staging site must be level to ensure that the splice is properly formed. Furthermore, sufficient space must be available to allow for maneuvering of the assembled girder during erection. The assembled girder is then transported from the staging site and lifted into place as a single piece. During the erection of the assembled girder, care must be taken to prevent damage to the splice; this method of erection is only recommended when the splice is post-tensioned again after final erection. Using this assembly technique, large-capacity lifting equipment and/or launching truss equipment may be required to handle the final piece weight. (Abdel-Karim and Tadros 1992)

If the weight of an assembled girder is excessive, or if site conditions do not allow the girder to be lifted, the entire girder assembly may be loaded onto a rolling trolley and moved laterally into place along a rail on an adjacent temporary structure. After sliding the girder onto the temporary support, two cranes, one on each end of the span, can then place the girder over the supports. An example of this procedure, as done during the construction of Rock Cut Bridge, is shown in Figure 2-9 (Nicholls and Prussack 1997; Joint PCI-PTI Committee 1982). For more details, see Nicholls and Prussack, 1997.



Figure 2-9. Launching assembled girder using trolley (Nicholls and Prussack 1997)

Alternatively, when a staging location is not available, the separate pieces are lifted into position and supported with either a strong-back assembly or temporary piers and falsework until the splice connections have been constructed and have reached the specified strength. The construction of a splice in-place requires accurate alignment of the two girder segments. Shimming of the temporary formwork may be necessary to

achieve accurate alignment of the post-tensioning ducts. To mitigate the costs, the temporary falsework can be constructed concurrently under all girder lines at the splice location, such that the pairs of girder segments can be spliced simultaneously. The primary advantage to this technique is the reduced handling of the girder segments. Another advantage is that the crane capacity need only be sufficient to handle the heaviest segment (Abdel-Karim and Tadros 1992). Despite these advantages, this method of erection is the least preferred, due to the additional time, cost, and effort expended to complete the difficult mid-air post-tensioning procedure.

A construction technique for splicing together two precast prestressed girders was presented by Gerwick (1993) (Figure 2-10). In this approach, the tendon for the full span is prestressed and a gap is left in the beam at midspan during casting. The units are folded about the midspan and transported side-by-side to the site. The segments are then placed on falsework in the final configuration and jacked apart in the splice region to stress the prestressing strands. With the jacks in place, the splice concrete is cast. After curing, the jacks are removed, leaving the splice concrete in a prestressed state.

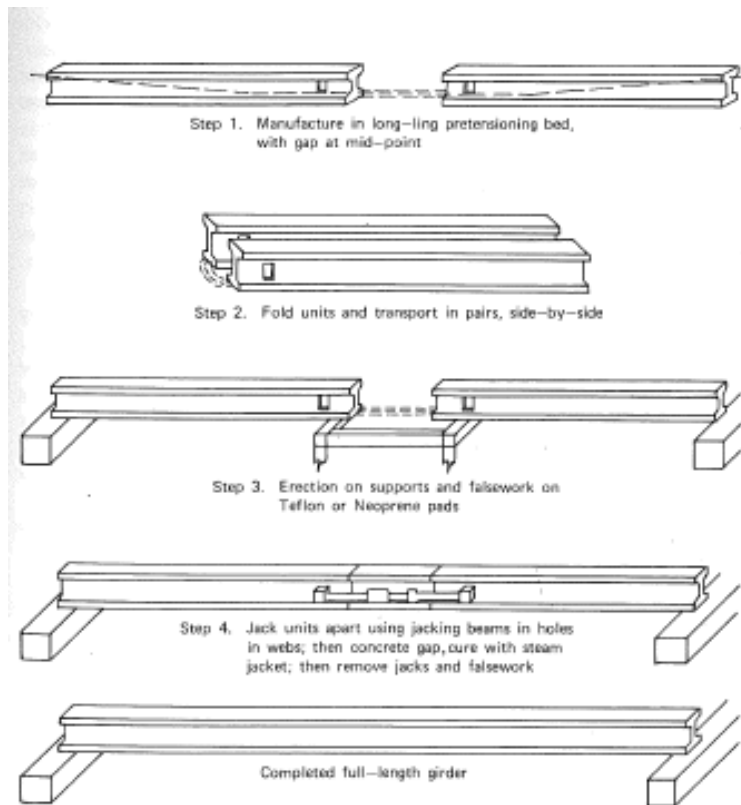


Figure 2-10. Prestressing against internal restraint (Gerwick 1993)

2.7 Current Construction Techniques: Design

The current AASHTO-LRFD code considers precast spliced girder systems as conventional bridge structures with additional requirements for the joint area, distinguishing these systems from segmental construction. Whereas the spliced precast bridge system itself is given separate consideration, the joint area, however, is treated the same as segmental construction joints and is required to meet the same stress limits. (AASHTO 2007)

AASHTO-LRFD specifies several construction considerations to be made concerning the joint area. For a cast-in-place joint, when preparing the area for the closure pour, the end of the precast members should either be intentionally roughened to expose the coarse aggregate, or include shear keys (Figure 2-11). The width of the

closure joint between the two precast members is limited to a minimum of 300 mm (12 in.), or 100 mm (4 in.) for joints located within a diaphragm, in order to allow enough clearance to properly splice the reinforcement, as well as to adequately compact the closure pour concrete. (AASHTO 2007)

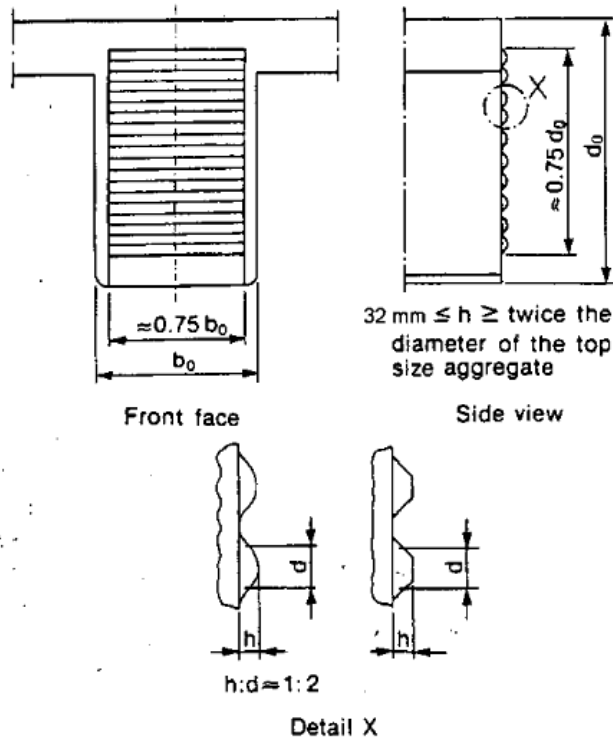


Figure 2-11. Shear keys required by AASHTO-LRFD (AASHTO 2007)

Tensile and compressive stress limit states for the joint areas of precast spliced girders are the same as those specified for joints in segmental construction. The joint area may be designed to provide either zero or some tensile capacity, as determined by the joint's location in the span. If the joint area is designed to resist tensile stress, bonded auxiliary reinforcement capable of resisting the calculated tensile force at a maximum tensile stress of $0.5 f_y$ must be supplied across the joint. The prestressed concrete tensile stress limit for the joint area must be limited to a maximum of $0.25\sqrt{f'_c}$.

(ksi). Both tensile stress limits must be met at all times during the life of the structure (both before and after prestress losses). (AASHTO 2007)

After the girder segments have been joined, if the system meets all service limit states prescribed in Section 5.14.1.3, the code provisions indicate that the assembled system may be considered fully continuous for all subsequent load limit states. The joint area, therefore, must provide the same compressive capacity as the rest of the segment for the required service limit states. (AASHTO 2007)

The design of the 204th Street Bridge (Figure 2-12) is the closest example of the system type targeted by this research. The simple-span single point interchange, as described by Jaber et al. (2006), consisted of 14 girder lines constructed as two structures (for each lane of traffic). Two short end segments were bridged together with a long center segment to span a total of 207 ft.

Splicing of the segments was completed mid-air, using temporary towers to provide support at the joint. The authors describe as one of the most challenging design aspects the determination of the girder elevations at the splice locations so as to provide a smooth riding surface and to prevent sag in the girder-soffit profile. Screw jacks were used to refine the girder elevation as required. The precast concrete girders were spliced together with a cast-in-place joint, aligning the post-tensioning ducts running through each segment. After the closure pour reached the specified strength, the assembled precast girder system was post-tensioned along its entire length. (Jaber et al. 2006)



Figure 2-12. 204th Street Bridge (Jaber et al. 2006)

The splices were designed to resist zero net tension. No special reinforcement was detailed in the splice area. To prevent tensile stresses in this area during the service life, prestressing was specified to provide adequate precompression. The specified compressive strength at the joint was less than that required in the girders; conventional concrete was adequate for the closure pour. (Jaber et al. 2006)

It is the intent of this research, on the other hand, to investigate methods to splice the girder segments locally, with no or little post-tensioning.

2.8 Prestressing Strand Couplers

Prestressing strand couplers provide an economical and time-effective solution for restoring prestress force to severed strands of moderately damaged girders. Figure 2-13 shows several examples.

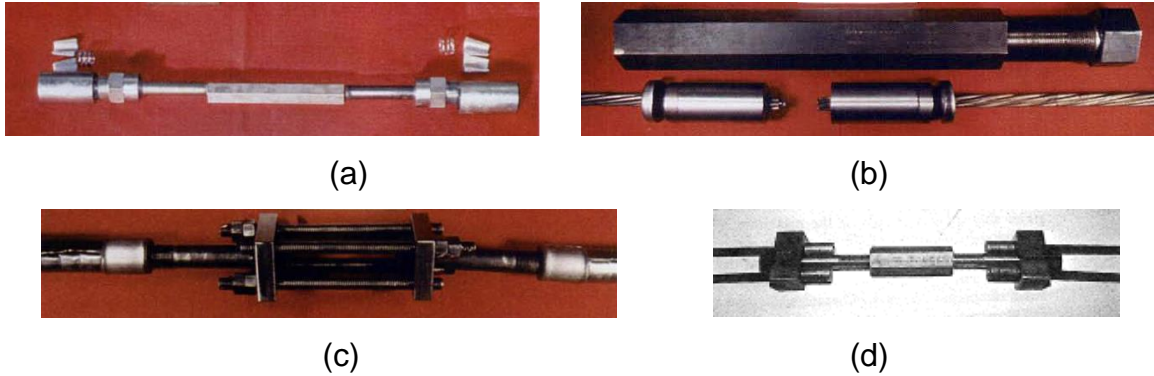


Figure 2-13. Prestressing strand coupler types: (a) turnbuckle-style, (b) Alberta, (c) swaged for single strand, (d) swaged for two strands (Zobel and Jirsa 1998; Shanafelt and Horn 1985)

Several states, including Florida, California, Texas, and Oregon, have utilized prestressing couplers to repair damaged prestressed concrete bridge girders in place; strand couplers are included as a part of these states' standard practice for girder rehabilitation (Saidii et al. 2000; Johnson 2011). The use of prestressing couplers to restore strength is not a universal practice; in some states, a damaged girder with severed prestressing strands is immediately replaced (Shanafelt and Horn 1980).

Figure 2-14 shows the strand repair coupler currently permitted by FDOT (Bridge Maintenance and Repair Handbook 2012) for repair of damaged strand in prestressed concrete girders. It is adjustable and 0.5-in. dia. versions of this coupler have been used to repair damaged prestressing strand in concrete girders for approximately the past thirty years (Waheed et al. 2005). The 0.5-in. dia. coupler has been used to repair bridges in several states. No problems have been reported post-repair (Waheed et al. 2005; Johnson 2011). Figure 2-15 shows a damaged girder in Ontario that was rehabilitated with couplers (Ministry of Transportation of Ontario 2011).

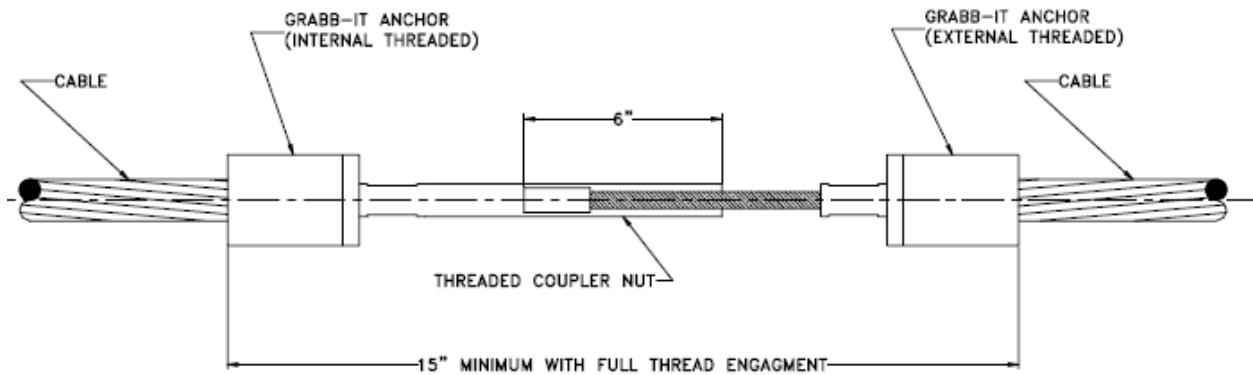


Figure 2-14. Turnbuckle-style coupler (FDOT 2010c)

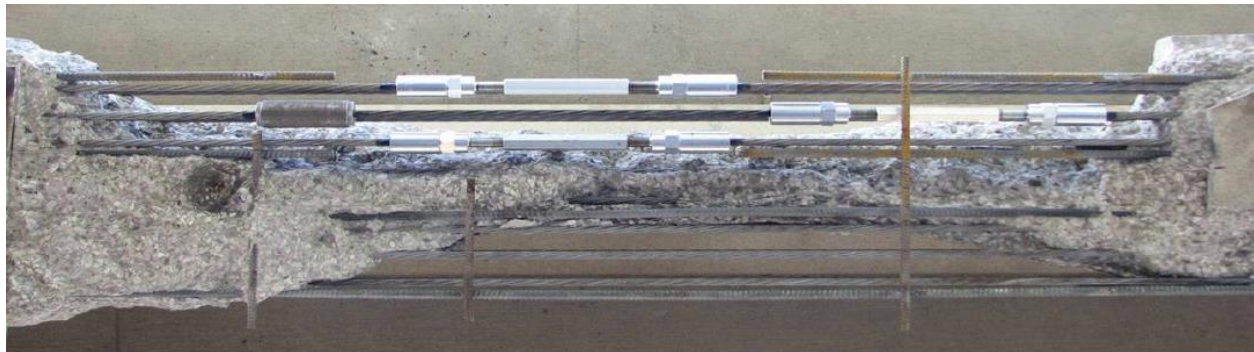


Figure 2-15. Repair of severed strand using a coupler (Ministry of Transportation of Ontario 2011)

A survey of research on the commercially-available couplers was completed. Shanafelt and Horn (1985) investigated two types of couplers for 0.5-in. dia. prestressing strand: a turnbuckle-style coupler similar to Figure 2-13(a), and a swaged coupler similar to Figure 2-13(d). Component tensile testing of both coupler types was performed. In each case, the coupler, with strand attached on either side, was loaded in tension in a Universal Testing Machine (UTM). After several adjustment cycles using a torque wrench to tighten the system and stress the strand, the components were loaded statically to failure. The turnbuckle-style coupler test reached ultimate load

when the strand broke at the chuck, at approximately 36.6 kip, or 88% of the strand's specified strength. The swaged coupler failed at 40.1 kip, or 98% of the strands' specified strength. The coupler appeared to be fabricated from commercially available components, though the manufacturer of the turnbuckle-style coupler is not identified.

In addition to component testing, Shanafelt and Horn (1985) investigated the turnbuckle-style coupler in the repair of severed strand in a full-size AASHTO Type III girder. Using the coupler to reconnect four (of 16 total) strands, and preloading the specimen during the repair, they found the coupler capable of restoring the prestress force to that of the non-severed strands—approximately 158 ksi, or $0.6f_{pu}$.

Zobel (1998) investigated four mechanical couplers (Figure 2-13), evaluating their ease of installation and performance as a repair mechanism in a girder previously in service which had been removed brought to the lab for testing. Mock repairs were conducted to investigate the feasibility of repairs using the different coupler types.

Laboratory testing of installed devices provides limited examination of coupler's behavior (Labia et al. 1996). In two tension strength tests by Zobel (1997) of 0.5 in. dia. coupler devices, the prestressing strand ruptured prior to the prestressing strand's specified ultimate strength at notches caused by gripping at wedge anchors. In the first test, the strand ruptured at the test grips at approximately 90% of the strand's specified ultimate strength; it was noted that the strand did begin to yield prior to the strand rupture. In the second test, the strand grips within the wedge anchors of the coupler device notched the strand causing strand rupture at 80% of the strand's specified ultimate strength. Zobel notes that the strand failure appears to result from the quality of the wedges. (1997)

In tests commissioned by the manufacturer of 0.5-in. dia. couplers, the prestressing strand ruptures at 95-102% of the prestressing strand's specified strength. Again, the failure occurred as the three-piece wedge anchors bit down on the prestressing strand, causing strand rupture. When tested alone in tension, the 0.5-in.-dia. coupler device itself exceeded the strand's specified ultimate strength by 11%, failing at the base of the externally threaded stem of the turnbuckle. (Law Engineering 1990)

The use of turnbuckle-style prestressing couplers has been covered by several researchers, and is generally prescribed for instances of limited scope. Shanafelt and Horn have described their use as effective for the reconnection of a small quantity of severed strand, recommending that the spliced quantity be limited to no more than approximately 25% of the total number of strands. In instances where the repair requires splicing of more than 25%, it is recommended that another form of strengthening complement the repair. Based on their test results, Shanafelt and Horn believe that a rupture at the spliced strand will cause local distress. Research on internal strand coupling concluded that such devices are sensitive to cyclic loading, and as such, should only be used to repair a limited number of strands per damaged girder. Potential fatigue issues as one reason for limiting coupler use for ultimate capacity, and list congestion as a second concern. (Shanafelt and Horn 1985)

CHAPTER 3 PROTOTYPE DESIGN–FIB96

The design and development of the splice focused on an intended application: a simply-supported I-girder with a span length of greater than 200 ft. Utilizing the FDOT's longest spanning I-girder section, the FIB96, a prototype beam design provided the shear and moment demand on the splice. This chapter describes the splice development and prototype beam design for the intended application. Additional details regarding the design can be found in the FDOT report.

3.1 Splice Conceptual Design

Several splice concepts were developed and submitted to FDOT for consideration as part of the prototype design process. Based on this initial submittal and the discussions that followed, the following limitations were imposed on the final design of the splice:

- Concrete in splice region must be prestressed
- Prestressing strands in the splice region must be stressed to a minimum of $0.6f_{pu}$
- Prestressing strands must be stressed with little or no post-tensioning
- For aesthetic reasons, the cross-section geometry must be maintained through the splice length, which would make the splice visually indiscernible from the rest of the span length.

With these limitations in mind, a variation of the concept presented by Gerwick (1993) was adopted (Figure 2-10). In this approach, the tendon for the full span is prestressed and a gap is left in the beam at midspan during casting. The units are folded about the midspan and transported side-by-side to the site. The segments are then placed on falsework in the final configuration and jacked apart in the splice region

to stress the prestressing strands. With the jacks in place, the splice concrete is cast. After curing, the jacks are removed, leaving the splice concrete in a prestressed state.

As illustrated in Figure 3-1, the presented in Gerwick (1993) splice method was modified for the prototype design such that the strands are cut prior to transport and then spliced on site. Prestressing force is applied to the system by a hydraulic jack on each side of the girder web. External brackets transfer the force from the hydraulic jacks to the precast segments by thru-bolts that pass through the web of the beam. The internal restraint provided by the coupled prestressing strand resists the jacking force, and the prestressing strand is stressed. The eccentricity between the applied jacking force and the resisting strand creates in a lifting moment that is resisted by the self-weight of the precast segments and external tie-downs. If the splice is placed low enough on the section, then tie-downs may not be necessary. After the target stress is achieved, the hydraulic jacks are locked and the splice concrete is placed.

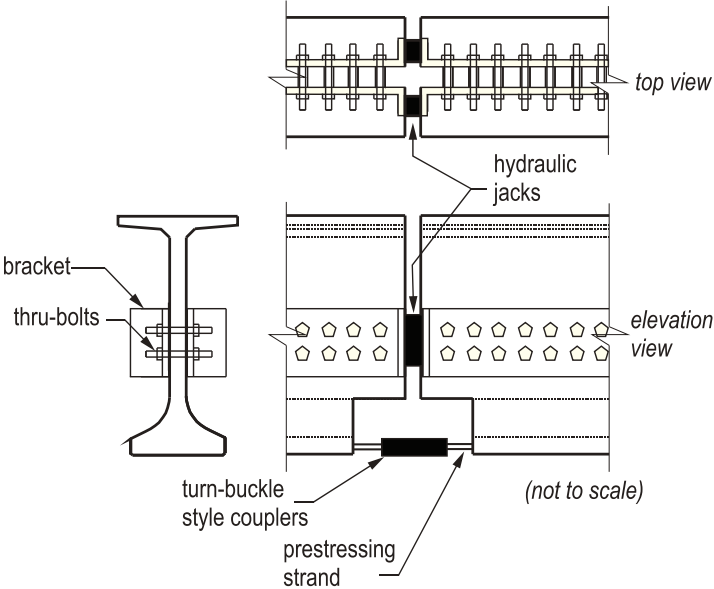


Figure 3-1. Prototype splice design

The primary aim of incorporating a splice into the prototype design was to reduce the length of the elements so that they can be transported by tractor-trailer. Several options were considered for splice locations with the final configuration illustrated in Figure 3-2. It was decided to use two symmetrically placed splices rather than a single splice to minimize moment (thus avoiding midspan splice). One added benefit of the symmetrical layout is that the number of prestressing strands required for strength and serviceability need not pass through the splice to the end of the beam. Only the number strands needed for the moment at the splice must be carried through the splice into the end segment. This symmetrical double splice approach was also used in the design of the simply-supported 207-ft span 204th Street Bridge in Douglas County, NE (Jaber et al. 2006).

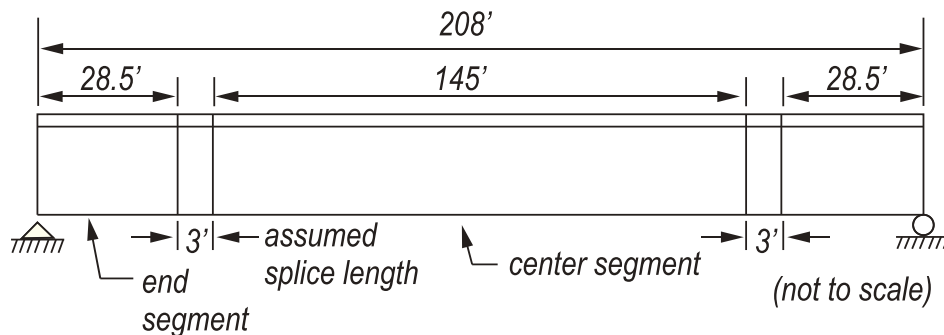


Figure 3-2. Elevation view of FIB96 with two splices

3.2 Prototype Bridge and Beam

To fully utilize its anticipated capacity as a long-span section, the FIB96 (Figure 3-3(a)) girder was used to develop a prototype splice connection design. The exterior girder of the bridge shown in Figure 3-3(b) was designed using the FIB96 in accordance with AASHTO-LRFD 2007 (AASHTO 2007) and the FDOT Structural Design Guidelines (SDG) (FDOT 2010).

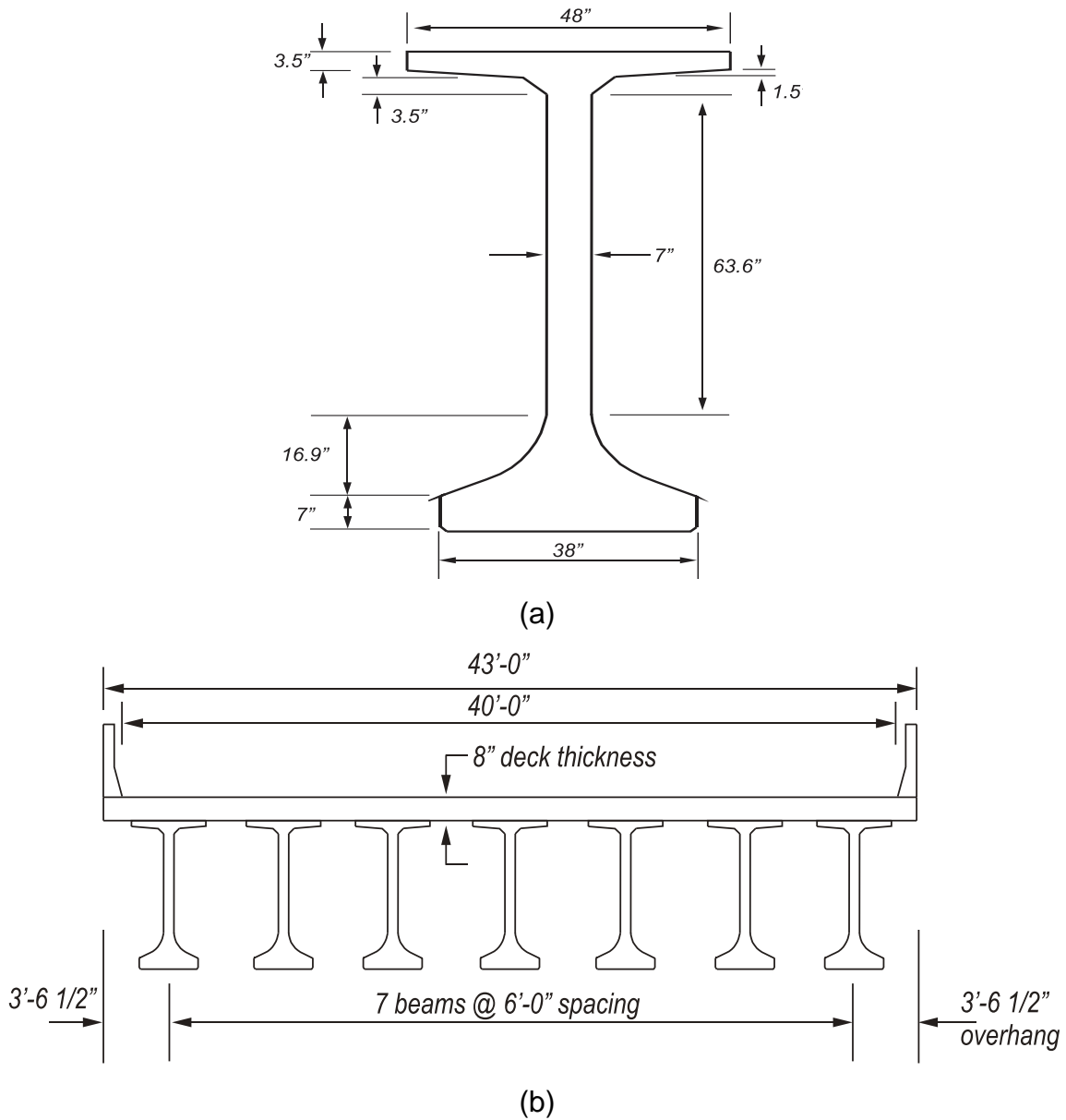


Figure 3-3. Prototype design (a) FIB96 girder and (b) bridge cross-section

3.3 Bridge Design Details

Details of the bridge geometry are:

- Beam length = 208.0 ft
- Design span length = 206.7 ft
- Number of lanes = 4
- Number of beams = 7

Assumed precast beam properties are:

- Concrete strength at transfer, $f'_{ci} = 6$ ksi
- Concrete strength at 28 days, $f'_c = 8.5$ ksi
- Initial concrete modulus of elasticity = 4010 ksi (AASHTO-LRFD 5.4.2.4)
- Concrete modulus of elasticity = 4780 ksi (AASHTO-LRFD 5.4.2.4)
- Concrete unit weight = 150 pcf (structural concrete, per SDG)
- Prestressing strands: 0.6-in. dia. ASTM A416, Grade 270, low-relaxation, seven wire strand
- Mild steel reinforcement: ASTM A615, Grade 60.

Assumed cast-in-place deck properties are:

- Slab thickness = 8 in.
- Concrete strength at 28 days = 4.5 ksi
- Slab modulus of elasticity = 3480 ksi

Composite section properties are based on transformed section properties, which incorporate an effective slab width (Figure 3-4). The effective slab width is calculated for the exterior beam as

$$SlabWidth = \frac{BeamSpacing}{2} + Overhang = 6.54 ft$$

Modular ratio between slab and beam concrete,

$$n = \sqrt{f_{c.beam} / f_{c.slab}} = 1.37$$

Transformed slab width, for use in calculation of composite section properties,

$$b_{eff} = \frac{SlabWidth}{n} = 4.77 ft$$

and result in the non-composite and composite section properties shown in Table 3-1.

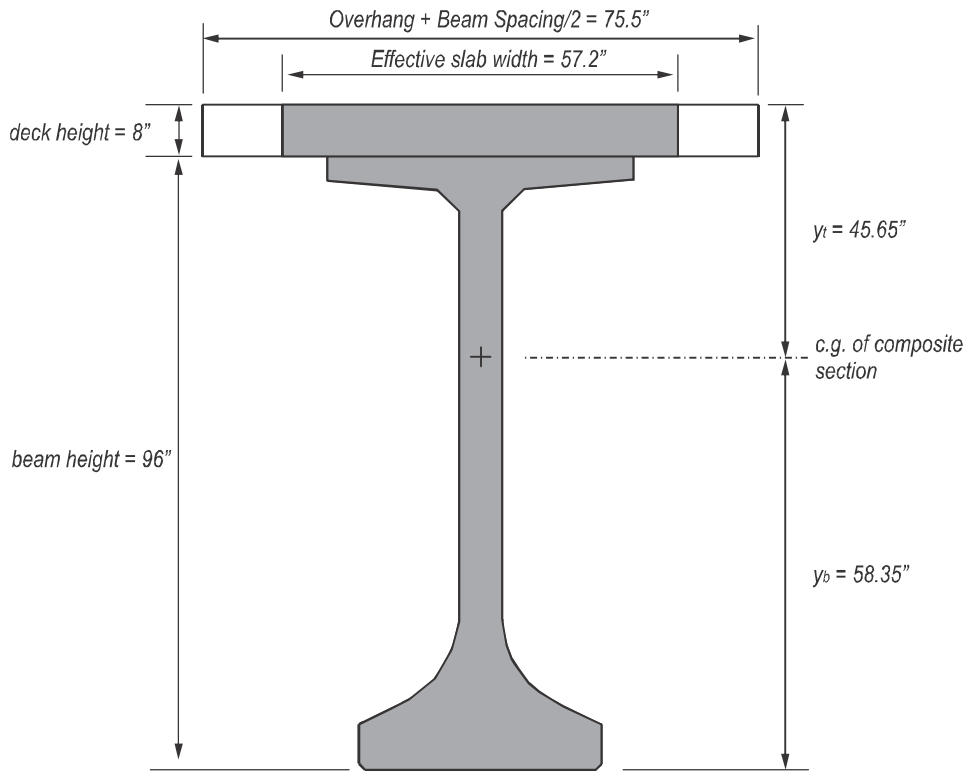


Figure 3-4. Composite section

Table 3-1. Typical FIB96 section properties

| FIB96 | Non-composite | Composite |
|------------------------------|---------------|-----------|
| Area (in. ²) | 1227 | 1685 |
| I_{xx} (in. ⁴) | 1,516,558 | 2,608,976 |
| y_t (in.) | 53.22 | 45.65 |
| y_b (in.) | 42.78 | 58.35 |
| S_t (in. ³) | 28496 | 57152 |
| S_b (in. ³) | 35450 | 44713 |
| Depth(in.) | 96 | 104 |

3.4 Loads

Loads were determined per the SDG (FDOT 2010). The dead loads assumed to be acting on the non-composite section are shown in Table 3-2.

Table 3-2. Non-composite dead loads

| Load source | Uniform load (kip/ft) |
|-------------|--------------------------|
| Girder | 1.279 |
| Deck | 0.695 |
| Forms | 0.02 |
| Total | 1.993 |

The dead loads acting on the composite section are summarized in Table 3-3.

Table 3-3. Composite dead loads

| Load source | Uniform load (kip/ft) |
|------------------------|--------------------------|
| Future wearing surface | 0.075 |
| Barrier | 0.21 |
| Total | 0.285 |

The beam was designed for vehicular load requirements prescribed by AASHTO-LRFD, with deviations for load rating as prescribed by SDG 1.7 (FDOT 2010). The design live loads are a combination of:

1. Design truck with dynamic allowance. Three conditions:
 - a) AASHTO-LRFD HL-93 design truck. (32 kip, 32 kip, and 8 kip loads spaced at 14 ft.)
 - b) AASHTO-LRFD HL-93 design tandem. (Two 25 kip loads spaced at 4 ft.)
 - c) Special Florida F-120 truck for permit loading. (53.33 kip, 53.33 kip, and 13.33 kip loads spaced at 14 ft.)
2. Design lane load of 0.64 kip/ft./lane. No dynamic allowance applies.

The dynamic allowance, which applies only to truck loads, is 33% (or 15% for fatigue) as prescribed by AASHTO-LRFD. The AASHTO-LRFD live load distribution factors are not applicable in this beam design. Truck loads were distributed assuming lever rule. All live loads were assumed to act on the composite section.

Because fatigue has been identified as a concern for the coupler device, the amount of prestress force at the splice location was checked to ensure that the section remains uncracked. Stress state checks for fatigue were determined using the fatigue truck with no distributed load, and included the dynamic load allowance of 15%, and by determining the worst case positioning (transverse and longitudinal) which maximizes the stress range. The beam should remain uncracked for this limit state. The bottom fiber stress at the splice is provided for reference.

The beam design was checked for the limit states described in Table 3-4, as prescribed in AASHTO-LRFD and modified by the SDG (AASHTO 2007; FDOT 2010).

Table 3-4. Design limit states

| Limit State | Load Combination | Loads |
|---|-------------------------------|---|
| Strength I—Load combination considering normal vehicular use, without wind effects. | 1.5DW + 1.25DC + 1.75LL | DW: dead load due to the wearing surface DC: dead load due to component and attachments LL: live load due to HL-93 truck (with dynamic amplification) and lane loading |
| Strength II— Load combination considering permit loads, without wind effects. | 1.5DW + 1.25DC + 1.35LL | DW: dead load due to the wearing surface DC: dead load due to component and attachments LL: live load due to FL-120 truck (with dynamic amplification) and lane loading |
| Service I—Load combination relating to normal operational use of the bridge with all loads taken at their nominal value. Wind loads are considered negligible. This limit state is intended to check compression. | 1.0DL + 1.0LL | DL: total dead load LL: total live load |
| Service III—This limit state is intended to check tension at midspan for crack control. | 1.0DL + 0.8LL | DL: total dead load LL: total live load |
| Fatigue | 0.75LL | LL: fatigue truck only, with dynamic load allowance |

3.5 Prestressing Strand Pattern Design

The FDOT LRFD Beam Design MathCAD worksheet (FDOT 2010b) was used to select the number and position of 0.6-in. diameter prestressing strands for each segment. The required number of strands in each segment was dependent on both the construction staging and final configuration and was adjusted to meet both service and strength limit states requirements (Figure 3-5). Taking advantage of the segmental nature of the span, 37 of the strands in the center segment were terminated at the splice, leaving 31 strands to continue to the end of the beam.

Continuity of the strands through the splice was necessary to ensure that the strands in the splice were prestressed to $0.6f_{pu}$ and that there was sufficient flexural strength to resist the factored moment at the splice. This continuity was ensured by using strand couplers. Because the coupler occupies a larger cross-sectional area than the strand, it was necessary to arrange the strand pattern with sufficient space surrounding each strand to prevent interference. This spacing is apparent in the end segment pattern shown in Figure 3-5. Further, as the strand in the splice region will be prestressed to $0.6f_{pu}$ and the prestressing strand in the precast segments of the beam will—as is standard—be stressed to $0.75f_{pu}$, the discrepancy in stress level required the specification of additional dormant strand, to be prestressed only in the splice region. The final strand pattern for each segment was chosen as closely in accordance with the SDG standard FDOT strand pattern layout as possible (FDOT 2010). A notable exception was a modification of the standard strand pattern in the web to include additional strands to achieve the required moment capacity.

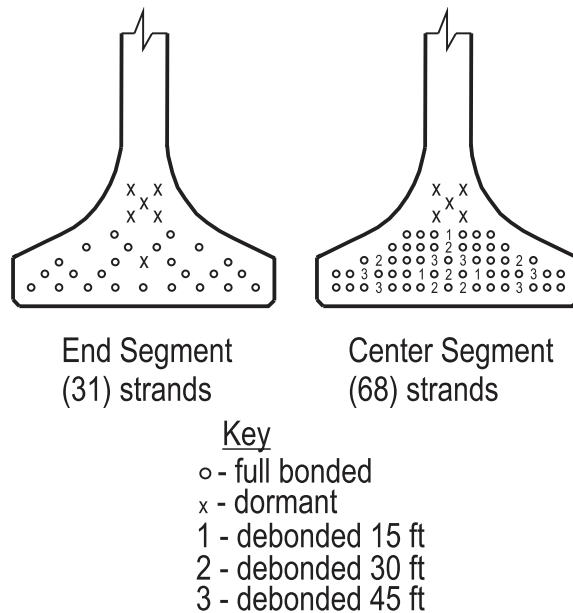


Figure 3-5. Strand layouts

Initially, the end and center segments were analyzed individually using both the FDOT MathCAD worksheet (FDOT 2010b) and a supplemental worksheet to address the concrete stresses at the time of prestress release for each segment. The transformed section properties were used for these calculations. Beam segments were assumed to be detailed with tensile reinforcement in the top of the section so that $0.19\sqrt{f'_c}$ (ksi) limit on concrete tensile stress was used. The following allowable stresses at release were used to check the calculated stresses shown in Table 3-5.

- Compressive stress limit: $0.6f'_c = 3600$ psi (AASHTO-LRFD 5.9.4.1.1)
- Tensile stress limit (outer 15% of segment): $12\sqrt{f'_c}$ (psi) = 930 psi (SDG)
- Tensile stress limit (inner 70% of segment): $0.19\sqrt{f'_c}$ (ksi) = 533 psi (AASHTO-LRFD 5.9.4.1.2)

Table 3-5. Summary of Service I limit states (precast segments at release)

| Segment | Position (ft)* | Tensile Stress (psi) | | Compressive Stress (psi) | |
|---------|----------------|----------------------|-------|--------------------------|-------|
| | | Applied | Limit | Applied | Limit |
| End | 4.275 | 485 | 930 | 1920 | 3600 |
| | 14.25 | 452 | 533 | 1893 | 3600 |
| Center | 21.75 | 730 | 930 | 3309 | 3600 |
| | 72.5 | 265 | 533 | 3485 | 3600 |

*distance from end of segment

The segments were assumed to be shipped to the site in their separate configurations and spliced and erected for deck placement. Table 3-6 presents the Service I limit states check using non-composite section properties for loads during deck placement. The following limits were checked:

- Compressive stress limit at 1.0DL: $0.45f_c = 3830$ psi
- Tensile stress limit: $0.19\sqrt{f_c}$ (ksi) = 533 psi

Table 3-6. Summary of Service I limit states (deck placement)

| Position (ft)* | Tensile Stress (psi) | | Compressive Stress (psi) | |
|----------------|----------------------|-------|--------------------------|-------|
| | Applied | Limit | Applied | Limit |
| 2.8 | 537 | 533 | 2823 | 3825 |

*distance from end of spliced beam

The beam was checked for Service I and Service III limit states load combinations with full dead and live loads (Table 3-7 and Table 3-8). Additionally, the bottom fiber stress was checked for the fatigue load combination (Table 3-9), to ensure that the splice location remained uncracked. The transformed, composite section was used to make these checks. The following limits were used:

- Service I (1.0DL+1.0LL):
- Compressive stress limit: $0.6f_c = 5100$ psi
 - Tensile stress limit: $0.19\sqrt{f_c}$ (ksi) = 533 psi

Service III (1.0DL+0.8LL):

- Compressive stress limit: $0.4f'_c = 3400$ psi
- Tensile stress limit: $0.19\sqrt{f'_c}$ (ksi) = 533 psi

Fatigue (1.0DL+0.75LL):

Tensile stress limit: $7.5\sqrt{f'_c}$ (psi) = 690 psi

Table 3-7. Summary of Service I limit state check at the extreme top fiber

| Position (ft)* | Tensile Stress (psi) | | Compressive Stress (psi) | |
|-------------------|----------------------|-------|--------------------------|-------|
| | Applied | Limit | Applied | Limit |
| 2.8 | 498 | 533 | n/a | n/a |
| 30 | n/a | n/a | 1775 | 5100 |
| 104 | n/a | n/a | 4353 | 5100 |

*distance from end of spliced beam

Table 3-8. Summary of Service III limit state check at the extreme bottom fiber

| Position (ft)* | Tensile Stress (psi) | | Compressive Stress (psi) | |
|-------------------|----------------------|-------|--------------------------|-------|
| | Applied | Limit | Applied | Limit |
| 2.8 | n/a | n/a | 2727 | 3400 |
| 30 | n/a | n/a | 1078 | 3400 |
| 104 | 475 | 533 | n/a | n/a |

*distance from end of spliced beam

Table 3-9. Fatigue limit state check at the extreme bottom fiber at splice

| Position (ft)* | Tensile Stress (psi) | |
|-------------------|----------------------|-------|
| | Applied | Limit |
| 30 | 280 | 690 |

*distance from end of spliced beam

Table 3-10 presents the Strength I moment and shear factored combinations at the location of the splice and at the beam midspan, as well as the associated design moment strengths. Table 3-11 presents the Strength II combinations and limiting values.

Table 3-10. Strength I flexure and shear checks for spliced length

| Position (ft)* | ϕM_n (kip-ft) | M_u (kip-ft) | $\phi M_n/M_u$ | ϕV_n (kip) | V_u (kip) | $\phi V_n/V_u$ |
|-------------------|------------------------|-------------------|----------------|---------------------|----------------|----------------|
| 30 | 14,700 | 11,200 | 1.31 | 770 | 340 | 2.26 |
| 104 | 26,600 | 23,100 | 1.15 | 484 | 0 | n/a |

*distance from end of spliced beam

Table 3-11. Strength II flexure and shear checks for spliced length

| Position (ft)* | ϕM_n (kip-ft) | M_u (kip-ft) | $\phi M_n/M_u$ | ϕV_n (kip) | V_u (kip) | $\phi V_n/V_u$ |
|-------------------|------------------------|-------------------|----------------|---------------------|----------------|----------------|
| 30 | 14,700 | 10,100 | 1.46 | 770 | 310 | 2.48 |
| 104 | 26,600 | 20,900 | 1.27 | 484 | 0 | n/a |

*distance from end of spliced beam

3.6 Moment-Curvature

Another important aspect of the splice design that is not explicitly covered in the AASHTO-LRFD is the flexural ductility of the section. Because the strands will be mechanically coupled at the beam splice, the flexural ductility of the section at that location will depend on the stiffness and seating movement of the strand couplers. To evaluate the ductility the beam splice, moment-curvature analysis was conducted considering the effect of the strand couplers on ductility. The coupler stress-strain model established with testing described in CHAPTER 4 was utilized to assess the cross-section with 31 strands coupled using a 0.6-in. dia. coupler (Figure 3-6). The Ramberg-Osgood model was used to analyze the cross-section as if the strands were continuous across the splice, without any coupling device.

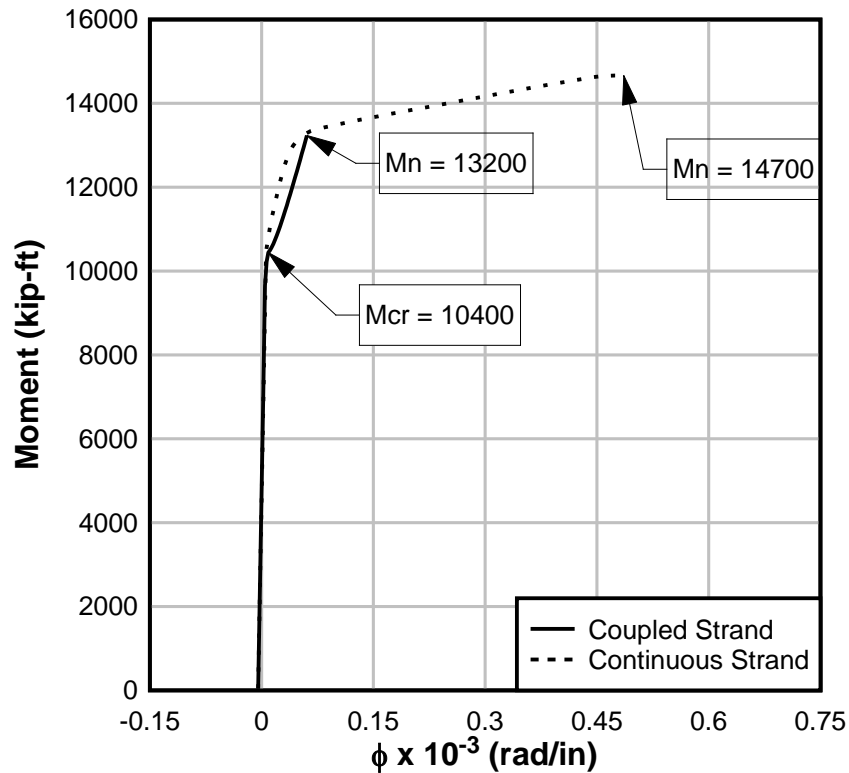


Figure 3-6. Moment-curvature of FIB96: Continuous strand vs. coupled strand

Both models were assumed to have the same effective prestress force.

Consequently, both models exhibited the same precracking behavior, with both beams cracking under an applied moment of 10,400 kip-ft.

The predicted ultimate capacity of both sections was also approximately equal. The FIB96 with continuous strand has a moment capacity of 14,700 kip-ft—an additional moment-carrying capacity of 40% beyond the cracking moment. In comparison, the FIB96 with coupled strand has an ultimate capacity of 13,200 kip-ft, approximately 27% beyond the cracking moment. The addition of nonprestressed or partially prestressed strand across the splice region may be required to achieve the design moment capacity.

After cracking, however, the two sections exhibit different behavior: the difference in ductility of the two sections is considerable. Compared with a section reinforced with

continuous strand, the lower stiffness of the coupled strand causes greater curvature of the section at lower stress. Because the coupled strand stress-strain model does not include strand yielding, the behavior is similar to that of a section reinforced with mild steel; the moment curvature of the section with coupled strand does not have a smooth rounded shape. At capacity, the coupled strand ruptures prior to the development of 0.003 compressive strain in the concrete (Figure 3-7). The failure mode is brittle and sudden.

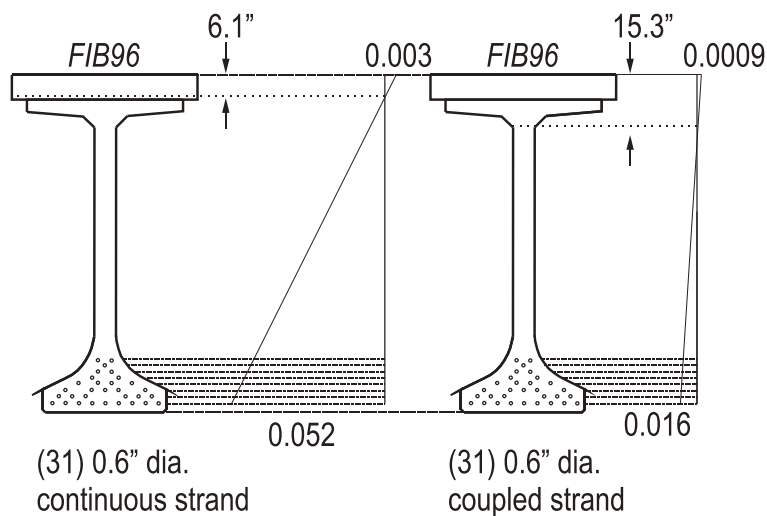


Figure 3-7. FIB96 strain at flexural capacity: Continuous vs. coupled strand

Brittle behavior was similarly observed in ultimate load tests of a box girder repaired with couplers. At ultimate capacity, the repaired box girder (with 2 of 30 strands coupled using 0.5-in. dia. couplers) failed at slightly less load, but considerably less deflection than equivalent intact (non-damaged) box girders; the repaired girder exhibited 35% less deflection. (Labia et al. 1996)

The above moment-curvature analysis was based on test results from a single tensile test of a 0.6-in. dia. coupler (the test is described in CHAPTER 4) and was completed to develop a prediction of the couplers' influence on the failure behavior. To

verify the coupler stress-strain model, it is recommended that additional testing of the couplers be conducted.

3.7 Splice Considerations

Figure 3-1 illustrates the bracket required to push the segments apart after the strands have been coupled. The bracket and connection design itself is relatively simple, but must be capable of transferring shear and moment and requires a slip-resistant connection. Placement of the bracket on the girder web provides an easy-to-access, flat face for the brackets to bear against. Whereas attachment of the brackets to the flat face of the bottom flange would have reduced the eccentricity of the jacking force with that of the prestressing strands, it was considered impracticable due to the large amount of steel in these regions. The use of thru-bolts allowed for in-line delivery of the jacking force, and reduced the prying action of the brackets on the precast girders. To prevent spalling of the girder web concrete, steel sleeves were detailed for the thru-bolts.

Outside of geometric considerations, the primary objective was to develop moment-carrying capacity at the splice location. To do this, the prestressing strand was designed to be coupled within the splice region, to provide continuous prestressing strand along the span length for ultimate capacity. By relying on couplers to provide continuity of the existing prestressing strand, the cross-section of the FIB section could be maintained. The number of coupled prestressing strands was determined based on the design of the FIB96 prototype and the strand pattern was spaced with the larger volume of the couplers in mind. The coupled prestressing strand was designed to be “prestressed” to achieve the required $0.6f_{pu}$ for service.

CHAPTER 4 STRAND COUPLER SELECTION AND TESTING

Several strand coupler devices were discussed in the literature review. A commercially available turnbuckle coupler—called a Grabb-it - was selected for the test specimen. The use of turnbuckle-style couplers permits adjustment to compensate for different strand lengths; the turnbuckle can be used to equalize the gap length between the precast segments so that prestress force is delivered equally to each strand while also eliminating prestress losses that would otherwise occur due to wedge seating.

Figure 4-1 shows the components of this turnbuckle-style mechanical connection. A prestressing chuck threaded onto a tensioning bolt is connected by a tensioning nut to another chuck and tensioning bolt pair. One chuck and tensioning bolt pair is threaded opposite to the other pair, so that the device does not “unwind” when the tensioning nut—or turnbuckle—is torqued. Teethed wedges and a tapered spring inside each chuck grab the prestressing strand at each end.

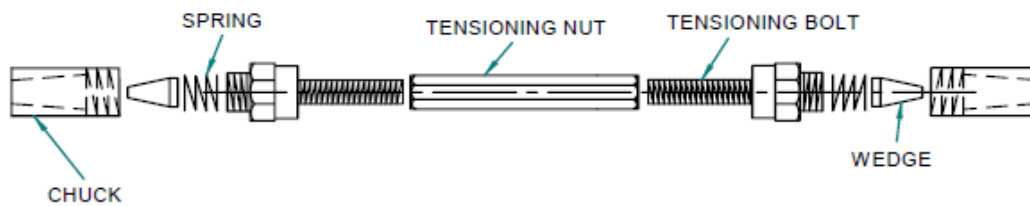


Figure 4-1. Turnbuckle-style coupler components (Waheed et al. 2005)

Couplers for both 0.5-in. and 0.6-in. diameter strands were tested in tension in a universal test machine. The couplers for 0.6-in. diameter strands were tested to ultimate capacity so that the actual stress-strain relationship of the coupler could be used in the moment-curvature analysis conducted on the prototype girder. In addition, the results were compared with the ACI and AASHTO-LRFD requirements for post-

tensioned anchorages and coupling devices that require the development of at least 95% of the specified ultimate strength of the prestressing strand (ACI 318-08 2008; AASHTO 2007). Although the 0.6-in. dia. coupler was made available for lab testing by the manufacturer, it is not currently in commercial production.

Strain gages were applied to the couplers for 0.5-in. diameter strand and the couplers were tested to develop a calibration of strain versus load. Calibration data were used during the splice prestressing process to corroborate readings from the load cells placed on the unbonded portion of the prestressing strands in the spliced test specimens.

4.1 Ultimate Strength Tests of 0.6-in. Diameter Coupler

Two tension tests were conducted on the 0.6-in. dia. couplers to be used in the proposed splice design. The first test was performed at the FDOT State Materials Office. In this test, the coupler was used to splice two lengths of 0.6-in. dia. 270-ksi lo-lax prestressing strand. One end of each strand was prepared with white glue and fine sand prior to the test, in accordance with ASTM A1061; the sand-prepared end was gripped by the wedge grips of the test machine (ASTM A1061 2009). Load was applied at a displacement-controlled rate of approximately 0.2 in./min. The test ended when the strand ruptured near the top wedge of the coupler device (Figure 4-3(a)) at an applied tensile load of 53.6 kip, or 91% of the strand's specified ultimate strength. At rupture, the prestressing strand stress was 247 ksi; though near the proportional limit of lo-lax strand, the stress-strain plot of the coupled device shows that the prestressing strand did not exceed this point, and did not begin to yield prior to rupture. The strand ruptured at notches caused by the wedges (Figure 4-3(b)).

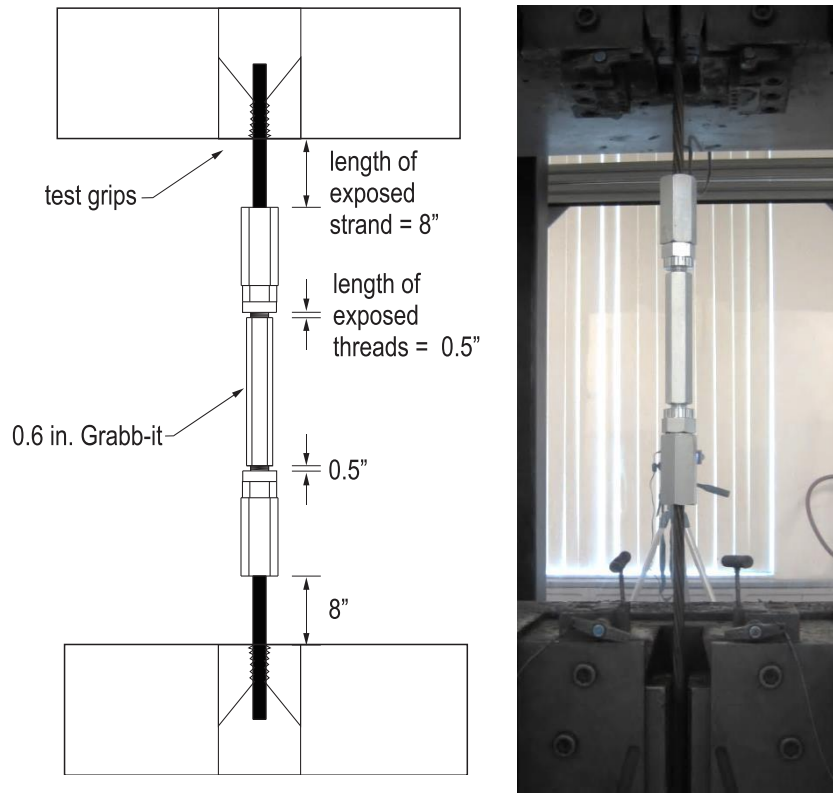


Figure 4-2. SMO tensile tests of 0.6-in. dia. coupler



(a)



(b)

Figure 4-3. Strand rupture of 0.6-in. dia. coupler

For comparison purposes, a second test was performed at the UF laboratory in accordance with the static testing requirements of AC303 from the International Code Council Evaluation Service (ICCES) for post-tensioning anchorages (ICCES 2011). In this test, the chuck bodies were disconnected from the turnbuckle and attached to the ends of the prestressing strand - similar to tests of strand chucks (Figure 4-4).

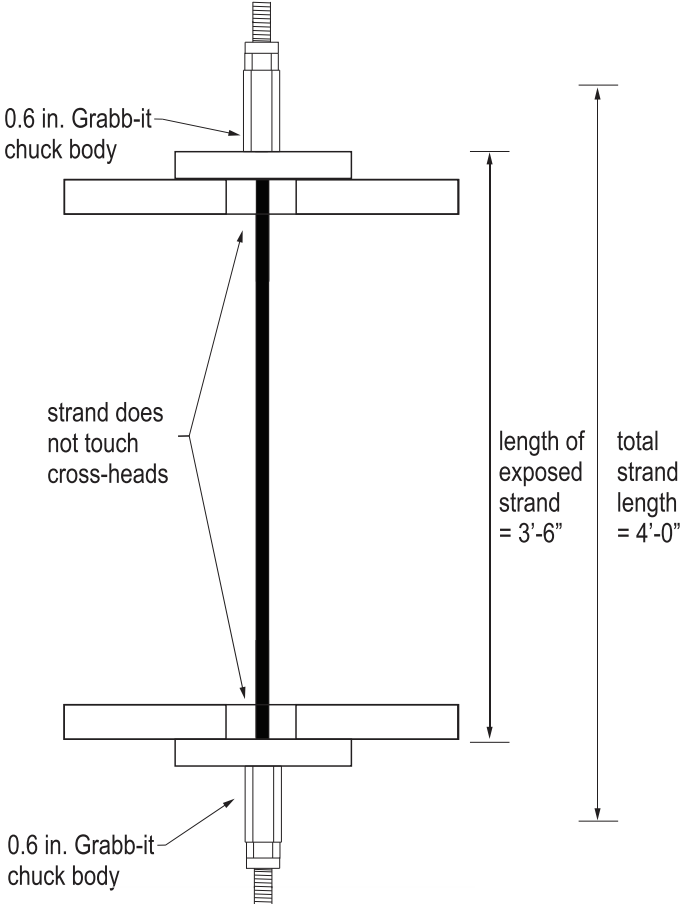


Figure 4-4. UF tensile test set-up of 0.6-in. dia. coupler

Unlike the first test, no preparation of the strand ends was performed prior to attaching the chucks. The test was performed on the same coupler that was used for the first test with fresh (previously unused) wedges. Load was applied at a

displacement-controlled rate of approximately 0.75 in./min., in accordance with ICCES test procedures.

The UF test was terminated when the strand ruptured at the chuck, at an applied tensile load of 61.5 kip, or 103% of the strand's specified ultimate strength. At rupture, the prestressing strand stress was 277 ksi - past the proportional limit of lo-lax strand and into the yield plateau. The stress-strain plot of the coupled device shows that the coupled strand began to yield prior to rupture. It was observed that the strand ruptured at notches caused as the wedge anchors bit into the strand.

Figure 4-5 shows the stress-strain plot for the two tensile tests of the coupler with strand. Also shown is the stress-strain plot for just the strand (uncoupled), tested per ASTM A1061 (2009).

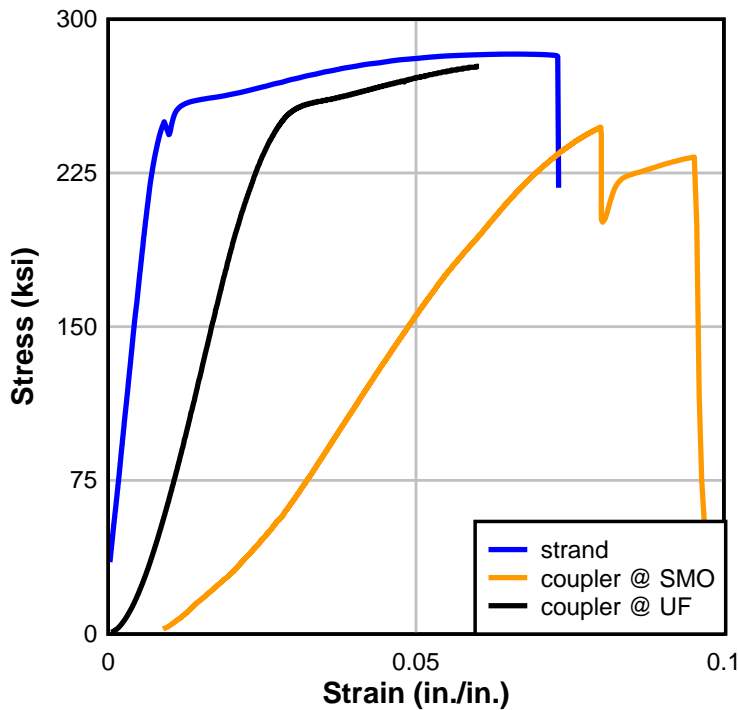


Figure 4-5. Comparison of 0.6-in. dia. coupler and strand behavior

The increased elongation seen in the coupler in the second (UF) test is unknown. Walsh and Kurama (2010) describe similar observations throughout a series of tests on a single reusable anchor; it is possible that the same phenomenon is occurring in the UF test. Alternately, the apparent strand yield may be due to the increase in the strand length of the UF test set-up. The stress-strain results of the tensile test with the fully assembled coupler (as tested at the SMO) were used in the moment-curvature analysis described in Section 3.6.

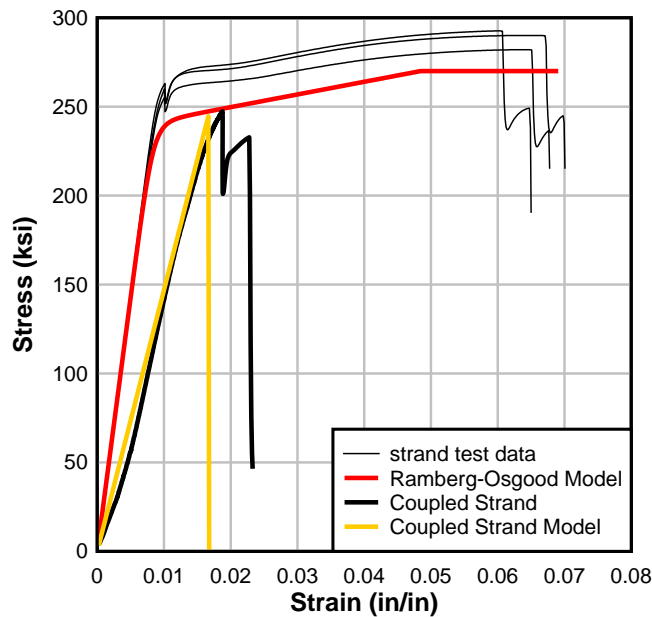


Figure 4-6. Stress-strain models and test data for coupled and continuous strand

4.2 Calibration of 0.5-in. Diameter Coupler

Coupler calibration tests using the test setup shown in Figure 4-7 were also performed to develop calibration data for the couplers that were going to be used in the spliced test specimens. Calibration of the strain to applied load allowed for direct measurement of the force in the spliced prestressing strand during the splice assembly procedure.

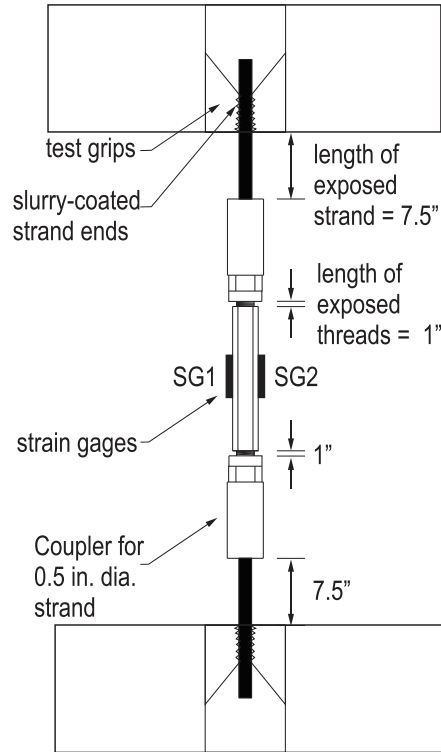


Figure 4-7. SMO tensile test set-up of 0.5-in. dia. coupler

Two specimens were tested, each instrumented with two strain gages.

Prestressing strand from the same coil as used in the unbonded segment of the spliced specimens was used in the coupler calibration. One end of the prestressing strand was slurry-coated with white glue and fine sand, in accordance with ASTM A1061 (2009).

The uncoated end was fit into the chuck body of the coupler; the slurry coated end was fit into the test grips of the crossheads, as shown. Each specimen was loaded to 35 kip three times, as summarized in Table 4-1.

Table 4-1. 0.5-in. dia. coupler calibration load procedure

| Load Cycle | Procedure |
|------------|-----------------------------|
| 1 | 0-35 kip, unload to 5 kip |
| 2 | 5-35 kip, unload to 5 kip |
| 3 | 5-35 kip, completely unload |

Figure 4-8 shows the plot of the load versus microstrain of the two coupler strain gages. The two strain gages on the couplers produced very consistent readings as load was increased, indicating that there was very little bending of the coupler occurring. The strain readings also indicate that the coupler was behaving linear-elastically at the tested load range. Also shown in the plot is the approximate linear curve-fit used to relate the coupler strain to an applied tensile load. This relationship was used in later data analysis to relate measured strain in the coupler to strand load.

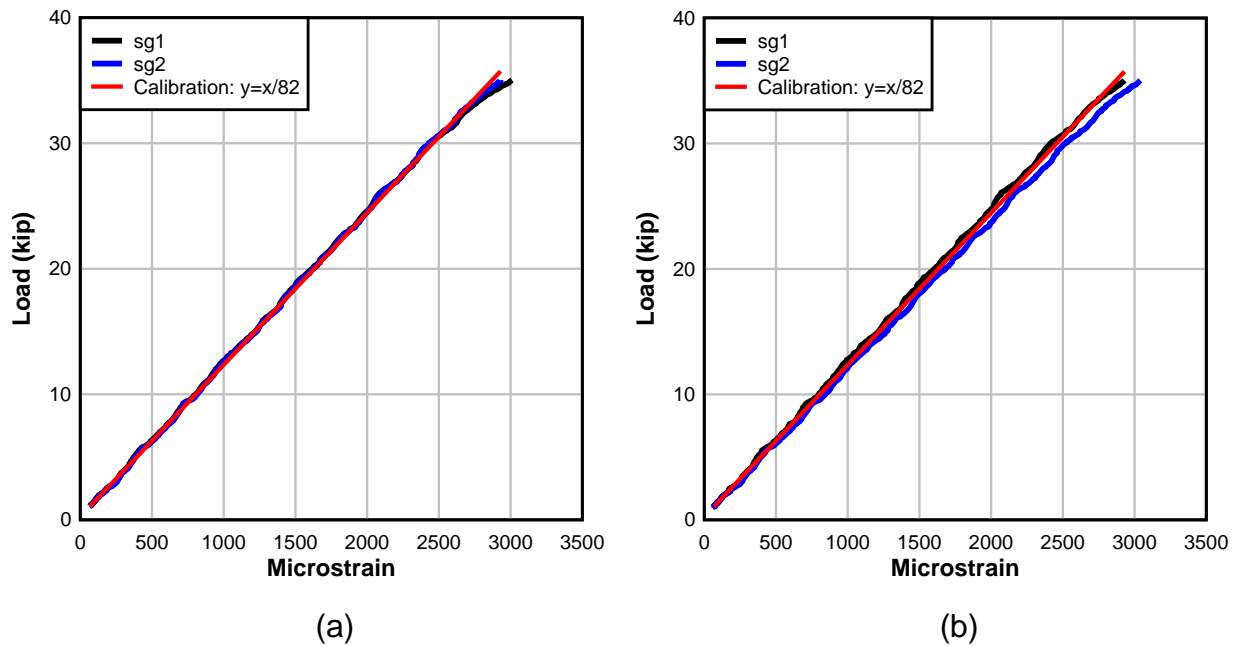


Figure 4-8. Coupler strain gage calibration (a) specimen 1 and (b) specimen 2

CHAPTER 5 TEST SPECIMEN DESIGN

A comprehensive investigation of the selected splice was necessary to assess its constructability as well as its flexural, shear, and fatigue performance. Comprehensive testing of the FIB96 prototype, however, was not possible due to limitations in laboratory capabilities and research budget. Consequently, the behavioral aspects of the splice deemed most critical were tested using an AASHTO Type II cross-section; due to its smaller size, it was possible to construct duplicate test specimens to investigate the various behaviors.

Matching the strain gradient of the FIB96 prototype to the test specimen was impossible due to the gross height difference of the two geometries. As a result, calibration of the test procedures and loading was based on matching the stress state of the test specimen and the FIB96 prototype at a particular point along the vertical axis of the FIB96 cross-section. The point of interest varied depending on the behavior under investigation.

A 25-ft long AASHTO Type II girder with an 8-in. slab was selected as a test specimen. Based on the capacity of the loading actuators in the laboratory, the strand quantity was limited to five strands. The strand pattern was arranged to create a similar pattern of congestion as would occur in the FIB96 prototype. The intent was to recreate any issues related to clearance that would be encountered in the prototype beam. A sixth strand with an 11-ft bonded length was included to prevent cracking of the unbonded segment during transport to the lab. This additional length of bonded strand was reproduced in the control beams. The AASHTO Type II was fabricated at a

precasting yard and the deck was placed by lab personnel following delivery to the laboratory. The specimens are shown in Figure 5-1 and Figure 5-2.

The materials chosen for the test specimen beam design were as follows:

Precast beams:

- Dimensions and strand pattern(Figure 5-1): AASHTO Type II
- Concrete strength at transfer, $f'_{ci} = 6$ ksi
- Concrete strength at 28 days, $f'_c = 8.5$ ksi
- Initial concrete modulus of elasticity = 4012 ksi (AASHTO-LRFD 5.4.2.4)
- Concrete modulus of elasticity = 4,776 ksi (AASHTO-LRFD 5.4.2.4)
- Concrete unit weight, $w_c = 150$ pcf (structural concrete, per SDG)
- Beam length = 25.0 ft

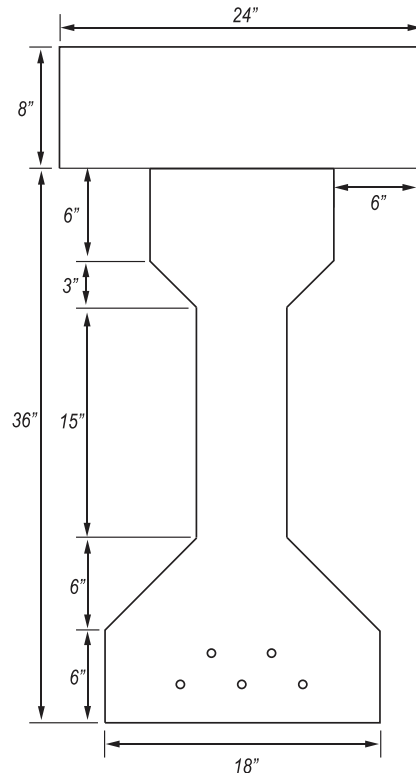


Figure 5-1. AASHTO II cross-section

Cast-in-place slab:

- Slab thickness = 8 in.
- Concrete strength at 28 days = 4.5 ksi
- Prestressing strands: 1/2 in. dia., seven wire lo-lax strand

- Area, per strand = 0.153 in.²
- Ultimate strength, $f_{pu} = 270$ ksi
- Prestressing strand modulus of elasticity = 28,500 ksi
- Prestress level at jacking = 0.6 f_{pu}

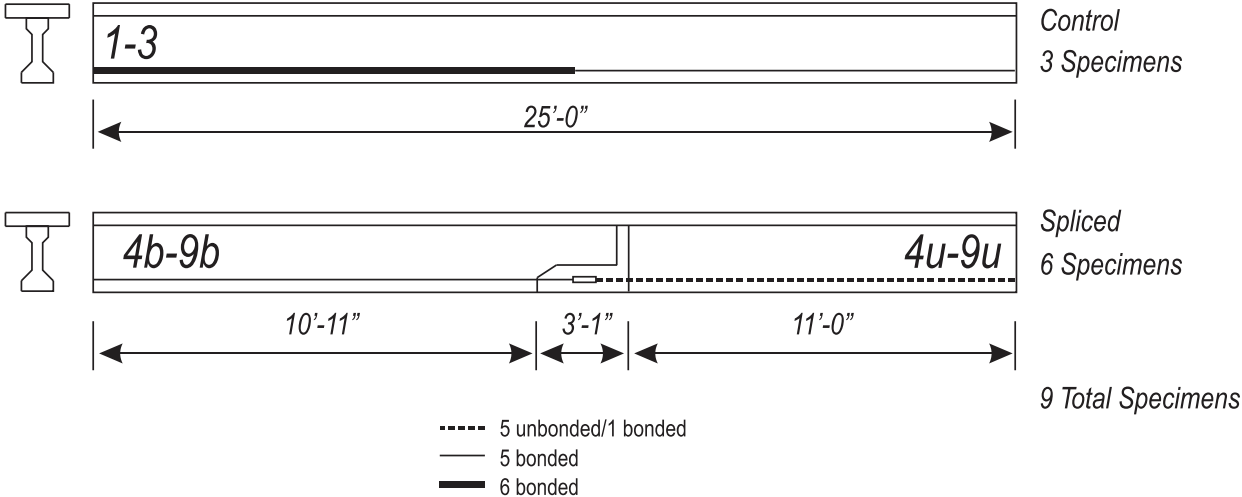


Figure 5-2. Test specimens

5.1 Detailing Considerations

Special detailing was included the segments to be spliced to accommodate personnel during the splice assembly, to prevent cracking, and to provide additional strength capacity. Special detailing for the joint area included shear keys, additional rebar around the notched area of the bonded segment, and special stirrups. Additionally, the geometry of the splice area was also considered. This section covers these detailing considerations. Figure 5-3 shows the key detailing considerations of the joint area.

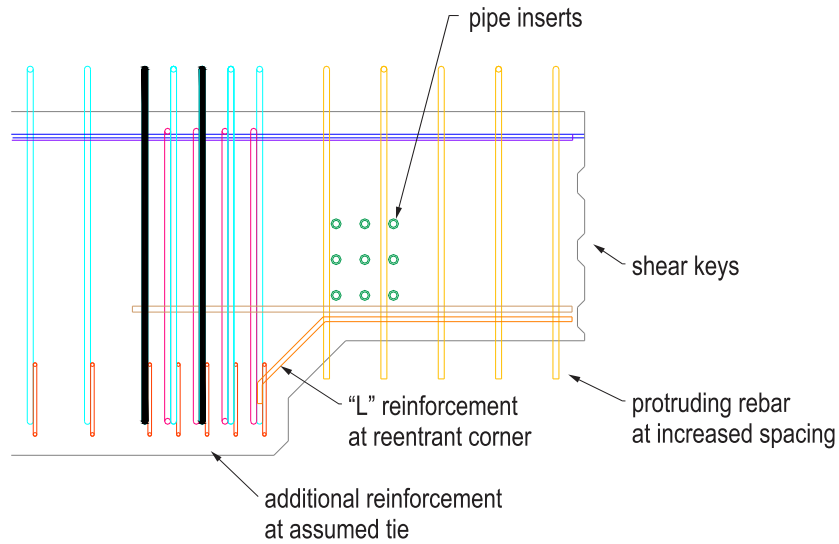


Figure 5-3. Detailing considerations

The geometry of the splice region was controlled by considerations of working space and the space required for strand coupler installation; common practice and code recommendations for precast joint design were also maintained. As discussed in Section 2.5, the length of the closure pour was controlled by two considerations: the closure length must be sufficient to allow splicing of the prestressing steel, but was limited by design (due to the limited quantity of prestressing steel and the small amount of longitudinal reinforcement). As a minimum, AASHTO-LRFD recommends 12 in. to provide enough clearance to properly splice steel reinforcement (AASHTO 2007). The distance between the top flanges of the closure pour (6 in.) was in accordance with AASHTO-LRFD recommendations for construction joint widths (AASHTO 2007).

The chosen method of introducing prestress force into the coupled strand during splice assembly was to jack the precast segments apart, by applying force to removable brackets which are attached to either face of the girder web (Figure 5-4). Steel brackets were constructed by the FDOT structures lab.

To secure the brackets on the test specimen with thru-bolts, pipes were designed to pass through the girder web. By applying the jacking force via thru-bolts and pipes passing through the girder web, the eccentricity of the applied force was reduced versus attempting to transfer the force through anchored connections on each face of the girder web. This approach is similar to that described by Gerwick (1993) (described further in Section 3.1).

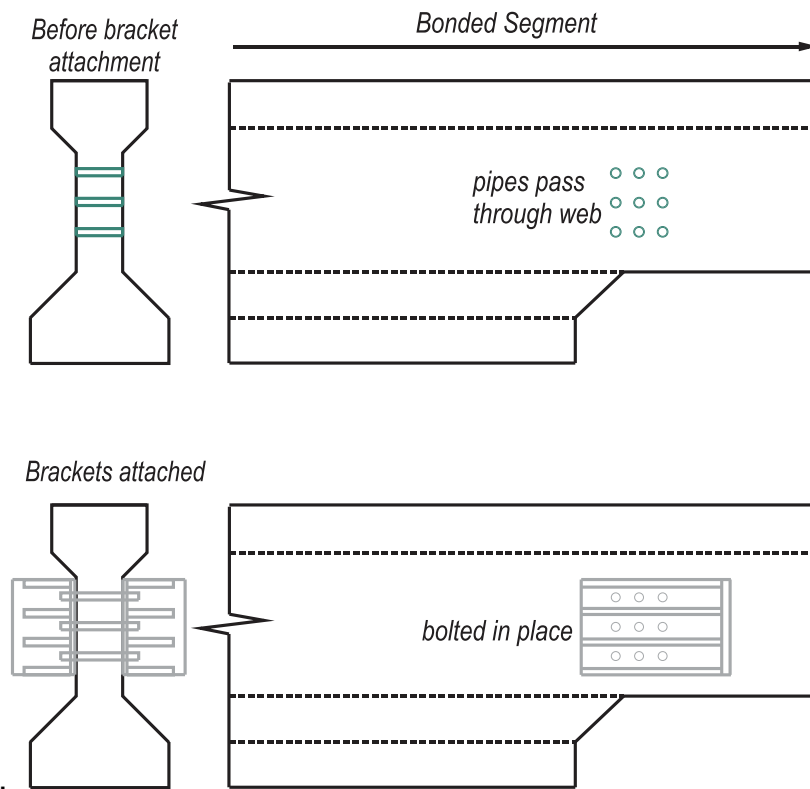


Figure 5-4. Bracket attachment to beam

Pipe inserts were constructed by the FDOT Structures Lab prior to precast of the beams. To maintain the orientation and alignment of the nine 1-in. dia. schedule 40 steel pipes during beam precast, the pipes were welded to a small rebar cage. Template plates held the pipes in position and relatively in line with one another during welding; accurate alignment of the pipes was crucial to provide non-eccentric load

application to the precast concrete during the stressing of the splice region. The alignment and levelness of each pipe insert was checked after the welding was complete.

Small diameter (#3) rebar was used in the pipe insert, in an effort to reduce the steel congestion in this area and allow the concrete to flow around the pipes. The rebar also acted as a convenient tie location when positioning the pipe inserts in the steel reinforcement. Stirrup locations in the region of the pipe inserts were adjusted (spacing in the area was increased) to avoid conflicts with the pipes. Twelve pipe inserts were fabricated by the FDOT Structures Lab and provided to the precaster as assembled units. The pipe inserts were installed at the precast yard during the stirrup placement. Installation of the pipe inserts is covered in Section 6.1. The pipe insert can be seen in Figure 6-2 and Figure 5-3.

Detailing of construction joints requires special consideration of the precast ends (PCI 2004). The precast faces were prepared prior to formation of the closure pour to provide adequate shear transfer across the joint. Shear transfer can be accomplished through a number of methods, including roughening the precast concrete after it has cured, providing stirrups which cross the joint or detailing formed shear keys in the precast concrete.

Shear keys were detailed on the to be spliced ends of both the bonded and unbonded segments, to provide mechanical interlock to increase the shear capacity of the interface between the precast concrete and the closure pour concrete. The shear keys are shown in Figure 5-5. Design recommendations are provided by AASHTO-LRFD (2007) regarding the geometry of shear keys; these recommendations are

dependent on the size of the aggregate and the width of the web and were considered for the determination of the shear key dimensions (Figure 2-11).

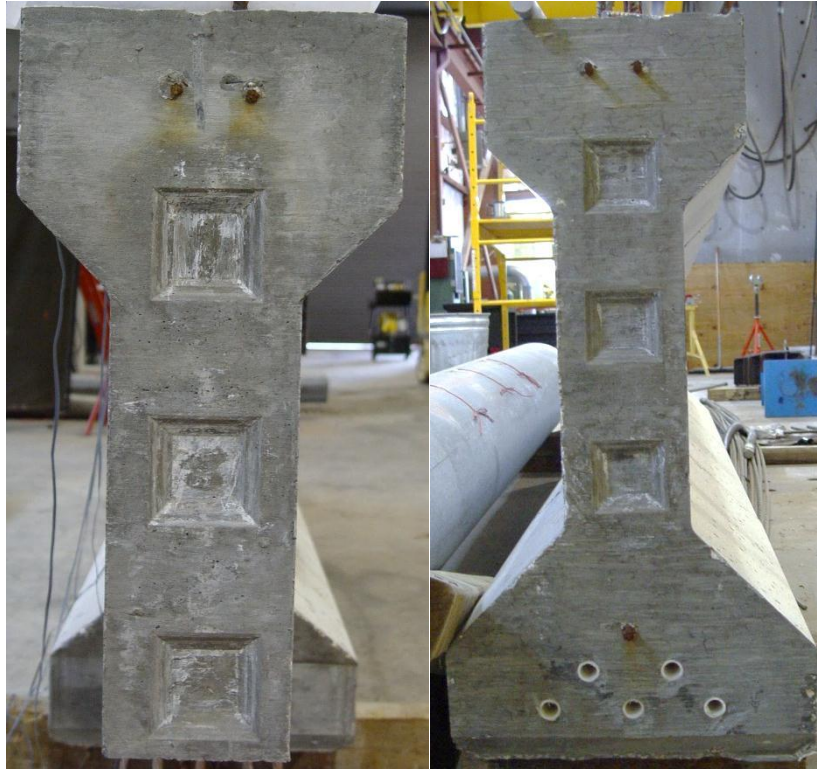


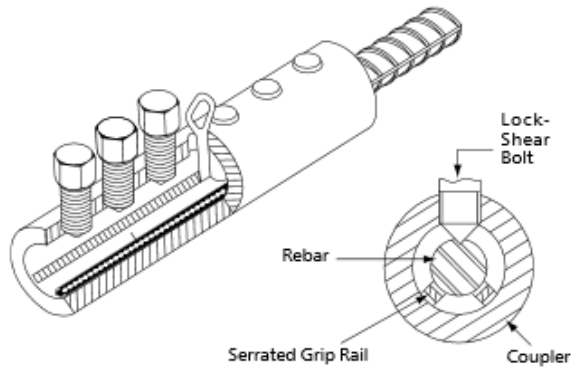
Figure 5-5. Shear keys in test specimen

In the last four splices, both faces of the precast segments were roughened by gouging the concrete with a cutting disk. This did little to roughen the concrete and likely did not contribute to shear resistance, as will be discussed later. Epoxy application to the faces of the precast segments of the last four splice assemblies was also done in an effort to increase shear resistance and bond between the precast and the closure pour.

Steel reinforcement of the area near the closure pour was designed with multiple considerations in mind: handling, tie formation during stressing of the closure pour (STM model) the need for additional confinement reinforcement at each end of the precast to

control cracking during prestress release, and straight stirrups for shear reinforcement along the closure pour length. These details can be seen in Figure 5-3. An “L” shaped #5 rebar was placed around the reentrant corner of the bonded segment, to mitigate cracking during handling and transport. Additional rebar were detailed in the region identified by the strut-and-tie model as the area of likely tie-formation. This additional reinforcement also served as confinement reinforcement during prestress transfer. The stirrups in the notched region of the bonded segment were installed without a lower hook. This was done to reduce congestion in the splice region so that the prestressing strand could be more easily reached for coupling during the splice assembly in the laboratory. The bottom hook of the stirrups were later added using a rebar coupler. The stirrup spacing was increased in the region of the coped area of the bonded segment to accommodate the congestion caused by the size of the rebar couplers and pipe inserts.

The selected rebar coupler is a commercially available product which does not require preparation of the rebar. It mechanically connects two pieces of rebar, using a series of screws to engage each rebar piece. Serrated guide rails within the coupler provide additional mechanical grip. A cotter pin serves to set the length of each rebar within the coupler. The rebar coupler is shown in Figure 5-6.



* U.S. Patent No. 4,666,326 & 5,046,878

Figure 5-6. Rebar coupler

Prestressing strand protruding from the bonded segment was detailed to extend into the coped area approximately 26 in., in order to ensure adequate length for later strand splicing. The strand was protected during the precasting and storage by the wooden block-out.



Figure 5-7. Protruding strand

5.2 Flexure Service and Cracking Test Design

The splice location of prototype beam was designed to remain uncracked under service loads; the splice behavior was anticipated to remain linear-elastic under service

loads. As a result, the Service I and III load cases were not particularly interesting, unless the prestress losses over time became significant enough to result in cracking.

The behavior of the splice under service loads was evaluated for:

1. Effective prestress force;
2. Splice stiffness vs. precast segment stiffness;
3. Strain field.

To match the stress state for Service III, the bottom face was chosen as the reference point, as the prototype beam at the splice location is still compressed. Table 5-1 presents the Service III bottom fiber stresses for the FIB96 prototype at the splice location.

Table 5-1. Stress state of FIB96: Serviceability

| Load case | f_{bot} (psi) |
|-------------|--------------------|
| DL only | -50 |
| Service III | -486 |

The applied moment required to match the bottom fiber stress of the test specimen to that of the FIB96 prototype under Service III loads was determined and are presented in Table 5-2. In addition, the applied moment required to reach the cracking stress ($7.5\sqrt{f'_c}$ (psi)) based on the specified prestress is provided for reference.

Table 5-2. Stress state of test specimen: Serviceability

| Load Level | f_{bot} (psi) | Moment (kip-ft) | Load, 2P (kip) |
|-------------|--------------------|--------------------|-------------------|
| Service III | -486 | 409 | 82 |
| Cracking | -691 | 445 | 94 |

A four-point bending set-up, with the splice region encompassed in the constant moment region, was chosen to investigate the flexural behavior of the test specimen. The 5-ft distance between the load points was selected to encompass the entire splice region. The general flexural test set-up is shown in Figure 5-8.

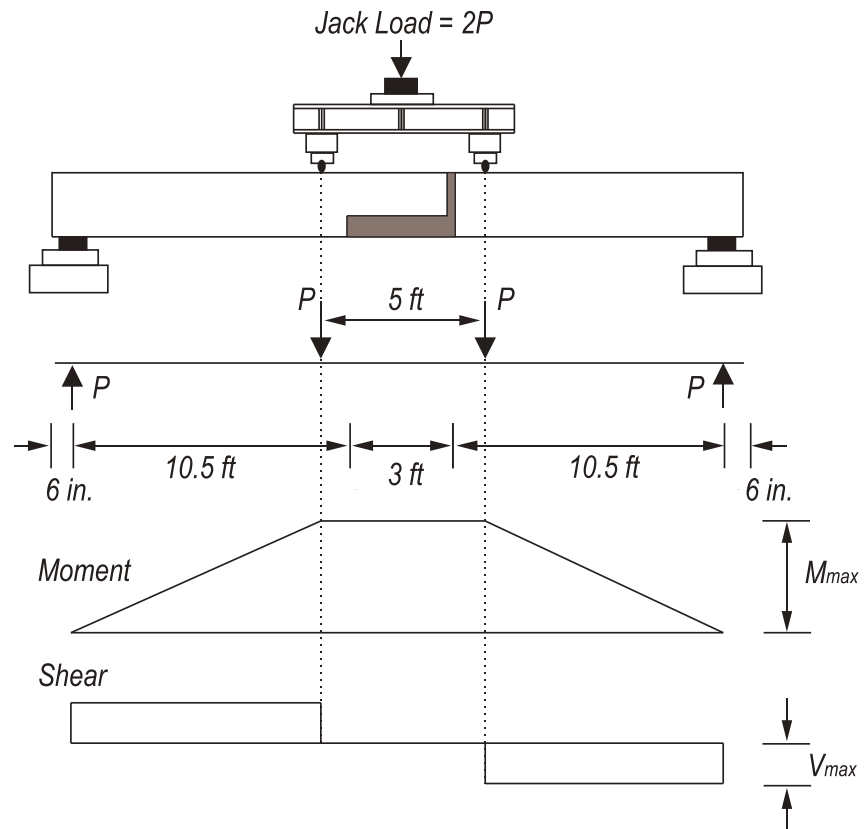


Figure 5-8. Flexure test set-up

Of primary importance to the long-term performance of the girder is the size and extent of cracking that occurs in the splice when the net tension in the extreme fiber exceeds the cracking strength of the concrete. Such cracking will adversely affect the stiffness and the durability of the girder in the splice region. Although the FIB96 prototype is designed to remain uncracked in service, overloads of a structure do occur.

For this reason, cracking behavior of the control versus the spliced test specimens was evaluated.

5.3 Moment Strength Test Design

Based on past simple-span highway bridge designs utilizing I-girders (Jaber et al. 2006), a bridge design was developed utilizing FIB96 beams spliced at two locations to achieve a 208-ft simply-supported span. Unlike splices for precast I-girder sections in continuous spans, the proposed splice will be located away from any inflection point of the moment diagram and must have significant moment strength. The factored moment in the prototype FIB96 at the splice location (each splice is located 30 ft from a bearing) is approximately 1200 kip-ft.

Because the splice is designed to remain uncracked under service loading, load testing to ultimate strength provides insight into the following performance characteristics for overload conditions, including:

1. Splice device (coupler) and strand behavior;
2. Crack development;
3. Splice stiffness after cracking;
4. Changes in the strain field up to capacity;
5. Interface issues, including opening of the splice between the precast and cast-in-place concrete;
6. Deflections after cracking.

Previous investigation of the FIB54 as a suitable test specimen proved that a shorter section could provide valuable insight into the behavior of the splice region; however, due to concerns regarding the coupler capacity and failure mode, a smaller

shape was selected as a test specimen so that more specimens could be constructed, in order to test a variety of loading conditions. Existing equipment in the FDOT structures laboratory can handle an AASHTO Type II cross-section and load it to failure. For these practical reasons, although a deeper FIB section would closer approximate the FIB96 prototype, an AASHTO Type II was chosen as the test specimen. To validate the use of an AASHTO Type II, a moment-curvature analysis was performed to compare the strain states of each cross-section at loads between cracking and ultimate capacity.

Using the high performance compressive concrete strength model as presented in Collins and Mitchell (1991), the tensile concrete strength model by Hsu (1993) and the Ramberg-Osgood empirical steel model presented by Collins and Mitchell (1991) for lo-lax 270-ksi prestressing strand, moment curvature analyses were performed on an AASHTO Type II cross-section and a simplified version (for computation purposes) of the FIB96 cross-section. For this analysis, the prestressing strand was considered to be continuous 270-ksi lo-lax, and the coupler was ignored. This simplification assumes that issues at the coupler can be resolved through additional testing of the coupler, or through selection of an alternate coupler. The entire concrete section was assumed to have a compressive strength of 8.5 ksi. Figure 5-9 shows the simplified geometry used for calculating section properties of the FIB bottom-flange.

There were 31 strands prestressed to $0.6f_{pu}$ present in the FIB96 prototype at the splice location (Figure 5-9).

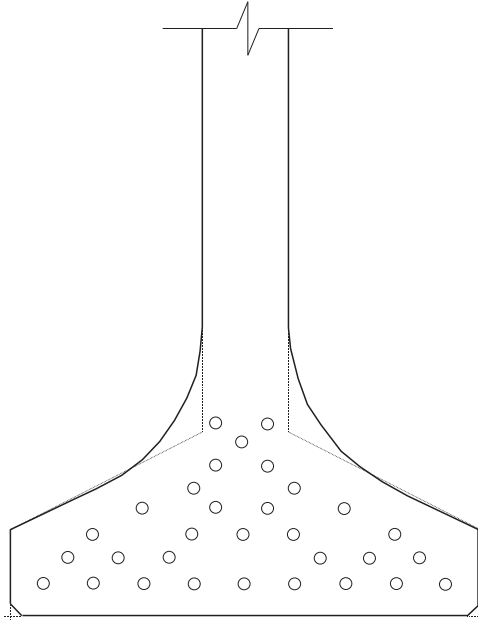


Figure 5-9. Simplified bottom flange of FIB96 cross-section

To assess its feasibility as a test specimen, a moment-curvature analysis of the AASHTO Type II with a strand pattern of five 270-ksi 0.5-in. diameter lo-lax strands prestressed to $0.6f_{pu}$ was performed. The AASHTO Type II shape and strand pattern are shown in Figure 5-1. When the extreme compression fiber was at 0.003, the maximum tensile steel strain in the FIB96 prototype was 0.052 (in./in.) and in the AASHTO Type II test specimen was 0.053 (in./in.).

ASTM A416 tensile testing of 270-ksi lo-lax strand revealed that the steel stress increased approximately 5% from yield to rupture (Figure 5-10; ASTM A416 2006), though the measured yield and ultimate strengths of the steel samples exceeded those predicted by the Ramberg-Osgood steel model. Assuming the steel in the splice region follows the Ramberg-Osgood model, both the FIB96 prototype and the AASHTO Type II test specimen began to yield and the prestressing steel stress in each beam reached the stress-strain plateau. The steel strains present at the ultimate capacity of the

AASHTO Type II were comparable to those of the full-size FIB96 prototype at its capacity. A scaled representation of the two cross-sections and their respective strain gradients at flexural capacity is shown in Figure 5-11.

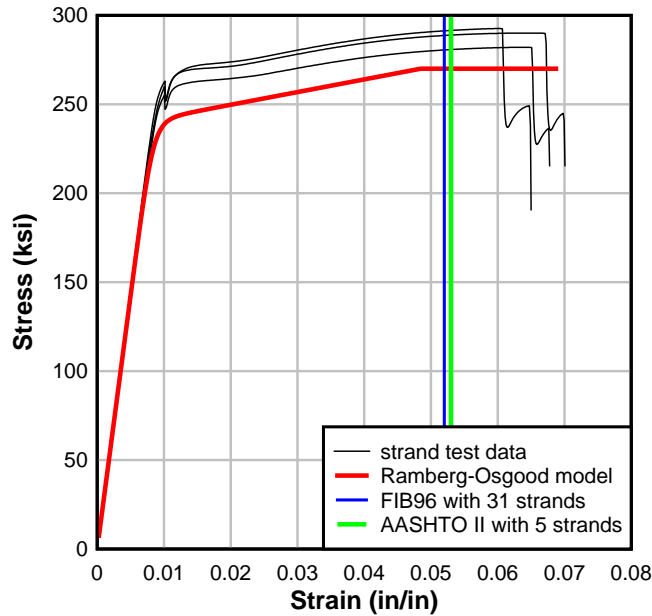


Figure 5-10. Material properties of 270-ksi lo-lax strand

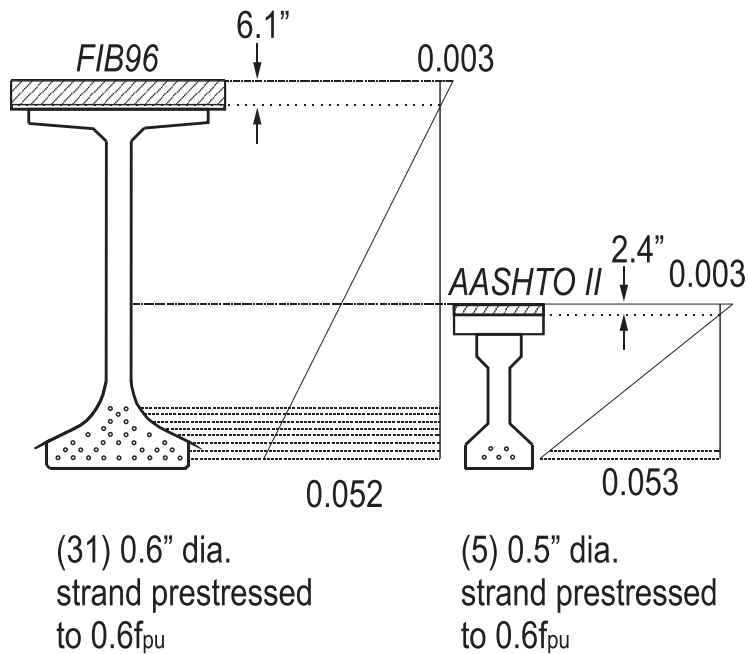


Figure 5-11. FIB96 prototype vs. AASHTO II test specimen: strain state at flexural capacity

The AASHTO-predicted moment capacity of the test specimen was calculated two ways: assuming the test specimen to be fully bonded and unbonded. Both capacity calculations were performed because the spliced test specimen includes unbonded tendons. The bonded flexural capacity of the test specimen is 631 kip-ft; the unbonded capacity is 589 kip-ft. These values do not include the strength reduction factor (ϕ factor).

5.4 Shear Test Design

Shear behavior of the splice design was investigated in three spliced specimens. Because the length of the test specimen is much less than the length of the FIB96 prototype, the M/V ratio could not be matched. Instead, the splice design was tested in a conservative set-up, with a much lower M/V .

To test the specimen in shear, the shear on the splice region was maximized as much as possible without introducing local effects. To achieve this, one side of the beam was cantilevered to shorten the span, and the main span was loaded in three-point bending. The load point was placed at the midspan of the non-cantilevered span, away from the closure pour. The test set-up is shown in Figure 5-12.

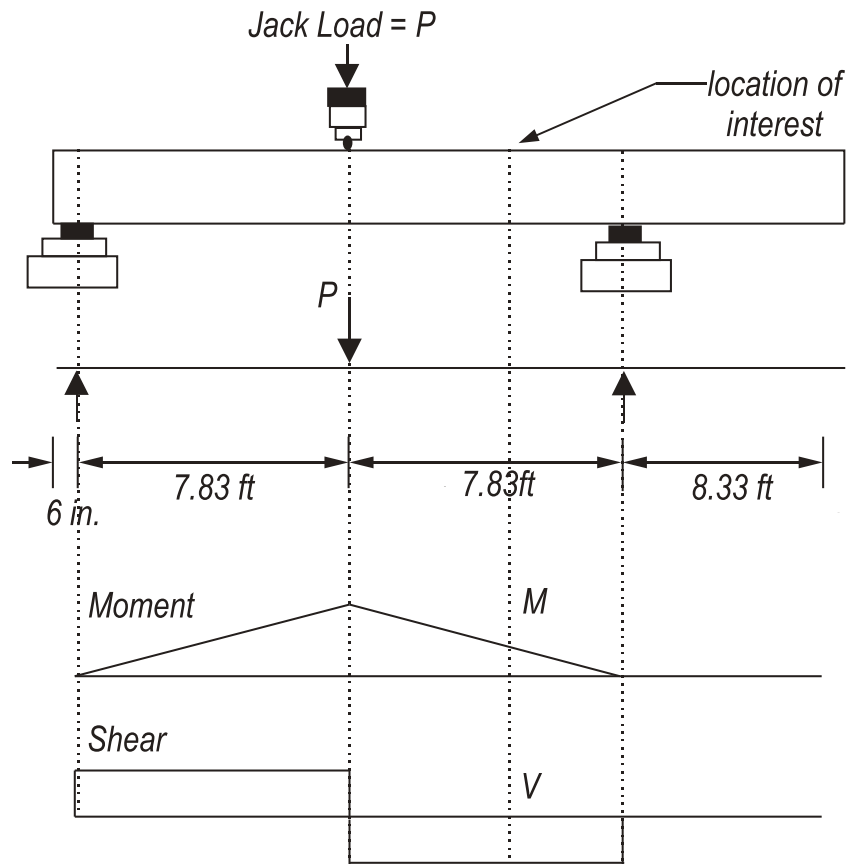


Figure 5-12. Shear test set-up

The placement of the supports and load points in this orientation ensured that local effects on the splice region were minimized; the applied concentrated load was located as far away from the splice as possible, while still forcing the shear to be greatest across the splice region.

In the prototype design, such direct shear on the splice region would not occur, as the splice region would be located further away from the supports. The selected shear test setup resulted in a M/V ratio of 3.7 versus the prototype FIB96 design M/V ratio of 32.9.

5.5 Fatigue Test Design

Fatigue is not a concern if adequate precompression of the splice region can be achieved and maintained such that the service stresses never cause cracking at the splice. However, an overload could cause cracking in the splice region, exposing the splice area to fatigue loading. The mechanical nature of the chosen coupler makes fatigue an important concern; investigation of the specimen for fatigue was completed to investigate the possibility of brittle failure at the device.

A four-point bending set-up, with the splice region encompassed in the constant moment region, was chosen to investigate the fatigue behavior of the test specimen. The distance of 5ft between the load points was selected to encompass the entire splice region, including all of the closure pour and the couplers. The general test setup is shown in Figure 5-8 and is the same setup used to evaluate static flexural behavior.

All specimens were precracked to expose the critical component—the prestressing strand and the coupler - to the cyclic stress. This approach has been taken in previous research (Rao and Frantz 1996, Russell and Burns 1993, Rabbat et al. 1979). Cracking was determined visually and confirmed by inspection of the load-displacement plot. Cracks were marked prior to load removal.

Decompression tests of each specimen were then performed to evaluate the effective prestress level. Each specimen was statically loaded until the previously formed cracks re-opened. The re-opening of these cracks was determined by the strain readings of gages placed on either side of the crack.

Following the decompressions tests, each specimen was then cycled to evaluate its fatigue life. To assess the test specimen under fatigue loading, the in place state of the FIB96 prototype and the cracking load of the test specimen were used to determine

the applied load range. In typical fatigue assessments, the dead load state and the cracking state are used to determine the stress range of the cyclic loading. This approach has been used by other researchers (Russell and Burns 1993, Overman et al. 1984, Roller et al. 1995). Of interest to the current research is the effect of the stress cycling between the in place—dead load only- state of the FIB96 and tensile stress limit—defined in AASHTO-LRFD as limited to $6 \sqrt{f'_c}$ - or the load state associated with cracking. Because the stress range affects the expected life of a beam more than the applied stress magnitude, the dead load of the prototype beam was chosen as the lower load limit, to more closely approximate the stress range expected in the FIB96 prototype. The upper limit of the load was determined based on the cracking load of the test specimen.

The bottom fiber stress in the FIB96 prototype was determined from present dead load and is shown in Table 5-3. The stress in the FIB96 calculated using the moment induced by the fatigue live load is provided only for reference. As seen in Table 5-4, the FIB96 prototype beam at the splice location is designed to remain uncracked in the fatigue load case.

Table 5-3. Stress state of FIB96: Fatigue

| Load case | f_{bot} (psi) |
|-------------------|--------------------|
| DL only | -50 |
| 0.75LL Fatigue | -280 |

Table 5-4. Stress state of test specimen: Fatigue

| Load Level | f_{bot} (psi) | Moment (kip-ft) | Applied Load (kip) |
|--|--------------------|--------------------|--------------------------|
| Specimen DL | 468 | n/a | n/a |
| Specimen DL + Preload = Prototype DL | -50 | 200 | 42 |
| $6\sqrt{f'_c}$ | -553 | 392 | 83 |
| $7.5\sqrt{f'_c}$ | -691 | 445 | 94 |

The fatigue test parameters were determined by stress matching to equate the stress range in bottom fiber of the test specimen to the calculated stress range in the prototype beam expected between the dead load state and cracking load of the test specimen. Using these two stress states, the load to be applied was calculated and is presented in Table 5-5.

Table 5-5. Loading procedure: Fatigue

| Specimen | Lower Limit Load (kip) | Upper Limit Load (kip) | Load Application |
|----------|------------------------------|------------------------------|---|
| FC | 40 | 72 | 0.2 kip/sec until the mean load of 56 kip was reached. Load amplitude was increased to target load range over 400 cycles. |
| F1 | 40 | 54 | 0.2 kip/sec until the mean load of 47 kip was reached. Load amplitude was increased to target load range over 200 cycles. |
| F2 | 40 | 72 | 0.2 kip/sec until the mean load of 56 kip was reached. Load amplitude was increased to target load range over 200 cycles. |

Because the test specimens have less dead load stress at the bottom fiber than that of the FIB96, a minimum superimposed load must be maintained during fatigue cycling to match the FIB96 dead load stress state. Matching the stress in the bottom fiber, the preload required to match the dead load stress state of the FIB96 prototype is 42 kip—rounded down to 40 kip for simplicity.

The upper limit load was determined on a specimen-by-specimen basis. The load at cracking, as determined from inspection of each specimen's load-displacement plot, was used as the upper limit load for the control specimen (FC) and the first spliced specimen (F1). Because the stress range of F1 was lower than that of FC, the second spliced specimen (F2) was tested using the load range of the control. In this way, the disparate effective prestress values of the control and spliced specimens were eliminated as a variable.

Following the fatigue testing, each test specimen was statically loaded to failure in the same four-point bending set-up to assess the effects of fatigue degradation.

CHAPTER 6 SPECIMEN CONSTRUCTION AND SPLICE ASSEMBLY

The intent of this research is to develop and assess a splice design simple enough to be assembled without a subcontractor, for use in future construction projects without needing to post-tension. Throughout the development of the splice for the FIB96 prototype, the ease of the precast segment construction and the splice assembly procedure was considered, guiding development of details, coupler selection, and strand layout. Section 6.1 describes the precast segment production.

Assembly of the splice in the AASHTO II test specimen in the laboratory provided an opportunity to evaluate and adjust the procedure. Dimensions and lay-out of the assembly frame setup for the splice procedure is described in Section 6.2. The general splice assembly is described in Sections 6.3, 6.4, and 6.5.

6.1 Segment Production

Fifteen precast pretensioned beam segments were constructed at a precast concrete plant. Three beams 25-ft long were constructed as control beams (Specimens 1-3). Six segments with bonded prestressing 13.5 ft long (referred to as segments 4b-9b) and six segments with PVC pipes (in future strand locations; referred to as segments 4u-9u) 11-ft long were also constructed, to be spliced together at the laboratory to form a 25-ft long completed beam (Figure 6-1). The control beams and bonded segments were constructed in the first pour; due to space limitations and safety concerns regarding completely unbonded strand, the unbonded segments were constructed in a separate pour.

To reduce the likelihood of strand recoil during detensioning, segments for the first pour were arranged in the bed as shown in Figure 6-1; segments were located close to one another, but away from the abutments.



Figure 6-1. Bed layout

The prestressing strands were stressed to $0.6f_{pu}$; the relatively low level of prestress also acted to reduce the likelihood of strand damage during detensioning. The prestressing report and detensioning sequence are given in Table 6-1. The mild steel reinforcement was tied in, with particular care taken in the coped regions of the bonded segment. The plywood block-out served to form the coped area and protect the protruding strand. Holes were drilled into the block-out to allow for straight-ended stirrups to be placed in this region. Epoxy was used to seal holes to prevent leakage of concrete paste into the wooden block-out.

Following stirrup placement, pipe inserts were aligned and secured with tie wire. Reinforcing bars used to fix the pipe inserts were also used to tie the fixture into place.

The pipe assembly was then leveled and supplementary reinforcing bars were tied in to further secure the pipe insert placement. Following the installation of the pipe inserts, the side forms were locked into place. The pipe assembly fit snugly against the side of the forms to prevent intrusion of paste during concrete placement.

A high slump concrete mixture was used to ensure good flow around the congested areas near the pipe inserts. The same concrete mixture design was used for both pours; the mix design and field properties are provided in the FDOT report. The concrete was consolidated with internal and side-form vibrators. Care was taken near instrumented rebar to ensure gage integrity. The tops of the beams were roughened for future deck placement and the bed was covered with tarps for the curing period. The dates of strand stressing, casting and detensioning are given in Table 6-1.



(a)



(b)

Figure 6-2. Coped region of bonded segments (a) stirrup placement and (b) pipe insert



Figure 6-3. Segments after concrete is cast with top roughened for deck placement

Table 6-1. Construction and testing schedule

| Segment | Strand Stressed | Concrete Cast | Strand Detensioned | Splice Assembled | CP Cast | Deck Cast | Tested |
|---------|-----------------|---------------|--------------------|------------------|----------|-----------|----------|
| 1 | 3/20/12 | 3/22/12 | 3/26/12 | n/a | n/a | 8/7/12 | 1/4/13 |
| 2 | 3/20/12 | 3/22/12 | 3/26/12 | n/a | n/a | 8/7/12 | 8/24/12 |
| 3 | 3/20/12 | 3/22/12 | 3/26/12 | n/a | n/a | 12/13/13 | 1/30/13 |
| 4b | 3/20/12 | 3/22/12 | 3/26/12 | 9/13/12 | 9/19/12 | 10/2/13 | 10/18/12 |
| 5b | 3/20/12 | 3/22/12 | 3/26/12 | 10/19/12 | 10/24/12 | 11/6/12 | 11/16/12 |
| 6b | 3/20/12 | 3/22/12 | 3/26/12 | 2/27/13 | 3/1/13 | 3/21/13 | 4/15/13 |
| 7b | 3/20/12 | 3/22/12 | 3/26/12 | 2/8/13 | 2/12/13 | 2/22/13 | 3/20/13 |
| 8b | 3/20/12 | 3/22/12 | 3/26/12 | 1/11/13 | 1/16/13 | 1/31/13 | 2/8/13 |
| 9b | 3/20/12 | 3/22/12 | 3/26/12 | 11/30/12 | 12/4/12 | 12/13/12 | 12/20/12 |
| 4u | 3/26/12 | 3/27/12 | 3/30/12 | 1/11/13 | 1/16/13 | 1/31/13 | 2/8/13 |
| 5u | 3/26/12 | 3/27/12 | 3/30/12 | 10/19/12 | 10/24/12 | 11/6/12 | 11/16/12 |
| 6u | 3/26/12 | 3/27/12 | 3/30/12 | 2/8/13 | 2/12/13 | 2/22/13 | 3/20/13 |
| 7u | 3/26/12 | 3/27/12 | 3/30/12 | 11/30/12 | 12/4/12 | 12/13/12 | 12/20/12 |
| 8u | 3/26/12 | 3/27/12 | 3/30/12 | 2/27/13 | 3/1/13 | 3/21/13 | 4/15/13 |
| 9u | 3/26/12 | 3/27/12 | 3/30/12 | 9/13/12 | 9/19/12 | 10/2/13 | 10/18/12 |

Table 6-2. Specimen identification

| Specimen | Segments | Load Test |
|----------|----------|------------|
| XC | 1 | 8/24/2012 |
| SC | 2 | 1/4/2013 |
| FC | 3 | 1/30/2013 |
| X1 | 4b-9u | 10/18/2012 |
| SB | 5b-5u | 11/16/2012 |
| SU | 9b-7u | 12/20/2012 |
| SU2 | 8b-4u | 2/8/2013 |
| F1 | 7b-6u | 3/6/2013 |
| F2 | 6b-8u | 4/15/2013 |

The specified concrete strength for transfer, f'_{ci} , was 6000 psi. The specified compressive strength at 28-days, f'_c , was 8500 psi. The tested 32-day compressive strengths for the first concrete pour (specimens 1-3 and segments 4b-9b) was 8990 psi; for the unbonded segments completed in the second pour ((segments 4u-9u), the tested 28-day compressive strength was 10700 psi.

Rather than flame-cutting the strands (typical procedure), they were released slowly using a single-strand jack at the live end. After the live end was slack, the strand at the dead end was cut using a plasma torch. No beam movement was visually observed during this process and the portions of the strands in the cope (that would receive the strand coupler) were not permanently deformed. Completed segments were shipped to the FDOT Structures Laboratory in Tallahassee, FL for splice assembly, deck placement, and load testing.

6.2 Segment Assembly Frames

Pushing the segments apart with hydraulic jacks placed eccentric to the strand centroid created an internal moment. This internal moment caused uplift that was resisted by the structural steel frames and tie-down connections shown in Figure 6-4. Four steel frames were positioned and bolted to the strong-floor using 1.5-in. diameter threaded rod. Two interior frames were used as tie-downs, resisting the uplift force during the stressing procedure. All four frames were designed to resist beam roll-over and to guide the longitudinal movement of the rolling segment during stressing. Tie-down connections were positioned and welded onto their respective frames. The fixed tie-down connection was constructed of steel plate with a load button receiver welded to a pair of channels bolted to Frame F. The roller tie-down connection was constructed by welding a Hilman roller to a steel plate, which was then welded to a pair of channels bolted to Frame R. To ensure smooth translation of the rolling beam, the Hilman roller was leveled prior to welding it to the frame.

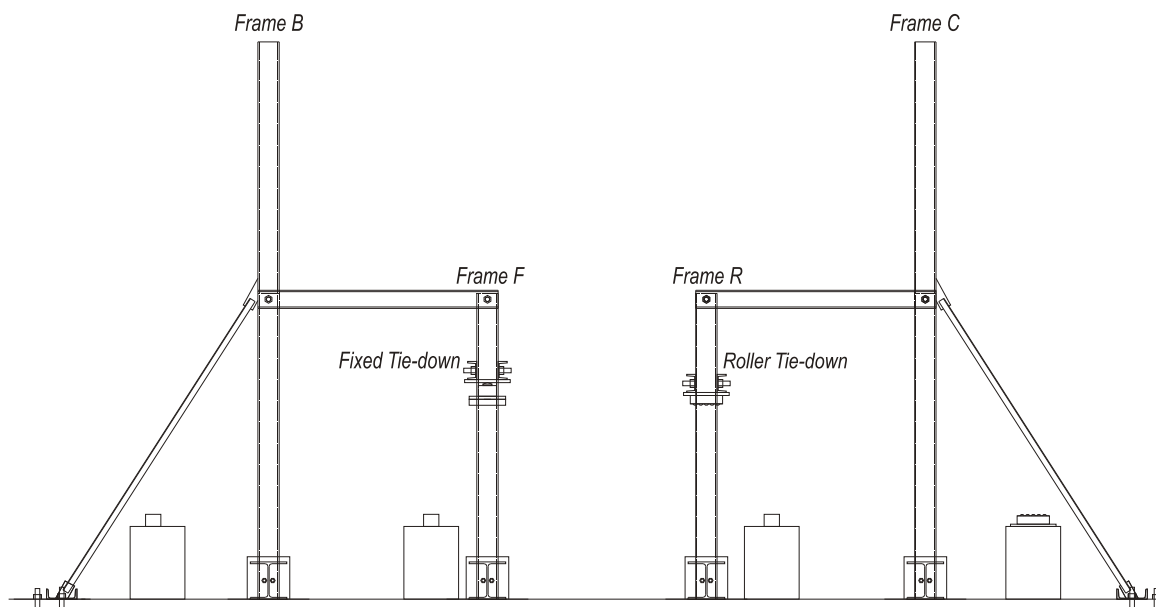


Figure 6-4. Elevation of assembly frames

6.3 Segment Alignment Procedure

Figure 6-5 shows the placement of the segments along with the strand couplers, beam brackets, and stressing jacks. Segments were maneuvered into position within the assembly frames and set down on their respective supports. The bonded segment was supported at both ends by wooden blocks set on steel blocks. The left end of unbonded segment was supported by a wooden block set on a steel block; the right end of the bonded segment was supported by a Hilman roller welded to a steel block. During the stressing procedure, the beam segments lift off the temporary supports; wood was selected to allow their easy removal.

Segments were then aligned within the frames and relative to one another. To ensure even distribution of uplift force, the segments were first oriented laterally within the frames, centering the beam segments' major axis under the tie-down points of Frames F and R. The beam segments were then aligned longitudinally with one another, ensuring a 5-in. gap between the two segments at the top of the closure gap. Finally, the heights of the segments were adjusted to ensure that the strands to be coupled were in alignment. The height of the prestressing strand was used as the controlling point of reference because each beam segment was of slightly different dimensions; aligning the centroid of the strand provided non-eccentric line of action for the induced prestressing force.

Once the beam segments were aligned, the wooden cribbing was adjusted to allow unrestrained longitudinal movement of the segments along the segment's main longitudinal (same direction as the beam span). The load cell at the fixed tie-down was slid into position and the load button was unthreaded to touch the load button receiver.

Proper alignment of this tie-down was critical to prevent rotation of the bonded segment, and to ensure accurate readings in the load cell. The prestressing jacks (Enerpac CLL 504s) were placed into the bracket cradles on each side of the segments. Hydraulic hand pumps were attached and set aside.

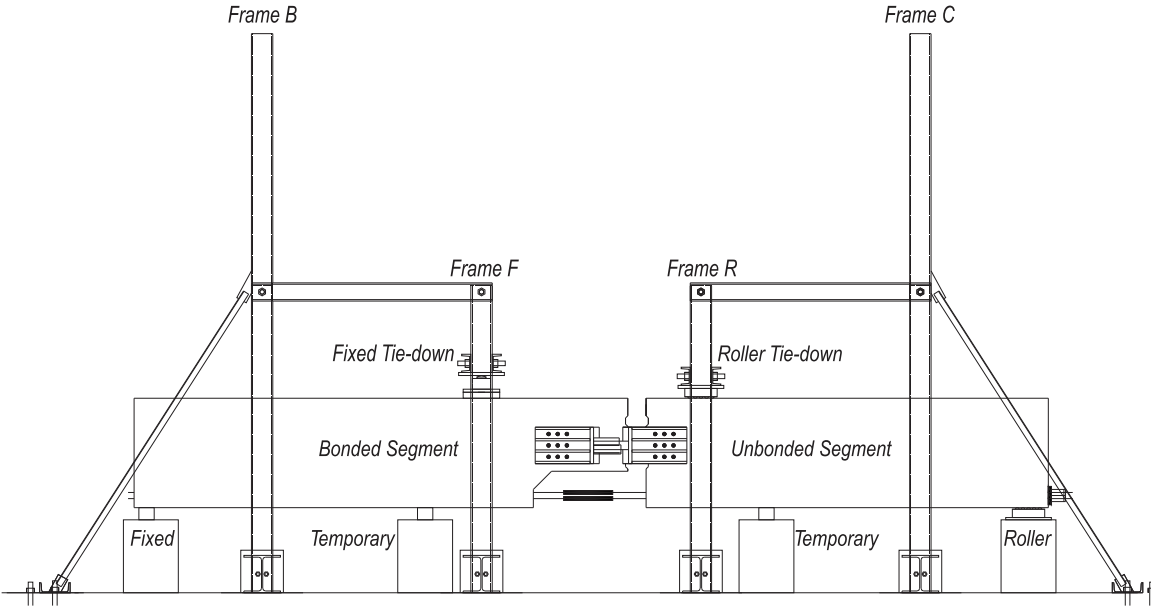


Figure 6-5. Photo and schematic of splice assembly frame and beam segments

Strand couplers were adjusted to have approximately 1 in. of thread visible on either side of the turnbuckle, to ensure adequate length for later adjustment. Couplers were first installed on the strand protruding from the bonded segment. Engagement of the wedges in the coupler was checked by hand. Couplers were then attached to the strand protruding from the unbonded segment (Figure 6-6). Engagement of the coupler wedges was again checked by hand. At this point, the coupled strands were not taut in the closure pour region and occasionally appeared to bend across the closure pour length (Figure 6-7). Next, rebar couplers were attached to the rebar protruding into the notch. The couplers were used to attach the bottom hook of the stirrups in the splice region (Figure 6-8).



Figure 6-6. Coupler installation on unbonded strand

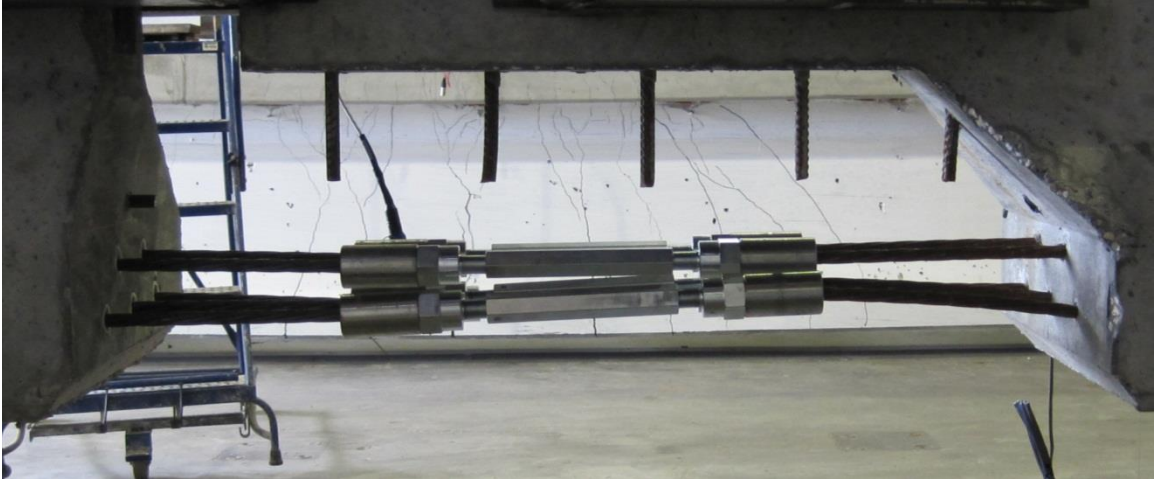


Figure 6-7. Coupled strand prior to prestressing



Figure 6-8. Coupled stirrups

Next, hardware was attached to the end of the unbonded segment. With the string-pots loose, the prestressing jacks were simultaneously pressurized until they engaged the brackets on each side of the unbonded segment. The lock-nuts were engaged and hydraulic pressure was released from the jacks. This was done to prevent translation of the unbonded segment on the Hilman roller during attachment of the hardware and initial adjustment of the coupler turnbuckles.

The detensioning chair (Figure 6-10) was then threaded onto the protruding strand from the unbonded segment. The chair was shimmed to the proper height and leveled to provide clear passage of the prestressing strand through each hole. Chucks, load cells, and anchor plates were then installed.



Figure 6-9. Extend plunger



Figure 6-10. Detensioning chair, chucks, and load cells on the unbonded segment

Prestressing strand couplers were then tightened to hold the detensioning chair against the unbonded segment (Figure 6-11.). One person was required to adjust each turnbuckle in the closure pour until the coupled strand was taut while the second person

monitored and adjusted the alignment of the detensioning chair, the load cells and the prestressing chucks. Proper positioning of the hardware included clear, unrestrained passage of the prestressing strand through the detensioning chair and the load cells; unobstructed placement of each prestressing chuck relative to one another; and flush seating of the detensioning chair on the end of the beam.



Figure 6-11. Tightening the turnbuckles to seat detensioning chair

With unbonded strands secured with chucks at both ends, an initial load was put into each strand to straighten the prestressing strand across the closure gap, and to provide an “even” starting point for later stressing. This was done by adjusting the turnbuckles on each coupler, alignment of the detensioning chair was monitored to ensure that the protruding strand passed clear through the detensioning chair and the load cells without obstruction. In addition, the load cell and coupler strain gage output were monitored. Alignment of the load cells was monitored to ensure that were bearing evenly on the detensioning chair and the prestressing chucks. Approximately 1 kip of load was achieved in each strand, or approximately 100 microstrain per coupler. Equalization of the force in each strand was an iterative process, requiring several

adjustments to each turnbuckle, as each adjustment affected the force in the nearby strands.



Figure 6-12. Tightening the turnbuckles

6.4 Strand Stressing

Following initial preloading, the string-pots across the gap between the segments were connected. Preload in each of the load cells was noted, as well as initial strain in the coupler strain gages. The DAQ was zeroed, stressing was initiated, and data acquisition was started. The prestressing jacks were pressurized synchronously with care taken to ensure the splice was stressed evenly. Pressure was held at 100 psi, then every 500 psi until 5600 psi, which corresponded to approximately 25 kip per prestressing strand (approximately $0.6 f_{pu}$).

At 5600 psi, the lock-nuts on both actuators were hand-tightened. In cases where the string-pots at the bottom of the closure indicated 1-in. of displacement prior to achieving 5600 psi in the prestressing jacks, the procedure was halted and the lock-nuts were tightened early. In cases where the gap opening between the segments and the

load cell readings were both low, jacking was continued until the jack pressure reached 6100 psi. The hydraulic pressure was then simultaneously and slowly released from the jacks.

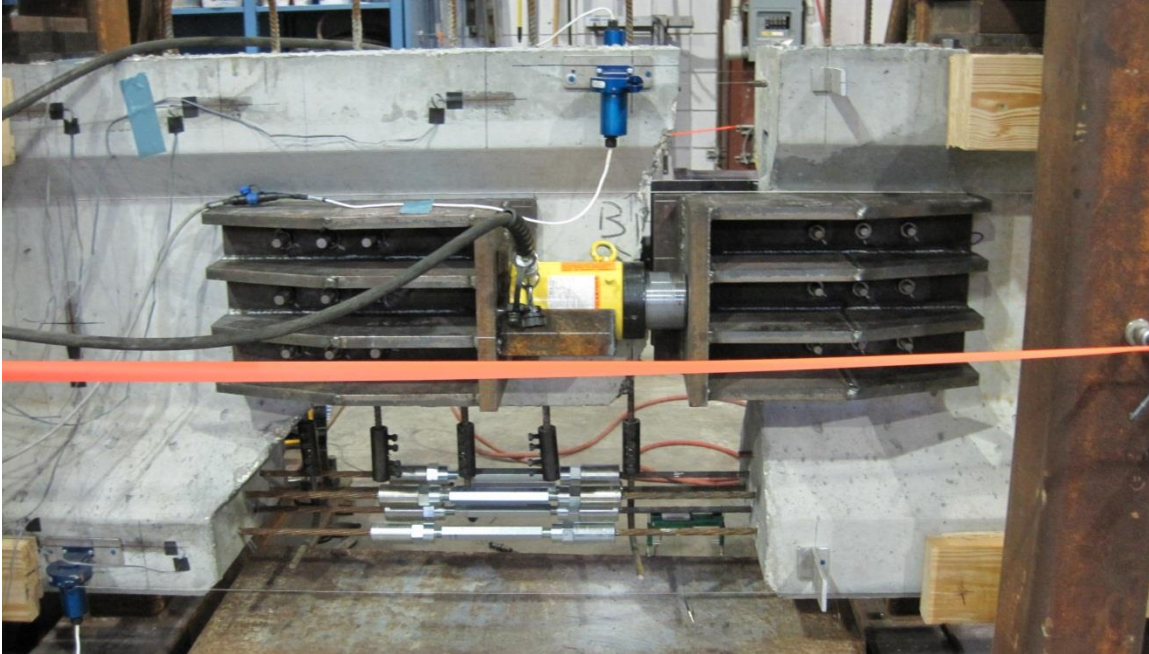


Figure 6-13. Splice stressed with lock-nuts engaged

6.5 Formwork and Concrete Placement

Formwork for the closure pour was then attached to the beam segments (Figure 6-14). The closure pour formwork consisted of two forms for the top flange, two forms for the bottom flange, a long form for the bottom of the beam and small pieces of plywood for the region between the actuators. Side forms were attached to the precast beam using expansion anchors and concrete screws. The bottom form was wedged into place, supported underneath by a steel support block. Seams were caulked and/or duct taped with foam backer rod to prevent leakage during the pour (Figure 6-15).



Figure 6-14. Closure pour formwork in place



Figure 6-15. Seams sealed

Concrete was lifted using 5-gal. buckets and tremmied into the closure with the aid of a plastic traffic cone (Figure 6-16). The cone was wedged deeply into the form at the start of the pour, and as the concrete level rose, the cone was slowly extracted to mitigate segregation of the mix and void formation.



Figure 6-16. Pouring the closure

A hand-held vibrator was used to vibrate the accessible parts of the pour; however, limited vibration of the closure concrete was possible due to hardware congestion and the placement of instrumentation.



Figure 6-17. Top of finished closure pour

The concrete was allowed to cure until the tested compressive strength—as determined by ASTM C39 tests of 6X12 cylinders made from concrete from the same delivery—reached approximately 8500 psi (ASTM C39 2010). This limit was chosen to

make sure the concrete developed some tensile strength prior to removal of the prestressing actuators (during which a small amount of tension is introduced into the joint). The formwork was then removed from the splice region (Figure 6-18).



Figure 6-18. Formwork removed (specimen X1 shown)

To remove the prestressing actuators, the jacks were pressurized until the lock-nuts could be loosened with a spanner wrench. In each case, the pressure required to free the lock-nuts was approximately equal to the pressure in the actuators when the lock-nuts were tightened. Jacks were re-pressurized slowly while monitoring the load in the strand load cells. This was to avoid creating tensile stress in the fresh concrete and potentially cracking the splice concrete.

Tie-down forces were then released. A jack was placed under the beam as near to the support under the bonded segment as possible. The inner support points (wooden supports) were removed to reduce restraint. The jack under the bonded segment was pressurized until the neoprene pad under the beam could be removed. Pressure was then released, which lowered the beam end sufficiently to remove tie-down forces at frames F and R. The stressing brackets were removed and the assembled beam was removed from the assembly frames, completing the splice procedure.

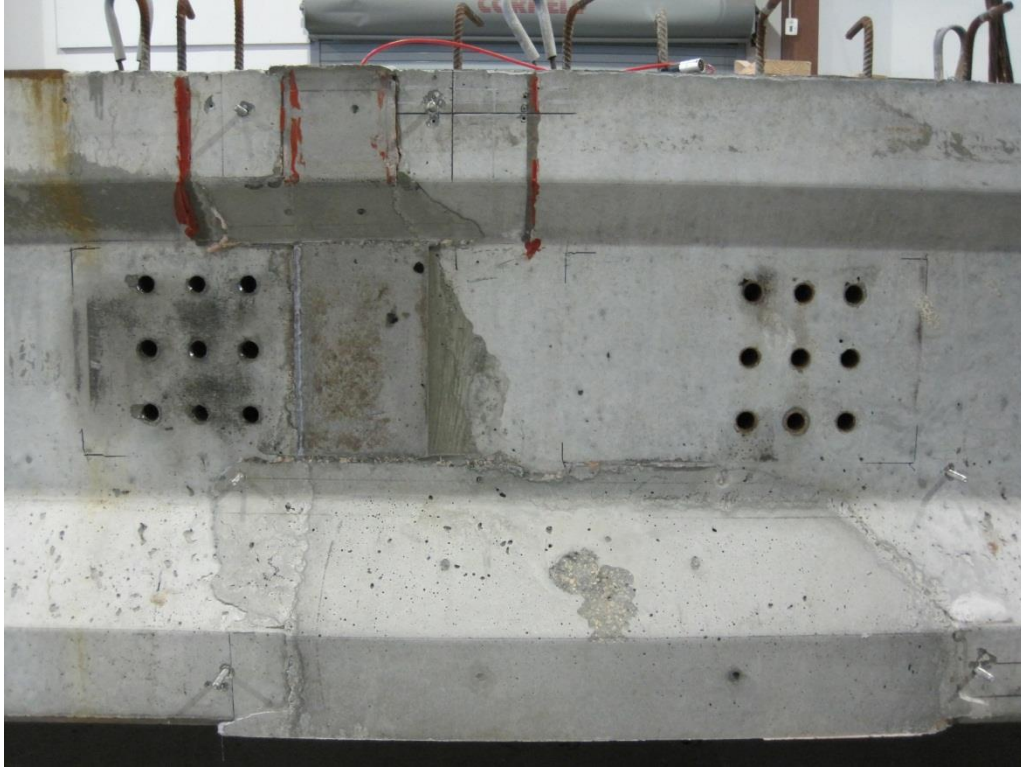


Figure 6-19. Splice complete

6.6 Splice Modifications

Several modifications were made to the splice design as specimens were completed and tested. Modifications included: scoring of the closure pour faces with a grinder, the inclusion of an additional rebar in the closure pour, and the use of epoxy on the faces of the closure pour.

- After the first two splice assemblies (X1), the precast faces of the closure pour of the remaining spliced beams (SU, SU2, F1 and F2) were scored using a cutting disk. This was done based on the clean break occurring in specimen X1, shown in Figure 6-20(a) (the first assembled beam).



(a)

(b)

Figure 6-20. Closure face:(a) bond at vertical interface X1 (b) scoring of SU

- In specimens SU2, F1 and F2, an additional stirrup was included in the closure to increase the shear capacity of the splice region. The additional stirrup was centered in the vertical portion of the pour and can be seen in Figure 6-21.

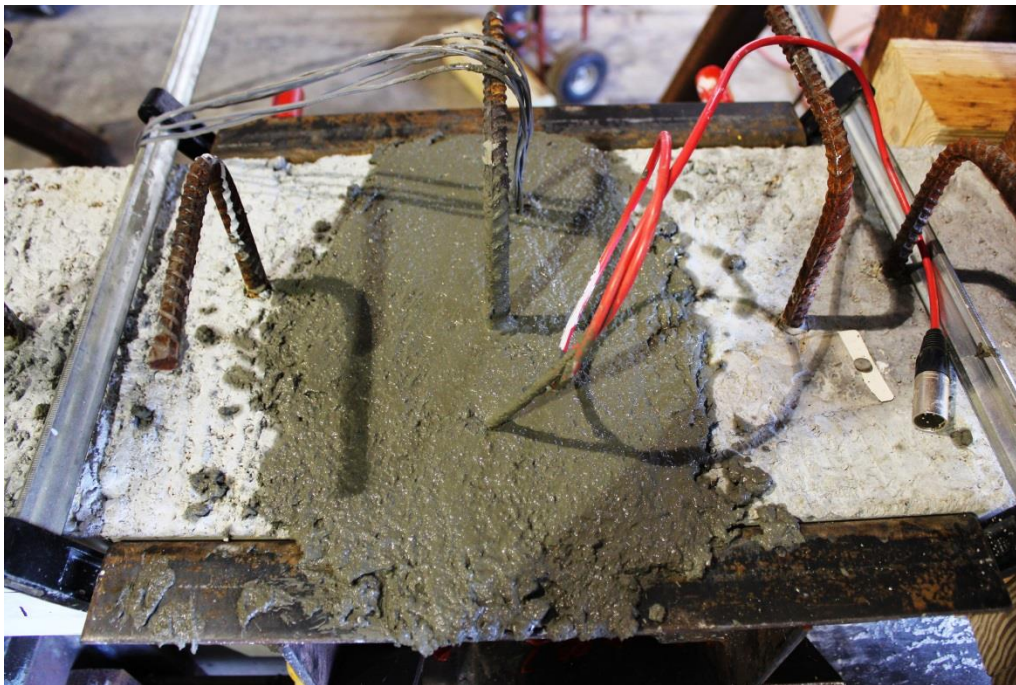


Figure 6-21. Additional stirrup

- Epoxy was not used in the first three splice assemblies (X1, SB, SU). Figure 6-20(a) shows the closure after demolition; it can be seen that—for the most part - the closure pour concrete broke away cleanly at the joint. In later specimens (SU2, F1 and F2), an epoxy (Master Builders Concrete Liquid LPL) was used to improve the bond.

Figure 6-22 shows view of the epoxy application. Approximately 10 minutes prior to the arrival of the closure pour concrete, the epoxy was mixed and applied to the joint. The epoxy was applied from above and below the beam, using a bristle paintbrush. Care was taken to cover the entire surface area with a generous coat. Following the application of the epoxy, the closure was poured; the pour was completed within one hour of epoxy application.



Figure 6-22. Epoxy in closure pour

CHAPTER 7 TEST PROCEDURE AND INSTRUMENTATION

This section describes the testing procedure and installed instrumentation used in each of the test specimens. In total, six spliced beams were assembled in the laboratory; data was recorded during each splicing procedure. The instrumentation for the splice assembly procedure is covered in Section 7.1; the splicing procedure is described in Chapter 6. One control and two spliced beams were tested in flexure; the instrumentation and testing procedure are covered in Section 7.2. One control and three spliced beams were tested in shear and are presented in Section 7.3. One control and two spliced beams were fatigue tested and are covered in Section 7.4.

7.1 Construction and Splice Assembly

Internal gages of two types were included in the specimens during the precasting: foil strain gages and vibrating wire strain gages. The foil strain gages were included to monitor strain in the stirrups during the splice assembly procedure. The vibrating wire strain gages were installed to monitor prestress losses over time, as well as strain changes during the load tests.

A single 3 mm foil strain gage was glued to two prepared rebar stirrups in the laboratory. These are shown in Figure 7-1. The stirrups were provided to the precaster for inclusion during the construction of the precast segments. The gaged stirrups were located at the assumed tie of the strut-and-tie model used to design the segment for the splice assembly.

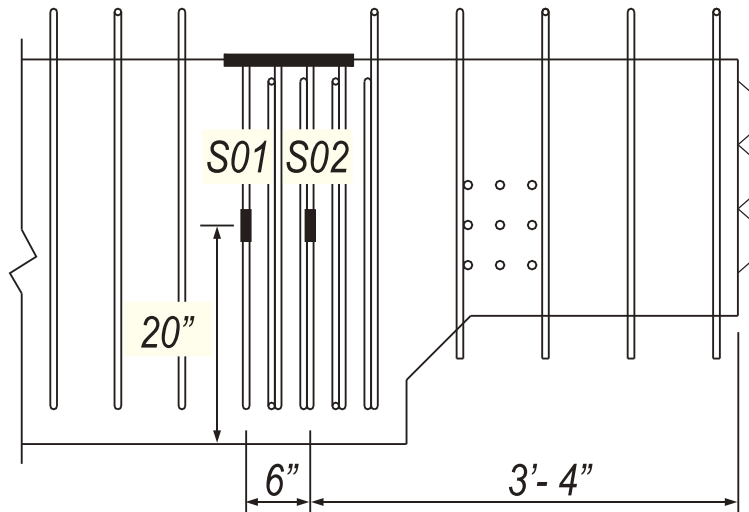


Figure 7-1. Gaged stirrup locations

Prestress losses were monitored using vibrating wire strain gages (VWSG). During precast construction, gages were installed at the midspan of the control specimens (Segments 1-3) and the bonded segments for the spliced specimens (Segments 4b-9b). VWSG readings were taken prior to and after detensioning to measure the compressive strain in the concrete caused by the prestressing on the section at the time of detensioning; from this an estimate of elastic losses resulting from shortening was calculated. VWSG readings were also taken just prior to load testing to estimate the time-dependent losses that occurred between detensioning and load testing.

During the splice assembly in the laboratory, a gage was installed near the midspan of the full spliced beam length prior to the closure pour. In all cases, the VWSG was installed at the approximate height of the strand pattern centroid. The locations of the VWSGs are shown in Figure 7-2. To ensure each VWSG remained at the set height, cable ties were used to attach the VWSG to the prestressing strand as shown in Figure 7-3.

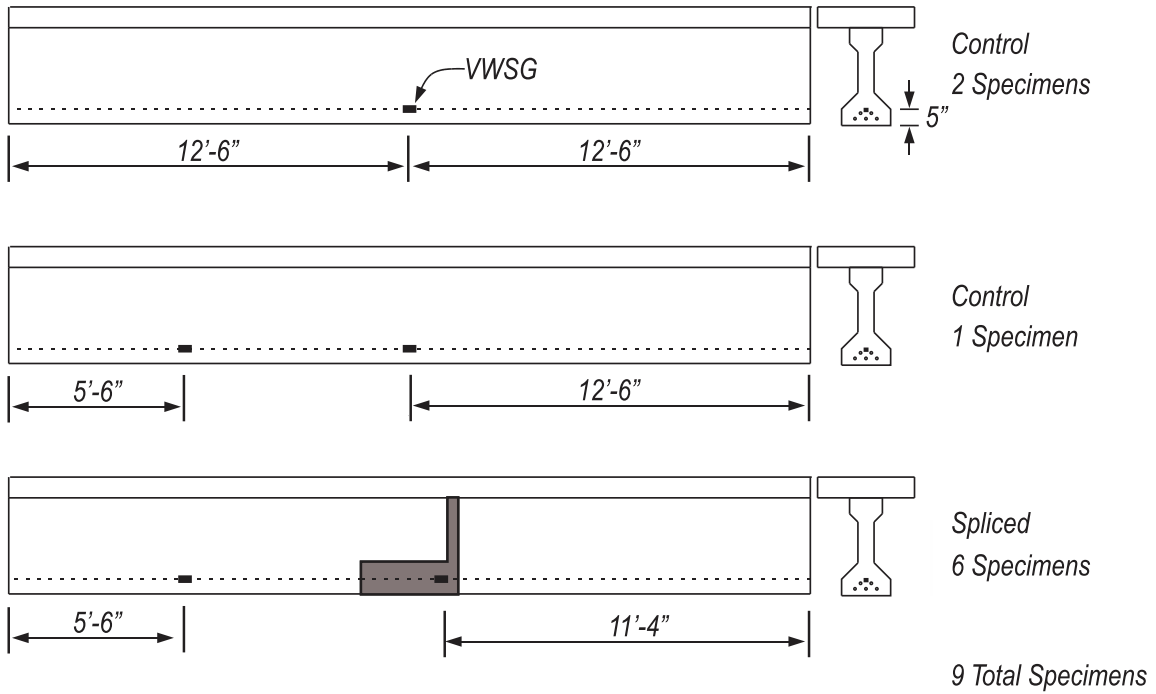


Figure 7-2. Placement of VWSG



Figure 7-3. VWSG installation near centroid of strand pattern

Readings were taken with a single-channel Geokon Model GK403 readout box at key points during the construction process and prior to load testing to assess the prestress losses.

Six spliced beams were assembled in the laboratory. Each specimen was arranged in the assembly set-up as shown in Figure 6-5. Each of the six splice assemblies was instrumented for evaluation of the splice technique and the effect of splicing on the precast segments. Strain, strand slip, load at the fixed tie-down, longitudinal opening at the splice location, and vertical displacement were monitored throughout the stressing of the spliced strand. Four 200 mm displacement transducers were used to monitor vertical displacement. One was placed over each of two exterior bearing to measure the support displacement and one was placed at each of the two tie-down locations. Five strand slip gages were placed on one end of each strand to monitor strand slip. For all but the first splice assembly, strain gages were placed on the flat face of the coupler turnbuckle to indirectly monitor strand load. Load was recorded in conjunction with the strain, strand slip and displacement data. A single vibrating wire gage at midspan of the bonded segment was monitored during loading, with readings taken manually at specified intervals during the strand stressing procedure.

The coupler strain gages (on the face of the turnbuckle with a lead wire coming out) and the VWSG (the blue gage to the right) in the closure pour are shown in Figure 7-4. Strain gages are shown in Figure 7-5.



Figure 7-4. Splice assembly: Instrumentation in closure joint

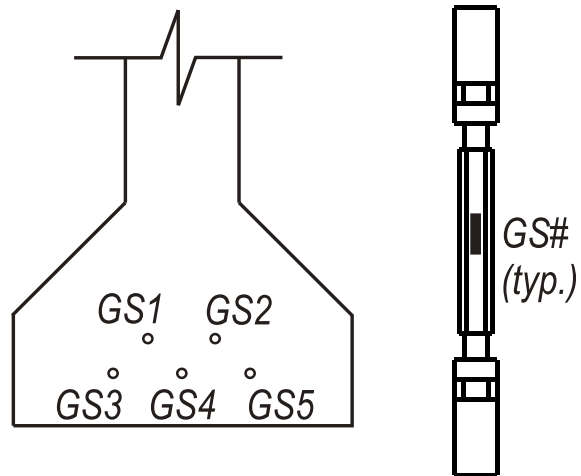


Figure 7-5. Splice assembly: Coupler strain

Placement of the vertical displacement gages is shown in Figure 7-6

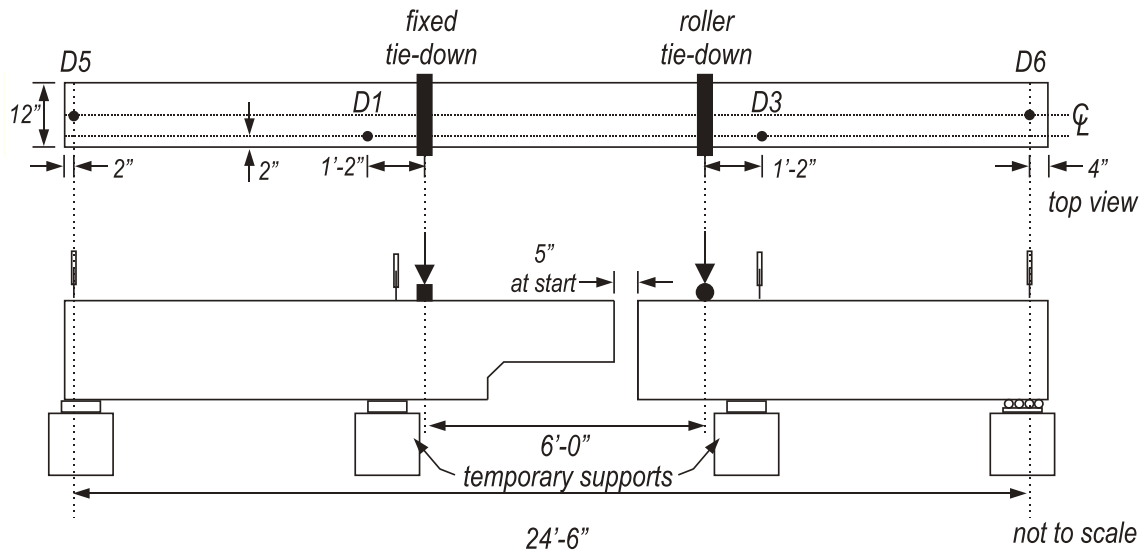


Figure 7-6. Splice assembly: Vertical displacement gages

The opening at the gap between the two segments was monitored with string-pots. Placement of the string-pots is shown in Figure 7-7. Relevant dates and ID information for the spliced specimens is given in Table 7-1. The strand stressing procedure is described in Section 6.4.

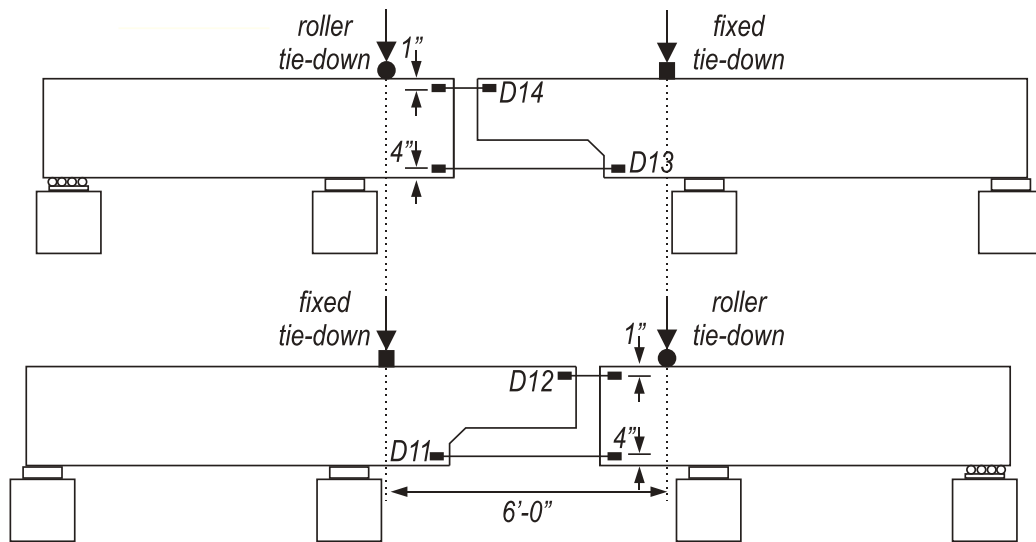


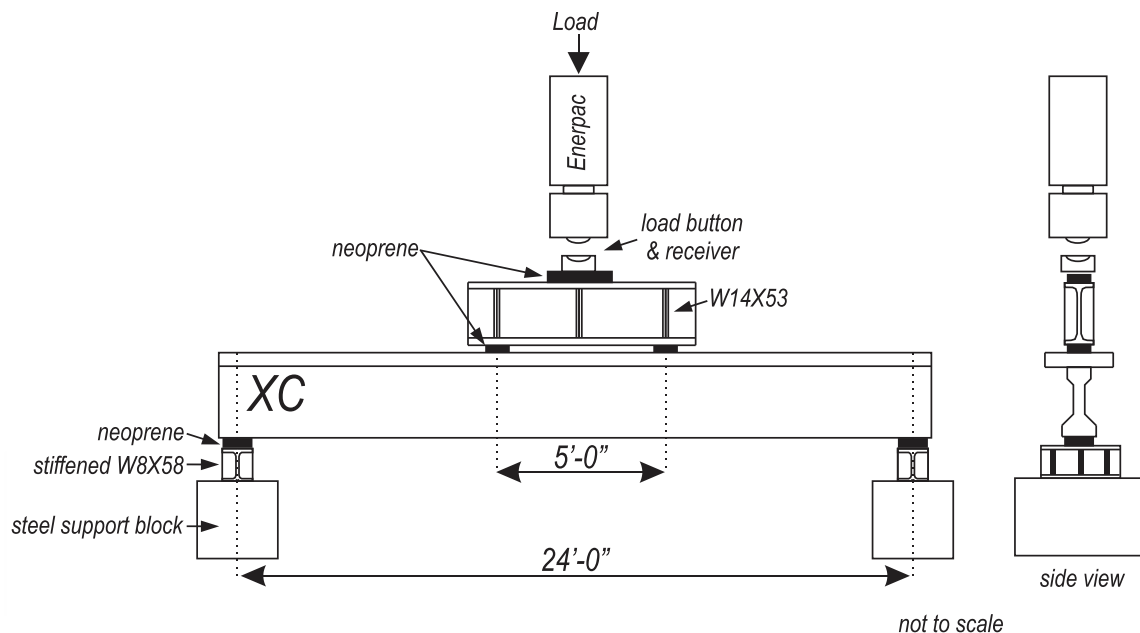
Figure 7-7. Splice assembly: Longitudinal displacement string-pots

Table 7-1. Spliced specimens

| Specimen | Bonded Segment | Unbonded Segment | Strand Stressed | Closure Poured | Closure Pour Stressed | Deck Pour | Load Test |
|----------|----------------|------------------|-----------------|----------------|-----------------------|-----------|-----------|
| X1 | 4b | 9u | 9/13/12 | 9/19/12 | 9/26/12 | 10/2/12 | 10/18/12 |
| SB | 5b | 5u | 10/19/12 | 10/24/12 | 10/30/12 | 11/6/12 | 11/16/12 |
| SU | 9b | 7u | 11/30/12 | 12/4/12 | 12/10/13 | 12/13/12 | 12/20/12 |
| SU2 | 8b | 4u | 1/11/13 | 1/16/13 | 1/28/13 | 1/31/13 | 2/8/13 |
| F1 | 7b | 6u | 2/8/13 | 2/12/13 | 2/19/13 | 2/22/13 | 3/6/13 |
| F2 | 6b | 8u | 2/27/13 | 3/1/13 | 3/8/13 | 3/21/13 | 4/15/13 |

7.2 Flexure

Four-point bending flexure tests were performed on one control beam with continuous prestressing and one spliced specimen with coupled prestressing strand. The control specimen is referred to as XC; the splice specimen is referred to as X1. A spreader beam was used to create a constant moment region encompassing the spliced region. The specimens were arranged in the test setup as shown in Figure 7-8.



(a)

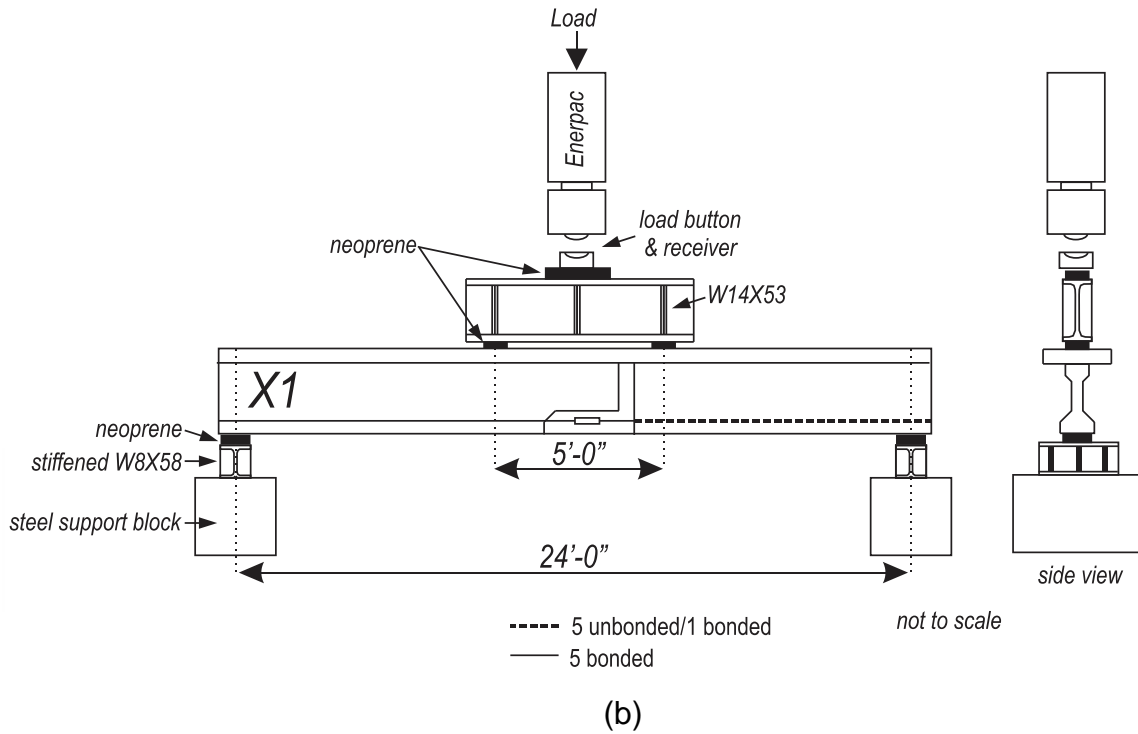


Figure 7-8. Four-point flexural test set-up: (a) XC and (b) X1

Strain, strand slip, load, and displacement were monitored throughout the test. Seven 200 mm displacement transducers were used to monitor vertical displacement during testing. Two were placed at to either side of the load point of the spreader beam, one was placed at midspan and one was placed over each bearing to measure the support displacement. Six 50 mm displacement transducers were used to monitor out-of-plane displacement during testing. Five strand slip gages were placed on one end of each strand to monitor strand slip. Load application was recorded in conjunction with the strain, strand slip and displacement data. A single vibrating wire gage at midspan was monitored during loading, with readings taken manually at specified load intervals.

Placement of the vertical displacement gages is shown in Figure 7-9. Placement of the out-of-plane displacement gages are shown in Figure 7-10.

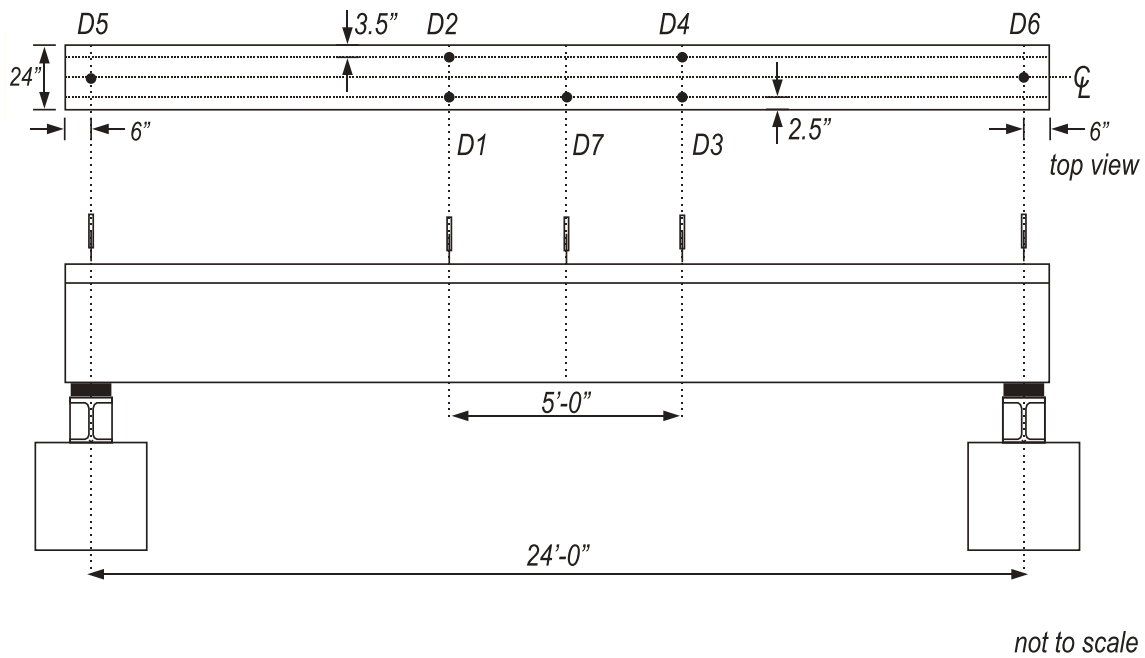


Figure 7-9. Flexure: Vertical displacement gages

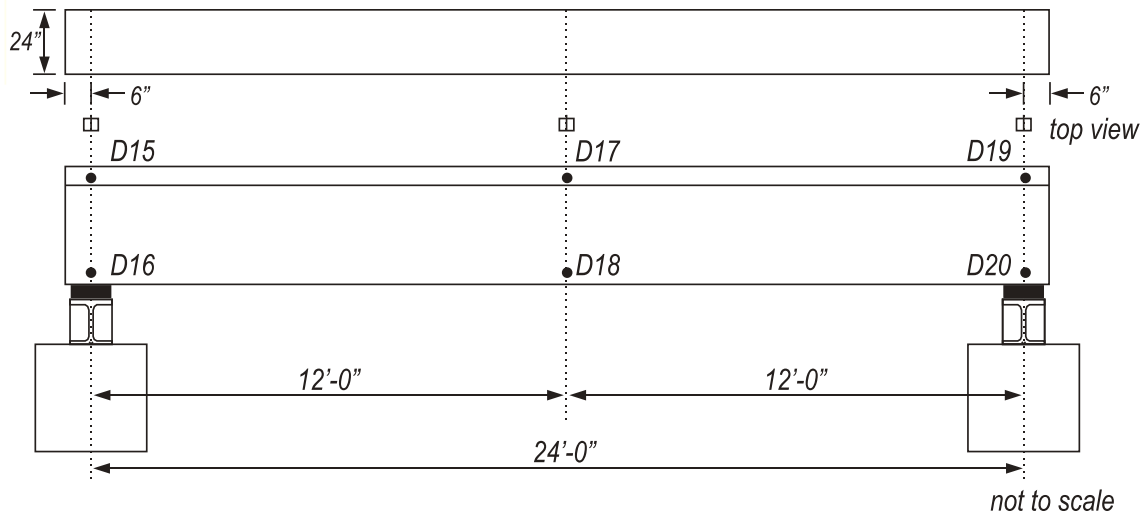


Figure 7-10. Flexure: Out-of-plane displacement gages

Specimen X1 had additional instrumentation to monitor splice behavior. Three load cells monitored the prestressing strand load and were placed on the bottom three

strands (Figure 7-11). Four string-pots spanning the closure pour length were also monitored, measuring longitudinal displacement along the beam axis (due to crack opening).

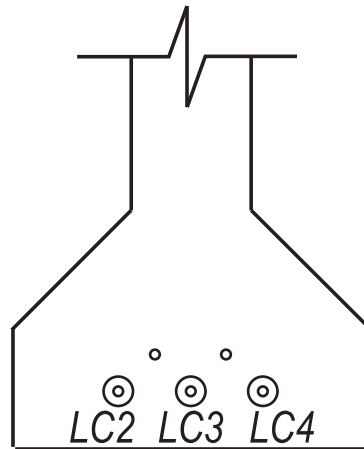


Figure 7-11. Spliced beams: Load cells

In each flexure test, load was applied at 0.2 kip/sec. When cracking was first visually observed, the load was held. The specimen was inspected and cracks were marked. Load application was then resumed at 0.2 kip/sec until termination of the load test. The test was terminated when either compressive failure occurred in the deck concrete, or when excessive deflection of the specimen threatened the instrumentation. In all tests, the flexural capacity (maximum load) was reached prior to end of test.

7.3 Shear

To investigate the effects of higher shear (lower M/S ratio) on the splice region, three-point bending tests were performed on a shortened span length with a cantilever of 8'-10". Two spliced specimens were tested, flipping the orientation of the splice

region and the location of the bonded/unbonded lengths of the specimen. The test set-ups for the spliced specimens are shown in Figure 7-12.

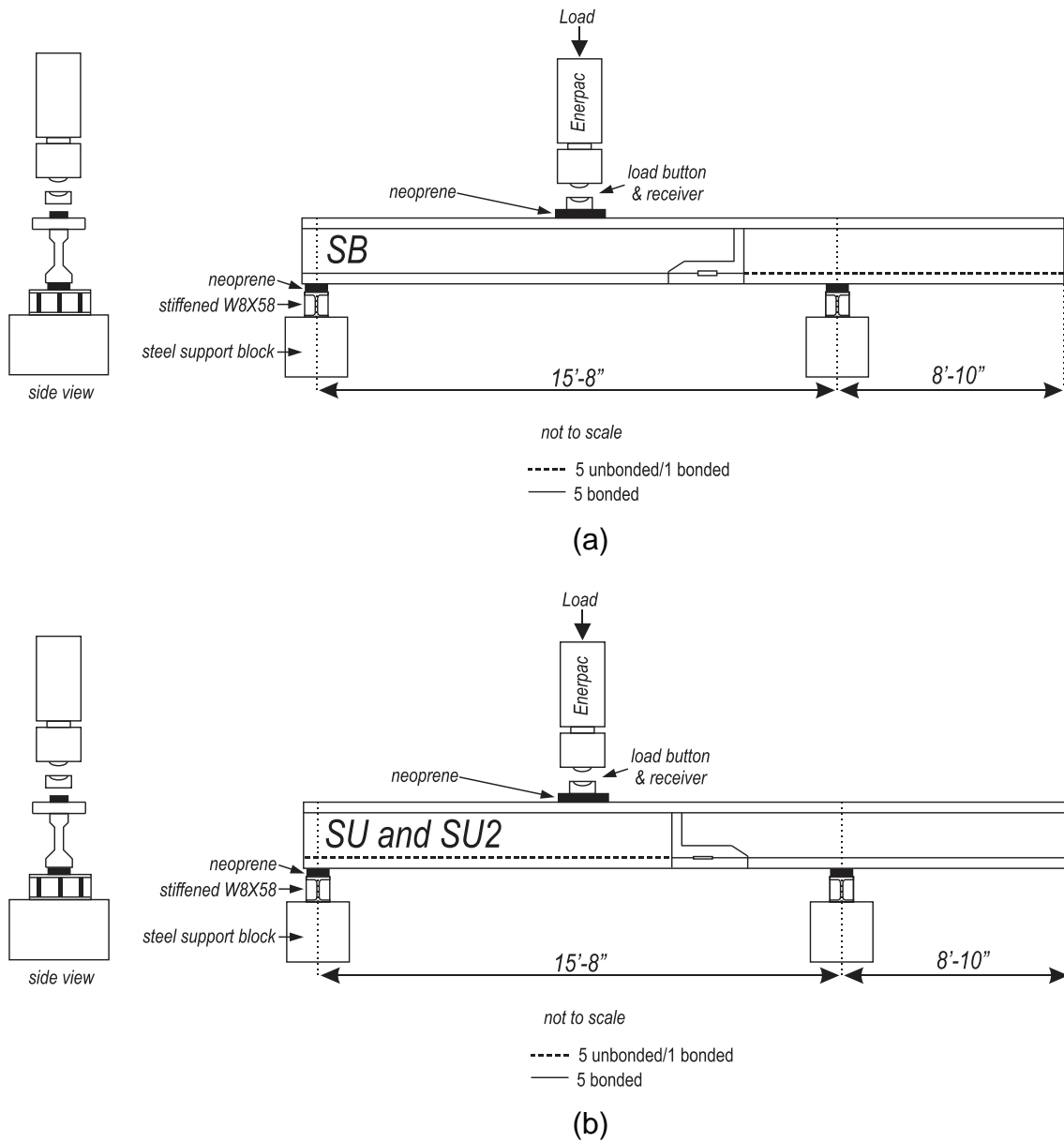


Figure 7-12. Spliced shear test set-ups for (a) SB and (b) SU and SU2

In each of the test set-ups, the left length of the span—or the tested span—is referred to as the “shear span.”

In the SB test set-up, the segment with five bonded strands (the segment shown to the left in the figure) is placed under the load point, in the shear span. In the SU (and SU2) test set-up, the segment with one bonded strand and five unbonded strands is placed under the load point, in the shear span. In all tests, the test specimen rested on two neoprene pads placed on steel supports which were grouted to the laboratory floor.

Considering the results of these tests, the orientation of the control specimen was determined; the control shear test specimen is shown in Figure 7-13. The control specimen is referred to as SC. In the chosen orientation, the six bonded strand were within the shear span, in an effort to match the same number of strands in the shear span as in the SU test set-up, which was determined to be the critical orientation for the shear tests. As in the SB tests, the beam rested on two neoprene pads placed on steel supports which were grouted to the laboratory floor.

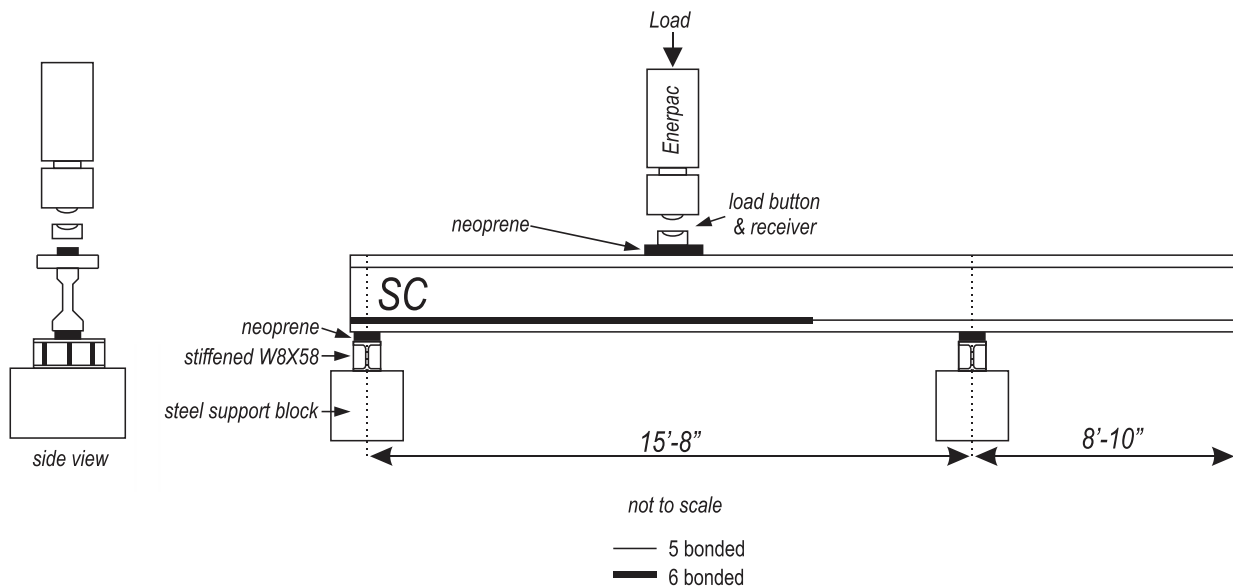


Figure 7-13. Control shear test set-up

Strain, strand slip, load, and displacement were monitored throughout each test. Four 200 mm displacement transducers were used to monitor vertical displacement during testing. Two were placed at to either side of the load point, and one was placed over each bearing to measure the support displacement. Five strand slip gages were placed on one end of each strand to monitor strand slip. Load was recorded in conjunction with the strain, strand slip and displacement data. A single vibrating wire gage (VWSG) at midspan was monitored during loading, with readings taken manually at specified load intervals. In the spliced specimens, load cells on three of the spliced strands were monitored.

Placement of the vertical displacement gages are shown in Figure 7-14.

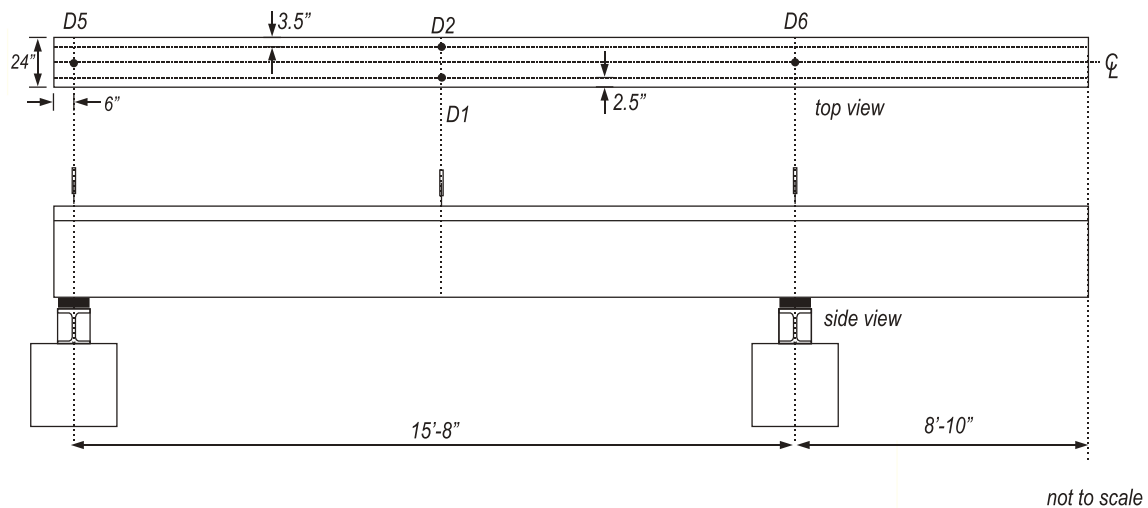


Figure 7-14. Shear: Vertical displacement gages

All of the spliced specimens had additional instrumentation to monitor splice behavior. Three load cells monitored the prestressing strand load and were placed on the bottom three strands (Figure 7-11). In the SU and SU2 specimens, five strain gages

placed on the flat face of the couplers' turnbuckle (and cast into the closure pour) were monitored; these can be seen in Figure 7-5.

In each shear test, load was applied at 0.2 kip/sec. When cracking was first visually observed, the load was held. The specimen was inspected and cracks were marked. Load application was then resumed at 0.2 kip/sec until the peak load was reached. The test was terminated when significant load (greater than 10 kip) drop occurred without recovery or when excessive deflection of the specimen threatened the instrumentation.

7.4 Fatigue

Four-point bending fatigue tests were performed on one control beam with continuous prestressing and on two spliced test specimens with coupled prestressing strand. The control beam is referred to as FC; the spliced specimens are referred to as F1 and F2. A spreader beam was used to create a constant moment region encompassing the spliced region. Each specimen was arranged in the test set-up as shown in Figure 7-15.

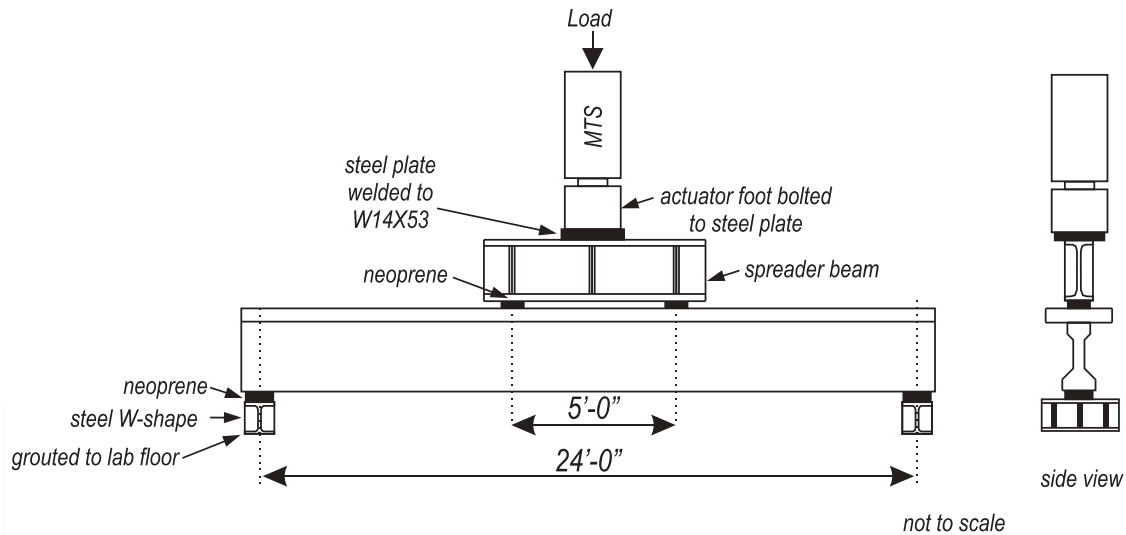


Figure 7-15. Fatigue test set-up

To reduce the effects on the test set-up during the cyclic loading, several precautions were taken to reduce movement within the set-up and supports. To reduce movement of the supports during the test, the steel W-shapes were grouted to the laboratory floor. To prevent the spreader from walking off the beam, it was welded to a plate which was then bolted to the actuator foot. Measured deflections are, therefore, reflective of displacement of the test specimen and the neoprene pads.

Strain, load, and displacement were monitored throughout the test. Four laser gages were used to monitor vertical displacement during testing. Two were placed at either side of the spreader beam at midspan and one was placed over each bearing to measure the support displacement. The lasers were pointed toward a white fabric tape target on the surface of the deck. Applied load was recorded in conjunction with the strain, strand slip and displacement data. A single vibrating wire gage at midspan was monitored during loading, with readings taken manually at specified load intervals.

Table 7-2. Fatigue specimen load procedure

| Load Procedure | Type | Load Rate | Load Range | # of cycles |
|----------------|--------|-------------|---------------------|-------------|
| Precracking | Static | 0.2 kip/sec | 0 kip-cracking | 1 |
| Decompression | Static | 0.2 kip/sec | 0 kip-decompression | 2-4 |
| Fatigue | Cyclic | 2 Hz | 40 kip -cracking | 2 million |
| Ultimate | Static | 0.2 kip/sec | 0 kip-failure | 1 |

CHAPTER 8 PRESTRESS LOSSES

Prestress losses were measured with the use of VWSGs; gage locations are covered in Figure 7-2. The spliced specimens contained two VWSGs—one in the bonded precast segment and one in the middle of the closure pour; for the discussion of prestress losses, only the VWSGs located within the closure pour of each spliced specimen are discussed. The control specimens contained a VWSG in the corresponding location; these gages are used to compute the effective prestress force for each control specimen.

Figure 8-1 shows the prestress in each specimen for both the precast control specimens and the spliced specimens versus the age of the concrete. For the VWSG in the precast concrete, a jacking prestress level of $0.6f_{pu}$ was assumed; this jacking prestress was verified with the precast yard's stressing records. To determine the jacking prestress of the splice region of the spliced specimens, the average value of the strand force measured by the three strand load cells was assumed to act at each strand. The x-axis represents the age of the concrete in which the VWSG is encased; this is either the precast concrete or the closure pour for the control and spliced specimens, respectively.

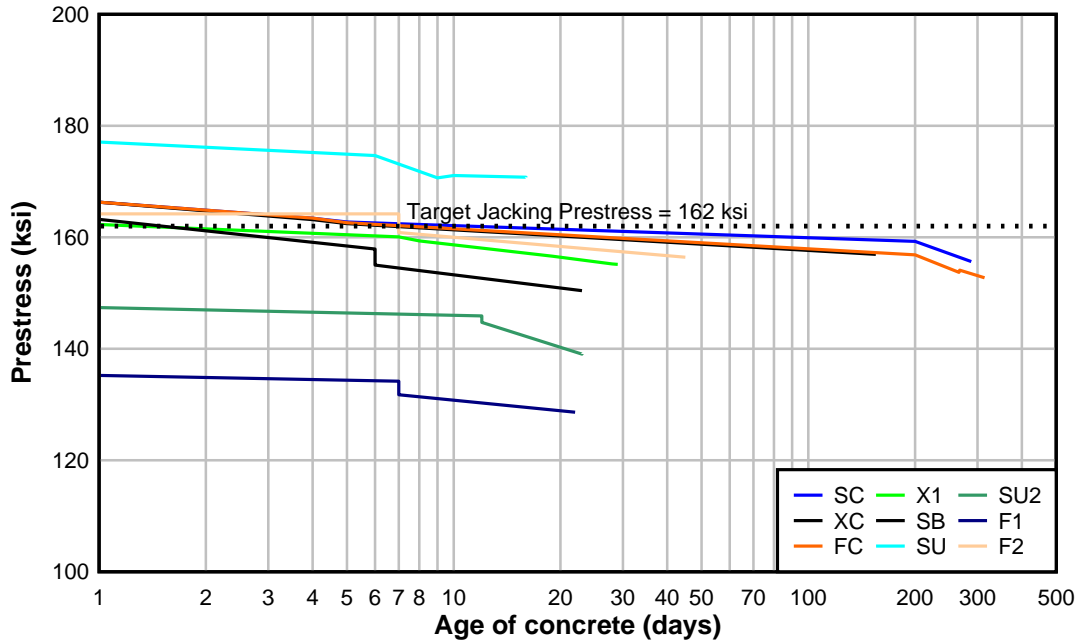


Figure 8-1. Prestress force

The control specimens exhibited similar prestress losses. All three control specimens were assumed to have the same prestress at jacking, 166.3 ksi. At prestress transfer (day 4), all three control specimens experienced an elastic loss of approximately 3 ksi. Between transfer and the load tests, the three specimens experienced similar long-term losses, as demonstrated by the similarity of the line slope.

The spliced specimens exhibited two interesting behaviors: prestress loss prior to release of the tie-downs and introduction of the prestress force in the closure pour, and decreasing elastic losses with concrete age. For each spliced specimen, the prestress force was introduced into the closure pour approximately 6-7 days after the pour was completed (except for specimen SU2, which was prestressed at day 12). During this time period (prior to prestress of the closure pour), the jacking load was locked off and held in the actuators, resisted by the anchorage at the free end of the unbonded segment. This held force resulted in some creep of the precast segments. Prior to

prestress of the closure pour, some prestress was lost as the concrete of the precast segments crept under the load. Additionally, the effect of the concrete age at the time of the closure pour prestressing is evident: the younger concrete had higher elastic losses. Following this trend, specimen SU2—with the longest cure prior to release - had the least elastic losses of the spliced specimens.

The VWSG mounted at the centroid of the spliced prestressing strands was used to determine the prestress losses at key points during the spliced beams' construction and life until load testing. For the precast control specimens, the jacking force was determined from the calibrated monostrand jack used to stress each strand, as recorded in the stressing records from the precaster. For the spliced specimens, the jacking force is considered to be the prestress force present at tightening of the lock-nut. This prestress force was calculated as the average measurement of the load cells instrumenting the three bottom strands acting in all five strands. The prestress forces at jacking are presented in Table 8-1.

Due to concern regarding the reliability of the load cell readings, later splice assemblies included strain gages on the flat face of the turnbuckle of each coupler—these readings were used to indirectly determine the strand force. Calibration of the strain gage readings to equivalent force was done in separate tensile tests. Based on the calibration, the strand force was also indirectly determined for each strand. The average of these readings is also provided in Table 8-1. In general, these measurements were taken as a redundant check of the strand force, to prevent overstressing the strand during the splice assembly process. The strand force

according to the calibrated strain gages is reported here for comparison; all calculations of prestress losses and strand force utilize the measurements from the strand load cells.

Table 8-1. Jacking prestress

| Specimen | Average Total Force by Load Cell (kip) | Average Total Force by Calibrated Strain Gage (kip) | Average Strand Stress (ksi) |
|----------|--|---|-----------------------------|
| SC | 127.2 | n/a | 166.3 |
| XC | 127.2 | n/a | 166.3 |
| FC | 127.2 | n/a | 166.3 |
| X1 | 124.2 | n/a | 162.3 |
| SB | 123.1 | 117.4 | 161.0 |
| SU | 135.5 | 116.4 | 177.1 |
| SU2 | 112.8 | 120.2 | 147.4 |
| F1 | 105.7 | 116.6 | 138.2 |
| F2 | 125.6 | 125.8 | 164.1 |

The initial prestress force is considered the jacking prestress force minus the elastic losses. For all specimens, it was calculated based on prestress losses measured by the VWSGs at the time of prestress transfer, based on the differential strain readings from the VWSG and the Young's modulus of the strand. For the precast control specimens, prestress transfer occurred when the strands were cut free from the bed. For the spliced specimens, the initial force is considered to be the prestress force present just after release of the tie-downs, when the prestress force was imparted to the splice region, causing an immediate elastic loss in the closure pour. Elastic losses between the jacking and the prestress transfer are then revealed.

Table 8-2 shows the initial prestress force for each completed specimen.

Table 8-2. Measured initial prestress

| Specimen | Average Total Force by VWSG (kip) | Average Strand Stress (ksi) |
|----------|-----------------------------------|-----------------------------|
| SC | 125.0 | 163.4 |
| XC | 124.8 | 163.2 |
| FC | 125.0 | 163.4 |
| X1 | 122.5 | 160.1 |
| SB | 118.5 | 155.0 |
| SU | 133.6 | 174.7 |
| SU2 | 110.7 | 144.8 |
| F1 | 100.8 | 131.8 |
| F2 | 123.1 | 160.9 |

Table 8-3 presents the effective prestress for all specimens, calculated as the force present at the time of the load test (for the fatigue specimens, the time of the first load test was used) based on the differential strain readings from the VWSG and the Young's modulus of the strand. Long-term losses, such as due to creep and shrinkage, between the jacking and the time of the load test are then revealed.

Table 8-3. Measured effective prestress

| Specimen | Average Total Force by VWSG (kip) | Average Strand Stress (ksi) |
|----------|-----------------------------------|-----------------------------|
| SC | 119.0 | 155.6 |
| XC | 120.1 | 156.9 |
| FC | 116.8 | 152.7 |
| X1 | 118.7 | 155.2 |
| SB | 115.0 | 150.4 |
| SU | 130.7 | 170.8 |
| SU2 | 106.4 | 139.1 |
| F1 | 98.4 | 128.6 |
| F2 | 119.7 | 156.4 |

Table 8-4 presents the measured prestress losses; both initial and time-dependent losses were calculated as a percentage of the jacking prestress (measured as described above).

Table 8-4. Measured prestress losses

| Specimen | Initial losses (%) | Concrete age at release (days) | Long-term losses (%) | Total prestress loss (%) | Concrete age at load test (days) |
|----------|--------------------|--------------------------------|----------------------|--------------------------|----------------------------------|
| SC | 1.7 | 4 | 4.7 | 6.4 | 288 |
| XC | 1.9 | 4 | 3.7 | 5.6 | 155 |
| FC | 1.7 | 4 | 6.4 | 8.2 | 314 |
| X1 | 1.4 | 7 | 3.0 | 4.4 | 29 |
| SB | 3.7 | 6 | 2.8 | 6.6 | 23 |
| SU | 1.4 | 6 | 2.2 | 3.6 | 16 |
| SU2 | 1.8 | 12 | 3.8 | 5.7 | 23 |
| F1 | 4.7 | 7 | 2.3 | 6.9 | 22 |
| F2 | 2.0 | 7 | 2.7 | 4.7 | 45 |

Prestress losses affect structure serviceability; therefore, accurate prediction of the anticipated losses for spliced specimens is important. The measured prestress losses compare well with typical 25-50 ksi (12-25% of a specimen stressed to $0.75f_{pu}$) of prestress losses (due to all immediate and long-term effects) observed in typical prestressed concrete sections (PCI 2004). The measured losses for all specimens were at the lower end of this range.

Predicted prestress losses were also computed for comparison using the PCI method (Zia et al. 1979) –though the prediction methods are intended only for pretensioned girders consisting of normal weight concrete and 270-ksi prestressing strand. Though the spliced specimens do not fall into this category, the estimates were

calculated and are provided for general reference. The specified concrete strength at transfer and the specified 28-day strength was used to estimate the modulus of elasticity at transfer as 4630 ksi and at time of loading as 5500 ksi (per ACI, $E = 33000w_c^{1.5}\sqrt{f'_c}$). Relative humidity was assumed to be 75%. Table 8-5 presents these predictions.

Table 8-5. PCI prestress losses

| Specimen | Elastic losses (ksi) | Long-term losses (ksi) | Total prestress loss (ksi) | Total prestress loss (%) |
|----------|----------------------|------------------------|----------------------------|--------------------------|
| SC | 3.8 | 10.2 | 14.0 | 8.4 |
| XC | 3.8 | 10.2 | 14.0 | 8.4 |
| FC | 3.8 | 10.2 | 14.0 | 8.4 |
| X1 | 3.7 | 9.7 | 13.5 | 8.3 |
| SB | 3.7 | 9.6 | 13.3 | 8.3 |
| SU | 4.1 | 11.4 | 15.5 | 8.8 |
| SU2 | 3.3 | 8.3 | 11.7 | 7.9 |
| F1 | 3.1 | 7.5 | 10.6 | 7.7 |
| F2 | 3.8 | 10 | 13.7 | 8.3 |

Figure 8-2 compares the measured and PCI predicted losses. In all cases, the PCI predicted prestress loss is greater than the measured loss. Overestimation of prestress losses by PCI has been observed by other researchers (Onyemelukwe et al. 2003).

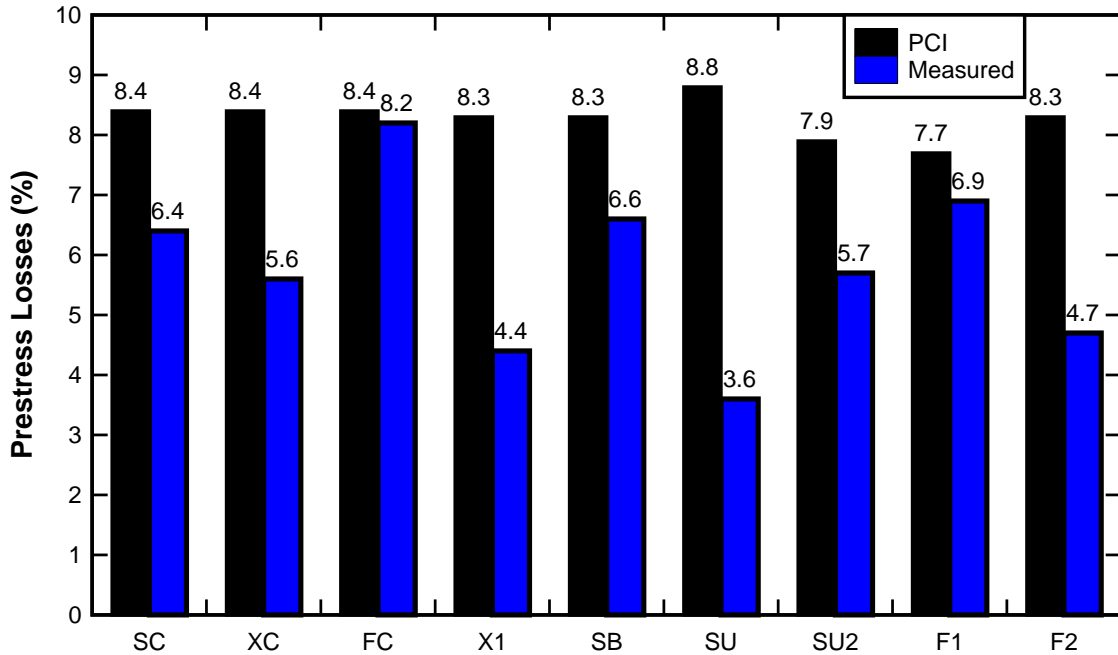


Figure 8-2. Measured prestress losses vs. PCI

For comparison, a crack opening test was performed on some specimens to determine the effective prestress level; the losses calculated using the decompression method were also determined. The crack opening tests are covered in the next section.

Decompression - or crack opening - tests were also performed on some test specimens as an alternate measure of the effective prestress force. For each of the decompression tests, the specimen was placed in the four-point bending test set-up shown in Figure 7-8.

While the specimen was loaded, the load-deflection plot and the beam were monitored for cracking. At first crack, the load was held and the crack location was identified and marked. The load was then removed from the beam and two strain gages were placed on opposite sides of, and perpendicular to, the crack, longitudinal to the beam axis (Figure 8-3). Load was then reapplied to the specimen. When the crack re-

opened, the slope of the load-strain plot changed, indicating that the pre-compression caused by the prestress force had been overcome. This method has been described by Pessiki et al. (1996).

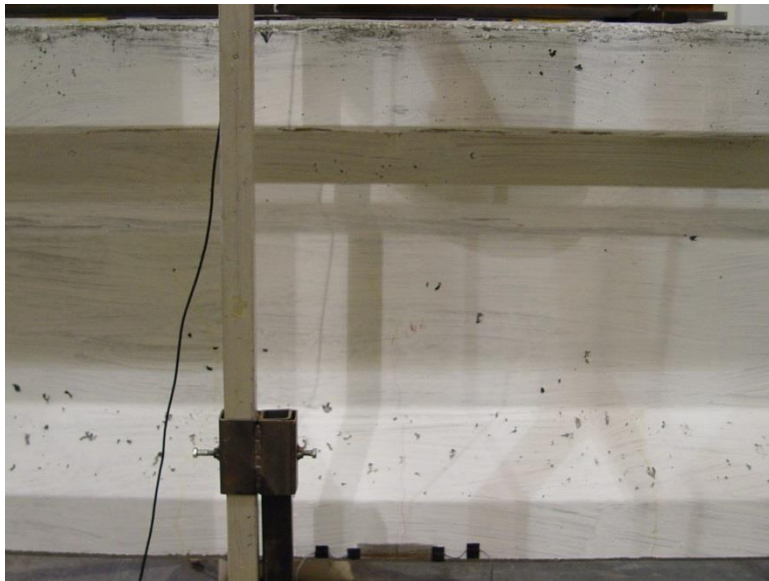
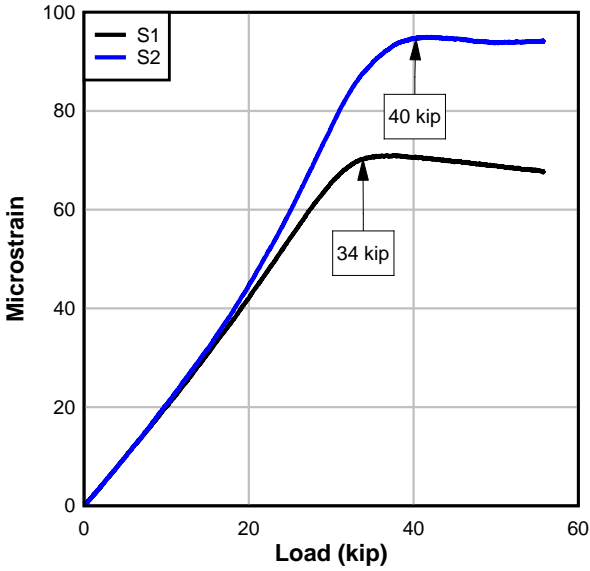
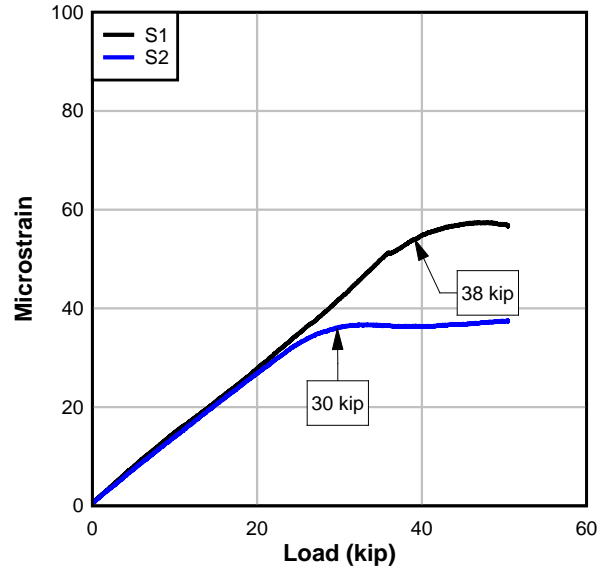


Figure 8-3. Decompression strain gages

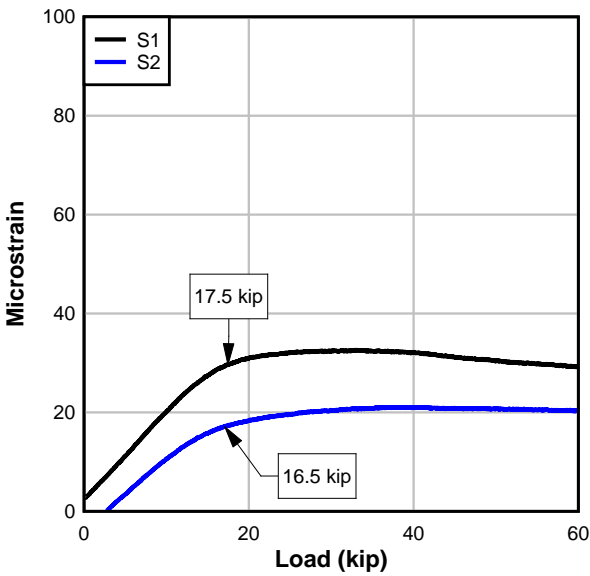
When the initial cracking load was removed, the prestress forced the crack closed and returned the beam section to full uncracked section properties. The decompression load is defined as the average of the two loads at which the strain load curve reaches a plateau. Figure 8-4 shows a plot of the strain data from the gages applied adjacent to the first visible crack on the control fatigue specimen and on the first spliced fatigue specimen.



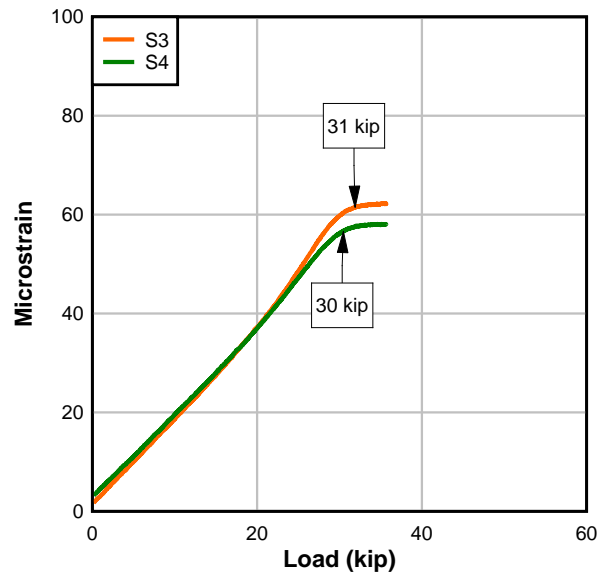
(a)



(b)



(c)



(d)

Figure 8-4. Decompression: (a) FC; (b) F1; (c) F2-joint and (d) F2-crack

Assuming the decompression load corresponds to zero stress at the bottom of the beam, the effective prestress can be calculated from the applied load required to reach decompression. To calculate the effective prestress, the compression caused by the prestress force and its eccentricity are equated to the tensile stress induced to reach

the decompression load using uncracked gross section properties. The effective prestress, as determined with this approach, is given in Table 8-6.

Table 8-6. Effective prestress force by decompression

| Specimen | Average Decompression Load (kip) | Calculated Total PS Force (kip) | Calculated Strand Stress (ksi) | f_{se} per Decompression/ f_{se} per VWSG |
|----------|----------------------------------|---------------------------------|--------------------------------|--|
| FC | 37 | 97.9 | 128 | 0.84 |
| F1 | 34 | 91.8 | 120 | 0.93 |
| F2-joint | 16 | 57.4 | 75 | 0.47 |
| F2-crack | 30 | 82.6 | 108 | 0.67 |

Decompression tests were performed on one control beam and two spliced beams. Because of the location of the constant moment region, only the test of the control beam can be used to evaluate the effective prestress induced at the precast yard. The effective prestress calculated from the decompression test of this control specimen corresponds to later test results: the effective prestress was lower than the anticipated prestress (based on the precast yard's stressing records minus the measured prestress losses). Based on this method, XC's strands had 19.6 kip/strand vs. the 23.4 kip/strand as determined by the stressing records and VWSG measurements—approximately 16% less prestress force.

Two measurements of decompression were taken of specimen F2. The first 'crack' which occurred and was instrumented was an opening of the vertical interface between the closure pour and the bonded segment, this is referred to as F2-joint. This location exhibited much less precompression, indicated by the low load at which the joint reopened. The first true crack—located at the bottom of the bottom flange in the middle of the closure pour—was also instrumented and is referred to as F2-crack. This

region exhibited higher precompression—indicating that the closure pour was successfully precompressed by the splicing procedure.

The decompression tests performed on the two spliced beams, based on the location of the crack, were indicative of the effective prestress force in the splice region of the beam. The calculated strand force based on the results of these tests closely matched the strand load as measured by the load cells for specimen F1. For example, for F1, the ratio of the calculated PS strand force per the decompression test/measured strand force per the load cells was 0.93. On the other hand, specimen F2's measured strand load via the load cells did not correspond well to the calculated strand force, based on the decompression test. The decompression method has been shown to be not wholly accurate (O'Neill and Hamilton 2009), but the results corresponded to the observed low cracking loads in the control specimens, suggesting that the initial prestress force in the precast segments was indeed lower than specified.

CHAPTER 9 SPLICE ASSEMBLY RESULTS AND DISCUSSION

Figure 9-1 shows the average strand load versus time for the splice assembly procedure of specimen X1. Also labeled are the jack pressures at each load hold. The shown plot is typical of the splice assemblies and will be used for discussion; all other splice assembly load-history plots are included in the FDOT report.

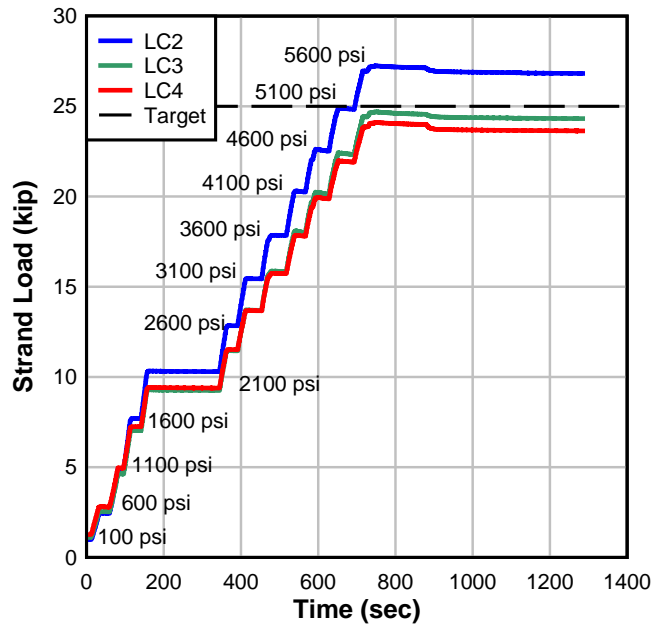


Figure 9-1. Load history of X1

During the splice assembly procedure, a pair of hydraulic jacks was pressurized in a series of steps, with holds every 500 psi of additional pressure. This was done due to repeatedly check that the manual nature of the stressing procedure (using hand jacks) was stressing the strands synchronously. At each hold, the corresponding jack pressure is labeled in the plot.

As the jacks were pressurized, the generated compression force was resisted by tension in the strands, which elongated as the stress increased, opening the gap between the precast segments. Figure 9-2 shows the general concept.

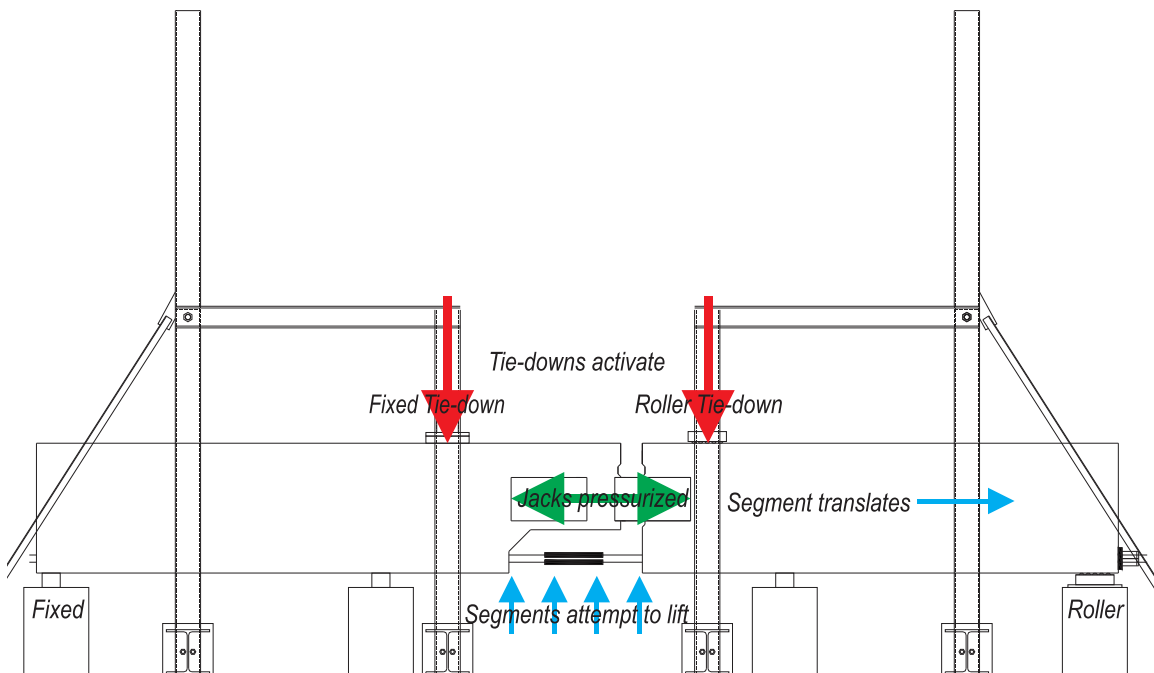


Figure 9-2. Stressing procedure

Metallic creaking noises were heard during the pressurization of the jacks, as the connections in the tie-down frame system resisted the applied force. The amount of noise heard was a function of how tightly each set-up was cinched down prior to the stressing procedure.

Figure 9-3 shows the average strand load (calculated as the average of the three hollow load cells on the bottom row of prestressing strands) versus the gap opening during the splice assembly of SB and SU. Gap opening was measured at four locations: at two locations on the top flange and two locations on the bottom flange at the approximate location of the strand centroid. The predicted elongation of the strand

(per PL/AE) was 1 in., assuming a target strand load of 25 kip, an unbonded length of (gage length) of 174 in. and a 7-wire 1/2 dia. 270-ksi lo-lax strand. Using the calibration charts provided by Enerpac for the CLL504 jack, the pressure required in each jack to achieve 25 kip/strand was 5690 psi/jack. The target elongation value (1 in.)—corresponding to $0.6f_{pu}$ prestress force in the strand - is shown on the plot for reference.

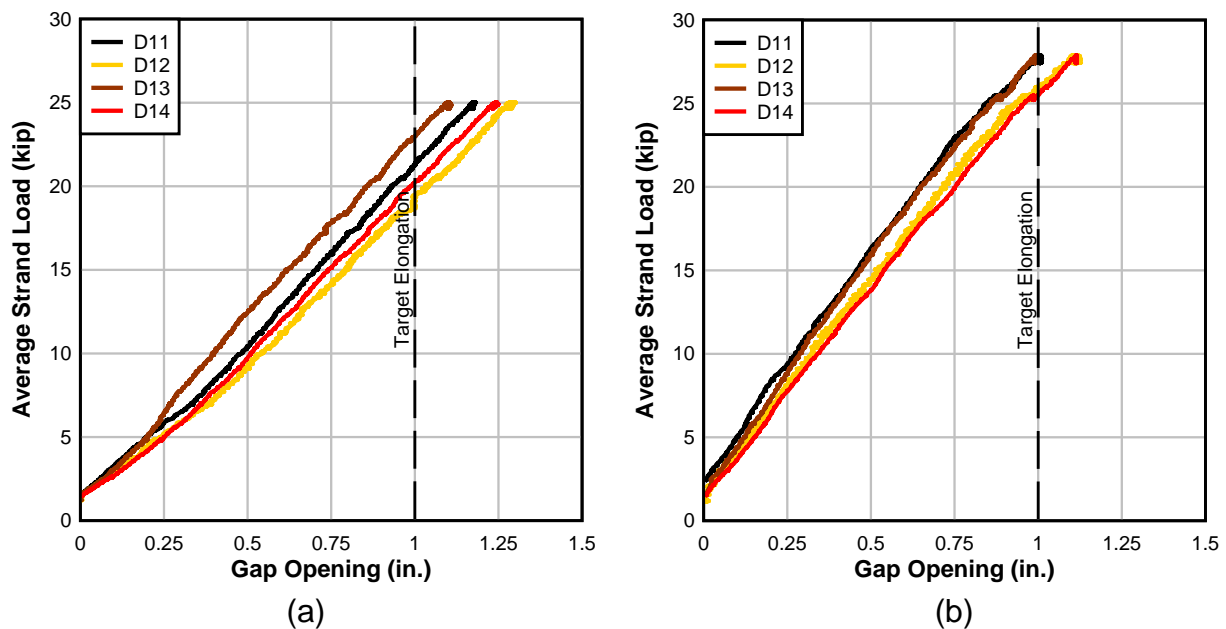


Figure 9-3. Strand load for (a) SB and (b) SU

In the shown plot, as the jack pressure increased, the prestressing strand load increased and the gap between the precast segments opened in a linear fashion—indicating that the strand was stressing linear-elastically. This relationship was shown to exist in every splice assembly.

In general, due to the moment generated by the eccentricity between the jack force and the coupled strands, the top of the gap “opened” more than the bottom. The difference between the top opening and the bottom opening at the final stressed

position was approximately 1/4-1/8 in. and was affected by the tightness of the system, i.e., how well the channels were tied down to the precast segments prior to the stressing of the strand. The moment generated caused the top strands to typically develop more prestress force than the bottom row strands; this relationship is also seen in the strand load as measured by strain gages on the couplers. Figure 9-4 shows the calculated strand force, based on a calibrated strain gage versus time.

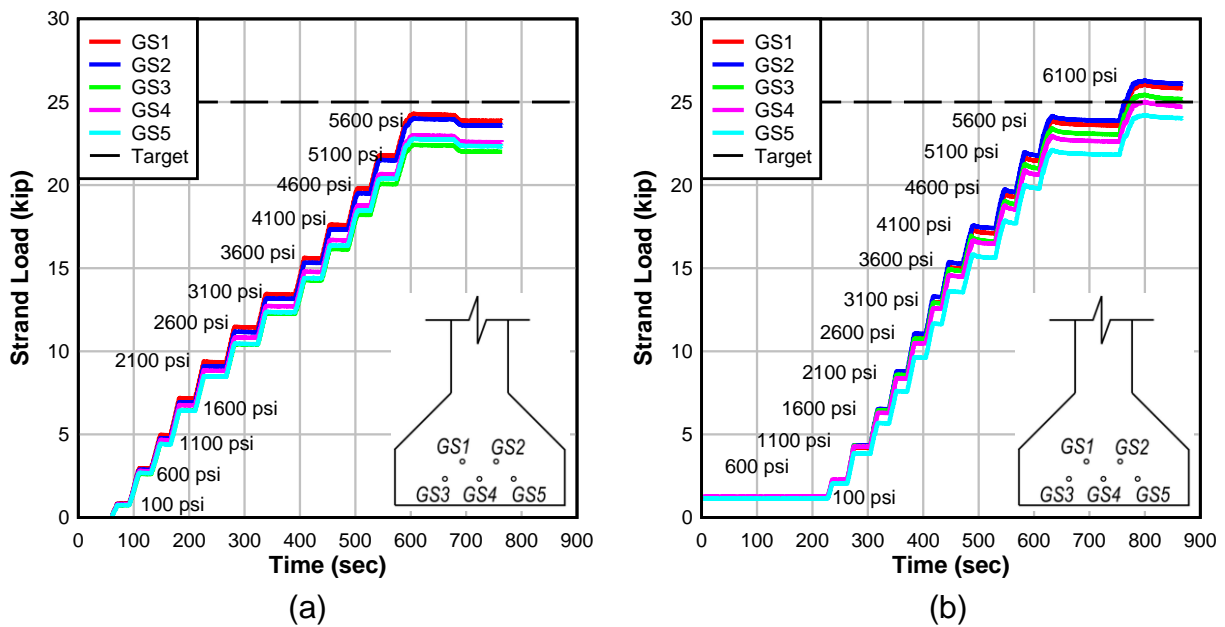


Figure 9-4. Strand load based on calibrated coupler strain for (a)SU2 and (b)F2

The magnitude of these vertical movements was affected by the conditions at each restraint. In each case, the roller tie-down—which consisted of a steel Hilman roller displaced upward more than the fixed tie down—which consisted of a neoprene pad and a load cell. An example is shown in Figure 9-5. The slackness of the rollers in the roller tie-down allowed more vertical movement than the neoprene of the fixed tie-down.

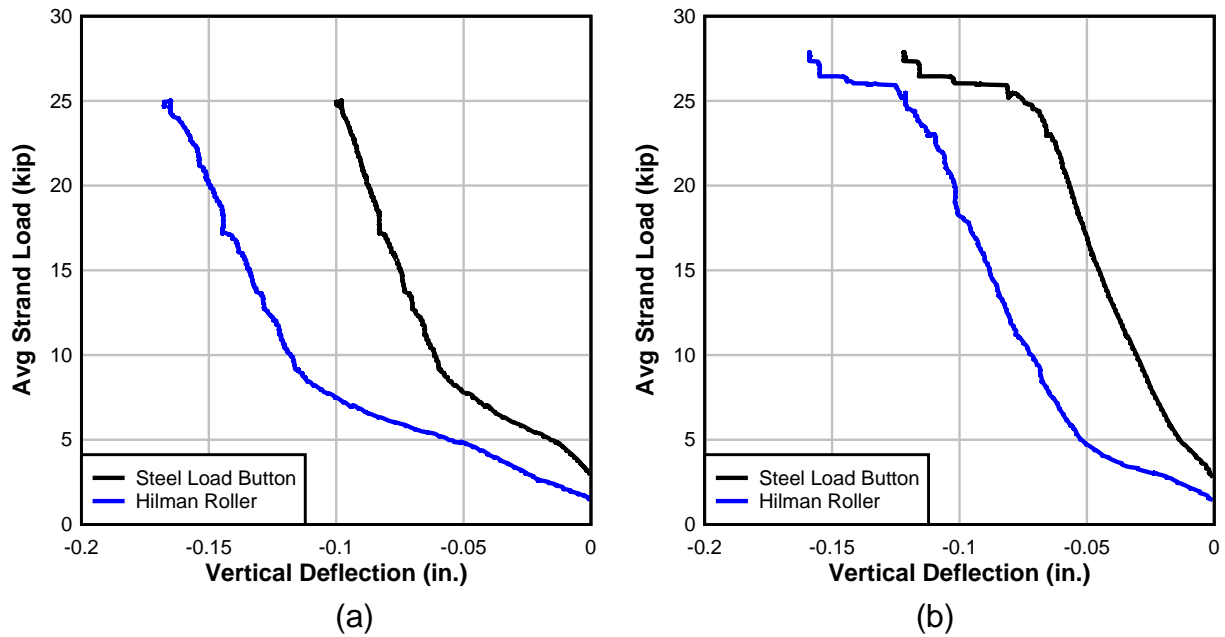


Figure 9-5. Tie-down deflections: (a) SB and (b) SU

The effect of the moment generated by the applied jacking force and the induced strand tension can also be seen in the vertical displacement at the tie-down and support locations. While the LVDT gages placed at the two tie-downs indicate an upward movement of the precast segments, the LVDT gages at each of the supports indicate downward movement, indicating that the segments were slightly rotating as the strands were stressed. An example of the support deflections is shown in Figure 9-6.

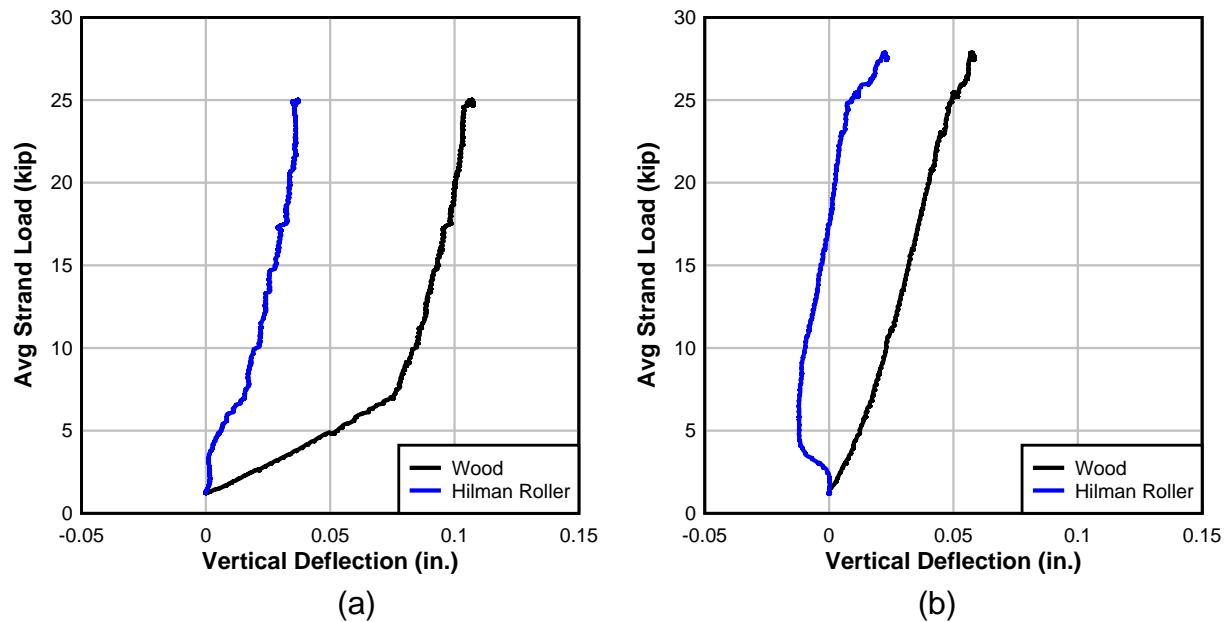


Figure 9-6. Support deflections: (a) SB and (b) SU

The bottom string pot readings were used to determine the cut-off point for the splice stressing procedure. The strand was stressed until gages D11 and D13 measured approximately 1 in.—corresponding to 1 in. of strand elongation or approximately 25 kip/strand. The string-pots were chosen as the critical criteria over the load cells as a safety consideration; because there was some concern of inaccuracies in the load cells, the strand elongation was considered the safer approach.

At approximately 1 in. of gap opening at the bottom flange, the stressing procedure was halted and a locking-ring on each jack was used to mechanically hold the achieved prestress force. Table 9-1 shows the strand loads for each of the splice assemblies as measured by the three load cells. The assumed prestress force is based on the average of the three load cells.

Table 9-1. Spliced specimens: strand loads per load cell

| Spliced Specimen | LC2 (kip) | | LC3 (kip) | | LC4 (kip) | | Average Strand Load (kip) | |
|------------------|-----------|-------|-----------|-------|-----------|-------|---------------------------|-------|
| | Preload | Final | Preload | Final | Preload | Final | Preload | Final |
| X1 | 0.98 | 26.73 | 1.10 | 24.23 | 1.27 | 23.55 | 1.12 | 24.84 |
| SB | 1.16 | 22.35 | 0.94 | 24.40 | 1.59 | 27.13 | 1.23 | 24.63 |
| SU | 0.82 | 23.27 | 0.91 | 23.07 | 1.83 | 34.97 | 1.19 | 27.10 |
| SU2 | 1.44 | 22.74 | 1.00 | 20.60 | 0.89 | 24.33 | 1.11 | 22.56 |
| F1 | 1.37 | 23.06 | 1.16 | 16.46 | 1.32 | 23.92 | 1.28 | 21.15 |
| F2 | 0.36 | 22.95 | 1.23 | 22.82 | 1.92 | 29.57 | 1.17 | 25.11 |

The reinforcement near the bracket attachment in the splice region was based on a strut-and-tie model. Instrumentation was installed in key areas to verify the design assumptions and consisted of strain gages placed in the assumed tie and compressive strut locations. These measurements were taken more to evaluate the behavior during the stressing procedure in a general sense on a global level than to assess the measurement magnitudes or local strains.

Figure 9-7 shows the simplification of the strut-and-tie model used to determine the reinforcement in the end of the precast segment required to resist the tensile stresses induced during the application of force to the bracket.

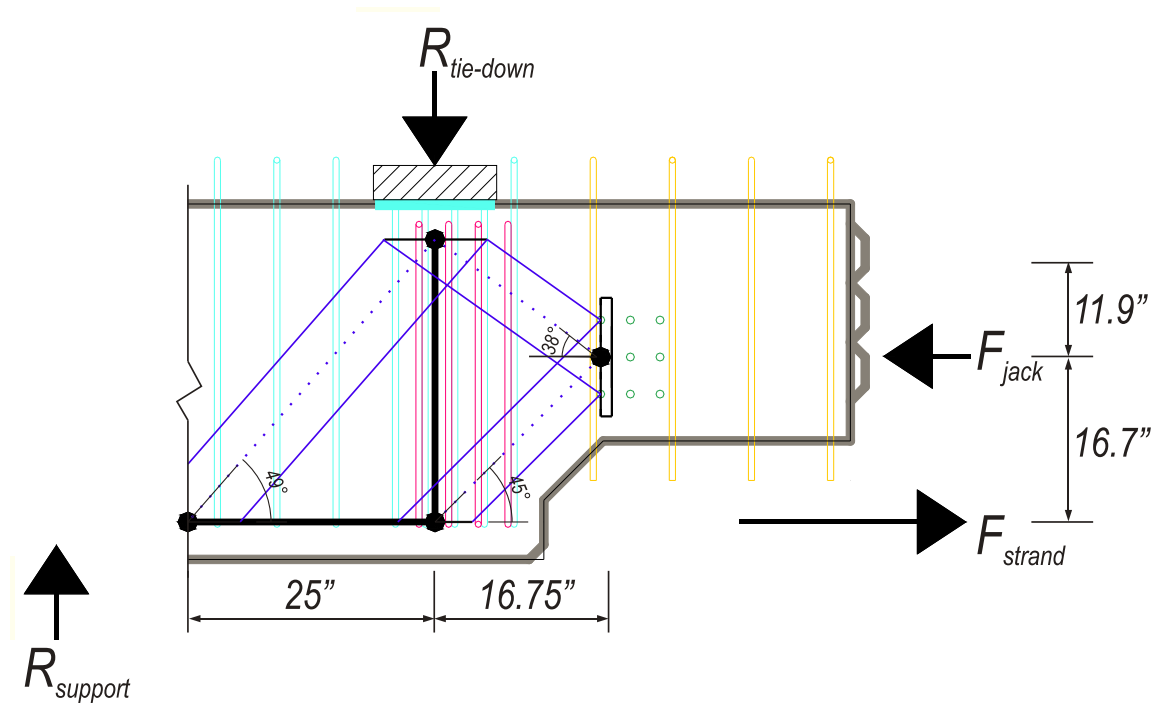


Figure 9-7. STM: assumed dimensions

The strut-and-tie model assumed application of an external compressive load due to the jack at the bolt group centerline, where the bracket transfers load to the precast segment (labeled F_{jack}). This compressive force is resisted by a tensile force in the prestressing cables; this force was assumed to act at the centroid of the strand pattern (labeled F_{strand}). Due to the eccentricity between the two loads, the segment attempts to lift; the movement is resisted by a reaction at the tie-down ($R_{tie-down}$) and at the support ($R_{support}$).

The location of these external forces and reactions determined the general geometry of the assumed strut-and-tie model. A compressive strut was assumed to form from F_{jack} up to the tie-down, or $R_{tie-down}$. Another compressive strut was assumed to extend to a tie at the centroid of the prestressing strand. Finally, another tie was

assumed to form directly under the tie-down force. At this assumed tie location, additional stirrups were detailed.

Two stirrups were instrumented with strain gages (S01 and S02) and placed within the precast segments during construction as described in Section 0. An external strain gage (S25) was also placed on the concrete surface of the precast segments prior to the splice assembly procedure at the same location along the beam length. This gage was used to verify the readings of the stirrup gages and to check the assumption of perfect bond between the rebar and the precast concrete. Based on the perfect bond assumption, the strain measured in the concrete should be approximately equivalent to the strain in the ties. Figure 9-8 shows the measured strain for the three strain gages versus the average strand load for the stressing of specimens X1 and SU. The gage locations are shown in Figure 7-4.

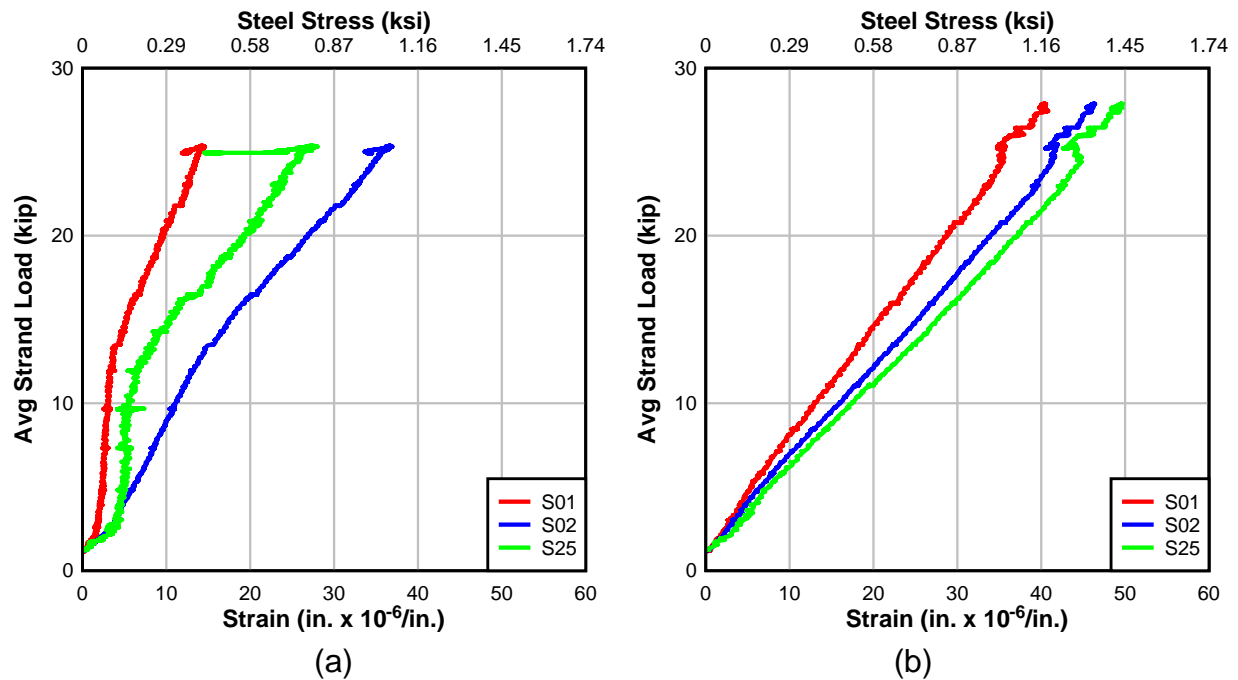


Figure 9-8. Tie strain (a) X1 and (b) SU

In each case, the measured strain in the tie region is tensile - as predicted by the strut-and-tie model - and increases linearly as the strand load increases. The measured rebar strain (gages S01 and S02) is approximately 10-50 microstrain—a corresponding stress of 0.3-1.2 ksi less than the cracking strain of the concrete. Similar measurements of tensile concrete strain were measured by the surface foil gage S25, which measured within 10 microstrain of the rebar gages. All gages recorded strains less than 100 microstrain, i.e., less than the typical concrete tensile strain at cracking. Though the strut-and-tie model did not form (cracking to reveal the reinforcement did not occur), its approximate location appears to be in this region.

Figure 9-9 shows a plot of the strain measured by gages along the beam top flange versus the average strand load. Also shown in the figure are the gage locations and the assumed strut-and-tie model. This field of strain gages was placed to approximately determine the node location of the compressive strut, i.e., the location of the compressive strut node nearest the tie-down. Because the angle of the strut is assumed and unknown, these measurements were taken to simply visualize the region affected by the compressive strut introduced during the stressing procedure.

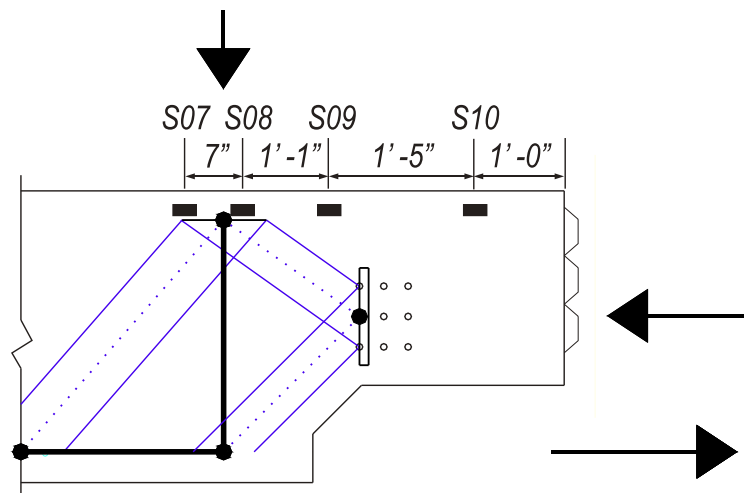
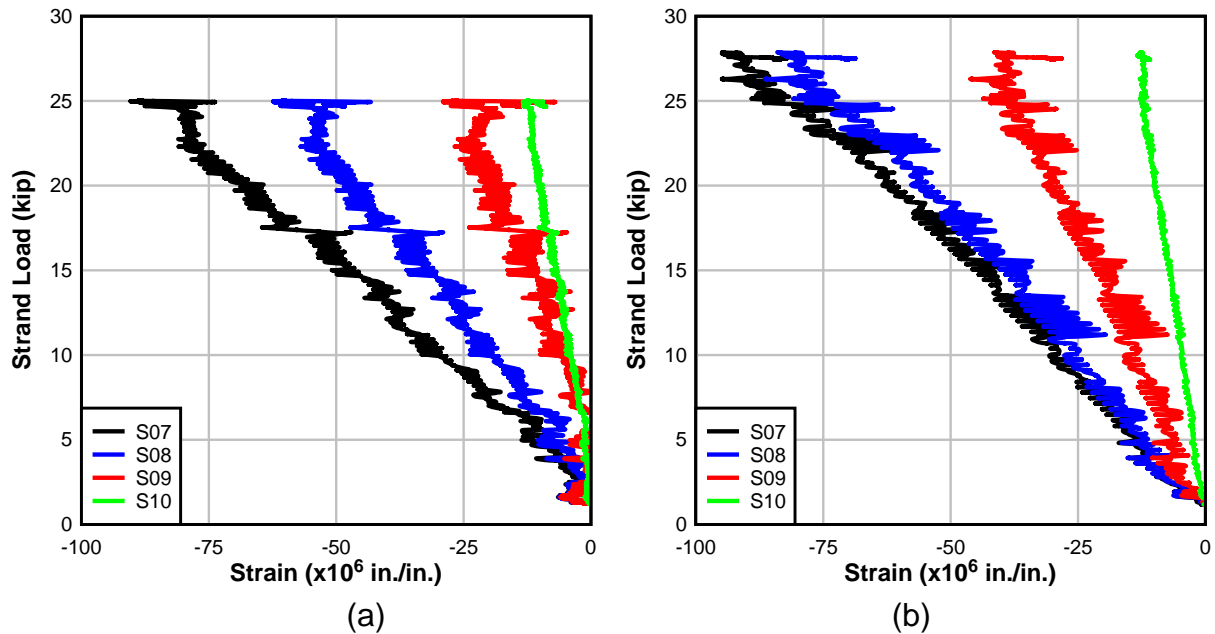


Figure 9-9. Strain in top flange for (a) SB (b) SU

Finally, strain gages were placed concrete surface along the bottom flange of the beam, at the approximate height of the tendon centroid (Figure 9-10). The strain measured by these gages captures the tensile strain imparted into the bottom flange of the beam as the prestressing strand was stressed. In general, however, this is an area of complicated force interaction; tension applied to the concrete via the stressed strand was not directly measurable with the strain gages, due to the interaction of the incoming

compressive strut. Figure 9-10 shows the strain in this region versus the average strand load.

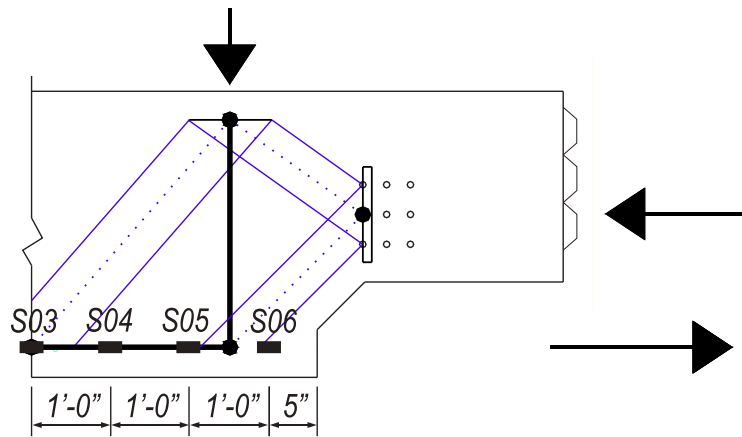
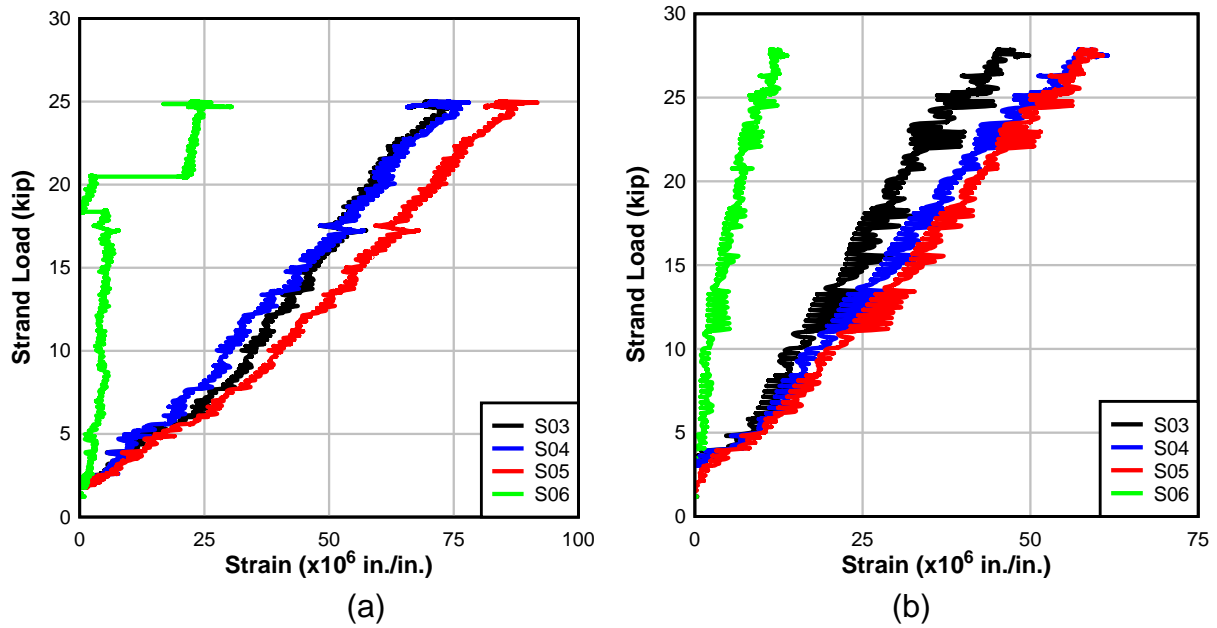


Figure 9-10. Transfer length strain (a) SB (b) SU

CHAPTER 10 FLEXURAL RESULTS AND DISCUSSION

Two specimens were tested in four-point bending to evaluate flexural behavior: one control specimen (XC) and one spliced specimen (X1). This chapter presents and discusses the results. The test set-up and procedure are described in Section 0.

10.1 Flexure–XC

Figure 10-1 shows the load-displacement plot of the control flexure test specimen XC. The XC specimen correlates to precast segment 2 of pour 1 (Figure 6-1). As load was applied, XC exhibited linear-elastic behavior up to a cracking load of approximately 77 kip.

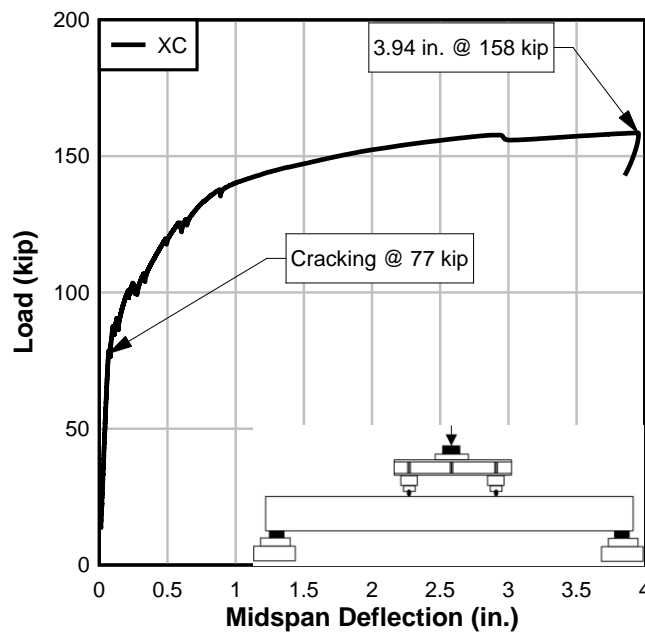


Figure 10-1. XC: Ultimate

At approximately 80 kip, a single crack extending from the bottom flange into the web was visually observed at midspan. The load was held and the crack was

measured; the crack was 0.015 in. wide at approximately 3 in. from the bottom of the beam (point 1) and 0.005 in. wide at point 2, as shown in Figure 10-2.



Figure 10-2. XC: First crack at midspan

As XC was loaded beyond cracking, sudden minor load decreases occurred periodically until the midspan deflection reached just less than 1 in. These decreases indicated flexural crack formation and were confirmed with audible cracking sounds and visual observations. Although the peak load had not been reached, the test was terminated at a deflection of approximately 4 in. (maximum load of 158 kip) to avoid damage to instrumentation. After the applied load was removed from the beam, a permanent set of 2.38 in. was measured at midspan (Figure 10-3).

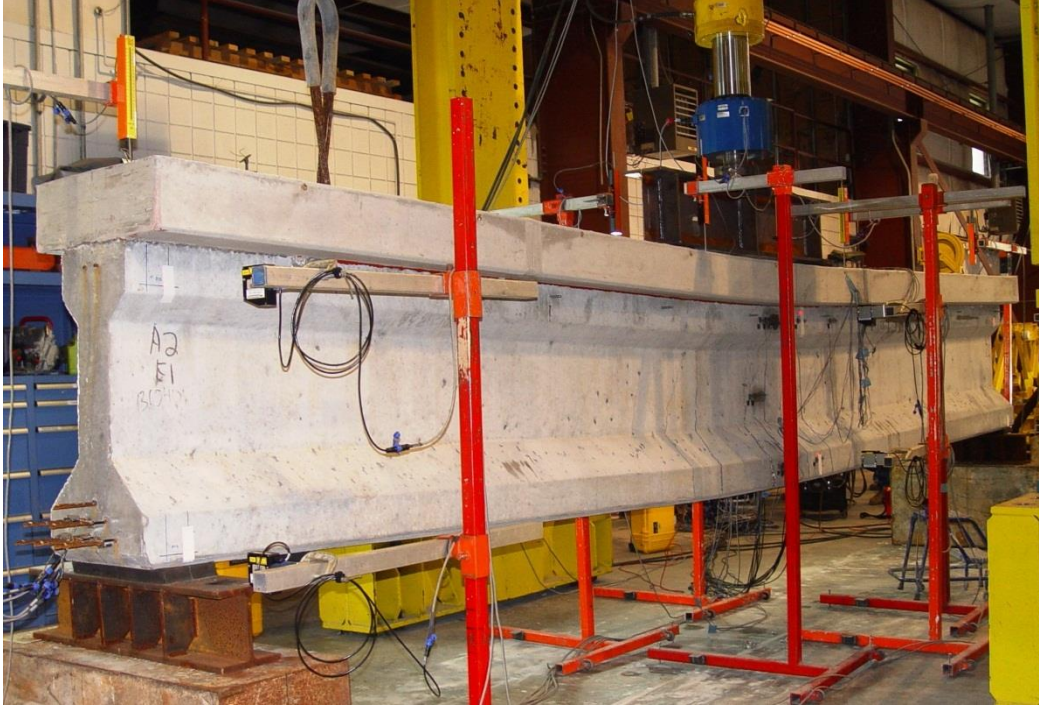


Figure 10-3. XC: Permanent set

Measured compressive concrete strains in the top of the deck at midspan were near 0.003 at termination of the test and the load-deflection plot was nearly flat, indicating that the prestressing strands were yielding and that the specimen's actual flexural strength would not have been significantly higher than the peak load of 158 kip (Figure 10-4). The strain gage at the top of the deck at midspan also indicates a change in slope at 77 kip, corresponding to the cracking load indicated by the load-displacement plot.

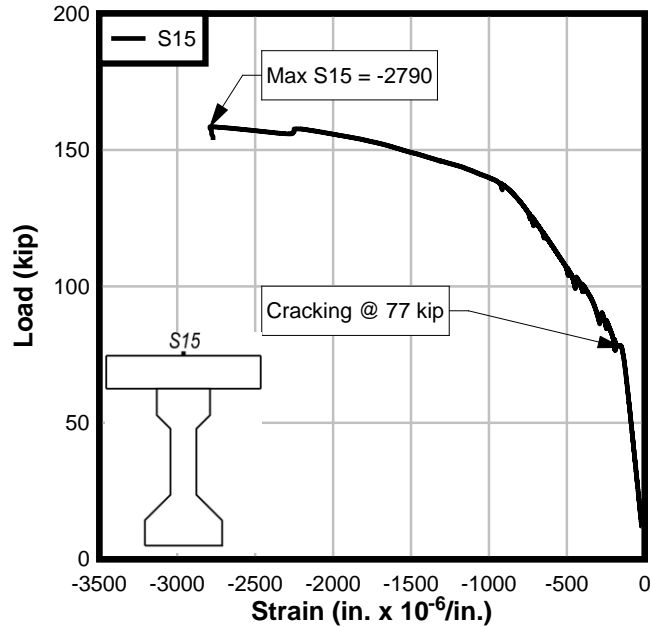


Figure 10-4. XC: Compressive concrete strain at midspan

Inspection of the strain load-strain plot of the gage on the bottom flange at midspan suggests that cracking of the section was predicated by microcracking (beginning at 73 kip).

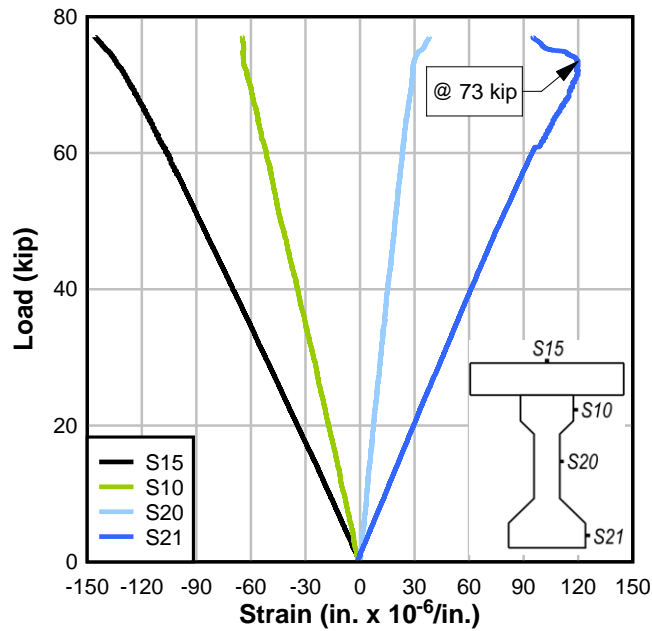


Figure 10-5. XC: Midspan strain profile

Out-of plane displacement was also monitored; very little out-of-plane movement occurred during the load test. No significant strand slip was recorded during the load test (the maximum was 0.0003 in.), indicating that the load points were far enough away from the supports to ensure a flexural failure mode under the area of interest.

10.2 Flexure-X1

Figure 10-6 shows the load-displacement plot of the spliced flexure test specimen X1. X1 was a spliced specimen constructed of segments 4b (from pour 1) and 9u from pour 2 (Figure 6-1). The plot indicates that as load was applied, X1 exhibited linear-elastic behavior up to an applied load of approximately 64 kip.

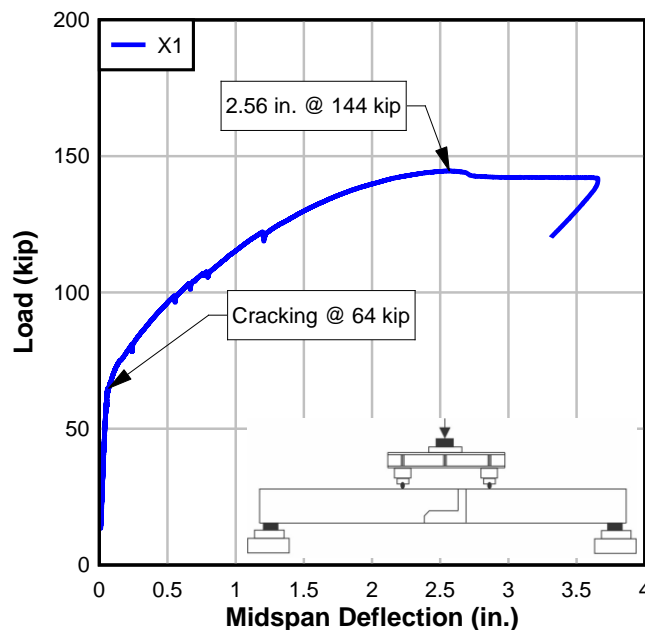


Figure 10-6. X1: Ultimate

At 68 kip, a single crack was visually observed at the vertical interface of the unbonded precast and the closure pour (Figure 10-7). Note that this was the only crack at this load; other inconsistencies in the white-wash seen in the figure are from incomplete white-wash application or rough surfaces of the concrete. Prior to 68 kip,

only superficial cracks where the closure pour overlapped the precast concrete were noted (Figure 10-8).

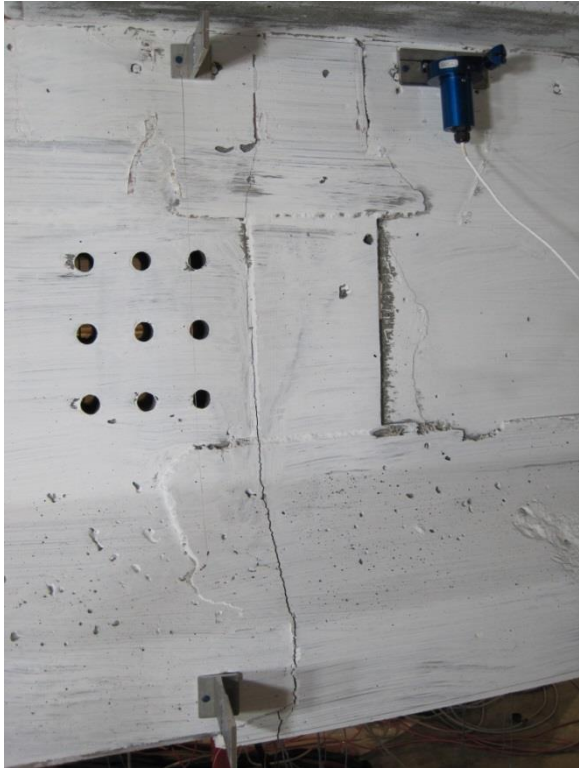


Figure 10-7. X1: Vertical crack at interface



Figure 10-8. X1: Superficial cracks at overlap

After cracking, X1's behavior became inelastic, indicated by the nonlinearity of the load-deflection plot as stiffness decreased. As additional load was applied, the single vertical crack continued to open, until approximately 80 kip, when flexural cracks began to develop in the bonded section of the specimen. From approximately 80 to 120 kip, sudden minor load decreases occurred periodically until the midspan deflection reached approximately 1.25 in. These decreases indicated flexural crack formation and were confirmed with audible cracking sounds and visual observations. Figure 10-9 shows the cracks after termination of the load test.

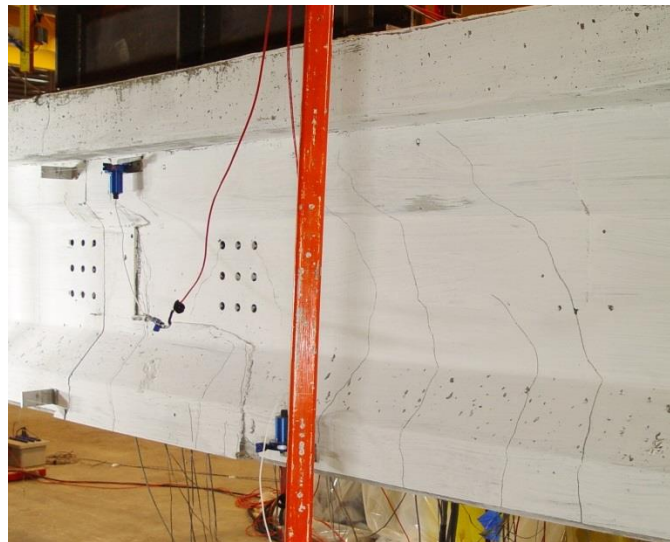


Figure 10-9. X1: Flexural cracking

At 144 kip, the peak load was reached as X1 deflected 2.56 in. at midspan. Following a load drop of approximately 2 kip, the specimen continued to deflect without resisting additional load. Failure of X1 occurred when the deck above vertical interface crushed; the failure was accompanied by pronounced vertical deflection of the specimen prior to deck failure. Figure 10-10 shows the measured deck strain at midspan (gage S15) and near the location of deck crushing (S16); the maximum

compressive strain of approximately 0.002 was measured nearest the crushed concrete.

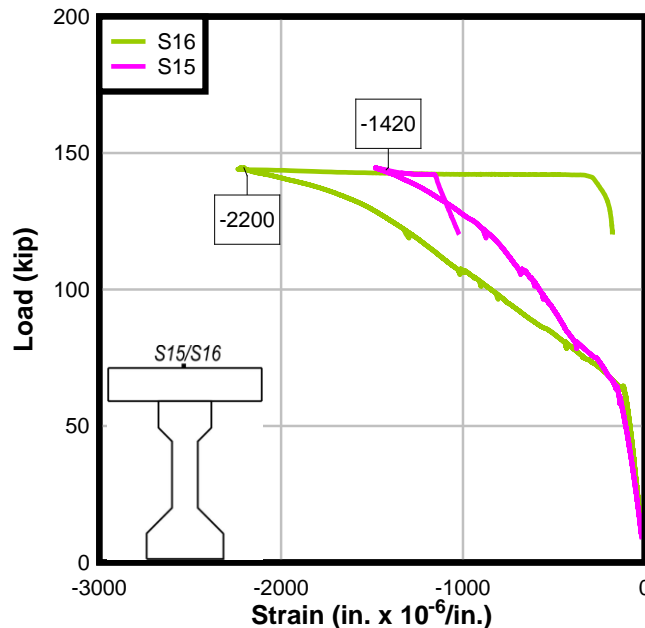


Figure 10-10. X1: Deck strain

No significant strand slip was recorded (the maximum was 0.004 in.) during the load test, indicating that the load points were far enough away from the supports to ensure a flexural failure mode in the area of interest.

10.3 Service and Cracking Behavior

To highlight the flexural service behavior, Figure 10-11 shows the load-displacement plot of XC and X1 up to a midspan deflection of 0.3 in. The secondary y-axis shows the ratio of the calculated bottom fiber stress to $\sqrt{f'_c}$ (psi). The bottom fiber stress is calculated assuming the effective prestress level calculated for XC based on the initial prestress reported in the stressing records minus the prestress losses measured by the vibrating wire strain gages. The load level corresponding to the

extreme fiber tensile stress at the splice location for the Service III limit state in the prototype FIB96 is shown for reference ($5.3\sqrt{f'_c}$ (psi)).

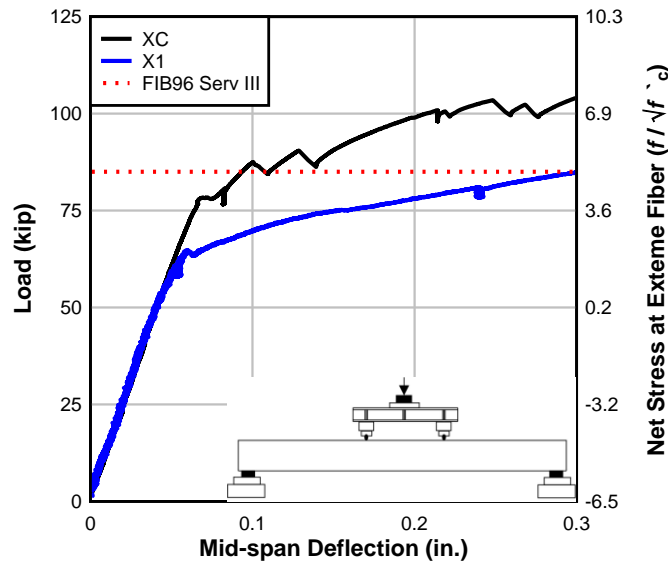


Figure 10-11. XC and X1: Elastic behavior

As shown in the plot, both test specimens exhibit either cracking or joint opening (in the case of X1) prior to both the prototype FIB96 Service III stress ($5.3\sqrt{f'_c}$ (psi)) and the predicted cracking load. Assuming that cracking occurs when the extreme bottom fiber tensile stress reaches $7.5\sqrt{f'_c}$ (psi), the predicted cracking load was calculated to be approximately 105 kip for both specimens, based on the measured effective prestress. The XC specimen cracked at an applied load of 77 kip, while the spliced X1 specimen developed a joint opening at 64 kip. These applied loads corresponds to an approximate bottom fiber stress of $3.8\sqrt{f'_c}$ (psi) and $2.2\sqrt{f'_c}$ (psi) in XC and X1, respectively.

Potential causes for the low cracking load were investigated, including the low specified jacking prestress of $0.6f_{pu}$ (vs. the more typical $0.75f_{pu}$), the achieved initial

prestress level at lock-off, and measured prestress losses. For the following discussion of the cracking load, the control specimen XC is considered.

The lower-than-usual specified prestress was investigated as a potential cause of the low cracking load caused by a longer than anticipated transfer length. Research done by Kaar et al. on beams prestressed with 7-wire 1/2-in. diameter 270-ksi prestressing strand with lower than typical effective prestress indicate that at lower levels of effective prestress, the measured transfer length is consistently less than the transfer length as calculated by AASHTO-LRFD (Kaar et al. 1963; AASHTO 2007). Similar trends have been reported by others. Further, research by Kaar et al. (1963) and Zia and Mostafa (1977) indicate that a gradual release of prestress, as was performed during the construction of the test specimens, reduces the transfer length.

Inspection of the precast yard stressing records confirms that the prestressing strand was tensioned to the specified $0.6f_{pu}$ and that temperature effects were considered. Due to the atypical specification of $0.6f_{pu}$, careful attention was paid by the precaster and UF personnel during the stressing operation. It is assumed that the specified initial jacking prestress was achieved and is not the cause of the low cracking load.

Excessive prestress losses were also investigated and dismissed as a potential cause of the low cracking load. Prestress losses were measured with vibrating wire strain gages at the approximate height of the strand pattern centroid. VWSG measurements of the differential strain change over time indicated a prestress loss of approximately 6% in both the XC and in the bonded segment of the spliced specimen X1 (location of X1's first crack).

The prestress loss measured with the VWSG corresponded well with the prestress loss predicted by PCI, which predicts an approximate loss of 8%. (A table of estimated prestress losses for all specimens based on the PCI method is included in CHAPTER 8.) As a further check of the VWSG reliability, VWSG strain measurements were compared with strain measurements of external foil strain gages at low applied loads (before cracking) while the test specimen was behaving elastically. Figure 10-12 shows the strain measurements of both the VWSG and the external foil strain gage at the midspan of XC, at approximately the same height. During the load test, VWSG measurements were recorded manually every 10 kip, while the foil gage measurements were recorded continuously by the DAQ. The VWSG readings have been corrected for batch and temperature effects. The gages correlate well, confirming the VWSG readings; it can be assumed that VWSG are reading properly.

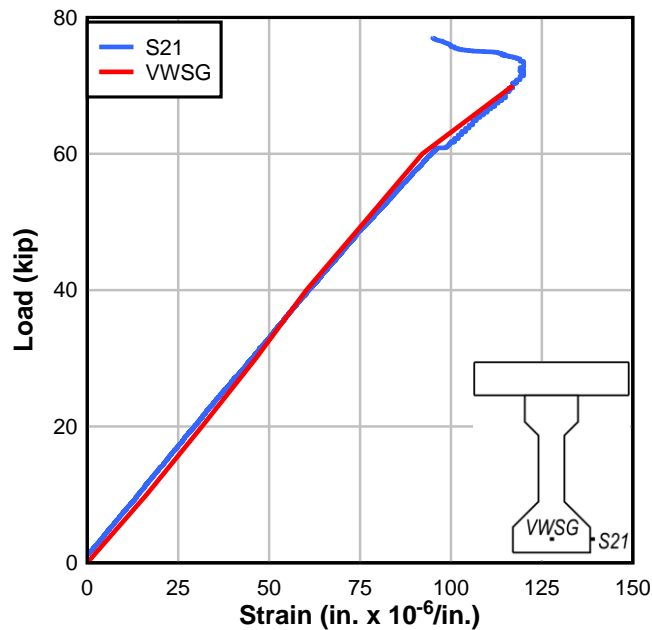


Figure 10-12. XC: VWSG vs. bottom flange strain gage

O'Neill and Hamilton (2009) observed the trend that girders with lower effective prestress force exhibit lower bottom fiber stresses ($6.1\sqrt{f'_c}$ (psi) to $7.6\sqrt{f'_c}$ (psi)) while the same girder section with higher effective prestress cracked at higher bottom fiber tensile ($12.1\sqrt{f'_c}$ (psi) and $14\sqrt{f'_c}$ (psi)); however in all cases, the measured cracking stresses were within the anticipated range of $6-7.5\sqrt{f'_c}$ (psi). The general trend (of lower than expected cracking load) may be seen in the experimental data, but it cannot be stated definitively, given that the magnitude of the cracking stresses is so low.

No cause of the low cracking load was identified; however, because the segments used to construct the spliced beams were constructed in the same manner during the same period and, in the case of the bonded segments, simultaneously, the cracking load of the control beam is used as a benchmark for further comparison with the spliced specimens. Whatever the mechanism, because all the specimens cracked at a low load, and based on the decompression/crack opening tests to back-calculate the induced prestress, it must be assumed that the prestress level in each of the precast segments is less than the effective prestress predicted by the specified value minus the measured prestress losses.

X1 cracked at a lower load than XC, as can be seen in the plot; consideration of the location of the initial crack, and the early crack development, explains this discrepancy. As in the case of a typical prestressed beam, XC cracks when the applied load overcomes the initial precompression of the beam and the modulus of rupture of the concrete; in the case of XC, the beam cracks when the bottom fiber stress is approximately $4\sqrt{f'_c}$ (psi). At the cracking moment, a flexural crack developed midway

between the load points. X1's first crack, however, occurred at the vertical face of the closure pour (Figure 10-13).

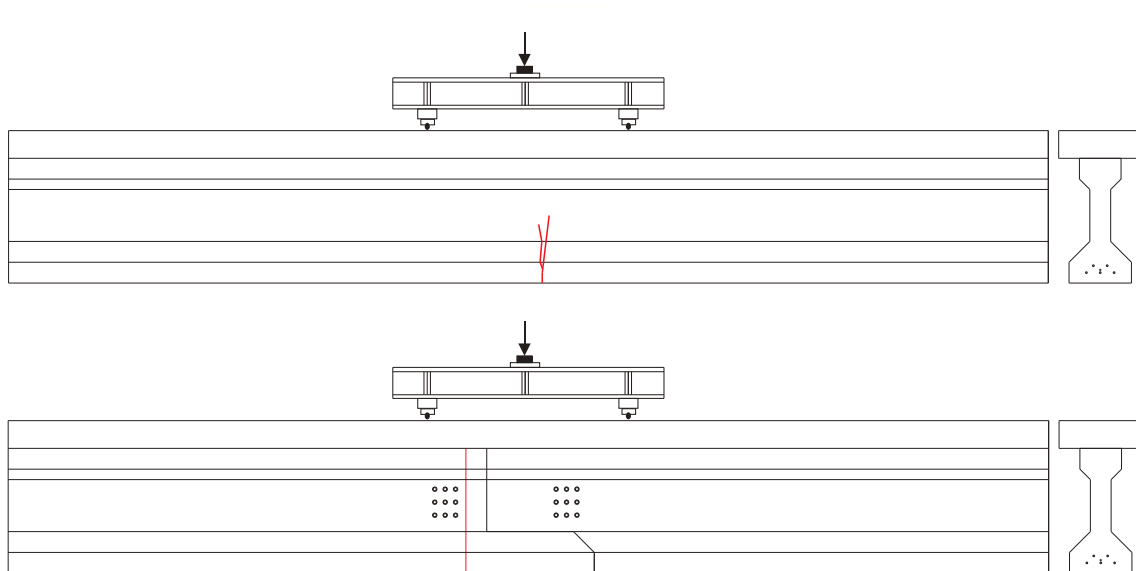


Figure 10-13. XC vs. X1: first crack

The abrupt change in stiffness noted in the load-displacement plot of X1 is not a cracking load, but rather the load required to overcome bond at the dry joint between the precast segment and CIP splice concrete. Consequently, a lower load - slightly greater than that required to reach the decompression moment—is required to open the joint (at approximately $2.2\sqrt{f'_c}$ (psi)). In contrast with XC, the “crack” occurred at a pour interface, and was dependent on the bond between the precast concrete and the closure pour concrete. This joint opening mechanism is confirmed by post-failure inspection of the pour interface. As shown in Figure 10-14, the concrete pours separated almost directly down the interface, with little break-off of either concrete - evidence of little bonding of the two segments.

It can also be observed from Figure 10-14 that the shear keys exhibited little damage, indicating that the keys had sufficient strength to transfer shear across the interface.

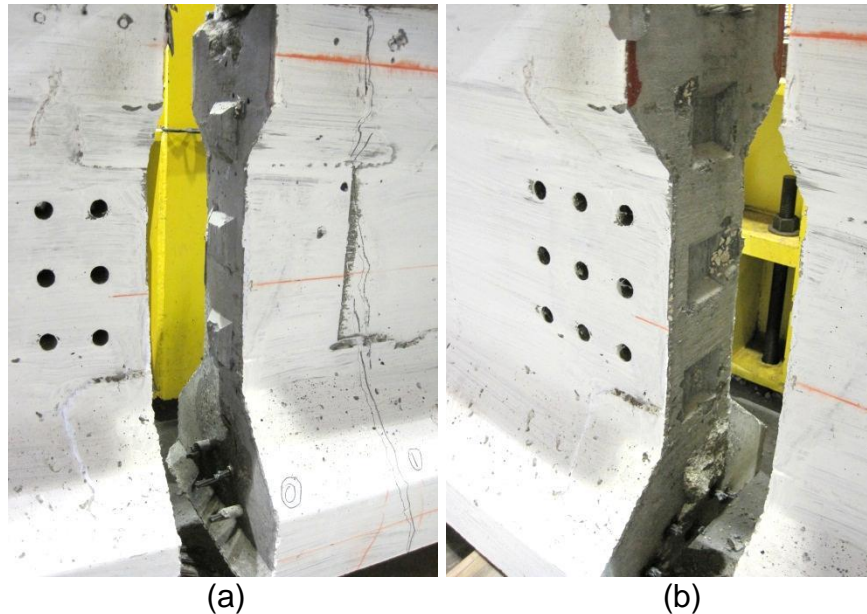


Figure 10-14. Dry joint interface post-demolition, looking at (a) the closure pour, (b) the precast

As loading progressed, XC cracks were noted to be uniformly distributed between the load points, which is typical of bonded prestressed beam behavior (Figure 10-15). Conversely, X1 behaved more like an unbonded, prestressed beam: the crack pattern focused around a single crack at the end of the unbonded length with some flexural cracks in the bonded segment.

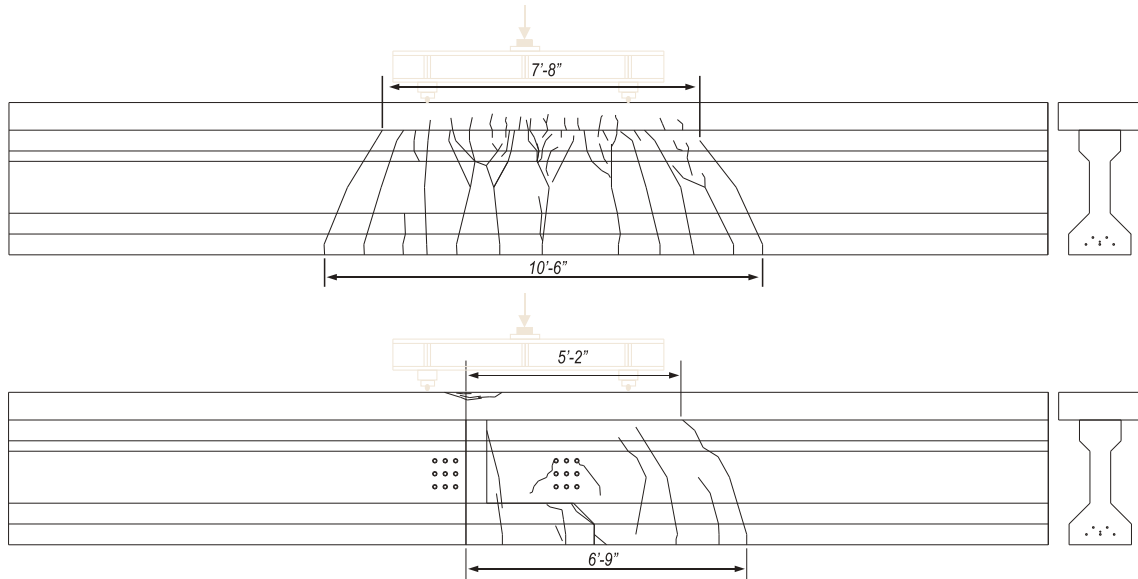


Figure 10-15. XC vs. X1: final cracking patterns

In XC, flexural cracks formed frequently as the load increased from 77 kip to approximately 135 kip as indicated by sudden minor drops in load (Figure 10-11). Furthermore, beyond 135 kip, XC resisted little additional load as the deflection increased. Formation of X1's first crack (at the vertical interface), however, occurred at 64 kip with no additional cracks forming until approximately 80 kip. This delay is reflected in the plot—no load drops are apparent from 64 to 80 kip. During the same load range in XC, several load drops and audible cracking were observed. Like in segmental bridge beams with unbonded tendons, the primary crack of X1 formed at the joint. After cracking, this primary crack continued to open with additional applied load, while the adjacent unbonded segment remained uncracked.

Figure 10-16 shows the displacement measured across the closure pour at the top and bottom of the precast section. Gages D11 and D13 measured the opening at mid-height of the bottom flange; gages D12 and D14 measured opening near the top of the top flange.

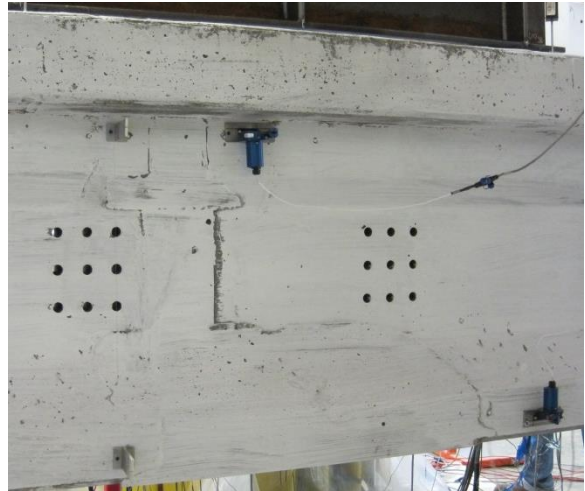
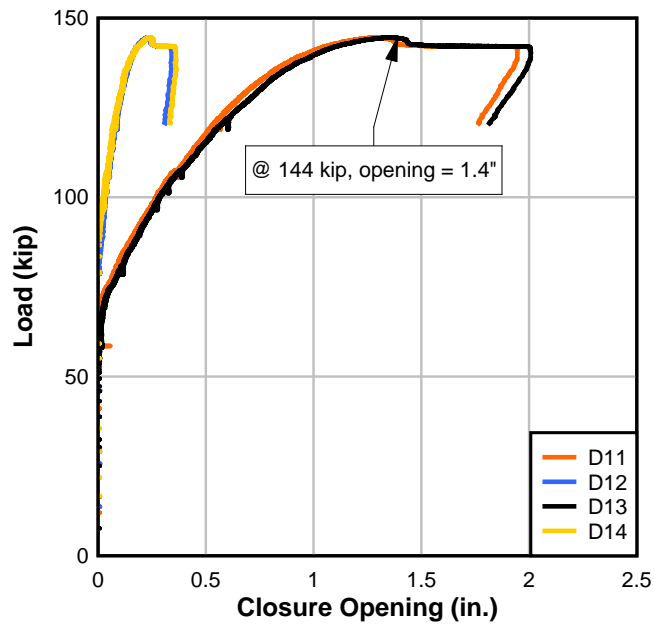


Figure 10-16. X1: String-pots across closure

At the maximum load, the four cracks contained in the interface opened a combined amount of approximately 1.4 in. at the mid-height of the bottom flange. As shown in Figure 10-17, most of the crack opening occurred at the joint.



Figure 10-17. X1: Opening at joint during test

There was some concern that out-of-plane movement of the splice specimen would be greater than normal, due either to the variable section stiffness along the beam's length or slight variation in the precast segment alignment due to the splice assembly process. To compare, out-of-plane displacement was monitored during load testing of XC and X1 (Figure 10-18). Both XC and X1 exhibited little out-of-plane displacement indicating that X1 behaved, at least longitudinally, like a homogenous, prismatic member under vertical load.

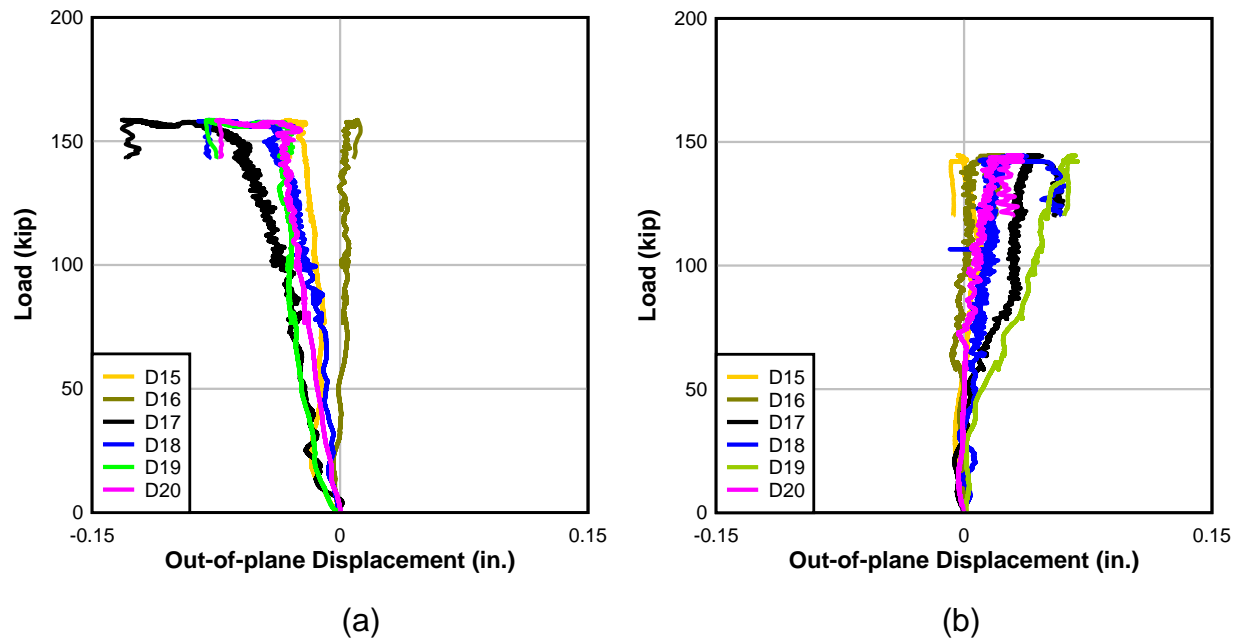


Figure 10-18. Out-of-plane displacement: (a) XC (b) X1

10.4 Comparison of Flexure Strength

The computed flexural strength is compared to their respective load-displacement plots in Figure 10-19. The strength was computed in accordance with AASHTO-LRFD using specified materials of 4.5 ksi deck concrete and 270-ksi prestressing steel. The predicted bonded moment capacity at 0.003 concrete compressive strain was 631 kip-ft, which corresponds to an applied load of 123 kip. For both XC and X1, the peak load exceeded the predicted design strength of a bonded prestressed member. Considering the cracking behavior and failure mode of the spliced specimen X1, the AASHTO-LRFD capacity was also calculated assuming the steel strands were unbonded. The calculated moment strength, assuming all five strands were unbonded, was 589 kip-ft, which corresponded to an applied load of 114 kip. X1 exceeded the anticipated capacity of an unbonded section.

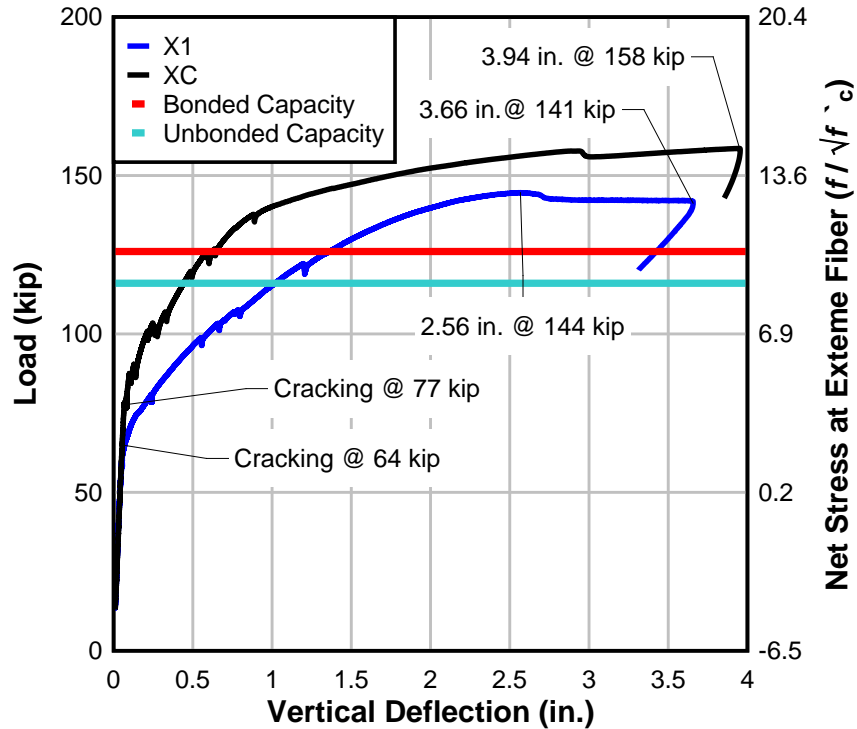


Figure 10-19. XC and X1: Flexural Strength

The flexural capacity of X1 was approximately 144 kip; compared with XC's capacity of 158 kip. This is only a difference of approximately 8%. Both specimens exhibited significant vertical deflection at midspan under maximum load. The displacement ductility of X1 was of interest in evaluating the influence of the coupler on the overall beam behavior. In preliminary strand-in-air tests of the couplers with strand, the wedge of the couplers caused the strand to rupture prior to yield. In the test of X1, however, the opening of the joint at the vertical interface (away from the coupler) prevented flexural cracking from occurring at or adjacent to the coupler and the strand yielded prior to the compressive failure of the deck. It appears the closure pour concrete contributed to the overall anchorage of the strand at the coupler, holding the coupler in place. Another possibility is that the concrete surrounding the anchor wedges

intruding into the wedges during pour of the closure. The wedges were thereby unable to slip at higher loads, preventing stress concentrations on the strand and thus delaying rupture.

At the maximum applied load of 145 kip, the beam continued to deflect without resisting additional load. The midspan deflection at the maximum applied load was approximately 2.6 in. with a permanent set 0.75 in. upon load removal. X1 exhibited a tension-controlled flexural failure as the deck concrete crushed (Figure 10-20).



Figure 10-20. Damage to X1 following testing with spalled concrete in compression zone and wide, permanent crack

Evidence of strand yielding can be seen in the strand load during and after the flexural load test (Figure 10-21). At the start of the load test, each strand had approximately 25 kip of prestressing force. Until the specimen cracked at approximately

64 kip of applied load, the prestressing strand showed little increase in force. After cracking, the strand load increased until the test was terminated. After unloading the specimen upon completion of the load test, the load cells read approximately 5 kip per strand—the loss in load indicating that the strand had yielded. Further, strand-in-air testing of the prestressing strand used in the specimen indicated that the yield strength (defined as 1% elongation) of the strand was approximately 39.2 kip (based on strand-in-air tensile ASTM A416 tests of the strand); every strand was loaded beyond this predicted yield point. In fact, the ultimate tensile strength of the strand was approximately 43.7 kip.

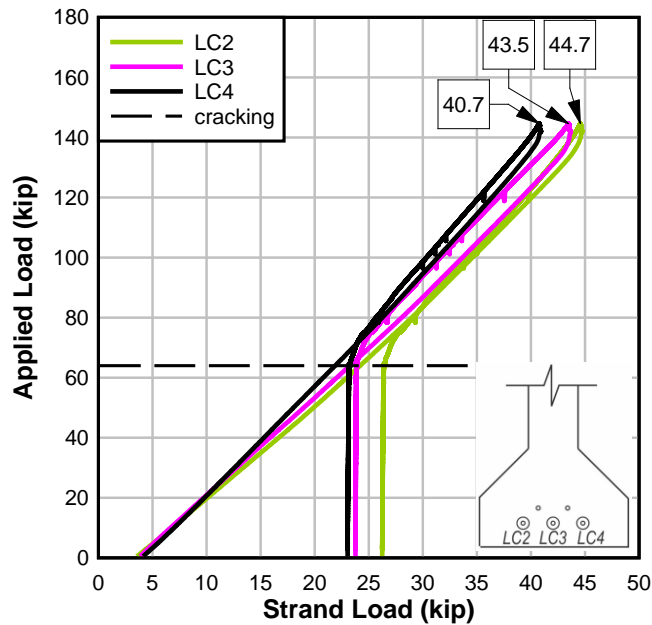


Figure 10-21. X1: Strand load

Despite concerns that the coupler would cause premature rupture of the strand prior to yield, the strand went well into its yield plateau prior to the compression failure of the deck concrete. Evidence of strand yielding is in the incomplete closure of the main crack after complete unload (Figure 10-20), in the reduction of the readings of the

strand load cells (Figure 10-21) and in the permanent deflection of the beam (Figure 10-3).

An interesting comparison of capacity can be quantified by comparing the observed failure moment and reserve capacity (if applicable) to the predicted cracking moment. XC reached its peak (and ultimate) load at 2.1 times its cracking load; X1 reached its peak load at 2.3 times its cracking load. After achieving peak load, X1 continued to carry approximately 98% of the peak load, deflecting nearly 1 in. prior to a crushing of the deck. Even taking into consideration that the control load test (XC) was stopped to protect the instrumentation prior to ultimate load, based on strain measurements both specimens exhibited nearly similar capacity prior to failure.

For purposes of design, it appears that, based on the performance of the spliced specimen, the flexural capacity of the splice region can be conservatively predicted by assuming bonded prestressing strands. A more conservative approach would be to assume unbonded strands in the splice region.

CHAPTER 11 SHEAR RESULTS AND DISCUSSION

Four specimens were tested in a three-point setup to evaluate shear behavior: one control specimen (SC) and three spliced specimens (SB, SU, and SU2). This chapter presents and discusses the results. The test setup and procedure are described in Section 7.3.

11.1 Shear-SC

Figure 11-1 shows the load-displacement plot of the shear control test specimen (SC)—a continuously prestressed precast beam. SC was precast segment 1 from pour 1 (Figure 6-1). The orientation of the SC load test was chosen to compare behavior with the SU and SU2 spliced specimen load tests. The plot indicates that as load was applied, SC exhibited linear-elastic behavior up to a cracking load of approximately 128 kip.

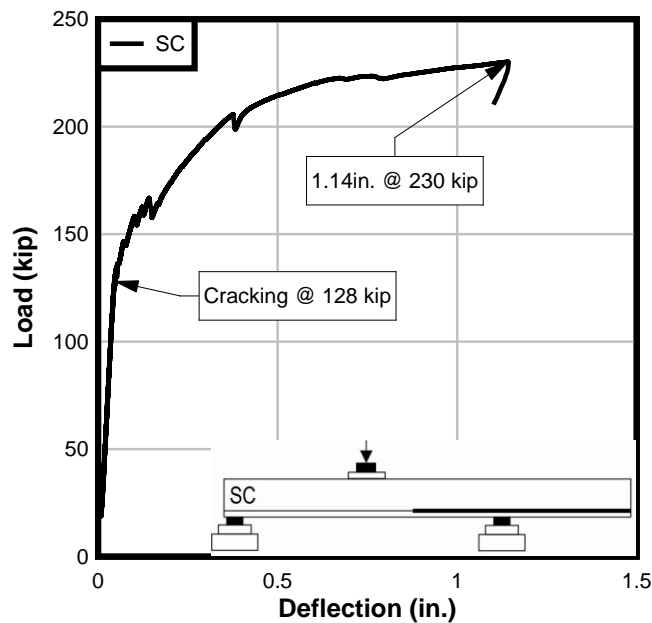


Figure 11-1. SC: Ultimate

The first visible crack was a flexural crack which occurred at 128 kip. It formed approximately under the load point (Figure 11-2). While SC is a homogenous precast specimen, the location of what would be the closure pour in a spliced beam has been sketched onto the beam to provide a reference for discussion.



Figure 11-2. SC: Crack pattern

As SC was loaded beyond cracking, sudden minor load decreases occurred periodically until the midspan deflection was approximately 0.4 in. These decreases indicated flexural crack formation and were confirmed with audible cracking sounds and visual observations of the crack development. At the peak load of 230 kip, the specimen deflected approximately 1.1 in. at the load point. A flexural failure mode was observed as the deck concrete crushed under the load point. A permanent set at the load point of 0.4 in. was measured after the load was removed.

Compressive strain measured in the deck strain at the load point reached approximately 0.003 (Figure 11-3). The strain gages become erratic prior to the peak load, indicating local cracking of the concrete in the top of the deck.

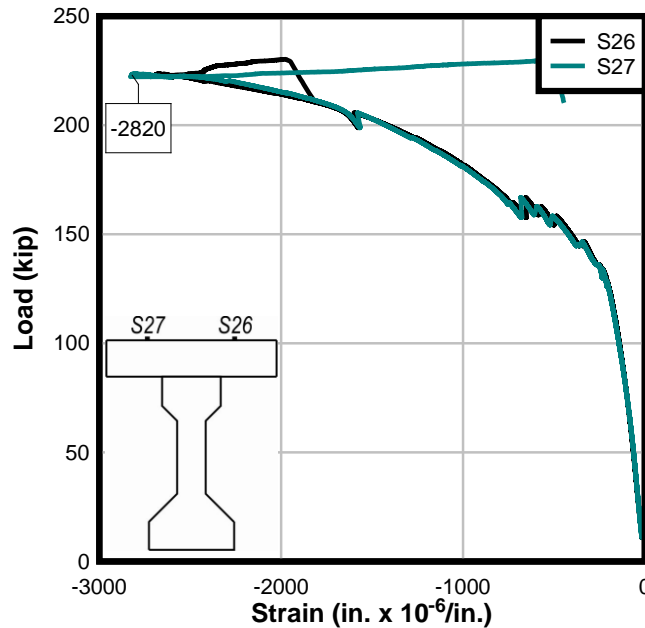


Figure 11-3. SC: Strain at load point

11.2 Shear-SB

Figure 11-4 shows the load-displacement plot of the spliced test specimen loaded with the load applied to the bonded segment. This is referred to as specimen SB - the spliced specimen constructed of bonded segment 5b and unbonded segment 5u (Figure 6-1). The plot indicates that, as load was applied, SB exhibited linear-elastic behavior up to a cracking load of approximately 120 kip; a crack was visually observed at this load. The first visible crack was a flexural crack located approximately under the load point. The load was held at 120 kip and the crack was marked. The first crack is circled in Figure 11-5.

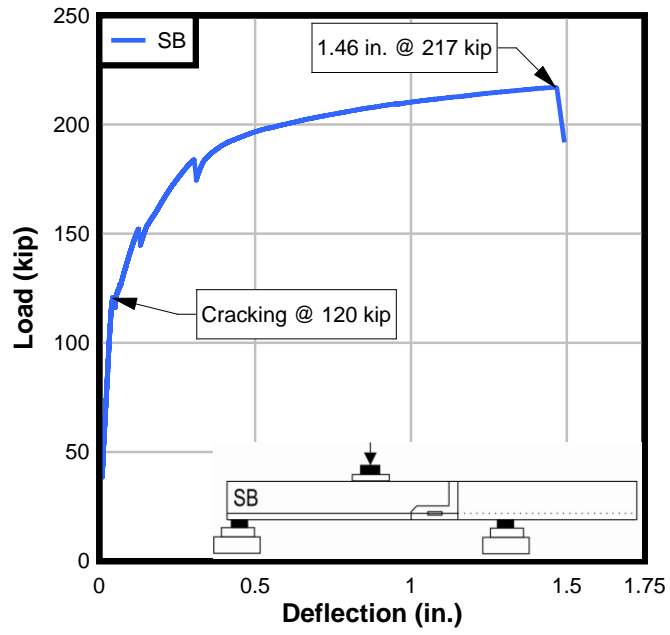


Figure 11-4. SB: Ultimate

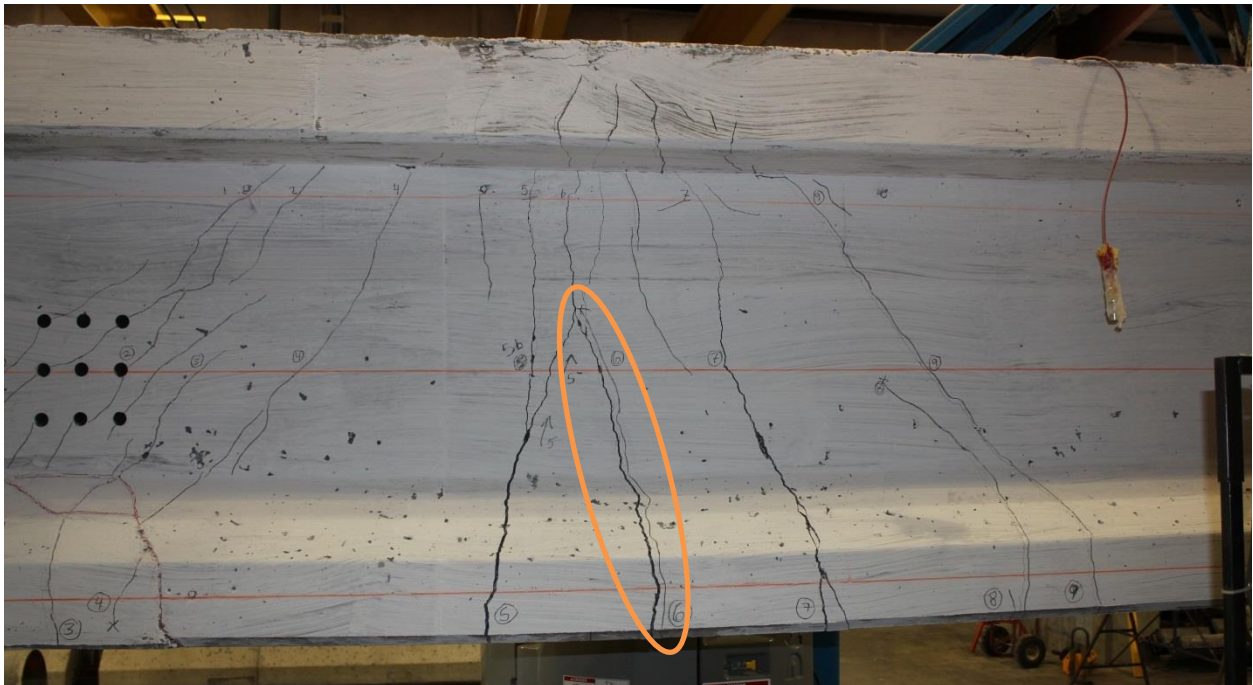


Figure 11-5. SB: First crack

As the specimen was loaded beyond cracking, two load decrease events occurred—one at 145 kip and one again at 183 kip. The load dropped was approximately 8 and 10 kip, sequentially. These load decreases correspond to slight changes in the strand slip gages (Figure 11-6); the magnitude of the strand slip readings suggest that the gages were jostled by the cracking of the beam, not strand slippage.

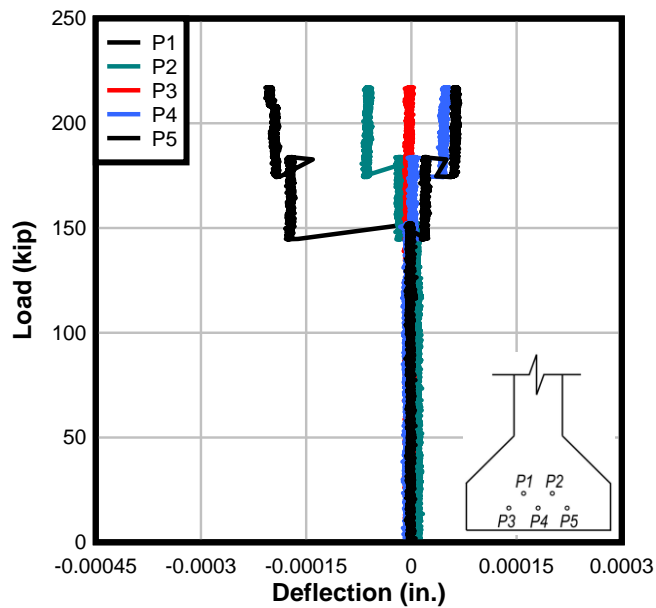


Figure 11-6. SB: Strand slip

The peak load was approximately 217 kip when the deck failed in compression under the load point (Figure 11-7); a maximum deflection of 1.5 in. occurred at the load point at the ultimate load.



Figure 11-7. SB: Deck at failure

Compressive strains at the top of the deck near the load point maxed out around 0.0035 at a load of approximately 208 kip (prior to the peak load); the plot is shown in Figure 11-8. From 208 to 217 kip, the deck concrete experienced local crushing around the concrete, indicated by the strain reversal measured by the gages.

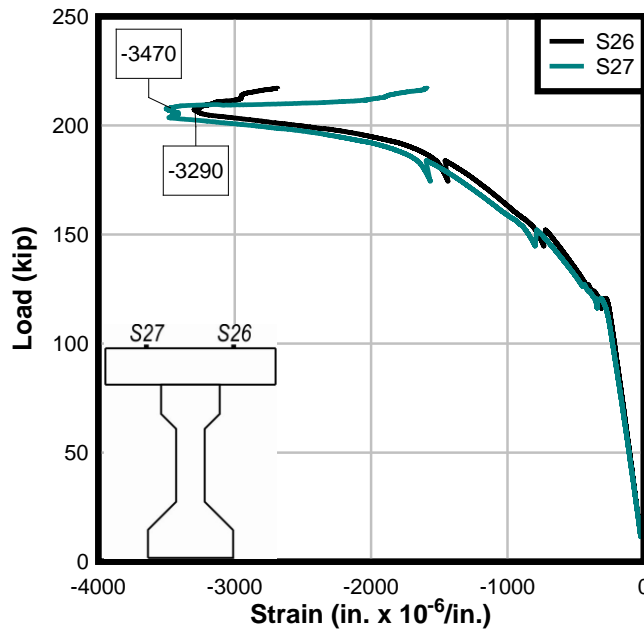


Figure 11-8. SB specimen: Strain at load point

11.3 Shear-SU

Figure 11-9 shows the load-displacement plot of SU with the load applied to the unbonded segment. SU was the spliced specimen constructed of bonded segment 9b and unbonded segment 7u (Figure 6-1). The plot indicates that, as load was applied, SU exhibited linear-elastic behavior up to a cracking load of approximately 125 kip.

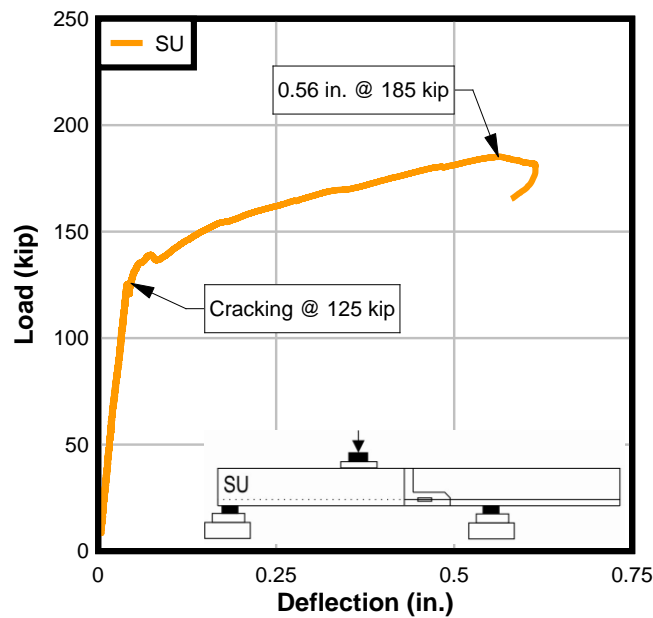


Figure 11-9. SU: Ultimate

The first visible crack was a web shear crack forming across the joint in the splice area (Figure 11-10).

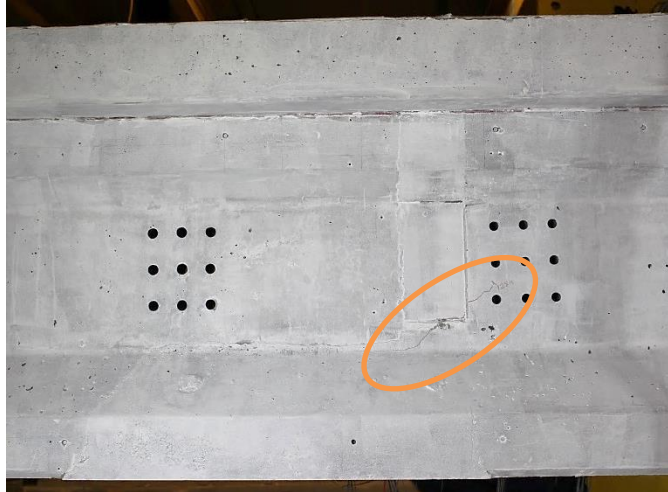


Figure 11-10. SU: First crack

As load application continued, the cracks propagated diagonally toward the load point. At 130 kip, an opening of the joint was observed at the vertical interface between the closure pour and the unbonded segment. SU exhibited a slightly reduced stiffness, until approximately 140 kip. Where a crack crossed a joint interface, the crack changed direction to follow the path of least resistance, i.e., the dry joint. From 140 kip to 185 kip, the load-deflection nearly plateaued, revealing marked reduction in specimen stiffness. Once the compression concrete was lost (through cracking of this region), the unbonded segment suddenly slipped downward. At the peak load of 185 kip, SU deflected approximately 0.6 in. at the load point. A shear failure mode was observed as the crack at the vertical interface propagated until a slip occurred between the closure pour and the unbonded precast segment. A torsional rotation of the top flange away from the bottom flange was observed. Figure 11-11 shows the spliced region cracking after failure.

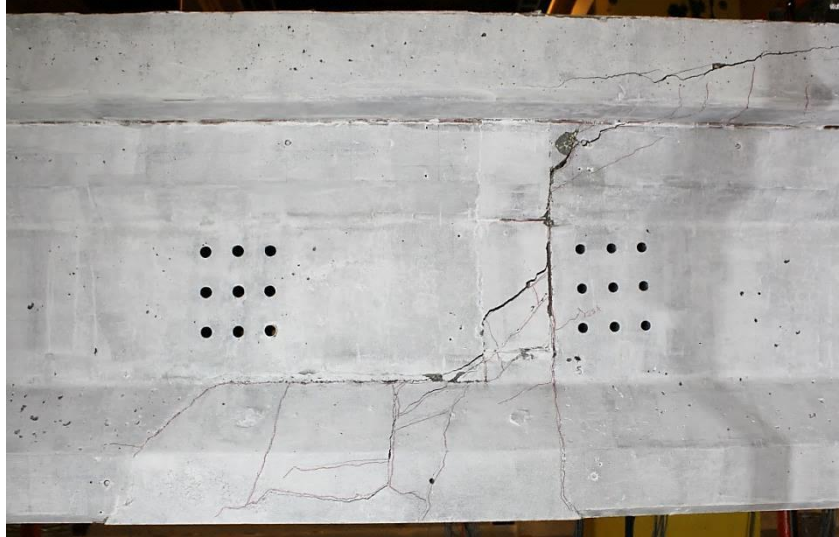


Figure 11-11. SU: Joint at failure

Compressive strain measured in the deck concrete at the load point did not reach 0.003 (Figure 11-12).

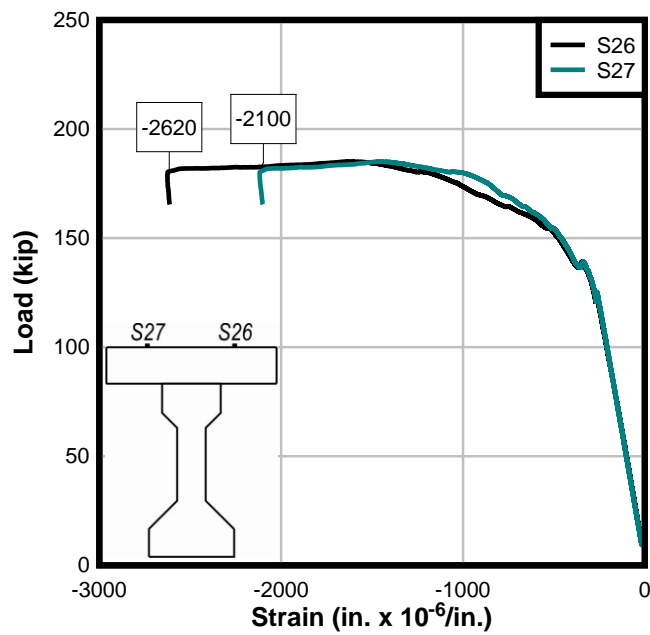


Figure 11-12. SU: Strain at load point

11.4 Shear-SU2

Figure 11-13 shows the load-displacement plot of the second spliced test specimen—hereafter referred to as SU2—with the load applied to the unbonded segment. SU2 was the spliced specimen constructed of bonded segment 8b and unbonded segment 4u (Figure 6-1). This load test was performed to verify the behavior of the first SU test. The plot indicates that as load was applied, SU2 exhibited linear-elastic behavior up to a cracking load of approximately 123 kip. The plot indicates that as load was applied, SU2 exhibited linear-elastic behavior up to a cracking load of approximately 123 kip.

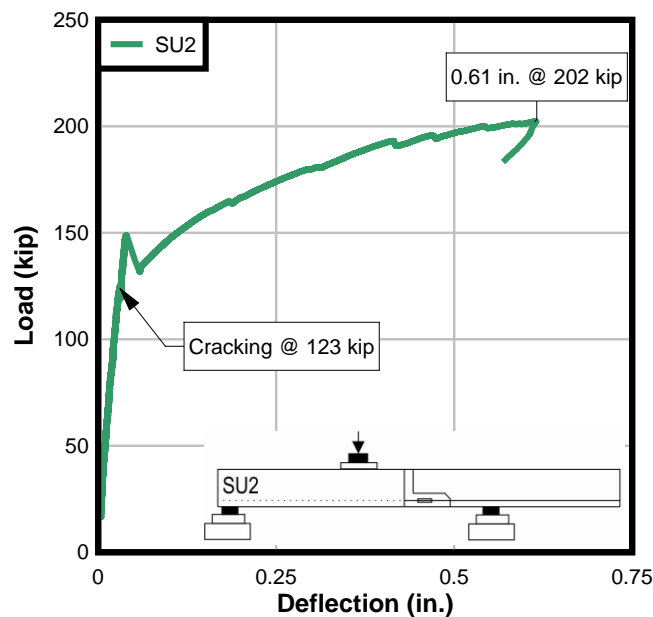


Figure 11-13. SU2: Ultimate

The first visible crack was a web-shear crack which formed in the precast concrete near the joint (Figure 11-14). At the cracking load, the crack affected only the precast concrete, halting at the closure pour.

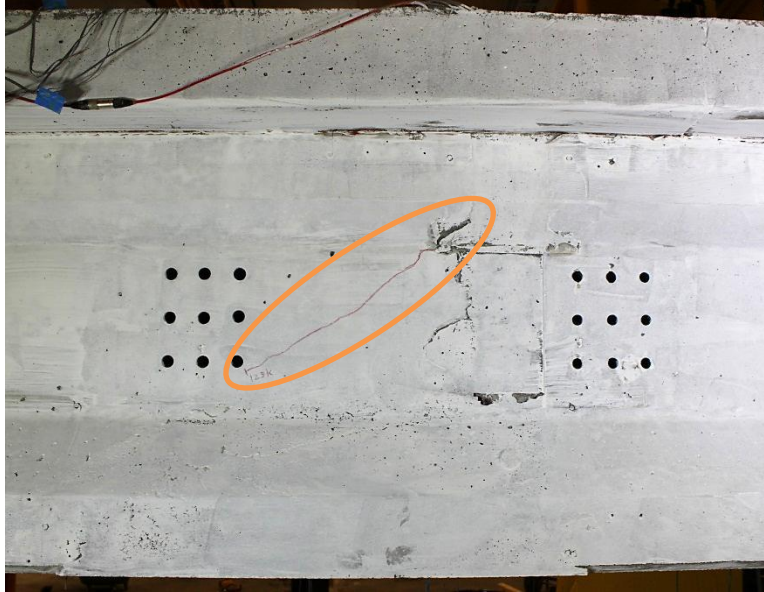


Figure 11-14. SU2: First crack

As additional load was applied, SU2 exhibited reduced—but nearly equal-stiffness, until approximately 149 kip. At 149 kip, a major load decrease of approximately 18 kip occurred when a flexural crack formed directly under the load point (Figure 11-15).



Figure 11-15. SU2: Flexural crack at 149 kip

At the peak load of 202 kip, SU2 deflected approximately 0.6 in. at the load point. A combined flexural-shear failure mode was observed as the main flexural crack under the load point continued to open and the web-shear crack (the first crack) propagated diagonally toward the load point; slip between the two segments at the vertical interface of the closure joint was again observed, similar to the test of the SU specimen (Figure 11-16).

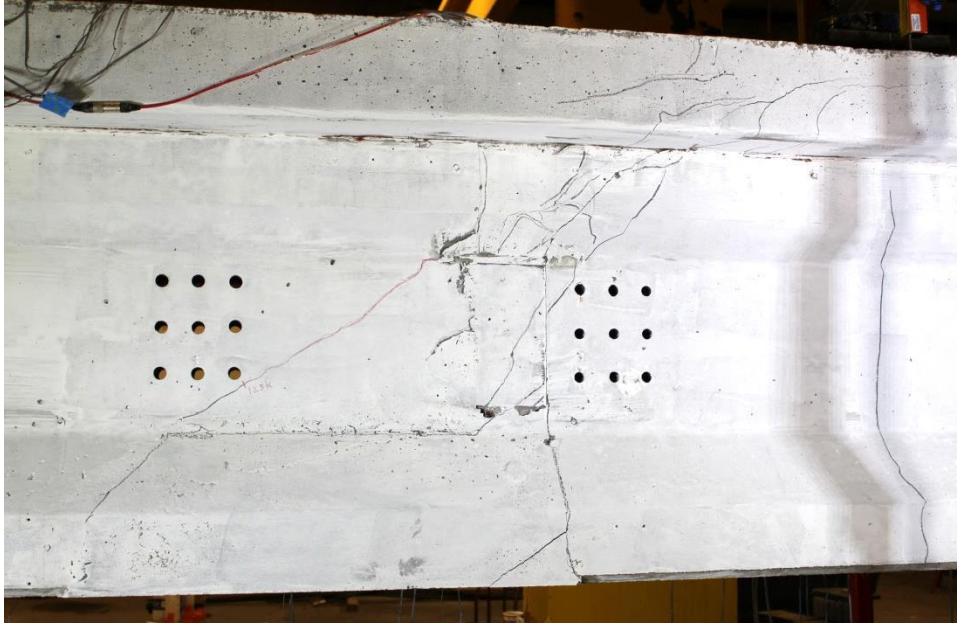


Figure 11-16. SU2: Joint at failure

Compressive strain measured in the deck strain at the load point exceeded 0.003 (Figure 11-17), corresponding with observed crushing of the deck concrete at the load point.

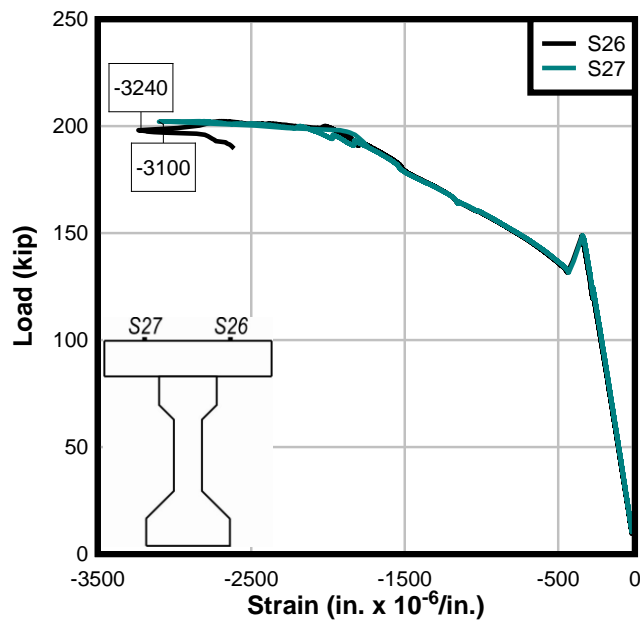


Figure 11-17. SU2: Strain at load point

11.5 Comparison of Service and Cracking Behavior

To aid the discussion of the shear specimens' service and cracking behavior, Figure 11-18 compares the test set-ups of the SC, SB and SU specimens and provides each specimen's bond pattern. As illustrated in the figure, several spliced specimens were tested, varying the orientation of the bond pattern to encompass the behavior of each side of the spliced beam. A single control specimen—with continuously prestressed, bonded strand—was oriented in the direction of most interest, based on the spliced specimen results. The chosen orientation of the control specimen (SC) placed the end with five bonded strands under the load point similar to the load tests of SU and SU2. The orientation of SC matched the quantity of strands in the shear span, but not the bonding pattern, to SU and SU2.

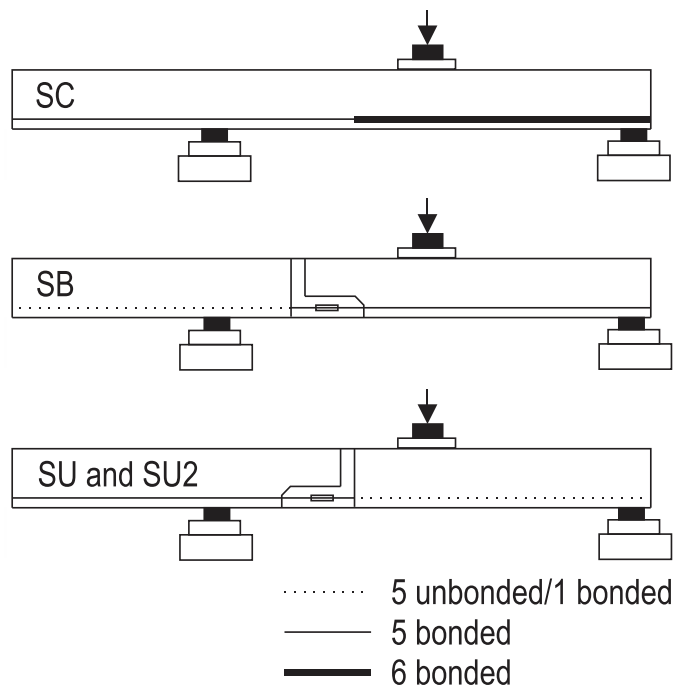


Figure 11-18. Bond patterns of shear tests

To highlight the elastic behavior the shear specimens, Figure 11-19 shows the load-displacement plot up to a deflection of 0.2 in.

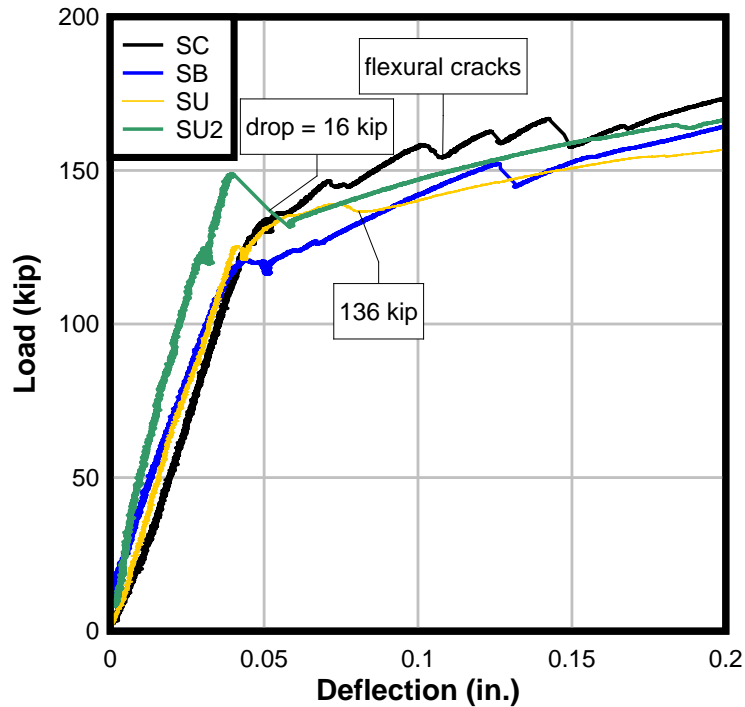


Figure 11-19. Shear comparison: Elastic behavior

Each specimen behaved linear-elastically up until cracking. Specimen SU2 exhibited slightly stiffer behavior than SC, SB, or SU. The cracking loads are given in Table 11-1.

Table 11-1. First crack of shear specimens

| Specimen | Crack Type | Cracking load (kip) |
|----------|------------|---------------------|
| SC | Flexure | 128 |
| SB | Flexure | 120 |
| SU | Web-shear | 125 |
| SU2 | Web-shear | 123 |

SC had the highest cracking load at an applied shear of 128 kip; all of the spliced specimens cracked within 10 kip of this value. Consideration of the location and type of crack is relevant.

Figure 11-20 shows the first crack location of each shear specimen. The first crack is shown as a thick red line.



Figure 11-20. Shear specimens: First crack locations

The first crack in the SC and SB specimens was a flexural crack and occurred in nearly the same location—approximately under the load point. Based on the effective prestress, as determined from the stressing records and the VWSGs, and the applied load, the bottom fiber stress at cracking of the SC and SB specimens was $4.1\sqrt{f'_c}$ (psi) and $3.6\sqrt{f'_c}$ (psi), respectively .

Both SU specimens exhibited similar service level shear behavior. In both the SU and SU2 beam, the first crack formed as a web-shear crack near the joint. In the SU beam, the web-shear crack crossed the interface between the precast concrete and the closure pour concrete. The formation of the SU crack in this location—crossing the pours—indicates composite action between the precast and closure pour. On the other hand, its development within the joint indicates a possible weak area of the splice, where the smaller size of the aggregate in the closure pour provides less aggregate interlock to resist shear and where the increased spacing of the stirrups has reduced contribution to the shear capacity. In contrast, the first crack of the modified SU2 affected only the precast concrete of the spliced specimen. The use of the epoxy bonding agent appears to have strengthened the joint region, forcing the first crack formation away from the joint.

As the crack development progressed after first crack, the specimens continued to exhibit very different behavior. The SC and SB specimens developed multiple flexural cracks, well-distributed under the load point, in the fan-like formation typical of crack patterns seen in three-point bending tests of bonded prestressed beams.

The SB specimen developed cracks across a larger portion of the span, especially around the pipe inserts. Two possibilities for the prevalence of cracks in this

area exist: the pipe inserts may have inhibited the consolidation of the concrete in this area during the precast pour, or the splice stressing procedure caused unnoticed cracking to occur at this location. SB did develop a few cracks along the closure pour interface, though those that did form followed the direction of the compressive strut under the load and continued in a diagonal direction toward the load point. Though the splice region appears to have affected some of the crack development, in general, the crack pattern is much like that of SC.

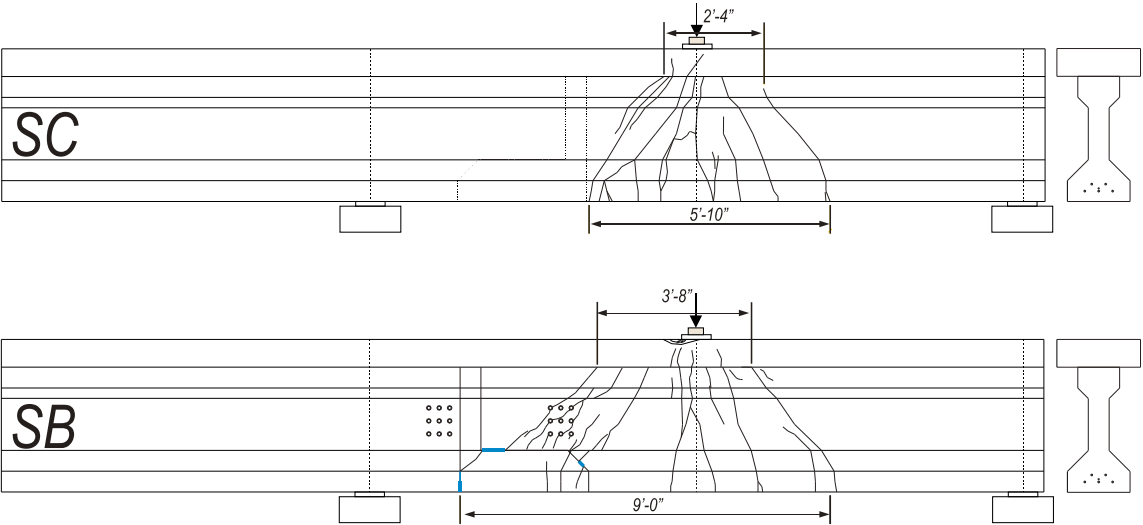


Figure 11-21. SC vs. SB: Crack pattern

Specimens SU and SU2 exhibited behavior more commonly associated with unbonded prestressed beams. Figure 11-22 shows the final crack pattern of the SU and SU2 specimens.

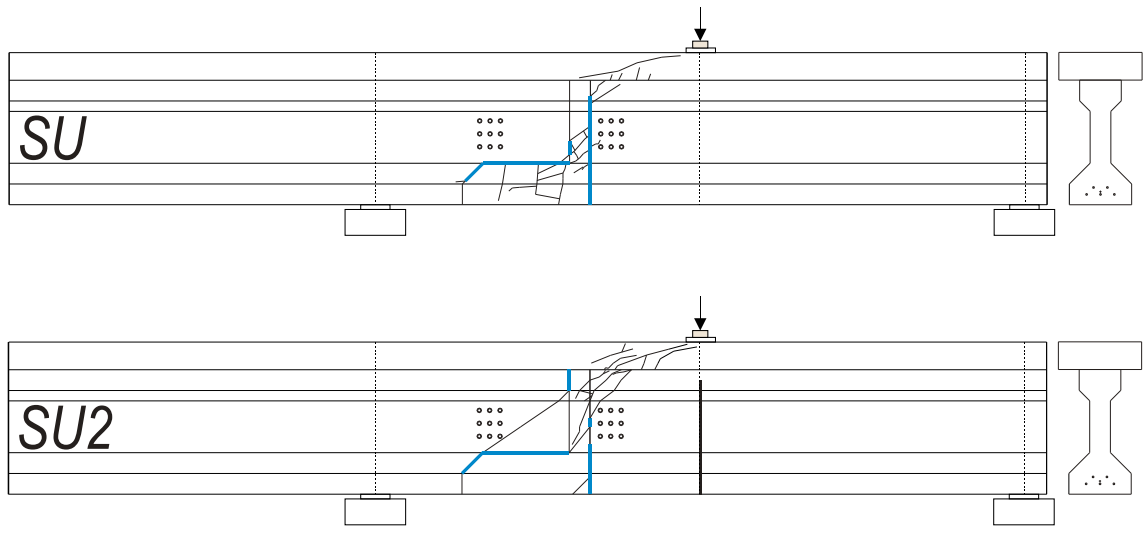


Figure 11-22. SU vs. SU2: Crack pattern

While the SC and SB beams developed a well-distributed fan pattern of flexural and flexural-shear cracks under the load point, the SU and SU2 specimens, on the other hand, developed flexural-shear and shear cracks concentrated toward the joint and the bonded segment of the shear span. In both the SU and SU2 specimens, all cracks initiated either at an interface between concrete pours, or within the splice concrete, except for the single vertical crack under the load point in SU2. Except for this crack, the unbonded segments of the span remained uncracked, except in the top flange, where cracks propagated as the load test neared its termination. Unlike the SB specimen, cracking around the pipe inserts did not occur in the SU or SU2 specimens.

In SU and SU2, crack opening occurred principally at the main vertical crack. From the vertical crack's first visual appearance until peak load, most crack width growth was visually observed to occur at this location in both specimens.

In the SU2 specimen, the main vertical crack formed directly under the load point, in the unbonded segment, and did not occur until approximately 149 kip—after the

development of much of the flexural cracking in the splice region. Strain gages on the bottom flange at this location registered the crack formation at 149 kip (Figure 11-23).

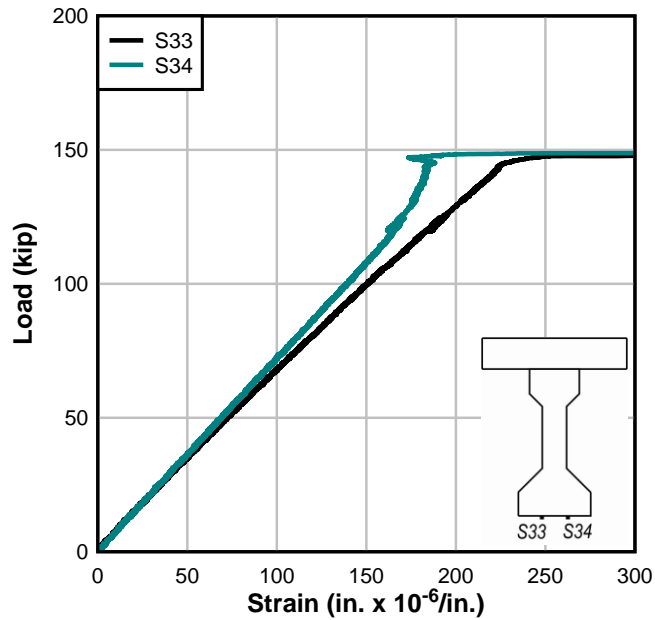


Figure 11-23. SU2: Bottom strain at vertical crack location

The formation of the vertical crack under the load point in SU2 marked a significant change in its behavior. The location of the crack—in the unbonded segment—exposed the entire unbonded tendon length to the load induced stress. As load was applied beyond 149 kip, the prestressing strand load increased beyond the prestress level. Figure 11-24 shows a plot of the load cells on three of the prestressing strands vs. the applied load. A reference line is provided at 149 kip, indicating when the vertical crack formed. A separate reference line is provided at 123 kip—formation of the first crack. Note that this crack did not cause increased strand load.

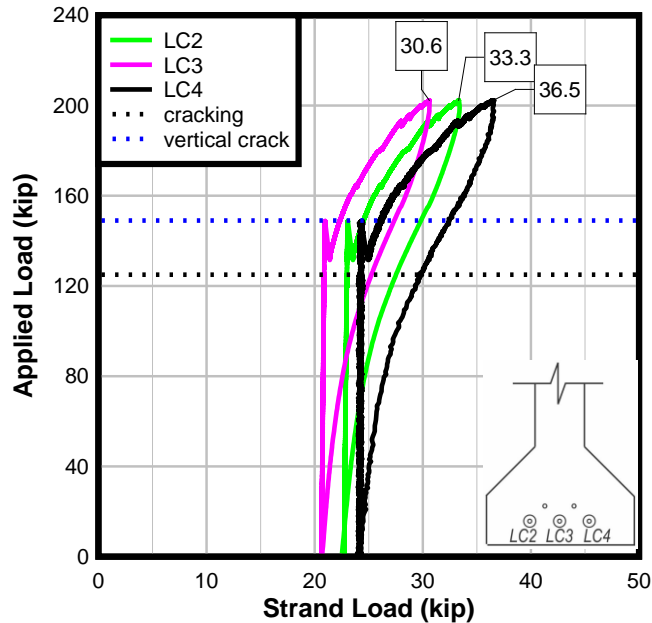


Figure 11-24. SU2: Strand load

Figure 11-25 shows the load-strain plots for the strain gages placed on the faces of the couplers for SU and SU2. These strain gages (hereafter referred to as GS gages) were placed during the splice assembly and were cast within the closure pour. Figure 11-25(a) shows the applied load vs. the strand load for SU. Reference lines are provided at 123 kip and 130 kip, the load at which the first crack and the joint opening, respectively, were visually observed. Figure 11-25(b) shows the applied load vs. the strand load for SU2. Reference lines are provided at 125 kip and 149 kip, the load at which the first crack and the vertical crack at the load point, respectively, were visually observed.

Unlike the SU2 load cells, the SU2 GS gages do not measure a significant change in slope when the vertical crack forms. Instead, the SU2 gages indicate a linear relation of a single slope from zero applied load until peak load, with only small jags in the data (corresponding the crack events). Based on this trend, it can be surmised that

the couplers remain bonded to the concrete through the duration of the SU2 test. Near peak load, the gages indicate a significant increase in strain, suggesting that the couplers were finally exposed. If the strand debonded such that the couplers—and therefore the GS gages- were part of the unbonded length of strand, we would see a change in slope at some point during the test.

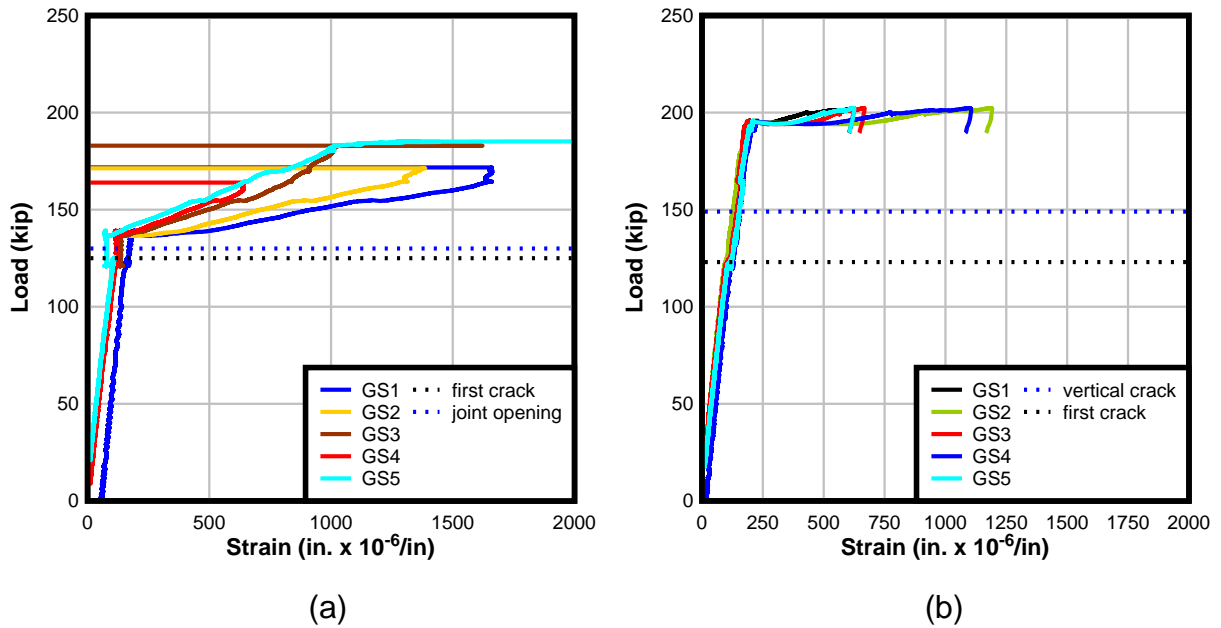


Figure 11-25. Coupler strain gages: (a) SU and (b) SU2

In specimen SU, the formation of the joint opening at the vertical interface was visually observed at approximately 130 kip, after the formation of two web-shear cracks in the closure pour. In contrast to the effect of cracking on SU2, the joint opening in SU did not have the same immediate effect on the prestressing strand load.

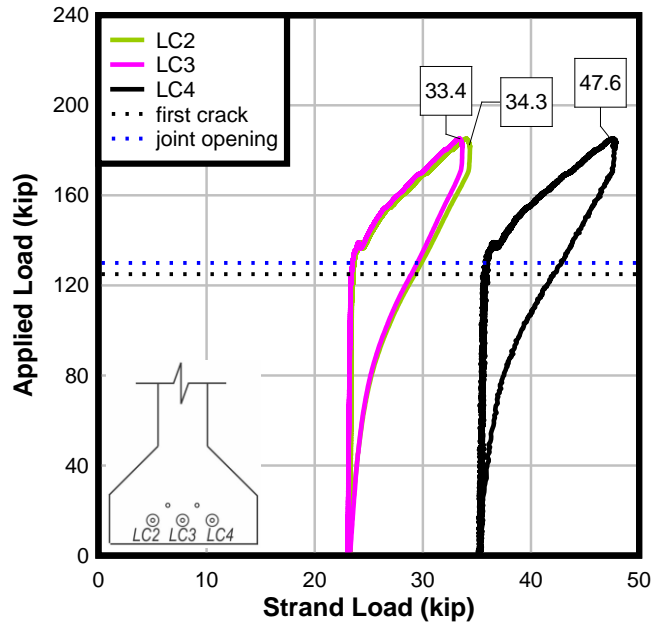


Figure 11-26. SU: Strand load

Based on the delay between the vertical crack formation and the gain in the strand load, it can be surmised that the crack at the interface did not expose the prestressing strand immediately. Inspection of the closure pour concrete after demolition of the specimen shows some bonding between the closure pour concrete and the precast concrete around the single bonded strand at this location (Figure 11-27). The bonding in this area may have slowed the exposure of the prestressing strand until approximately 139 kip, when Figure 11-26 indicates that the prestressing strand began to pick up load.



Figure 11-27. Post-test: End view of unbonded segment

In both Figure 11-21 and Figure 11-22, the thick blue lines indicate locations where the cracks developed along the interface. It can be seen that in both the SU and SU2 cases, cracks tended to follow the interfaces between two pours. The cracks were drawn to the weakest areas—or the joint areas—where the relatively weak bond between the two concrete pours serves as a crack development path. Cracks of this type are absent (understandably) from the control beam and only occur for short lengths in the SB specimen. The lower shear stress on the splice region, particularly the vertical interface of the joint, may contribute to their relative absence from the SB specimen.

Once a crack initiated at an interface, the crack progressed along it, with little bond between the new and old concrete, the crack formation path was predictable. The shear keys did not resist the “crack opening”, instead the segments simply separated.

In general, shear resistance of a reinforced concrete beam is provided by the concrete of the compressive chord, aggregate interlock, the steel stirrups and dowel

action of the longitudinal (prestressing) steel (though this is minimal). In the splice region, the aggregate interlock is reduced because of the smaller aggregate of the self-consolidating concrete. Steel contribution to the shear resistance is mainly provided by the stirrups, which have an increased spacing in the splice region to accommodate the congestion caused by the couplers. The coupled prestressing strand provides some, albeit limited, dowel action.

Based on observations of the SU tests, modifications were made to the splice design to increase the shear resistance at the joint. An additional stirrup—centered in the closure pour—was provided to provide additional resistance in the closure concrete, in an attempt to prevent crack formation in the vertical column of the joint. Additionally, an epoxy bonding agent was applied to all of the precast faces to provide additional bond to the closure pour. The expectation was that the epoxy would delay or prevent crack formation at the interfaces.

The effects of these modifications are evident when considering the crack development during the load test of SU2. The first crack in SU2 formed in the web of the bonded segment's precast, whereas, in SU, it had formed in the web of the closure pour.

11.6 Comparison of Shear Strength

The load-deflection plot of the four shear tests up to ultimate strength is shown in Figure 11-28. For discussion purposes, SC and SB are presented together in Figure 11-28(a) and SU and SU2 are shown in Figure 11-28(b). For reference, the applied load required to reach the AASHTO-LRFD calculated moment capacity (assuming bonded strands) is shown at 171 kip. Each specimen had a different shear capacity, due to different spacing of the stirrups in the splice region. AASHTO-LRFD shear

capacities are calculated for each specimen and given in Table 11-2. All calculations were performed assuming the section and specified material properties given in

CHAPTER 5.

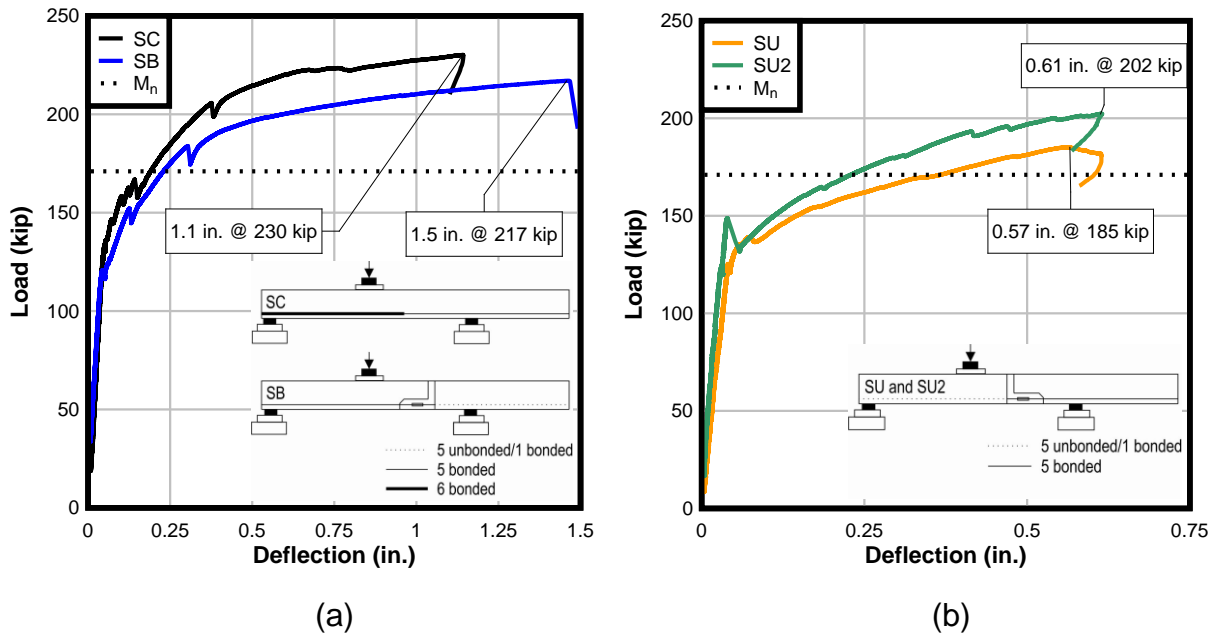


Figure 11-28. Ultimate behavior: (a) SC and SB and (b) SU and SU2

The experimental flexural capacity of all shear specimens—including the control and all spliced beams—was greater than the AASHTO-LRFD calculated design values (regardless of whether or not the strands were considered bonded).. Specimen SC reached the highest load and deflection at its ultimate state, when it failed in flexure as the deck crushed. Similarly, SB reached peak load when the deck under the load point crushed. Measured strain at this location indicated that the deck strain had exceeded 0.003 for both SC and SB. The failure mode can best be characterized as a tension-controlled flexural failure.

Figure 11-24 and Figure 11-26 show the strand load as the applied load was removed at the end of the test. In both SU and SU2, the strand load completely

recovered the prestress force present at the start of the test, indicating that the strand had not yet begun to yield in either test. The failure of SU is best characterized as a shear failure, occurring when the segments slipped apart when the cracks propagated diagonally towards the load point and compromised the deck. The failure of SU2 is best characterized as a compression-controlled flexural failure because the concrete crushed at ultimate, but the strand had not yet begun to yield.

Table 11-2 compares the ultimate behavior of the splice region of specimens SC, SB, SU and SU2 to the AASHTO-LRFD calculated design values at the location of interest: the vertical interface of the closure pour. Figure 11-29 shows the location of interest corresponding to the values given in Table 11-2. M_n was calculated in accordance with AASHTO-LRFD Article 5.7.3. V_n was calculated in accordance with AASHTO-LRFD Article 5.8.3.4.2 at the location of least shear resistance, the vertical column of the closure pour. A stirrup spacing of 12 in was assumed for the spliced specimens without the additional stirrup; 6 in. was assumed when the additional stirrup was used. The applied V_x and M_x are also given at this location. All calculations were performed assuming the section and specified material properties given in CHAPTER 5. Self-weight is included.

Table 11-2. Shear specimens' ultimate behavior at vertical interface

| Specimen | Deflection at load point, in. | M_x (kip-ft) | M_n Bonded (kip-ft) | M_n Unbonded (kip-ft) | V_x (kip) | V_n (kip) | M_x/M_n | M_x/M_n | V_x/V_n |
|----------|-------------------------------|-------------------|--------------------------|----------------------------|----------------|----------------|-----------|---------------|-----------|
| | | | | | | | Bonded | Unbonded d | |
| SC | 1.14 | 270 | 631 | n/a | 120 | 189 | 0.43 | n/a | 0.63 |
| SB | 1.46 | 254 | 631 | 589 | 113 | 92 | 0.40 | 0.43 | 1.22 |
| SU | 0.56 | 485 | 631 | 589 | 95 | 92 | 0.77 | 0.82 | 1.03 |
| SU2 | 0.61 | 531 | 631 | 589 | 104 | 141 | 0.84 | 0.90 | 0.74 |

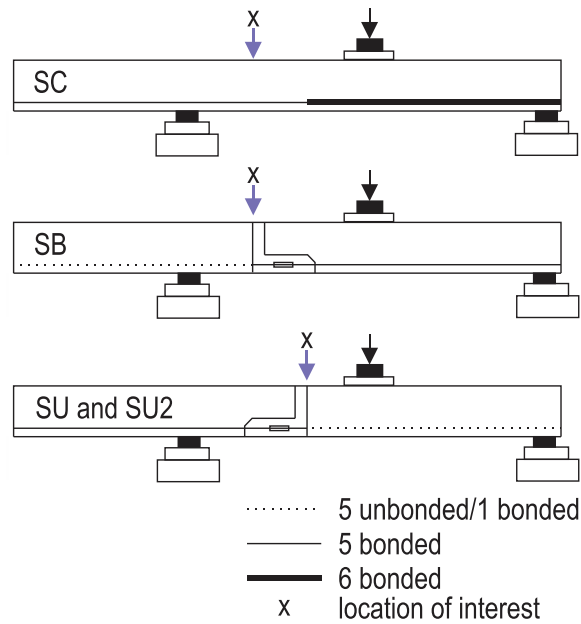


Figure 11-29. Shear location of interest

Again, the ultimate behavior of the control specimen (SC) and the bonded specimen (SB) are more alike than the two unbonded specimens (SU and SU2). However, due to the different stirrup spacing in each specimen, as well as the different bonding pattern placement in the tested shear span, it is most useful to compare each

specimen's applied shear at ultimate to the AASHTO-LRFD calculated design capacity, instead of attempting to compare the specimens to each other.

SC:

- Stirrup spacing at location of interest: 4 in.
- Greatest applied shear at ultimate load, but also the greatest capacity (due to shortest stirrup spacing).
- Flexural compression failure at load point. The applied shear to shear capacity ratio was 0.63 while the applied moment to moment capacity was 0.43. The flexural failure mode was as designed.

SB:

- Stirrup spacing at location of interest: 12 in.
- Flexural compression failure at load point. The applied shear to shear capacity ratio was 1.22; despite the applied load surpassing the design capacity, the specimen exhibited a flexural failure mode. The applied moment to moment capacity was 0.40. This was the same ratio as seen in specimen SC.

SU:

- Stirrup spacing at location of interest: 12 in.
- Shear failure. The segments slipped at the vertical interface. The applied shear to shear capacity ratio was 1.03; in this specimen (unlike SB), the application of shear beyond capacity resulted in a shear failure.

SU2:

- Stirrup spacing at location of interest: 6 in.
- Flexural compression failure at load point. The applied shear to shear capacity ratio was 0.74; in this specimen (unlike SB), the application of shear beyond capacity resulted in a shear failure. The applied moment to moment capacity was 0.84.

The service and ultimate improvement in performance of specimen SU2 over specimen SU can be attributed to the two modifications made to the splice design: the epoxied joint, instead of a dry joint, as well as the additional stirrup. The concentrated

rotation and deflection at a dry joint opening is reduced with the use of epoxy, allowing the specimen to achieve a greater ultimate load and deflection. This phenomenon has been noted by other researchers (Saibabu et al. 2013). The additional shear resistance contributed by the additional stirrup also contributed to SU2's improved ultimate behavior. Specimen SU – tested in the same set-up as SU2 – had an anticipated additional 50 kip of shear capacity at the location of interest (the vertical column of the closure pour). The applied shear at ultimate load of SU2 was indeed greater, yet did not result in the shear failure seen in SU.

The chosen shear test set-up creates a lower-bound solution for the shear behavior and capacity of the splice. This was intentional: considering that the actual moment-to-shear ratio could not be achieved with the test specimen length, the load and support locations were chosen to maximize the shear effects on the splice region. The resulting shear test set-up creates a lower M/V (3.7) than would be seen in the FIB96 prototype design (32.9). In other words, the loading situation tested is unlikely in an actual design; however, the tests provided a chance to examine the shear behavior and capacity of the splice region. Based on observed behavior during these tests, modifications were made which positively affected the service-level behavior of the splice region, and which increased the shear capacity of the splice region.

CHAPTER 12 FATIGUE RESULTS AND DISCUSSION

This chapter covers the fatigue testing of control specimen (FC) and two spliced specimens (F1 and F2) to determine the effect of fatigue cycling on the splice connection. Initially, the specimens were statically loaded to crack the specimen and to determine the stiffness prior to initiating the fatigue cycling. This initial cracking load was followed by several static loads to conduct decompression testing to aid in estimating the effective prestress force. These load cycles are covered in the *Static Conditioning* sections. The specimen was then loaded in fatigue for up to 2 million cycles at the selected load range; results and observations related to fatigue testing are covered in the *Fatigue Loading* sections. Finally, the specimens were tested to their ultimate strength following the fatigue loading; this load testing is described in the *Ultimate Strength Test* sections. The test set-up and procedure are described in Section 7.4.

12.1 Specimen FC

FC was precast segment 3 from pour 1, shown in Figure 6-1.

Static Conditioning

Figure 12-1 shows the load-displacement plot of the initial static loading of the control specimen FC. The trend is linear with some initial variation from 0 to approximately 20 kip attributed to the sensitivity of the laser gages and the inherent roughness of the deck surface, as well as take-up in the test fixtures. At 74 kip, the load-displacement plot shows a significant change in slope, indicating crack formation. This was confirmed by visual observation of two cracks at 76 kip (Figure 12-2).

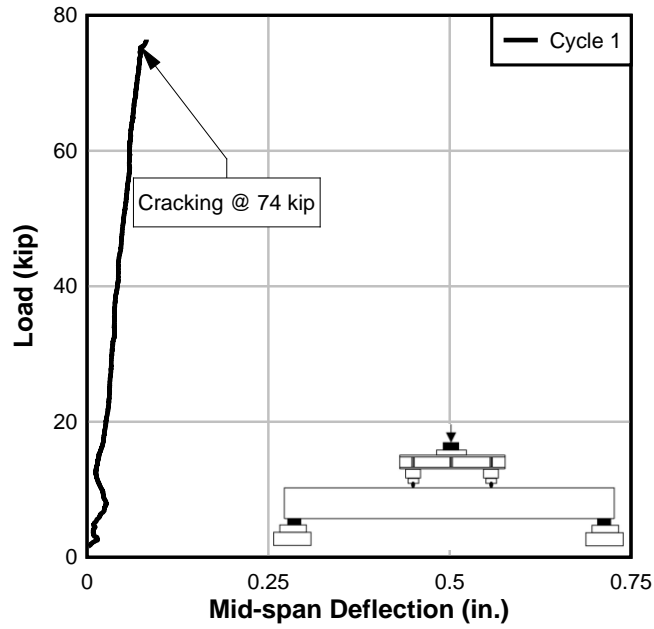


Figure 12-1. FC: Static conditioning

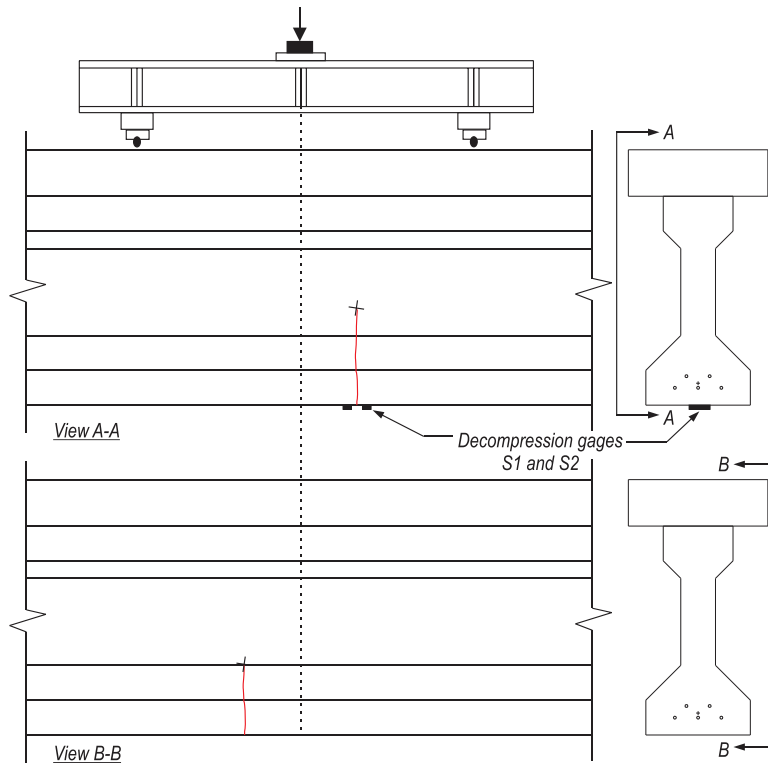


Figure 12-2. FC: First crack

After precracking, decompression tests were performed on one of the FC cracks to determine the effective prestress. Figure 12-3 shows the load-displacement plots for the three load cycles of this procedure. (Multiple load cycles were performed to ensure the repeatability of the strain readings used for determination of the effective prestress.)

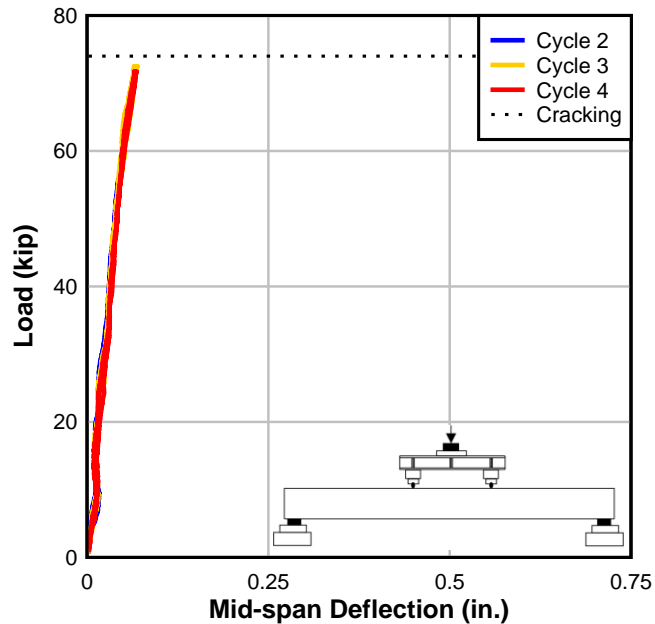


Figure 12-3. FC: Decompression load cycles

For the second load cycle (cycle 2), the specimen was loaded to 56 kip. In subsequent load cycles, the specimen was loaded to 72 kip. In all cases, the intent was to observe crack opening at the crack locations, which occurred at a load corresponding to a change in the strain readings of gages placed adjacent to the crack. No additional cracking of the specimen was observed during these load cycles.

Figure 12-4 shows the plot of strain versus applied load for the three decompression load cycles. In each of the load cycles, the strain gages S1 and S2 both gages change slope at an applied load of approximately 37 kip.

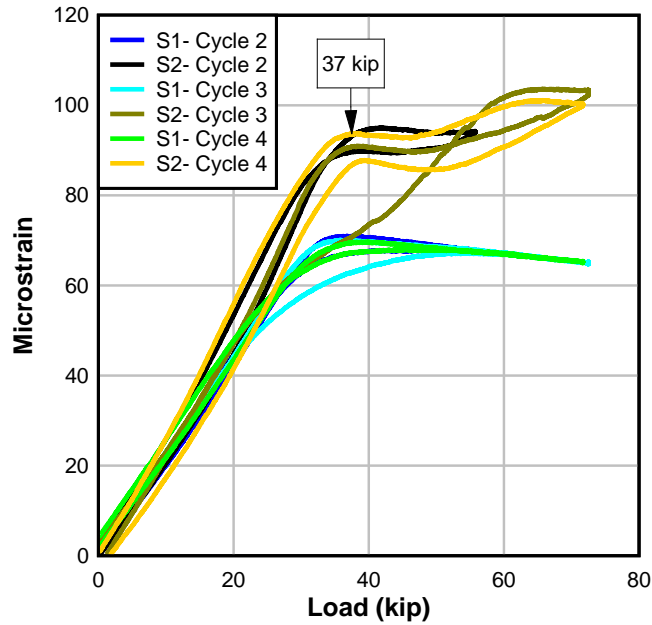


Figure 12-4. FC: Decompression strain readings

Fatigue Loading

FC was cycled at 2 Hz between 40 kip and 72 kip for 518,000 cycles. At the start of the test, this load range resulted in deflections from 0.034 in. to 0.071 in. Figure 12-5 shows a selection of load-unload cycles, recorded as the test progressed. The cycles shown were selected at intervals to demonstrate the degradation of the beam as the fatigue loading approached the end of the test.

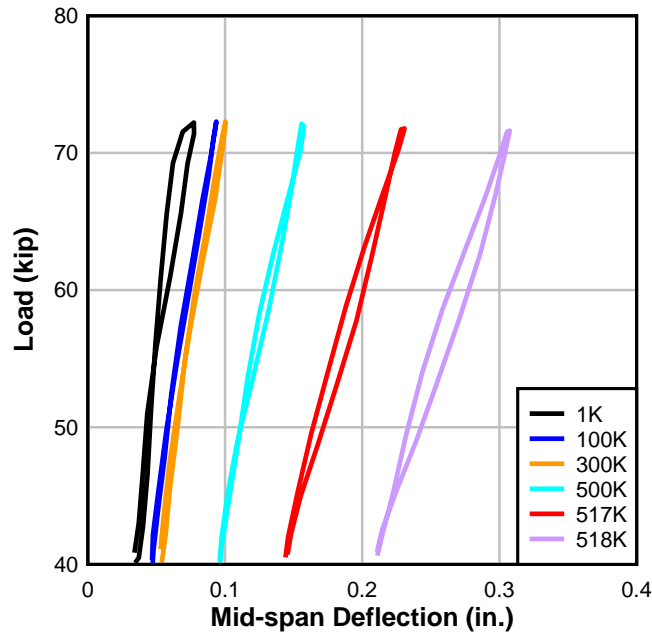


Figure 12-5. FC: Fatigue

Visual inspection of the specimen at approximately 80,000 cycles revealed the development of additional hairline cracks on one side of the beam. Cracks were observed at the bottom flange of the specimen at the location of each load point. The result of continued crack growth can be observed in the plot, which shows steady degradation of the specimen stiffness over time. Crack development continued throughout the test, as existing cracks lengthened and new cracks formed.

Between 517,000-518,000 cycles, the specimen began to rapidly degrade. Finally, at approximately 518,000 cycles, a severe change in specimen stiffness triggered the preset interlocks on the MTS, causing the cyclic load application to stop.

The beam was unloaded and inspected for damage. The primary crack was observed to remain open under beam self-weight. Flexural cracks in the constant moment region had propagated toward and had nearly reached the deck. Though degradation of the specimen was obvious by visual inspection and in the load-

displacement plots, the beam fatigue test was restarted. The specimen began to rapidly degrade, with increasing permanent deflections and after approximately 1000 cycles, the test was terminated to prevent instrumentation and equipment damage.

The strand stress ranges experienced in FC were predicted by calculation rather than direct measurement. The strand stress range was determined by the assumed strand strain due to effective prestress, the differential strain induced by loading (assuming the cracked moment of inertia) and the constitutive model of the prestressing strand, as determined with strand-in-air tests of the prestressing strand. The strand stress range at the crack location was approximately 20.5 ksi, or 7.6% of f_{pu} .

Ultimate Strength Test

Figure 12-6 shows the load-displacement plot of the ultimate strength test of FC. Before initiating the load test, the specimen had several cracks, which extended from bottom to top of the precast; the cracks did not appear to extend into the deck. These cracks were located within the constant moment region of the test set-up and can be seen in Figure 12-7(a).

As load was applied, the specimen exhibited early nonlinear behavior. Pre-existing cracks were observed to re-open, with the largest openings occurring in the cracks formed during static conditioning. Crack growth was only observed to occur in the pre-existing cracks; all cracks were located within the constant moment region.

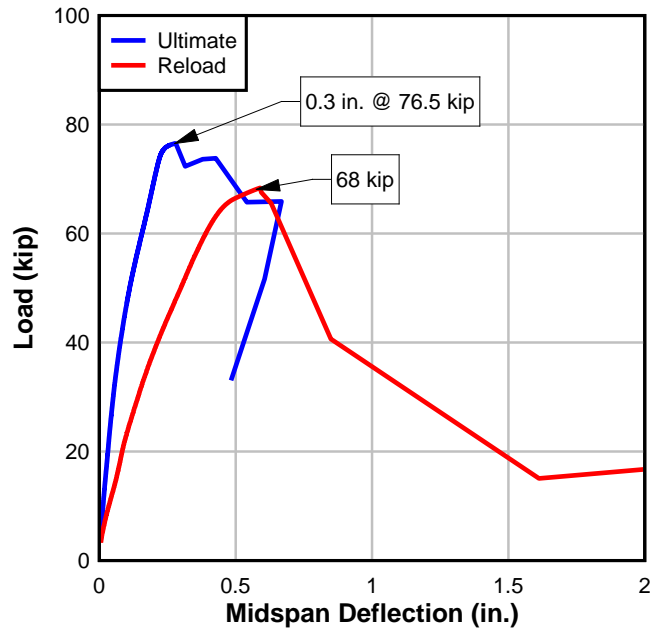


Figure 12-6. FC: Ultimate



(a)



(b)



(c)

Figure 12-7. FC crack progression at (a) no load; (b) ultimate (c) second loading

At approximately 77 kip, several loud reports were heard, indicating that prestressing wires had fractured. A load loss of more than 15 kip triggered the preset MTS interlock, and load application was halted. Ultimate load was approximately 77 kip and occurred at a beam midspan deflection of approximately 0.3 in. Upon removal of the load, the beam continued to carry its own self-weight (Figure 12-7(b)), but exhibited a permanent set of 0.25 in.

The interlocks were removed and the specimen was reloaded, achieving a maximum load of 68 kip. At 68 kip, more reports were heard and the specimen hit the floor. Figure 12-7(c) shows the specimen after termination of the second loading.

Ultimate strength was controlled by the rupture of prestressing strand, which was reached before compressive failure of the deck. The load-strain plots of gages on the top of the deck (Figure 12-8) confirms that strain was well below the ultimate compressive strain of 0.003 when peak load was reached, indicating that the deck crushing occurred as the specimen settled after strand rupture.

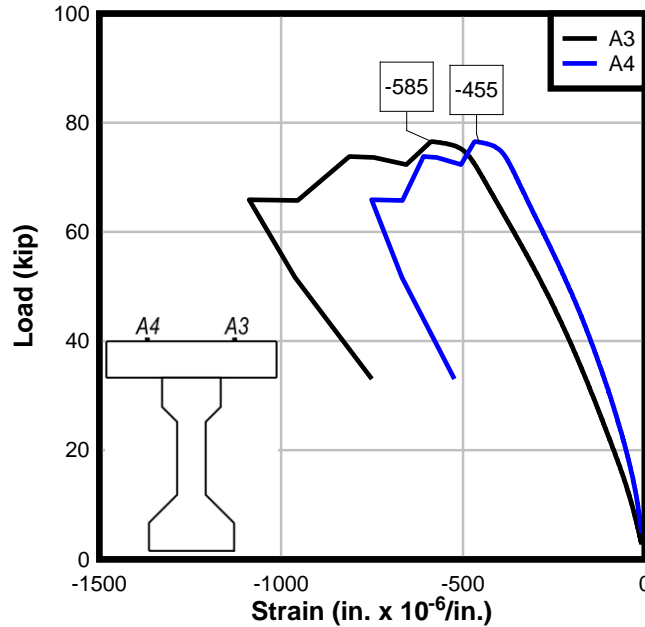


Figure 12-8. FC: Ultimate

Ruptured strands were inspected with a JEOL SEM-6400 scanning electron microscope for signs of fatigue wear. Many of the strands exhibited ductile failure surfaces such as shown in Figure 12-9(b). A number of strands, however, were noted to have varying degrees of fatigue cracking as shown in Figure 12-9(a). The crack initiation site (indicated by the arrow) is typically a point of contact either with an adjacent wire (center or outer wire) or reinforcing bar. Evidence of fatigue wear is noted in the beach-mark wear, characteristic of gradual crack formation during cyclic loading.

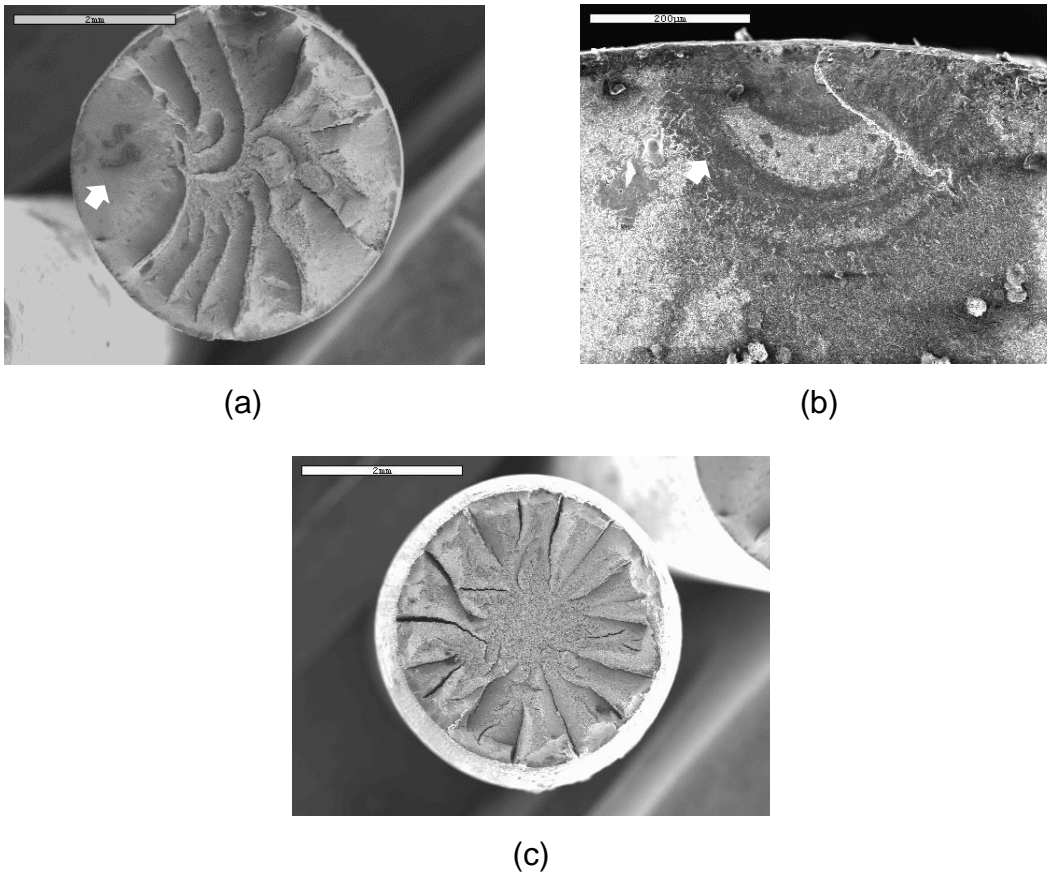


Figure 12-9. FC strand showing (a) fatigue (20X) (b) fatigue (200X) (c) yield (20X)

12.2 Specimen F1

F1 was the spliced specimen constructed of bonded segment 7b (from pour 1) and unbonded segment 6u (from pour 2), as shown in Figure 6-1.

Static Conditioning

Figure 12-10 shows the load-displacement plot of the initial static loading of F1. The trend is initially linear with some variation due to take-up in the test fixtures. At 54 kip, the load-displacement plot shows a slight change in slope, indicating a change in the specimen stiffness. This was confirmed by visual observation of the first 'crack' at 55 kip on one side of the beam (location shown in Figure 12-11). While the crack did

occur in the area of greatest bending stress, it is best described as an opening or separation of the bond at the closure interface. A similar opening was not observed on the opposite side of the beam.

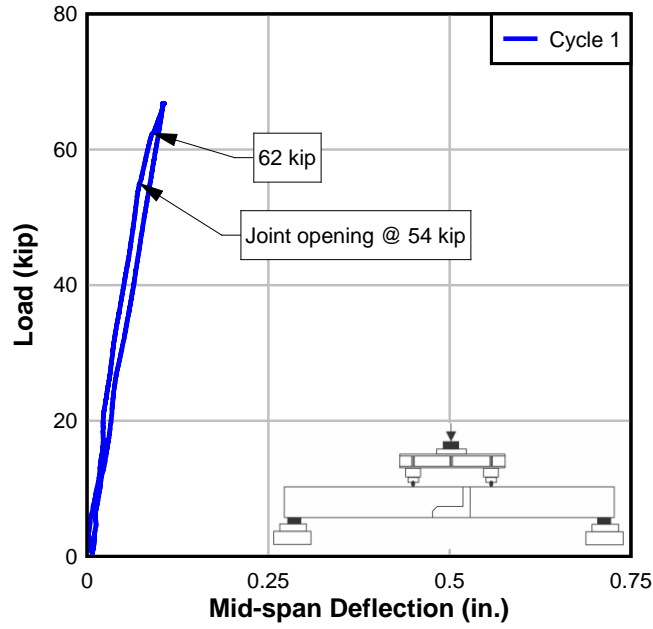


Figure 12-10. F1: Static conditioning

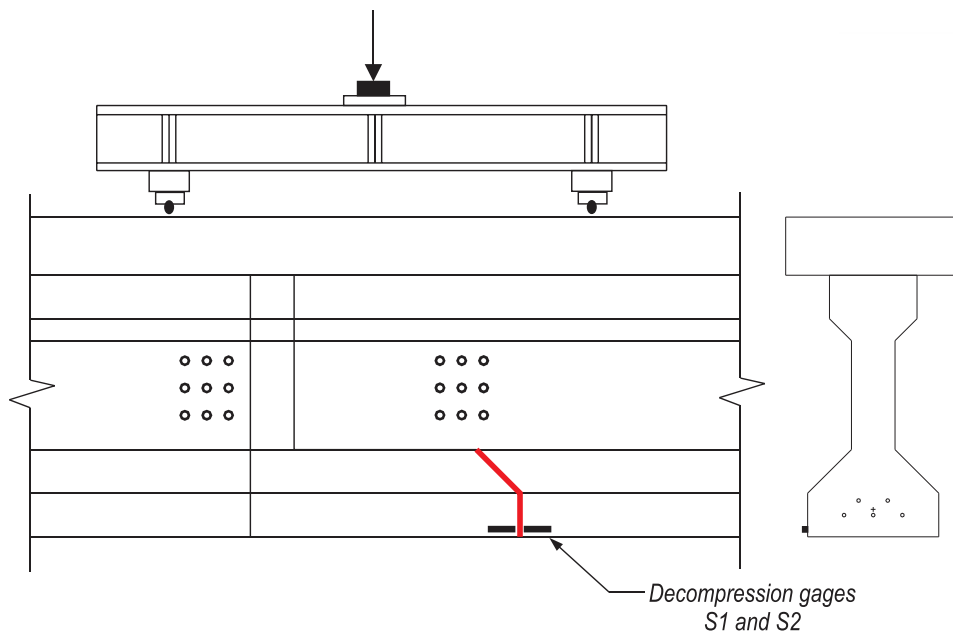


Figure 12-11. F1: Joint opening

Evidence of the joint opening can be seen in the plot of the coupler strain versus applied load (Figure 12-12). At 54 kip, the strain gages on the couplers located toward the opening side of the beam (GS1, GS3 and GS4) indicated a 'crack' had formed. The gages on the opposite side of the beam remained linear-elastic until 62 kip, indicating that the opening formed unsymmetrically as the load was increased and that—at 62 kip - the opening had propagated entirely through the width of the beam. Load application was continued until approximately 67 kip to develop the joint opening.

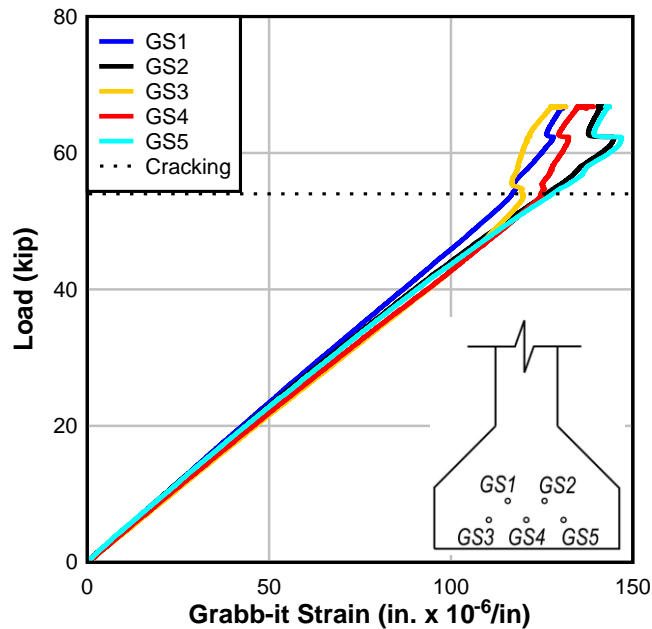


Figure 12-12. F1: Coupler strain

After precracking, decompression tests were performed on the joint opening of F1 to determine the effective prestress; gages were placed on either side of the first crack, as indicated in Figure 12-11. Figure 12-13 shows the load-displacement plots for the two decompression load cycles.

The specimen was loaded to 70 kip and 50 kip in successive load cycles. The intent was to observe crack opening at the first 'crack' location, which corresponded to a change in the strain readings of gages placed adjacent to the joint opening (gage locations shown in Figure 12-11). Figure 12-14 shows the strain vs. applied load plots for the second load cycle; strain data from the first load cycle was questionable and is not shown in the figure. The gages were replaced for cycle 3. Multiple load cycles were performed to ensure the repeatability of the strain readings used for determination of the effective prestress.

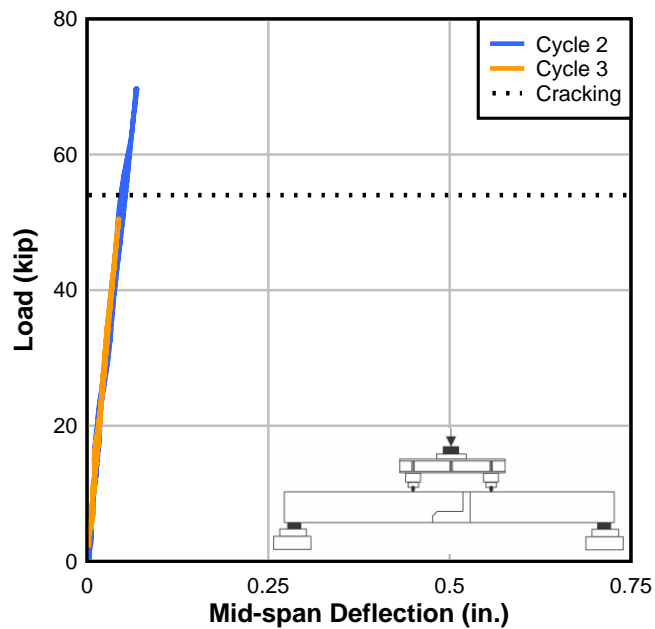


Figure 12-13. F1: Decompression load cycles

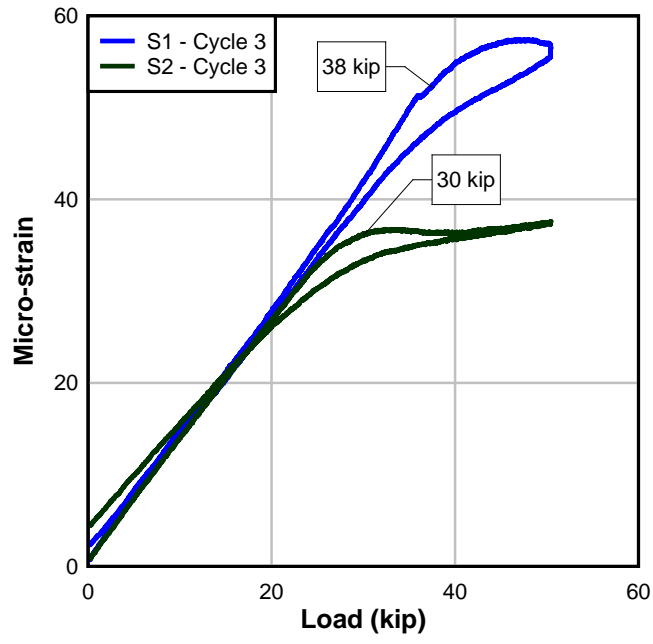


Figure 12-14. F1: Decompression strain readings

Fatigue Loading

F1 was cycled at 2 Hz between 40 kip and 54 kip for 2 million cycles. At the start of the fatigue loading, this applied load range resulted in deflections from 0.036 in. to 0.049 in. Figure 12-15 shows a selection of load-unload cycles, occurring at different times during the test. The cycles shown were selected at intervals to demonstrate the degradation of the specimen through the 2 million load cycles. At two million cycles, the specimen had only slightly decreased stiffness compared to the initial stiffness; at the end of the test, the specimen deflected between 0.054 in. and 0.070 in. at 40 kip and 54 kip, respectively.

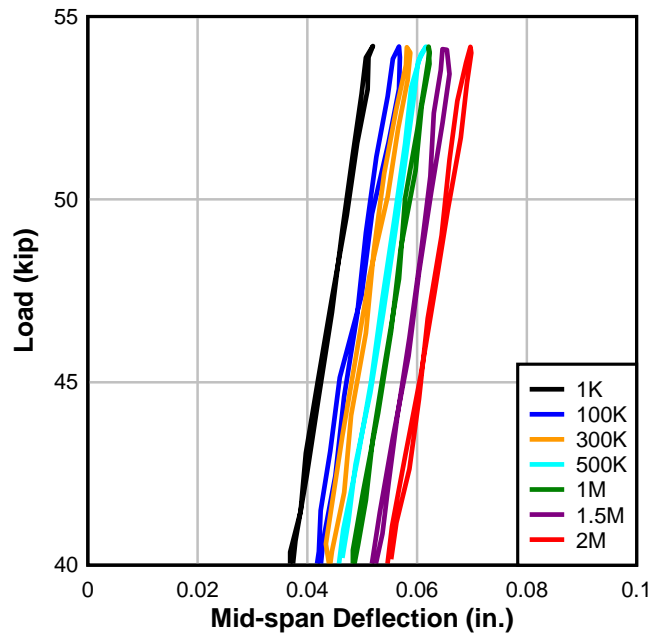


Figure 12-15. F1: Fatigue

The specimen was inspected after the 2 million cycles to evaluate crack growth; no additional cracking of the specimen was found. Propagation of the first crack was not observed.

The strand stress ranges experienced in F1 were predicted by calculation for later comparison with direct measurement. The strand stress range was determined by the assumed strand strain due to effective prestress, the differential strain induced by loading (assuming the cracked moment of inertia) and the constitutive model of the prestressing strand, as determined with strand-in-air tests of the prestressing strand. The strand stress range at the crack location was approximately 9 ksi, or 3.3% of f_{pu} .

Ultimate Strength Test

Figure 12-16 shows the load-displacement plot of the ultimate strength test of F1 after completion of fatigue cycling. The ultimate load test was performed in the four-point bending test setup (Figure 5-8) used to precrack the specimen. The plot indicates that as load was applied, the specimen exhibited linear-elastic behavior, until approximately 66 kip, when the vertical interface of the closure joint began to open. As loads were applied beyond 66 kip, the vertical opening propagated up toward the deck, allowing the specimen to significantly deflect under increasing load.

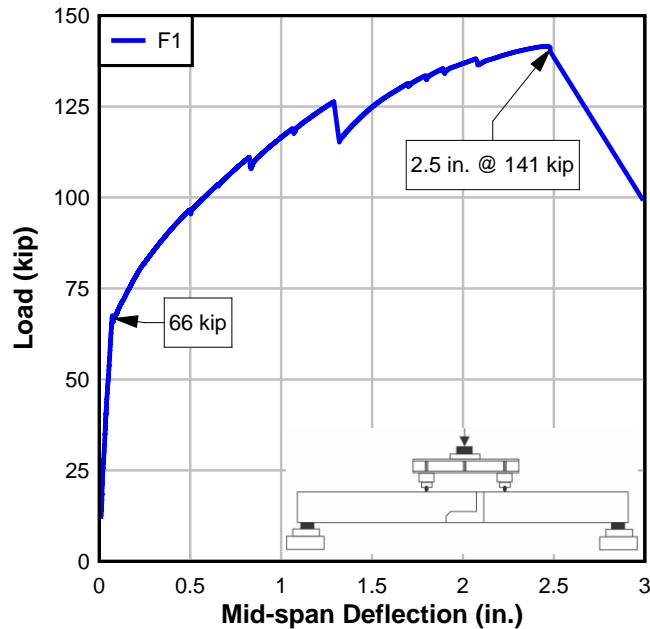
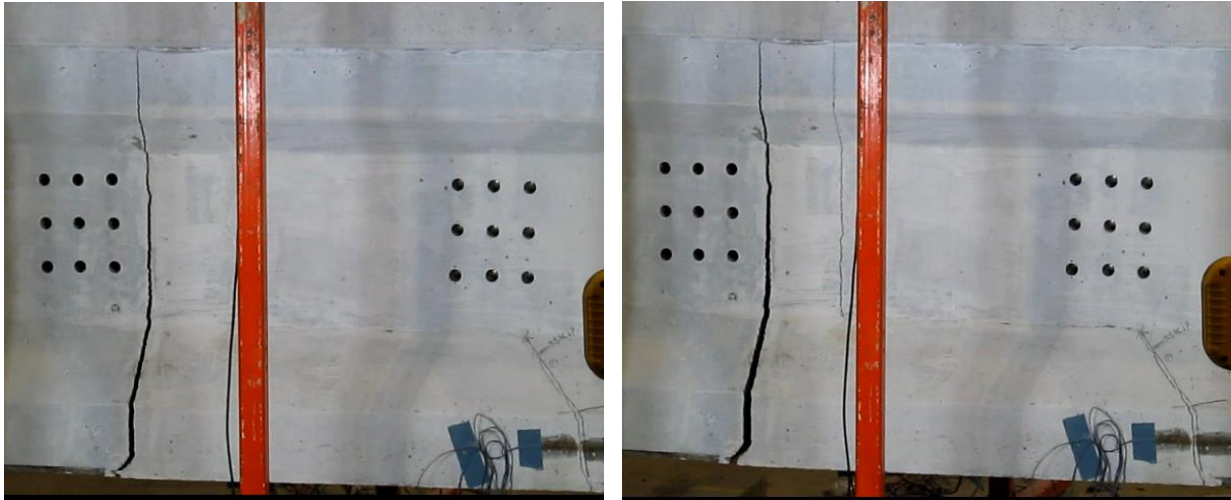


Figure 12-16. F1: Ultimate

Beyond 66 kip, the load-deflection plot reveals a change in specimen stiffness. At approximately 110 kip, several small load drops occurred, corresponding to audible cracking, which indicated the formation of additional cracks. At 125 kip, a significant load drop occurred accompanied by a loud report - likely due to prestressing strand wire or wires rupturing. A sudden opening of cracks around the outline of the closure pour occurred. Figure 12-17 shows the closure pour just before and just after this event. Several flexure-shear cracks were also observed to develop outside of the constant moment region.

At approximately 141 kip, the specimen reached ultimate load when strands ruptured near the first crack and the beam hit the floor. At failure, the principal flexural crack closed indicating that the couplers provided anchorage for the unbonded tendons to remain stressed. Figure 12-19 shows F1 after failure.



(a)

(b)

Figure 12-17. F1: Crack pattern at (a) 125 kip, prior to strand rupture (b) after load drop

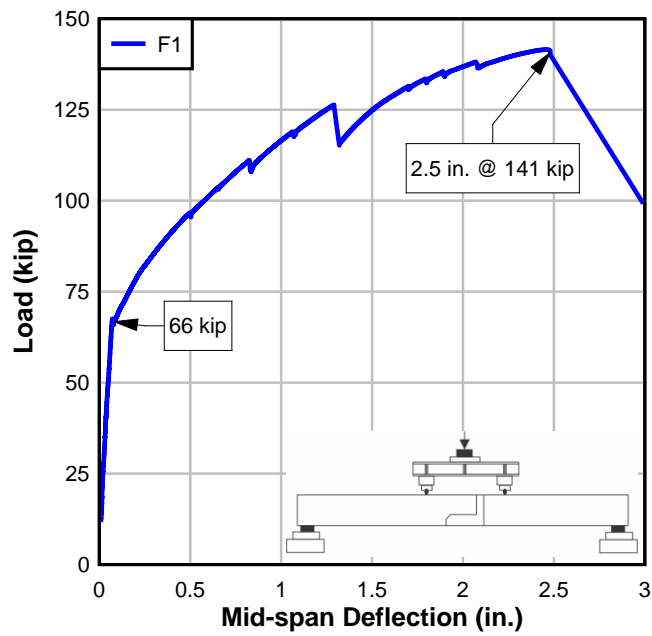


Figure 12-18. F1: Ultimate



Figure 12-19. F1: Post-failure

Fracture of the strand predicated compression failure in the deck. The maximum measured compressive strain in the constant moment region of the deck was approximately 0.0016 (Figure 12-20).

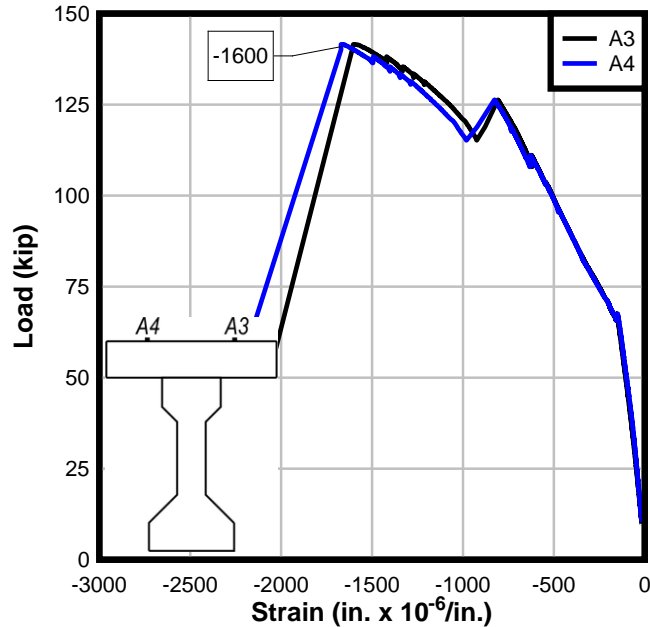


Figure 12-20. F1: Deck strain

Broken strands were inspected with a JEOL SEM-6400 scanning electron microscope for signs of fatigue wear. Inspection revealed most strands had yielded; some strands indicated fatigue wear. Figure 12-21 shows several examples of the strand failure surfaces. The crack initiation site (indicated by the arrow) was typically a point of contact either with an adjacent wire (center or outer wire) or reinforcing bar, though as shown in Figure 12-21(b), the crack initiation site in one of the top strands was within the coupler wedge, and occurred where the teeth bit into the strand. In post-failure inspection, it was observed that the wedge had improperly seated at this location (Figure 12-21(c)). This observed strand failure mode was unique to the F1 specimen. Additional discussion of observations is covered in Section 0.

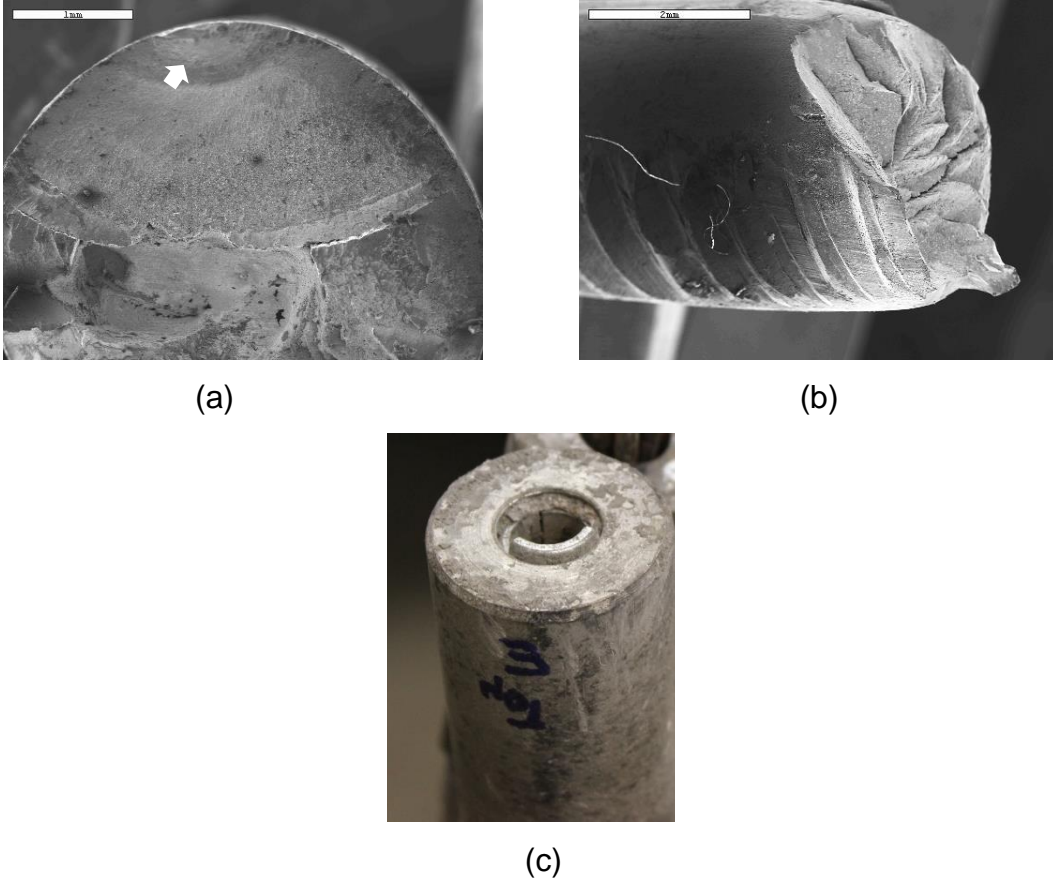


Figure 12-21. F1: (a) top strand showing fatigue (40X) (b) failure at teeth (20X)
(c) improper wedge seating

12.3 Specimen F2

F2 was the spliced specimen constructed of bonded segment 6b (from pour 1) and unbonded segment 8u (from pour 2), as shown in Figure 6-1.

Static Conditioning

Figure 12-22 shows the load-displacement plot of the initial static loading of F2. The trend is initially linear with some variation due to take-up in the test fixtures. A crack was visually observed at 63 kip which formed in the bonded precast segment and was associated with a change in slope of the load displacement plot. The crack was

within the constant moment region, but outside of the closure pour, extending underneath the beam and visible on both sides (Figure 12-23).

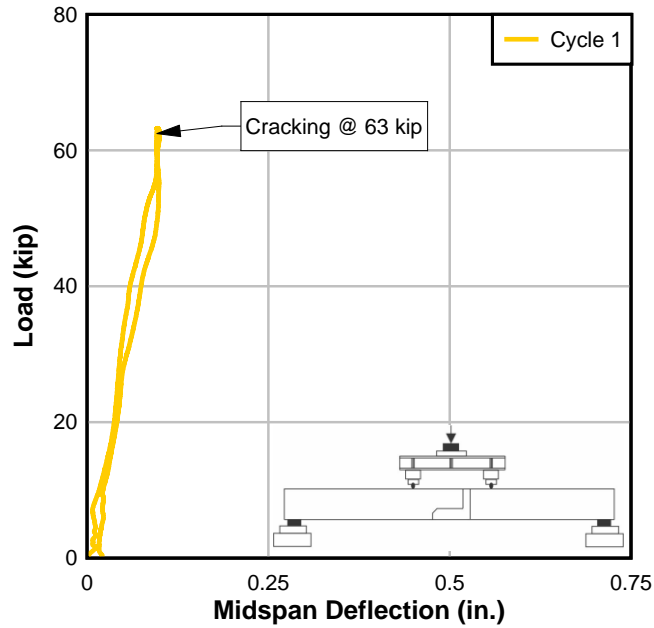


Figure 12-22. F2: Precrack

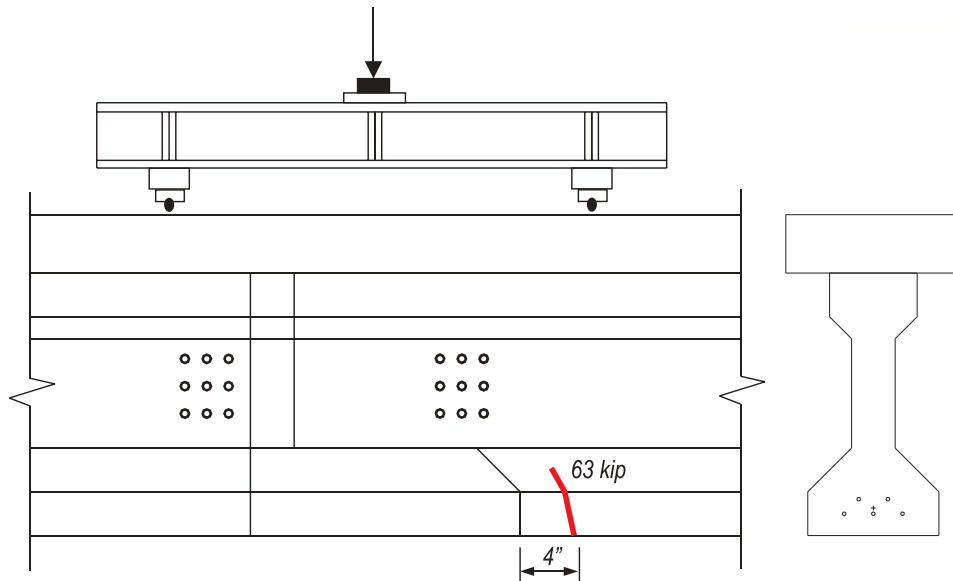


Figure 12-23. F2: First crack

Coupler strain (Figure 12-24) indicated possible micro-cracking prior to the observed cracking load. At 57 kip, the strain gages on the coupler located closest to the first crack (GS3) indicated cracking had initiated. At loads beyond 57 kip, the other gages (GS1,GS2, GS4, GS5) remained nearly linear-elastic up to cracking which occurred at 63 kip.

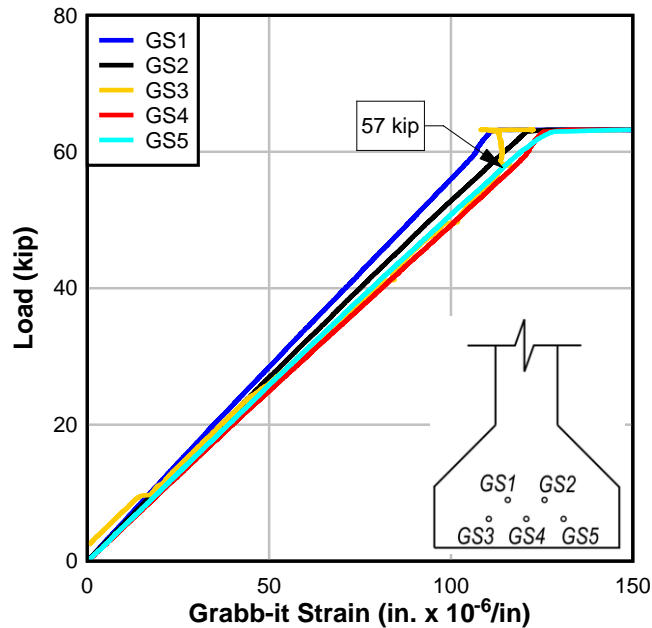


Figure 12-24. F2: Precrack coupler strain

After precracking, decompression tests were performed at two different cracks. Gage and crack locations are shown in Figure 12-25. Initially, three load cycles were applied with the strain gages mounted at the crack that formed in the bonded precast segment; the load-deflection plot is shown in Figure 12-26(a). Upon loading the specimen to 72 kip during the third static load cycle, a second crack formed at the specimen midspan, within the closure pour. Two strain gages were placed on either

side of this new crack and an additional three cycles were applied. The load-deflection plot for these three load cycles are shown in Figure 12-26(b).

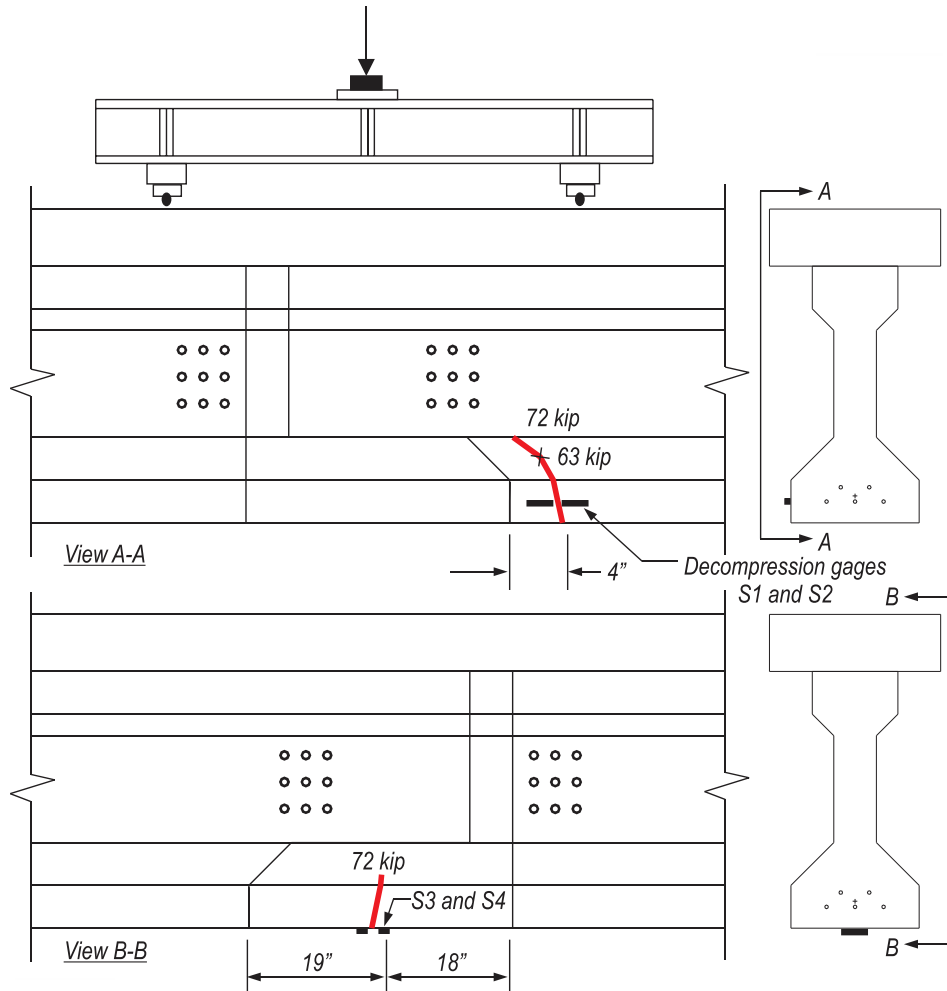


Figure 12-25. F2: First cracks with strain gages

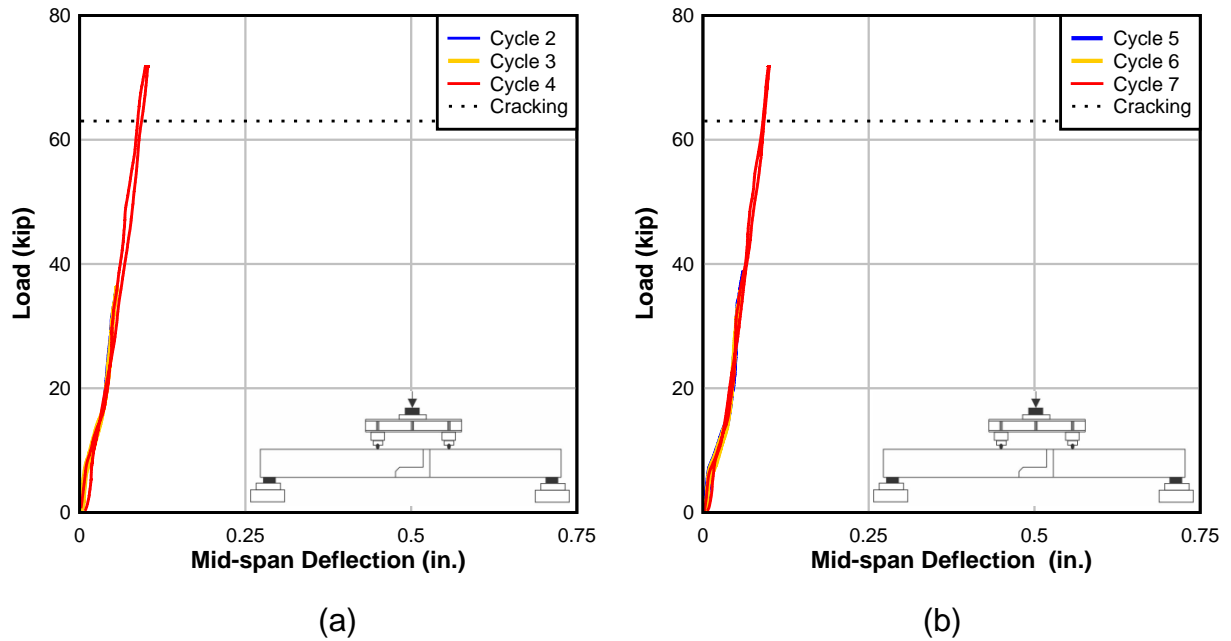
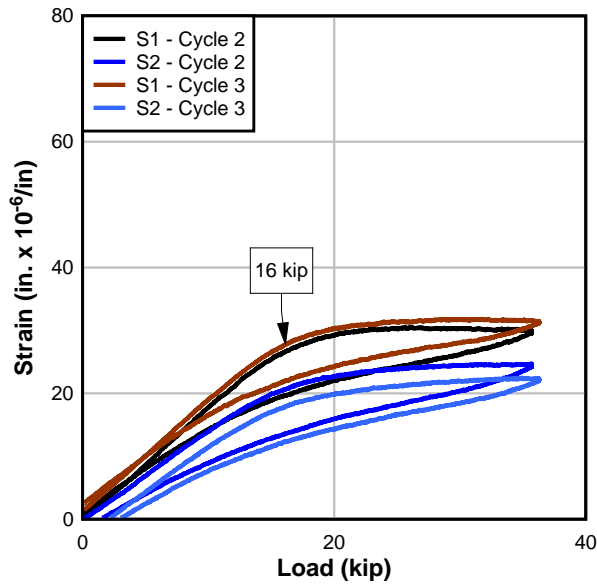
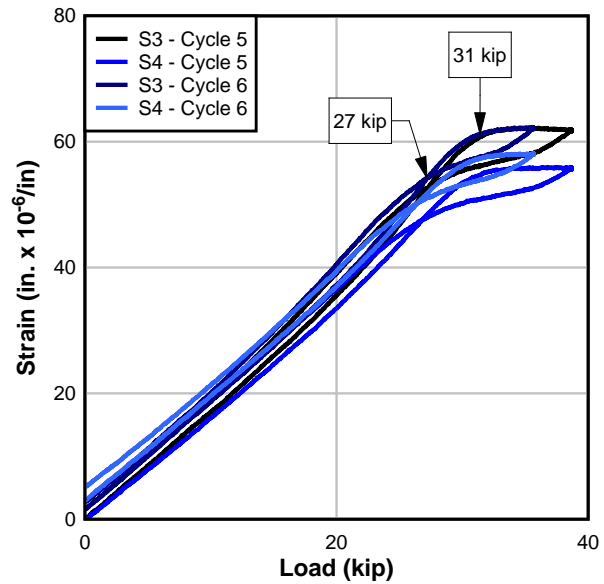


Figure 12-26. F2: Static load cycles (a) 2-4 and (b) 5-7

Figure 12-27(a) shows the strain for the first two cycles and Figure 12-27(b) shows the measured strain for cycles 5-6 which were taken on the second crack that formed. Because the cracks were located in different segments of the spliced specimen, different decompression moments were measured as indicated in the two plots.



(a) Cycles 1-2



(b) Cycles 4-5

Figure 12-27. F2: Decompression strain readings

Fatigue Loading

F2 was cycled at 2 Hz between 40 kip and 72 kip for 2 million cycles. At the start of the test, this load range resulted in midspan deflections from 0.035 in. to 0.056 in. Figure 12-28 shows a selection of load-unload cycles, occurring at different times during the test. The cycles shown were selected at intervals to demonstrate the degradation of the specimen over the 2 million load cycles. The bilinear slope of each cycle indicates that the section is exhibiting a change in stiffness, i.e., the crack was opening and closing. Between 1.5 million and 2 million cycles, the specimen exhibited a significant change in the cracked stiffness of the section, indicating degradation of the section due to fatigue. At the end of the test, the specimen deflected between 0.070 in. and 0.12 in. at 40 kip and 72 kip, respectively.

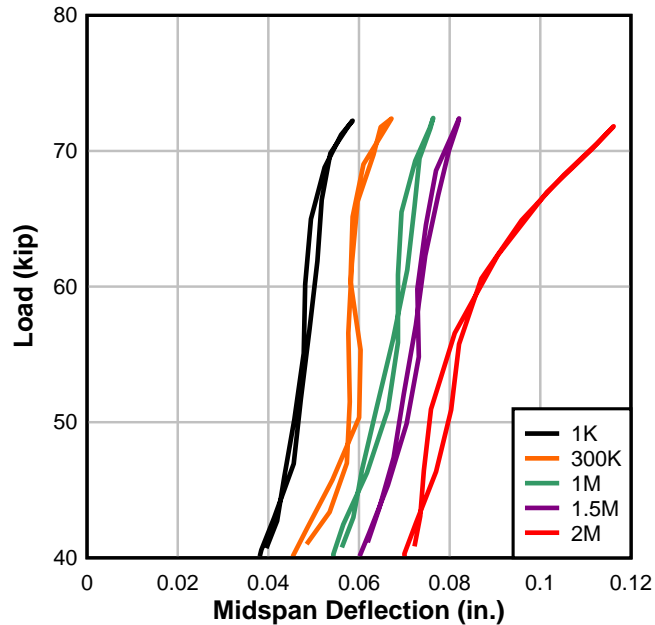


Figure 12-28. F2: Fatigue

The specimen was inspected throughout the 2 million cycles for crack propagation. Cracks were observed to grow, and new cracks formed. Most notably, an opening of the vertical interface of the closure pour was observed at approximately 1.7 million cycles. The cracks were marked as they propagated and can be seen in Figure 12-29.

The strand stress ranges experienced in F1 were predicted by calculation for later comparison with direct measurement. The strand stress range was determined by the assumed strand strain due to effective prestress, the differential strain induced by loading (assuming the cracked moment of inertia) and the constitutive model of the prestressing strand, as determined with strand-in-air tests of the prestressing strand. The strand stress range at the crack location was approximately 20.5 ksi, or 8% of f_{pu} ; this strand stress range matched that of the control specimen, FC.



Figure 12-29. F2: Cracking after 2 million cycles

Ultimate Strength Test

Figure 12-30 shows the load-displacement plot of the static failure of F2. The plot indicates that, as load was applied the specimen exhibited linear-elastic behavior until 76 kip, when a stiffness change occurred. As load was applied beyond 76 kip, most crack propagation occurred at the vertical crack at the closure pour interface. After the vertical crack reached the deck, propagation of the first crack—occurring in the bonded segment—began to occur more rapidly. This crack also propagated up toward the deck.

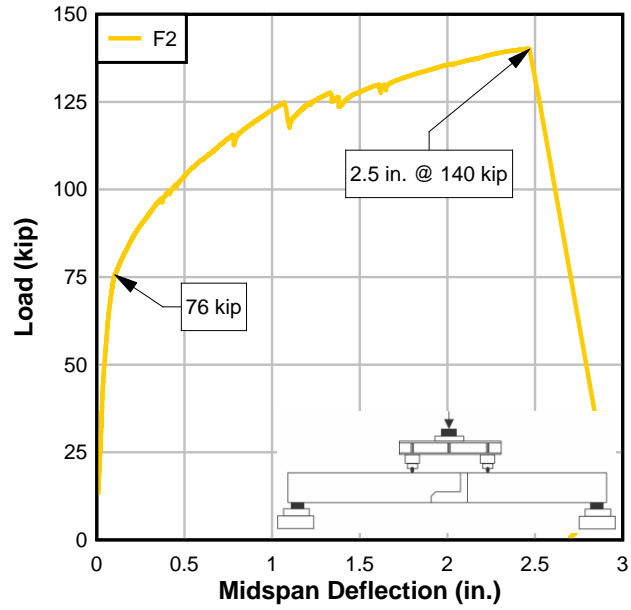
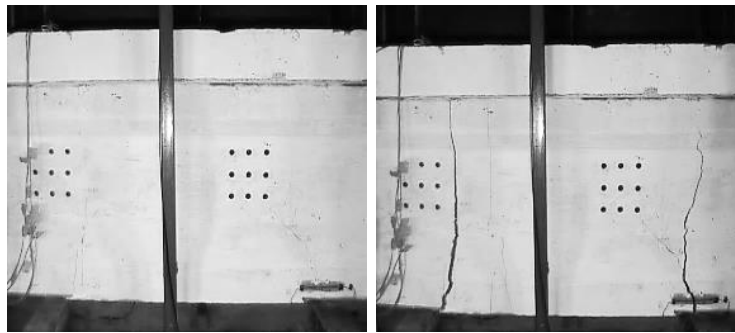


Figure 12-30. F2: Ultimate



(a)

(b)



(c)

Figure 12-31. F2 crack progression at (a) 70 kip, (b) 137 kip, and (c) ultimate (cracks marked)

From 115 to 130 kip, several sudden load drops occurred, indicating the formation of new cracks. These load drops were accompanied with audible and visible cracking of the concrete. A major load drop occurred at approximately 125 kip, though a new crack was not visually observed. A load drop at 130 kip corresponded to a shear-flexure crack observed in the bonded segment, outside of the constant moment region.

As ultimate load was approached, the opening at the vertical interface widened significantly—about 1 in. at the bottom - with an apparent hinge just below the deck (Figure 12-31). As load application continued, the significant flexural crack at the vertical interface of the closure pour (which had opened around 1.7 million fatigue cycles) propagated up to the deck and allowed the specimen to experience significant vertical deflection. The vertical interface crack opened more than 1 in., as the specimen approached the ultimate load. At approximately 140 kip of load and 2.5 in. of displacement, the specimen reached ultimate strength, and several strands fractured. Strand fracture was audible and was visually confirmed by inspection of the specimen post-failure.

Fracture of the strand predicated compression failure in the deck. The maximum measured compressive strain in the constant moment region of the deck was approximately 0.002 and occurred near a load point (Figure 12-32). Broken strands were inspected with a JEOL SEM-6400 scanning electron microscope for signs of fatigue wear. Inspection revealed that most strands had yielded; some strands indicated fatigue wear. All strands remained engaged by the couplers; strand rupture, if

it occurred, was located outside of the splice. Figure 12-33 shows the wire failures and several examples of the strand failure surfaces.

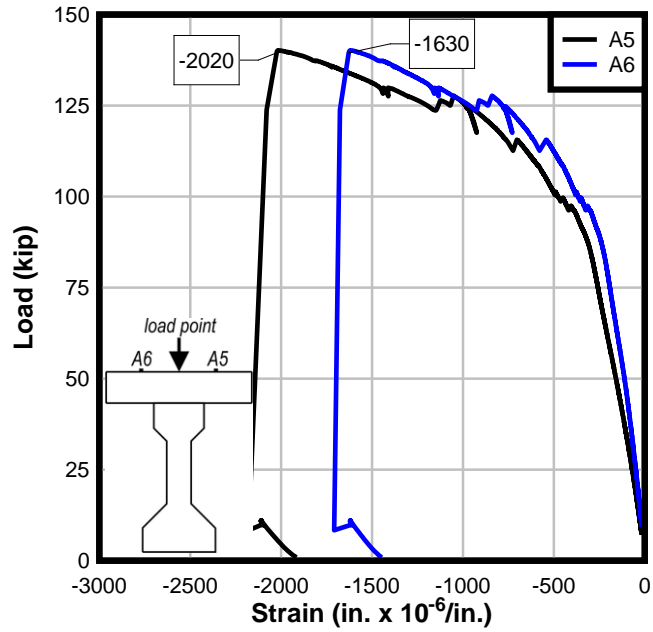


Figure 12-32. F2: Deck strain

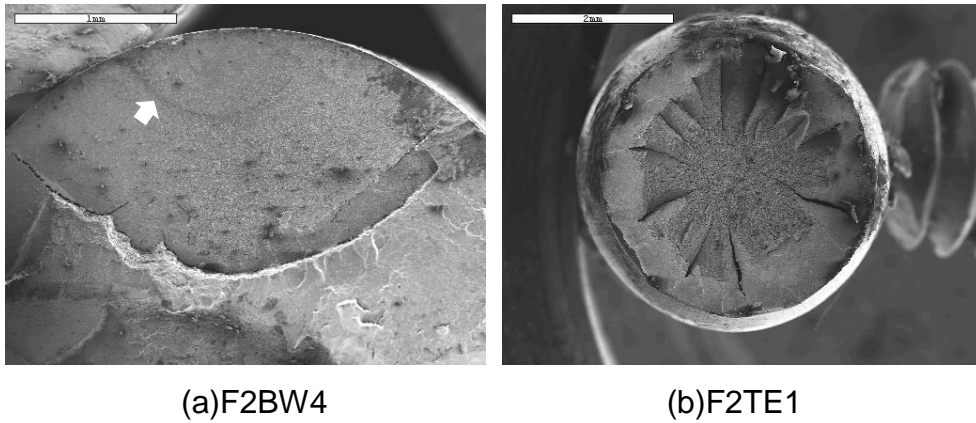


Figure 12-33. F2: (a) bottom strand showing fatigue (40X) (b) top strand yield (20X)

12.4 Discussion and Comparison of Behavior

Fatigue

Flexure cracks formed in different locations in spliced specimens F1 and F2. Fatigue of strands occurred near those locations during the cyclic loading, eventually becoming the location of strand rupture during the ultimate load test.

Figure 12-34 shows F1's first crack and bonding pattern, as it pertains to the discussion which follows.

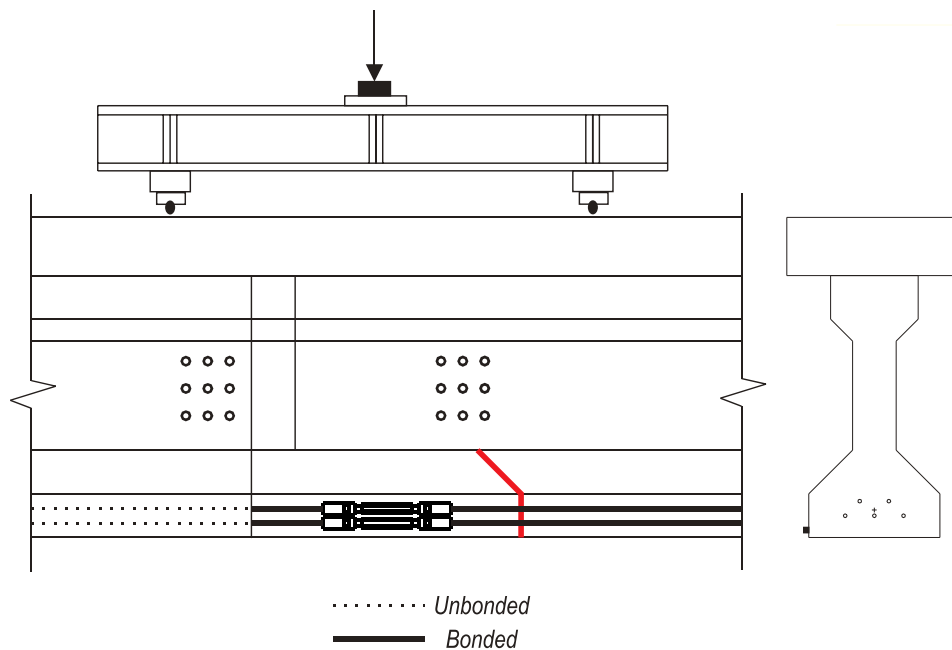


Figure 12-34. F1: Cracks at start of fatigue

F1's strands were fatigued at the notch interface. At this location, the strands were bonded to both the precast and the closure pour. Because the strand was bonded in this location, the free length of strand that was stressed during each cycle was only as wide as the crack, resulting in a high stress concentration on the strand. F1's theoretical strand stress range at the crack location (calculated based on cracked

moment of inertia and the differential strain induced by loading) was approximately 9 ksi, or 3.3% of f_{pu} . This is ultimately where the strands failed in the F1 specimen during the static ultimate load test. As shown in Figure 12-21(a), the strands exhibited fatigue wear at this location.

The fatigue stress range introduced on the strand is restricted to the crack length; this can also be seen in the load cell and coupler strain gage measurements. The load cells on F1 measured the strand stress range in the unbonded portion of the tendon; the coupler strain gages measured the coupler stress range (Table 12-1). (The measured stress range in the threaded portion of the coupler was calculated using the minimum net section of the threaded portion of the coupler.)

The load cells measure a strand stress range of only approximately 100 psi—a negligible measurement—indicating that the unbonded length of strand is not being fatigued during the load cycle. The magnitude of each measured strand stress range indicates that the length of strand between the coupler (which acts as an anchorage) and the chuck at the end of the unbonded length is not being fatigued by the cyclic loading. Meanwhile, the couplers—which are bonded within the closure pour—undergo a stress range comparable with that expected of an uncracked section subject to the applied cyclic load. The calculated stress range in the strands assuming gross section properties (an uncracked specimen) and a modulus of elasticity of 4776 ksi is approximately 0.88 ksi. The coupler strain gages measure a stress range of approximately 1 ksi. A VWSG located near the couplers at the approximate height of the strand centroid measured a similar stress range of approximately 0.78 ksi in the second load cycle. These measurements indicate that the couplers are experiencing a

stress range expected in an uncracked section—reaffirming the idea that the cyclic loading is only affecting/fatiguing the strands at the crack at the notch interface.

Table 12-1. F1: Stress ranges measured during fatigue cycling

| Strand | Cycle | Strand (ksi) | Coupler (ksi) |
|--------|-----------|--------------|---------------|
| 1 | 1,000 | n/a | 1.03 |
| | 2,000,000 | n/a | 0.975 |
| 2 | 1,000 | n/a | 1.07 |
| | 2,000,000 | n/a | 1.05 |
| 3 | 1,000 | 0.103 | 1.02 |
| | 2,000,000 | 0.127 | 1.00 |
| 4 | 1,000 | 0.151 | 1.06 |
| | 2,000,000 | 0.163 | 1.00 |
| 5 | 1,000 | 0.124 | 1.02 |
| | 2,000,000 | 0.113 | 1.06 |

Table 12-1 also shows stress ranges near the beginning and end of the fatigue load cycling. The stress range experienced by each strand is approximately the same (within a couple psi) at 1000 cycles as the stress range experienced at 2 million cycles. This was true for all strands in F1. Similarly, the coupler stress range at the start of the test was approximately equal to the stress range experienced at 2 million cycles. Because the stress range does not appear to change throughout the test, it can be inferred that the specimen’s moment of inertia was not affected by the fatigue test.

The occurrence of strand rupture at ultimate load—and the evidence of fatigue wear seen through the scanning electron microscope—indicates that the strand located at the initial crack must have experienced a significant stress range during the cyclic loading. The strand stress range at the crack location, based on calculations assuming a cracked moment of inertia, was approximately $0.03f_{pu}$.

Figure 12-35 shows F2’s first two cracks (which formed during static conditioning) and bonding pattern, as it pertains to the discussion which follows. F2’s

first crack - which was stressed by the fatigue loading - was located in the bonded precast segment, near where F1 was fatigued. At the start of the test, The F2 strand stress range at the first crack location, based on calculations assuming a cracked moment of inertia, was approximately $0.08f_{pu}$. A second crack (also shown in Figure 12-35) across the coupler exposed the coupler to fatigue loading.

Table 12-2 shows the stress ranges experienced by the F2 strands and the couplers at both the start of the test and the end of the test. Similar to the first crack of F1, F2's first crack creates a high stress concentration at the exposed bonded strand at that location. Because the second crack (Figure 12-35) exposes the couplers, all of the F2 couplers were subject to a higher stress range than the stress range predicted assuming an uncracked section (2 ksi). Neither crack exposed the unbonded length. Evidence of this can be seen in the load cell measurements: because the unbonded length was initially not subject to the cyclic load, the strand stress range measured by the load cells was very low—only a couple hundred psi.

Table 12-2. F2: Stress ranges measured during fatigue cycling

| Strand | Cycle | Strand (ksi) | Coupler (ksi) |
|--------|-----------|--------------|---------------|
| 1 | 1,000 | n/a | 5.96 |
| | 2,000,000 | n/a | 3.6 |
| 2 | 1,000 | n/a | 12.08 |
| | 2,000,000 | n/a | 8.36 |
| 3 | 1,000 | 0.543 | 2.84 |
| | 2,000,000 | 2.27 | 1.8 |
| 4 | 1,000 | 0.27 | 8.72 |
| | 2,000,000 | 1.15 | 3.8 |
| 5 | 1,000 | 0.459 | 15.7 |
| | 2,000,000 | 1.53 | 10.6 |

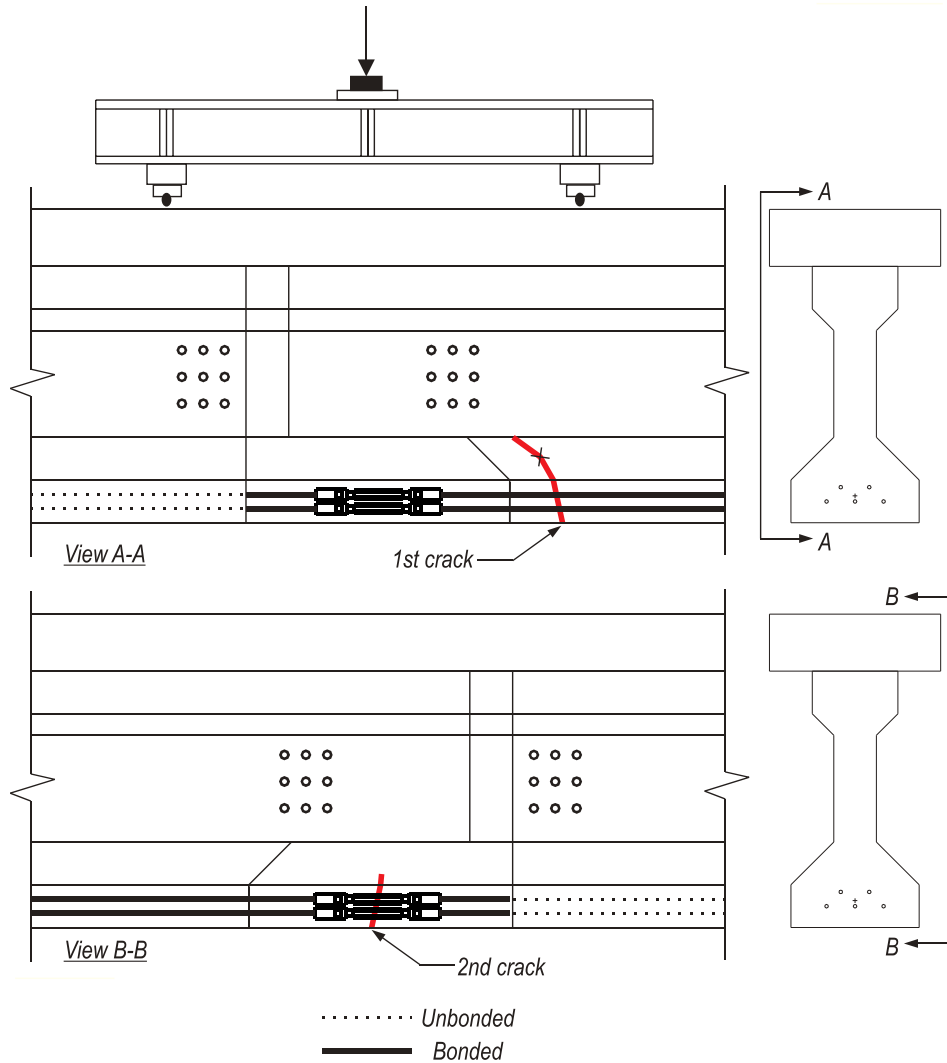


Figure 12-35. F2: Cracks at start of fatigue

Specimen F2 (subjected to a larger load range), in contrast to F1, did experience fatigue degradation over the duration of the fatigue test. Changes in the measured stress ranges in the strand and the coupler - as well as visually observed crack propagation - reveal the degradation of the specimen. From 1,000 cycles to 2 million cycles, the coupler data indicate a reduction in stress range for all five couplers. Two things are hypothesized: 1) that the coupler experienced strain relief, as cracks forming on either side of the coupler reduced the precompression of the concrete in the closure

pour, and 2) local debonding of the strand increased the gage length, reducing the strain. This is unlike what occurred in specimen F1, which did not develop additional cracking over the fatigue testing period. On the other hand, according to the load cell readings, the stress range experienced by each strand at 2 million cycles was greater than the stress range experienced at 1,000 cycles, indicating that some degradation of the specimen's cross-section/moment of inertia had occurred, increasing the strand stress range when the unbonded length was finally subjected to the fatigue loading. This is assumed to have occurred at approximately 1.7 million cycles, when an opening of the vertical interface was observed. Figure 12-36 shows the crack pattern at the end of the fatigue test, as well as the hypothesized debonding around the coupler.

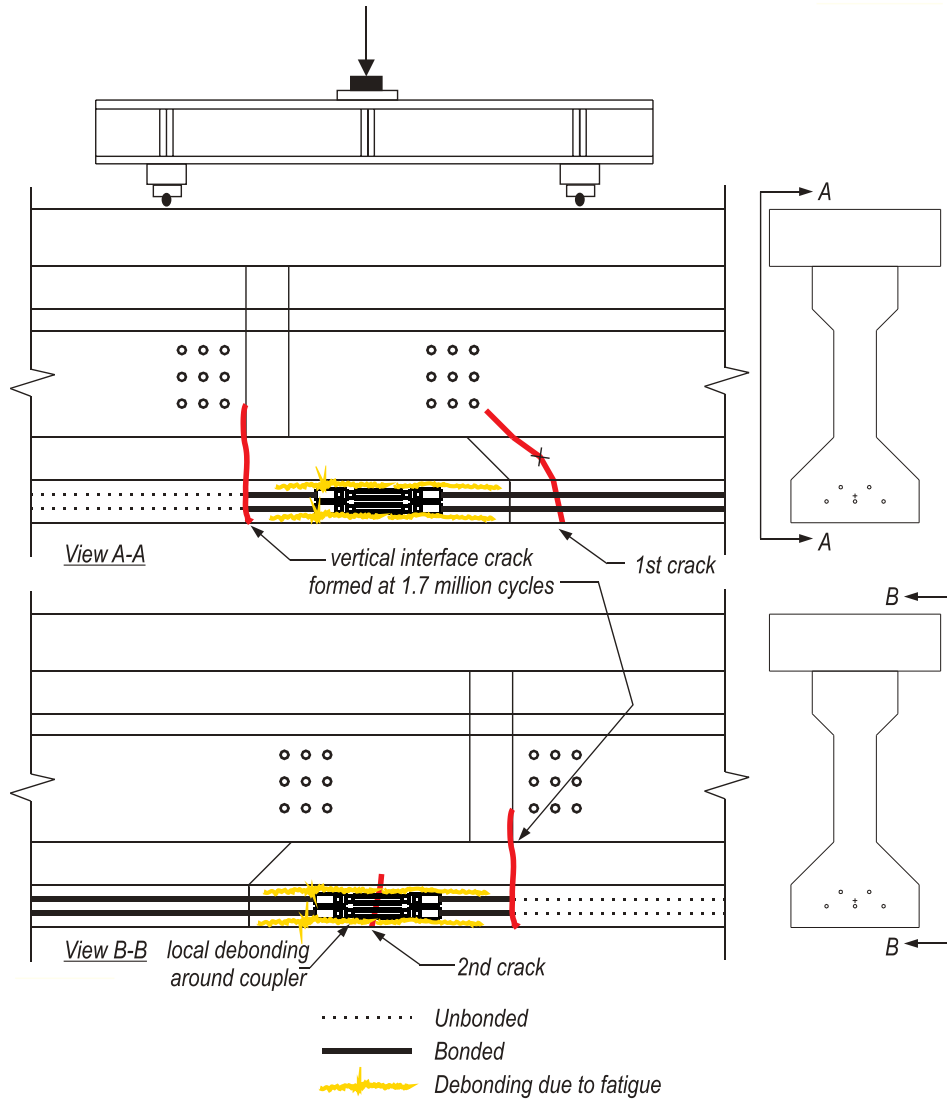


Figure 12-36. F2: Section degradation due to fatigue

Performance was also evaluated by comparison of the load-deflection plots over time. The plot shows the load vs. midspan deflection for the FC, F1 and F2 specimens at the start and end of fatigue loading. All fatigue tests were conducted in the same test set-up.

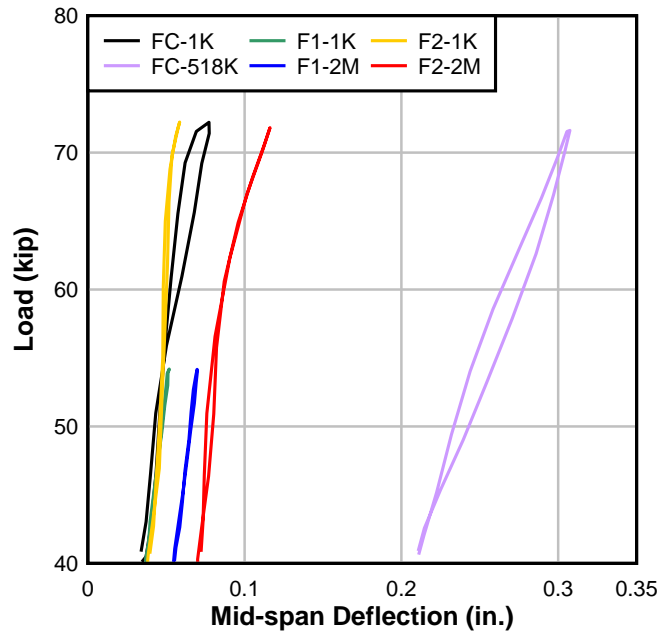


Figure 12-37. Fatigue: Deflection at start and end of tests

The plotted midspan deflection is the average of the two midspan laser displacement gage readings minus the average support displacement. At the start of each of the fatigue tests, the control FC and the two spliced specimens (F1 and F2) all have the same midspan displacement at 40 kip—approximately 0.04 in. The slopes are also nearly equivalent—indicating that each specimen had approximately the same stiffness at the start of the test.

The effect of the fatigue loading can be seen by comparing the 1,000th cycle vs. the last cycle. FC experiences a large loss of ductility and stiffness; that, combined with the sudden deflection change after 518,000 cycles and the reduced capacity when loaded to failure, indicates wires ruptured during fatigue cycling. The midspan deflection of the F1 specimen at 40 kip increases from 0.04 in. to 0.06 in., revealing a loss of ductility over time, though, because the slope does not change, the stiffness of the specimen has remained the same. On the other hand, the FC and F2 specimens

exhibit a loss of stiffness (increase in slope) and permanent set (loss of ductility; increase in magnitude of deflection at 40 kip) between the first thousand cycles and the last cycle. Both FC and F2 at their last cycle exhibit bilinear behavior, indicating that the specimen stiffness changes mid-load cycle.

Ultimate

Figure 12-41 shows the load-deflection plot for the ultimate load tests of all three fatigued specimens (FC, F1 and F2). For comparison, the AASHTO-LRFD predicted bonded (123 kip) and unbonded flexural capacities (114 kip) are also shown.

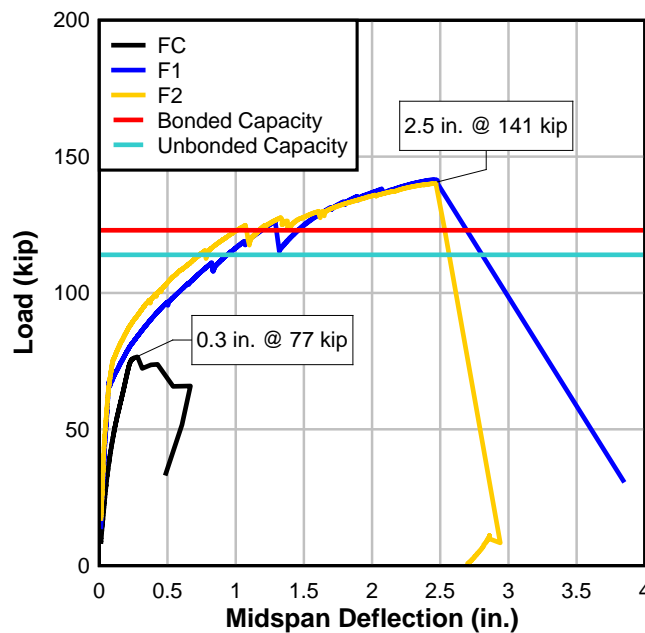


Figure 12-38. Post-fatigue failure: FC, F1 and F2

As can be seen in the plot, both spliced specimens had a higher tested capacity than the control specimen after fatigue loading. It is also worth noting that both specimens survived the 2 million fatigue load cycles, while the control specimen experienced rapid degradation around 518,000 cycles. The ultimate capacity of FC was

77 kip—only slightly larger than the high end of the load cycle (72 kip) and less than the capacity (both bonded and unbonded) as calculated per AASHTO. Meanwhile, both F1 and F2 exceeded the AASHTO-LRFD predicted capacity (both bonded and unbonded) and, though each had been subjected to different load ranges, developed the same ultimate capacity prior to failure. While F2 initially fatigued the strand at a bonded crack, it is hypothesized that bond degradation of the coupler (Figure 12-36) relieved the stress range on the strand in this area, thus allowing the specimen to reach a greater ultimate strength than FC. FC represented the worst case stress concentration of a bonded strand for a 40-72 kip load range. Though similar bond degradation around the coupler did not appear to occur in F1, the lower load range reduced the stress range on the bonded strand; the lower load range apparently did not affect the ultimate capacity of F1. Figure 12-39 shows a comparison of the tested fatigue to the AASHTO-LRFD calculated. The left y-axis compares the applied moment at ultimate to the AASHTO-LRFD bonded design capacity; the right y-axis compares the applied moment at ultimate to the AASHTO-LRFD unbonded design capacity.

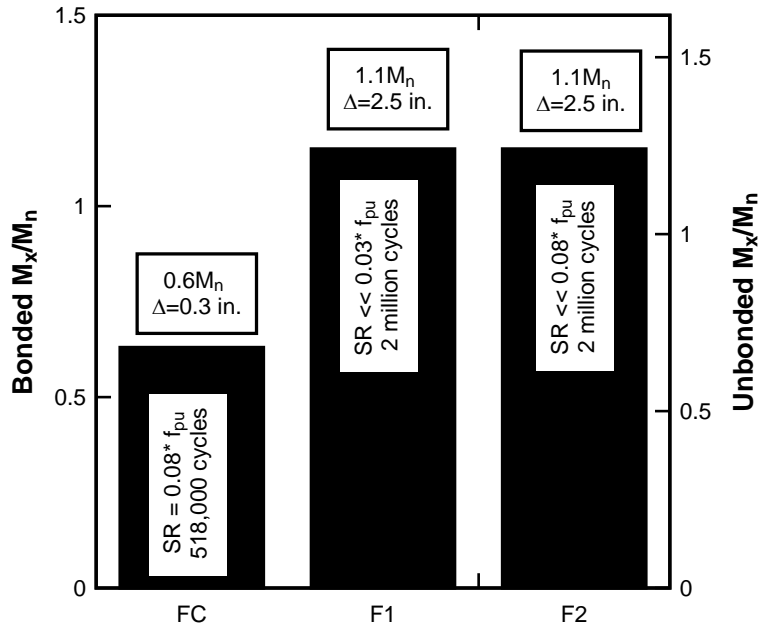


Figure 12-39. AASHTO: FC, F1, and F2

Figure 12-39 also presents the strand stress range due to fatigue loading, calculated based on cracked section properties. For bonded specimen FC, the strand stress range was approximately 8% of f_{pu} . If the spliced specimens had been bonded, the applied stress range was 3% and 8% on F1 and F2, respectively. Due to the lack of bond, the strand stress range was actually much less than either of these calculated values.

Fatigue performance of the spliced specimens FC, F1, and F2 was also evaluated through comparison with the static failure tests. The fatigued specimens were compared against the non-fatigued specimens to evaluate the effect of fatigue loading on the ultimate capacity and deflection at failure. Figure 12-40 shows the load-displacement plot for XC and FC, including the AASHTO-LRFD predicted bonded and unbonded capacity. Figure 12-41 compares the ultimate strength test of the non-fatigued spliced specimen X1 to those of the two fatigued specimens F1 and F2.

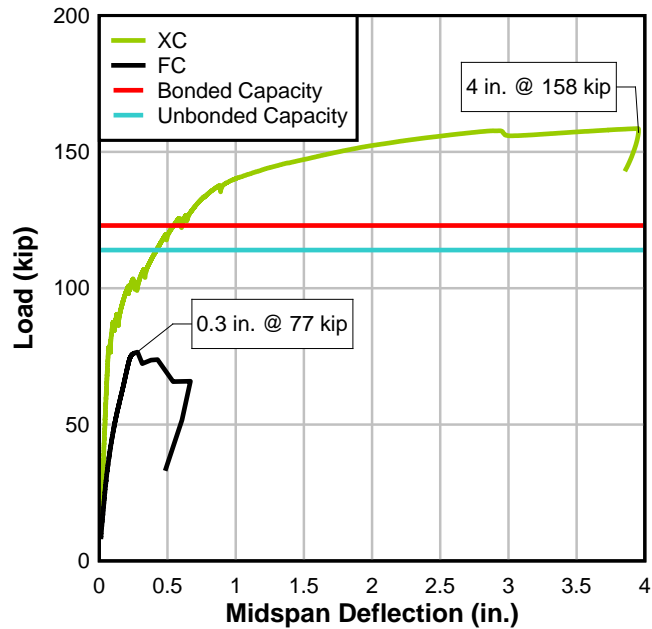


Figure 12-40. Static vs. Post-fatigue failure: Control specimens

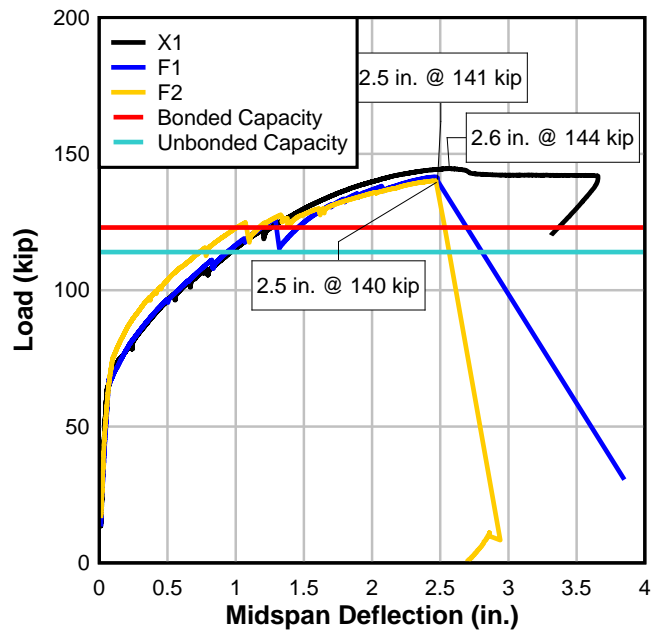


Figure 12-41. Static vs. Post-fatigue failure: Spliced specimens

As shown in Figure 12-40, the ultimate capacity of FC was affected by the fatigue loading, as expected due to the rupture of strand at 518,000 cycles. Both the ductility

and the ultimate load were significantly reduced. FC had an ultimate capacity of approximately 77 kip—nearly 50% less capacity than XC. X1 had only a slightly higher ultimate load (144 kip) and midspan deflection (2.6 in.) at failure than that of the F1 and F2, which both failed at approximately 140 kip and 2.5 in. of deflection. Additionally, the spliced specimens reserve capacity—the specimen’s ability to continue carrying load after ultimate—appears to have been affected by the fatigue. After achieving ultimate load, X1 lost some load (approximately 3 kip) but continued to deflect under a load equal to 98% of the ultimate load capacity achieving a maximum deflection of 3.7 in. before the concrete crushed. Conversely, the failures of the fatigued specimens F1 and F2 were sudden and caused by strand rupture; neither spliced specimen carried additional load after ultimate. Furthermore, less than 10% of the ultimate strength remained in load capacity after the peak load was reached. The flexural strength of the spliced beams was not affected by fatigue; the failure mode, however, became brittle and sudden.

Comparison of the ductility ratio μ_{cr} , (calculated as the ratio of the mid-span deflection at ultimate to the deflection at cracking) reveals the effect of fatigue on the specimens’ failure mode (Table 12-3). The FC ductility ratio μ_{cr} , calculated as the ratio of the deflection at ultimate to the deflection at cracking, was 4 versus XC, which had a μ_{cr} ratio of 60.

Table 12-3. Ductility ratios

| Specimen | Ductility Ratio, $\mu_{cr} = \Delta_{ult}/\Delta_{cr}$ |
|-------------|---|
| XC (static) | 60 |
| X1 (static) | 43 |
| FC | 4 |
| F1 | 35 |
| F2 | 25 |

The ductility ratio similarly reveals the effect of fatigue on the spliced specimens. Once again, the ratio is calculated as the mid-span deflection at ultimate to the deflection at cracking, where cracking was either when the specimen cracked or a joint opened (creating a change in specimen stiffness). X1, F1 and F2 have a ductility ratio of 43, 35 and 25, respectively: while the ultimate flexural strengths of the spliced specimens appear to have been unaffected by the 2 million cycles of fatigue loading, the ductility was affected. Additionally, the general trend appears to be that the specimen ductility is more affected by the higher applied stress range.

The location of the primary crack affected the strand rupture and ductility at ultimate. In the ultimate load test of F1, the crack at the notch interface became the location of strand rupture at ultimate load. In post-failure inspection of F1, it was observed that a single top row strand had slipped completely from the wedge. Post-failure inspection revealed that the wedge had improperly seated (Figure 12-43). All but one wire of the other top row strand remained engaged by the coupler; this strand ruptured at the notch crack. The bottom row of strands ruptured at the crack location (Figure 12-42).



Figure 12-42. F1: Post-failure



Figure 12-43. F1: Wedge seating

F2's strand ruptured at the primary crack location shown in Figure 12-23, approximately 14 in. away from a Grabb-it face. The ruptured strands are seen in Figure 12-44. It can be observed in the picture that the strand rupture has occurred at a rebar location; inspection of the strand found evidence of fretting between the rebar and the bottom row prestressing strand initiated the fatigue wear at this location (Figure 12-45).



Figure 12-44. F2: Post-failure

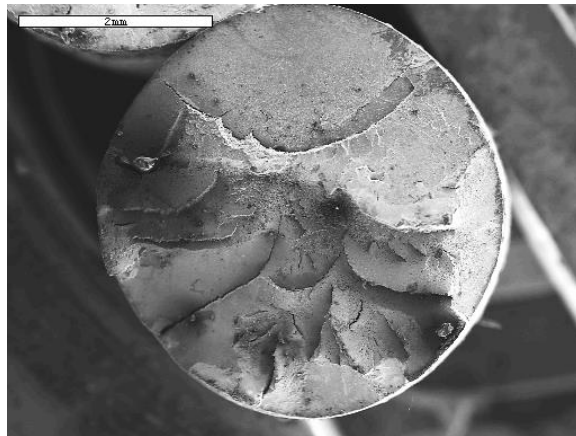


Figure 12-45. F2: Fatigue wear

In both spliced specimens, the Grabb-its acted effectively as anchorages post-failure, maintaining the prestress force in the unbonded strand. The effectiveness of the Grabb-its as anchorages will now be discussed.

Figure 12-46 shows the applied load versus the strand load for specimen F1. The plot shows that, after approximately 67 kip, the prestressing strands begin to take

on additional load, indicating that the precompression has been overcome. At 126 kip, a drop in the applied load corresponds with the sudden deflection shown in Figure 12-16 and a loud report, indicated strand rupture. At ultimate load, the load cells indicated a strand force reduction of approximately 5 kip, indicating that the some but not all of the prestress force had been lost.

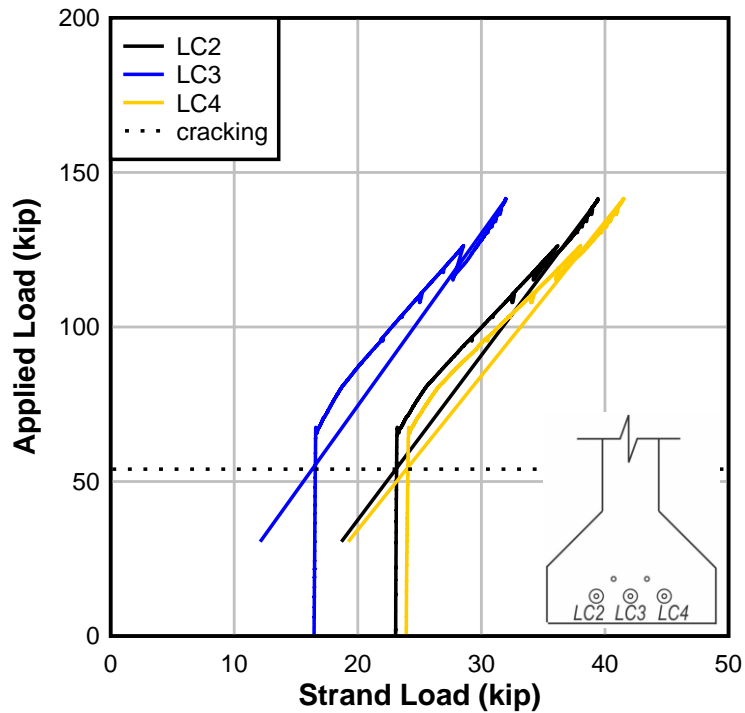


Figure 12-46. F1: Load cells

Figure 12-47 shows the applied load versus the strand load for F2. At ultimate load, the load cells indicated a strand force reduction of approximately 8 kip, indicating that the some but not all of the prestress force had been lost.

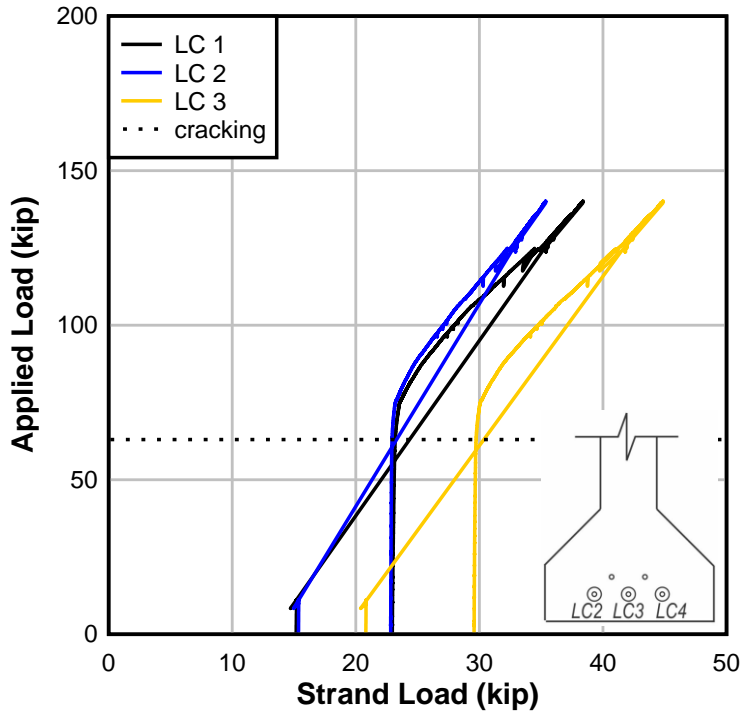


Figure 12-47. F2: Load cells

Both specimens F1 and F2's load cells indicate partial stress relief of the unbonded strand after ultimate failure of the specimen. In both specimens, when the strand ruptured at ultimate load, the large vertical crack between closure pour concrete and the unbonded segment slammed shut, completely closing the joint opening at the vertical interface of the closure pour (as seen in Figure 12-31). Because the failure of both specimens occurs at the fatigued crack near the bonded segment, the unbonded segment and closure pour remain prestressed, due to the anchorage action of the coupler.

CHAPTER 13
DISCUSSION AND OBSERVATIONS

Table 13-1 presents the applied moments, calculated cracking moment, and bottom fiber stress states for each specimen that experienced flexural cracking. Though specimens SC and SB were tested to examine shear response, their exhibited behavior was principally flexural in nature, and so they are presented here. The applied moment was calculated based on the applied load at cracking plus the self-weight moment. The calculated cracking moment was calculated assuming cracking to occur at a bottom fiber tensile stress of $7.5\sqrt{f'_c}$, assuming the effective prestress to be that measured by the load cells minus the prestress losses measured by the VWSG. The bottom fiber tensile stress was also calculated based on the measured effective prestress. The ratio of the applied moment to the predicted cracking moment is given for reference.

Table 13-1. Flexural cracking behavior

| Specimen | Crack Type | Calculated M_{cr} (kip-ft) | Applied M (kip-ft) | $f_{bot}/\sqrt{f'_c}$ per LC, ksi | Applied M / Calculated M_{cr} |
|----------|--------------|------------------------------|--------------------|-----------------------------------|---------------------------------|
| XC | Flexure | 542 | 412 | 3.8 | 0.76 |
| X1 | Flexure/Bond | 538 | 351 | 2.2 | 0.65 |
| SC | Flexure | 629 | 507 | 4.1 | 0.81 |
| SB | Flexure | 617 | 476 | 3.6 | 0.77 |
| FC | Flexure | 534 | 396 | 3.6 | 0.74 |
| F1 | Flexure/Bond | 489 | 305 | 2.3 | 0.62 |
| F2 | Flexure | 541 | 343 389 | 1.9 3.2 | 0.63 0.72 |

Although no reason was identified for the low cracking moment, each specimen was found to crack at a lower load than anticipated. In general, the ratio of the applied moment (including self-weight moment) to the cracking moment was 0.6-0.8.

Table 13-2 presents the applied shear at cracking and the calculated web-shear resistance (AASHTO-LRFD 5.8.4.4.3) for both specimens. Specimens SU and SU2 exhibited shear behavior, with the first crack developing as a web shear crack. The applied shear was calculated using both the jack load and the shear due to the specimen self-weight. The calculated web-shear resistance was calculated assuming the effective prestress to be that measured by the load cells minus the prestress losses measured by the VWSG. It was also assumed that the concrete strength was equal to the specified 8500 psi. The ratio of the applied shear to the predicted cracking shear is given for reference.

Table 13-2. Web shear cracking

| Specimen | Crack Type | V_{cw} (kip) | Applied V (kip) | Applied V/V_{cw} |
|----------|------------|-------------------|--------------------|--------------------|
| SU | Web Shear | 77 | 59 | 0.77 |
| SU2 | Web Shear | 78 | 58 | 0.74 |

Other post-ultimate test observations pertaining to serviceability, ultimate strength, and construction techniques are commented on in the following sections.

13.1 Closure Pour Observations

Several observations of note were made concerning the closure pour, including:

- The use of epoxy improved the closure pour bond. Epoxy was not used in the first three splice assemblies (X1, SB, SU). Figure 13-1(a) shows the closure after demolition; it can be seen that—for the most part - the closure pour concrete broke away cleanly at the joint. In later specimens (SU2, F1 and F2), an epoxy (Master Builders Concrete Liquid LPL) was used to improve the bond. In post-test inspections of these specimens, the failure planes occurred across the

different pours, indicating that the epoxy had some beneficial effect. An epoxied joint can be seen in Figure 13-1(b).

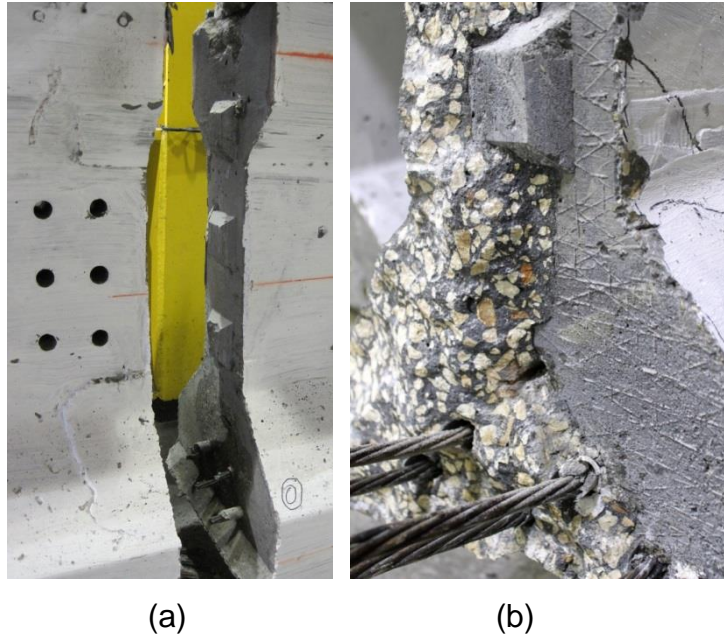


Figure 13-1. Bond at vertical interface (a) X1 and (b) F2

- Observed evidence of intrusion of the closure pour concrete into the unbonded segment's PVC sheathing. This indicates that the self-consolidating concrete used in the closure pour was sufficiently flowable to penetrate and potentially affect the behavior of the unbonded length.



Figure 13-2. F2: Concrete intruding into unbonded length

- Self-consolidating concrete worked well, with enough flowability to form a voidless pour, so long as the form sides were vibrated using a hand-held vibrator. In one splice assembly (SB), hand-held vibrators were not used, resulting in a void at the reentrant corner of the splice region (Figure 13-3). The void was repaired prior to testing.



Figure 13-3. SB: Void at reentrant corner

- Shear keys were observed to be effective when the specimen was tested in a high V/M ratio set-up with the unbonded length under the load point (both tests SU and SU2).



(a)



(b)

Figure 13-4. Shear keys (a) SU and (b) SU2

- Water transmission was observed along the bonded length of strand approximately ten minutes after the completion of the closure pour. Water was observed to wick the entire bonded length (approximately 13.5 ft) of every strand. Figure 13-5 shows the end of the bonded precast segment prior to the pour, at 35 minutes, and at 45 minutes after the pour of SU.

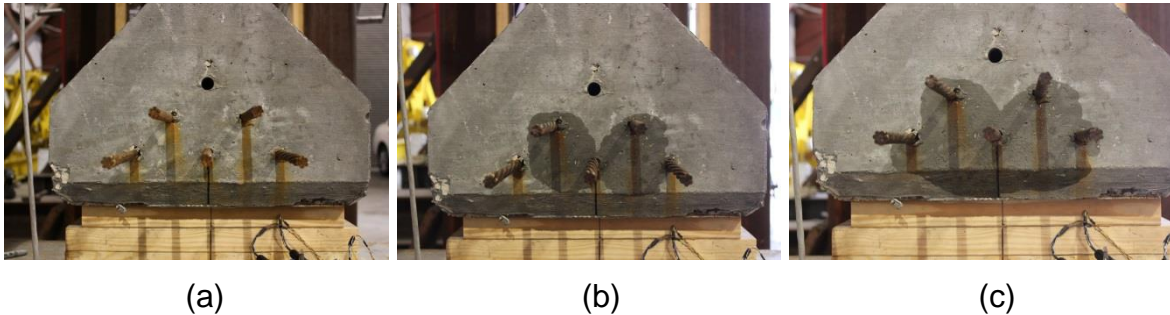


Figure 13-5. SU: (a) Prior (b) 35 minutes (c) 40 minutes

13.2 Coupler Observations

Evidence of improper seating of one wedge in specimen F1, perhaps resulting in notching of the strand and affecting the fatigue capacity. Figure 12-43 shows the coupler from one of the top row strands from specimen F1. The wedge was improperly seated, with concrete slurry holding it in place.

CHAPTER 14 SUMMARY AND CONCLUSIONS

This report presents research and development of a new splice technique to lengthen the span of transportable precast prestressed concrete girders. The design and development of the splice focused on an intended application: a simply-supported I-girder with a span length of greater than 200 ft. Utilizing the FDOT's longest spanning I-girder section, the FIB96, a prototype beam design for a 208-ft simply-supported span provided the shear and moment demand on the splice for an example case. The bridge was designed in accordance with AASHTO-LRFD 2007 (AASHTO 2007) and the FDOT Structural Design Guidelines (SDG) (FDOT 2010).

A splice design was then developed and integrated into the prototype design, in coordination with the FDOT design office. In the proposed splice design, transportable segments are pretensioned at a precast yard and the strands are cut prior to transport and then spliced on site. Prestressing force is applied to the system by a hydraulic jack on each side of the girder web. External brackets transfer the force from the hydraulic jacks to the precast segments by thru-bolts that pass through the web of the beam. The internal restraint provided by the coupled prestressing strand resists the jacking force, and the prestressing strand is stressed.

To evaluate the splice design assembly procedures and structural behavior, nine specimens were constructed using the AASHTO Type II cross-section; three control specimens and six spliced specimens were fabricated. To accomplish this, fifteen precast prestressed segments were constructed at a precast facility. The precast segments were then transported to the FDOT Structures Research Lab where six spliced specimens were assembled, splices stressed and closures poured. The

assembly and stressing procedure included instrumentation to evaluate the procedure. Decks were poured on each specimen in preparation for testing. Though labor-intensive, the prestressed splice concept was constructible.

Load testing of the completed specimens was conducted to evaluate flexural, shear, and fatigue behavior. Prestress losses were measured and cracking development was observed to assess service behavior. Additional component testing of the coupler used in the splice design was performed at the State Materials Office.

The following are significant findings from this research:

- Observed prestress losses in the splice region were ranged from 5-10%, which is less than typical values (10-20%).
- Crack opening occurred primarily at the vertical interface of the closure pour in tests of the spliced specimens.
- Flexural strength of spliced specimens exceeded the AASHTO-LRFD values for bonded strand by 15% and for unbonded strand by 24%.
- Fatigue of spliced specimens did not impact the strength or deflection at ultimate load; it did, however, affect ductility and failure mode. Fatigued specimens (FC, F1, F2) collapsed due to strand rupture at peak load.
- At ultimate load, the non-fatigued spliced specimen tested in four-point bending (X1) failed in compression (as the deck crushed); fatigued spliced specimens (F1 and F2) failed when strands ruptured.
- Fatigued spliced specimens (F1 and F2) exhibited greater fatigue resistance than the fatigued control specimen (FC). F1 and F2 survived 2 million cycles; FC survived only 518,000 cycles of cyclic loading.
- Fatigue cycling reduced displacement capacity when compared to static (non-fatigued) specimens during the ultimate load test. Non-fatigued XC and X1 had ductility ratios of 60 and 43, respectively. Fatigued specimens FC, F1 and F2 had ductility ratios of 4, 35, and 25, respectively.
- Non-fatigued flexure spliced specimen (X1) deflected an additional 1 in. beyond peak load-supporting at least 98% of the peak load.
- The shear test set-up imposed a moment to shear ratio (M/V) ratio of 3.7, which imposed a much higher relative shear than is present in the prototype FIB96

design (32.9). In the one specimen that did exhibit the characteristics of a shear failure, the vertical interface of the dry joint/closure pour was the location of failure and the shear strength of the spliced specimens exceeded the shear strength calculated per AASHTO-LRFD modified compression field theory.. All other specimens tested in the shear set-up failed in flexure.

- Shear strength of spliced specimens was shown to be moderately improved (9%) through additional stirrups and epoxy application to the joint.
- Disturbance of the “transfer length” region of the bonded segment occurred during the stressing procedure, resulting in an area susceptible to crack initiation.
- Couplers did not appear to generate excessive cracking in the closure pour concrete. Coupler congestion did not appear to affect the service performance.
- At ultimate, couplers acted as anchorage points, maintaining a significant portion of prestress force in the strand.

LIST OF REFERENCES

- AASHTO. (2007). AASHTO LRFD Bridge Design Specifications (4th edition with 2007 interim revisions). American Association of State Highway and Transportation Officials, Washington D.C.
- Abdel-Karim, A. M., and Tadros, M. K. (1992). "Design and Construction of Spliced I-Girder Bridges." *PCI Journal*, 37(4), 114-122.
- Abdel-Karim, A. M., and Tadros, M. K. (1992b). "State-of-the-Art of Precast/Prestressed Concrete Spliced I-Girder Bridges" Precast/Prestressed Concrete Institute, Chicago, IL.
- ACI 318-08. (2008). Building Code Requirements for Structural Concrete (ACI318-08) and Commentary. American Concrete Institute, Farmington Hills, MI.
- ASTM A416. (2006). Standard Specification for Steel Strand, Uncoated Seven-Wire for Prestressed Concrete. West Conshohocken, PA: ASTM International.
- ASTM A1061. (2009). Standard Test Methods for Testing Multi-Wire Steel Strand. West Conshohocken, PA: ASTM International.
- ASTM C39. (2010). Standard Test Method for Compressive Strength of Cylindrical Concrete Specimens. West Conshohocken, PA: ASTM International.
- Castrodale, R. W., and C. D. White. (2004). NCHRP Report 517: Extending Span Ranges of Precast Prestressed Concrete Girders. (Vol. 517). Transportation Research Board, Washington D.C.
- Collins, M. P. and Mitchell, D. (1991). *Prestressed Concrete Structures*. Prentice Hall.
- FDOT (Florida Department of Transportation). (1999). Gandy Bridge Construction Drawings, FDOT, Tallahassee, FL.
- FDOT (Florida Department of Transportation). (2004). New Directions for Florida Post-Tensioned Bridges: Design and Construction Inspection of Precast Concrete Spliced I-Girders. Vol. 4, FDOT, Tallahassee, FL.
- FDOT (Florida Department of Transportation). (2009). Temporary Design Bulletin C09-01, FDOT, Tallahassee, FL.
- FDOT (Florida Department of Transportation). (2009b). Temporary Design Bulletin C09-05, FDOT, Tallahassee, FL.
- FDOT (Florida Department of Transportation). (2010). FDOT Structures Manual, FDOT, Tallahassee, FL.

- FDOT (Florida Department of Transportation). (2010b). FDOT LRFD Prestressed Beam v 3.2 MathCAD program, FDOT, Tallahassee, FL.
- FDOT (Florida Department of Transportation). (2010c). *Bridge Maintenance and Repair Handbook*, FDOT (2010), Tallahassee, FL.
- Gerwick, B. C., Jr. (1993). *Construction of Prestressed Concrete Structures*. 2nd Ed. Wiley-Interscience, New York, NY.
- Hsu, T.T.C (1993). *Unified Theory of Reinforced Concrete*. CRC Press, Boca Raton, FL.
- International Code Council Evaluation Service (ICCES). (2011). Acceptance Criteria for Post-Tensioning Anchorages and Couplers of Prestressed Concrete. Whittier, CA: ICCES.
- Jaber, F., Tadros, M. K., Fallaha, S., Chuanbing, S., and Morgan-Girgis, A.F. (2006). "Nebraska Precast Record: 204th Street Bridge Spans Single Point Interchange." *PCI Journal* 51(6), 48-54.
- Johnson, Bruce. "RE: Citizen's Representative Office – Customer Entry." (Oregon DOT). Email to Natassia Brenkus. Aug 29 2011.
- Joint PCI-PTI Committee on Segmental Construction. (1982) "Recommended Practice for Precast Post-Tensioned Segmental Construction."
- Kaar, P.H., LaFraugh, R.W. and Mass, M.A, (1963). "Influence of Concrete Strength on Strand Transfer Length." *PCI Journal*, 8(5), 47-67.
- Kim, J., Chung, W. and Kim, J. H. J. (2008) "Experimental Investigation On Behavior Of A Spliced PSC Girder With Precast Box Segment", *Engineering Structures*, 30(11), 3295-3304.
- Labia, Y., Saiidi, M., and Douglas, B. (1996). CCEER-96-2 Evaluation and Repair of Full-Scale Prestressed Concrete Box Girders. University of Nevada, Reno, NV.
- Lacey, G. C., Breen, J. E. and Burns, N. H. (1971). "State of the Art for Long Span Prestressed Concrete Bridges of Segmental Construction." *PCI Journal*, Sept-Oct 1971, 53-77.
- Law Engineering (1990). Tensile test results of Enerpac Precision Sure-lock Grabb-it. Provided by Enerpac (manufacturer). Tests performed by Law Engineering.
- Loper, J. H., Marquis, E. L. and Rhomberg, E. J. (1988). "Precast Prestressed Long-Span Bridges." *ASCE Journal of Construction Engineering and Management*, 114(1), 95-103.

- Lounis, Z., Mirza, M. S. and Cohn, M. Z. (1997). "Segmental and Conventional Precast Prestressed Concrete I-Bridge Girders." *ASCE Journal of Bridge Engineering*, 2(3), 73-82.
- Ministry of Transportation of Ontario. (2011). "Many Innovations Make Light Work: Dingman Drive Bridge Repaired Using a Suite of Cost-Saving Innovations." *Road Talk*, 17(1), 1-2.
- Nicholls, J. J., and Prussack, C. (1997). "Innovative Design and Erection Methods Solve Construction of Rock Cut Bridge." *PCI Journal*, 42(4), 42-55.
- Nikzad, K., Trochalakis, T., Seguirant, S.J., and Khaleghi, B. (2006). "Design and Construction of the Old 99 Bridge—An HPC Spliced-Girder Structure." *PCI Journal*, Jan-Feb 2006, 98-109.
- O'Neill, C. M. and Hamilton, H.R. (2009). "Determination of Service Stresses in Pretensioned Beams." *FDOT Research Report No. 00063967*. FDOT, Tallahassee, FL.
- Onyemelukwe, O.U., Moussa Issa, P.E., and Mills, C.J. (2003). "Field Measured Prestress Concrete Losses Versus Design Code Estimates." *Experimental Mechanics*. 43(2), 201-215.
- Overman, T.R., Breen, J.E., and Frank, K.H. (1984). "Fatigue Behavior of Pretensioned Concrete Girders." *Research Report No. FHWA/TX-85/39+300-2F*. Texas State Department of Highways and Public Transportation, Austin, TX.
- PCI (2004). *PCI Design Handbook: 6th Edition*, Precast/Prestressed Concrete Institute, Chicago, IL.
- Pessiki, S., Kaczinski, M. and Wescott, H.H. (1996). "Evaluation of Effective Prestress Force in 28-Year-Old Prestressed Concrete Bridge Beams." *PCI Journal*, 78-89.
- Rabbat, B. G., Kaar, P.H., Russell, H. G. and Bruce (Jr), R.N. (1979). "Fatigue Tests of Pretensioned Girders with Blanketed and Draped Strands." *PCI Journal*, July-August 1979, 88-114.
- Rabbat, B. G., and Russell, H. G. (1982). "Optimized Sections for Precast Prestressed Bridge Girders." *Journal Prestressed Concrete Institute* 27.4: 88-104.
- Ralls, M. L., Aktan, A. E. and Culmo, M. P. (2000). *Concrete Bridges: Transportation in the New Millennium*. Transportation Research Board, Washington D.C.
- Rao, C. and Frantz, G.C. (1996) "Fatigue Testing of 27-Year-Old Prestressed Concrete Bridge Girder Box Beams." *PCI Journal*, Sept-Oct 1996, 74-83.

- Roller, J.J., Russell, H.G., Bruce, B.N. and Martin, B.T. (1995). "Long-Term Performance of Prestressed, Pretensioned High Strength Concrete Bridge Girders." PCI Journal, Nov-Dec 1995, 48-59.
- Ronald, H.D. (2001). "Design and Construction Considerations for Continuous Post-Tensioned Bulb-Tee Girder Bridges." PCI Journal, May-Jun 2001, 44-66.
- Russell, B.W. and Burns, N.H. (1993). "Static and Fatigue Behavior of Pretensioned Composite Bridge Girders Made with High Strength Concrete." PCI Journal, 116-128.
- Saibabu, S., Srinivas, V., Sasmal, S., Lakshmanan, N. and Iyer, N. R. (2013) "Performance Evaluation of Dry and Epoxy Jointed Segmental Prestressed Box Girders Under Monotonic and Cyclic loading", Construction and Building Materials, 38, 931-940.
- Saidii, M. S., Labia, Y. and Douglas, B. (2000). "Repair and Performance of a Full-Scale Pretensioned Concrete Girder." PCI Journal, Mar-Apr 2000, 92-101.
- Seguirant, S. J. (1998). "New Deep WSDOT Standard Sections Extend Spans of Prestressed Concrete Girders." PCI Journal, 92-105.
- Shanafelt, G.O. and Horn, W.B. (1980). NCHRP Report 226: Damage Evaluation and Repair Methods for Prestressed Concrete Bridge Members. Transportation Research Board, Washington D.C.
- Shanafelt, G.O. and Horn, W.B. (1985). NCHRP Report 280: Guidelines for Evaluation and Repair of Prestressed Concrete Bridge Members. Transportation Research Board, Washington D.C.
- Waheed, A. P., Kowal, E. and Loo, T. (2005). Repair Manual for Concrete Bridge Elements. Alberta Infrastructure and Transportation. Province of Alberta, Canada.
- Walsh, K.Q. and Kurama, Y.C. (2010). "Behavior of Unbonded Post-Tensioning Monostrand Anchorage Systems Under Monotonic Tensile Load." PCI Journal, Winter 2010, 97-114.
- Weigel, J. A., Seguirant, S.J., Brice, R. and Khaleghi, B. (2003). "High Performance Precast, Pretensioned Concrete Girder Bridges in Washington State." PCI Journal, 48(2), 28-52.
- Zia, P. and Mostafa, T. (1977). "Development Length of Prestressing Strands." PCI Journal, 22(5), 54-65.
- Zia, P., Preston, H.K., Scott, N.L., and Workman, E.B. (1979). "Estimating Prestress Losses." Concrete International, 1(6), 32-38.

Zobel, R. S., Jirsa, J.O., Fowler, D.W. and Carrasquillo, R.L. (1997) "Evaluation and Repair of Impact Damaged Prestressed Concrete Bridge Girders." Research Report No. FHWA/TX-97/1370-3F. Texas State Department of Highways and Public Transportation, Austin, TX.

Zobel, R.S. and Jirsa, J.O. (1998). "Performance of Strand Splice Repairs in Prestressed Concrete Bridges." PCI Journal, Nov-Dec, 72-78.

BIOGRAPHICAL SKETCH

Natassia R. Brenkus received her Bachelor of Science in 2006 from the University of Florida. She worked as a design engineer in commercial building construction for five years before returning to U.F. She received her Master of Engineering in 2013. Her research interests include structural behavior and durability of prestressed concrete.